2022

Multi-Modal Regualtion of Actin Networks

Lin Mei

MULTI-MODAL REGULATION OF ACTIN NETWORKS

A Thesis Presented to the Faculty of

The Rockefeller University

in Partial Fulfillment of the Requirements for

the degree of Doctor of Philosophy

by

Lin Mei

June 2022

Multi-modal Regulation of Actin Networks

Lin Mei, Ph.D.

The Rockefeller University 2022

Eukaryotic cells employ the actin cytoskeleton to maintain cell shape, support motility, and sense and respond to external mechanical stimuli. An intricate network of actin filaments constitutes the foundation of tissue architecture by forming key cellular structures including the muscle fiber, the filopodium, the lamellipodium, and the cell cortex. Cellular and tissue level studies have shown that more than 150 actin-binding proteins regulate almost every single aspect of actin physiology, such as actin polymerization, actin severing, and actin crosslinking, but at the molecular level, the structural mechanisms by which different actin binding proteins bind, assemble, and regulate different actin networks remain largely elusive. It is also known that the actin cytoskeleton mediates mechanical coupling between eukaryotic cells and their tissue microenvironments. Although cellular and tissue level studies suggest the architecture and composition of actin networks are modulated by force, it is still unclear how interactions between actin filaments and associated proteins are mechanically regulated. Force-sensitive actin binding interactions are fundamental for cells to sense and respond to mechanical stimuli by converting mechanical cues into biochemical signals, a key process known as cellular mechanotransduction.

In this thesis, single molecule biophysical techniques including simultaneous optical trapping and confocal microscopy assays and *in vitro* reconstituted myosin

motor-based total internal reflection fluorescence microscopy assays were employed to study how mechanical forces applied on actin filaments can regulate actin binding. A case study on a homologous pair of essential adhesion actin-binding proteins, α-catenin and vinculin, reveals α-catenin directly senses force on actin, while vinculin does not. Near atomic-resolution cryo-electron microscopy structures of both proteins bound to F-actin, structure-guided protein engineering, and ongoing nuclear magnetic resonance and force reconstitution cryo-electron microscopy studies demonstrate that α-catenin's C-terminus is a modular detector of F-actin tension and suggest a force-sensing mechanism.

Cryo-electron microscopy was also employed to study how adhesion actin-binding proteins and the calponin-homology domain actin-binding proteins assemble cellular actin networks by binding and crosslinking actin filaments. Actin binding by another essential adhesion actin-binding protein talin, and actin bundling by both α-catenin and vinculin were additionally structurally characterized. Using a unique calponin-homology domain actin-binding protein, T-plastin, as an example, the thesis established the structural mechanism by which T-plastin crosslinks actin filaments. In summary, with biochemical, biophysical, and structural methods, this thesis systematically studied the molecular mechanisms for the multi-modal regulation of actin networks by actin binding proteins.

Acknowledgements

First and foremost, I would like to thank my Ph.D. advisor, Dr. Gregory M. Alushin. Greg is a brilliant and rigorous scientist, a patient and responsible mentor, and above all else, a kind and generous man. It is in Greg's lab and because of Greg's mentorship that my academic life as a biochemist starts. If in the future I can become an independent scientist, it is because of everything Greg has taught me: From single-molecule biophysics to structural biology, from experimental design to data analysis, from scientific presentation to academic writing, I learned everything I need to learn as a scientist from Greg. I admire Greg's integrity, his passion for science, his outstanding achievements, and his extraordinary talent. There is no doubt Greg is one of the most gifted scientists in his generation, which makes it an almost bittersweet experience working with him because you will be constantly questioning yourself whether you are good enough to be a scientist. Like every other relationship in life, the relationship between me and Greg has ups and downs. We do have our differences, but I genuinely enjoyed our discussions, and I have never regretted joining Greg's lab in April 2017. For more than four years, it is Greg's support, encouragement, and friendship that has driven my growth, helped me navigate my life in the U.S., and helped me move forward. It is my distinct privilege to be Greg's first student and the first Ph.D. graduated from this lab. I wish Greg and the lab the very best in the future.

I would like to thank my collaborator and thesis committee chairman, Dr. Shixin Liu. Ever since our collaboration on the optical trapping experiments, Shixin has always

been willing to share with me his expertise and experience. To me personally, Shixin has always been a role model. I am truly indebted to him for his unwavering support at every step of this journey. I would like to thank my committee members Dr. Seth Darst and Dr. Morgan Huse, whose generous support and career advice have been invaluable. The annual committee meetings made sure I stayed on the right path. This thesis would certainly not be possible without the help of my committee members.

I would also like to thank Dr. William Weis of Stanford University for serving as my external examiner. For a young scientist who just entered the field of cell adhesion, it is truly an honor to have one of the pioneers of the field at the thesis defense.

I would like to thank Dr. Derek Tan, director of the Tri-Institutional Ph.D. Program in Chemical Biology (TPCB), Ms. Margie Hinonangan-Mendoza, and everyone from the TPCB management. I would also like to thank Rockefeller Dean's office, especially Ms. Kristen Cullen and Mr. Cris Rosario for all the assistance. Rockefeller is a great place to do science. I have never regretted joining TPCB and Rockefeller.

I would like to thank all my collaborators. Dr. Rachel Leicher in the Liu lab at Rockefeller helped me collect many optical trapping datasets during the COVID-19 pandemic. I would like to thank Dr. Tobias Meyer and his former postdoc Dr. Damien Garbett, with whom we have had a wonderful collaboration on T-plastin. I would like to thank Dr. Alex Dunn and his former graduate student Dr. Leanna Owen at Stanford University, with whom we have worked and will continue to work on talin. I would like to thank Dr. David Eliezer and his former graduate student Dr. Tapojyoti Das at Weill Cornell, with whom we managed to get beautiful NMR data of α-catenin. I would like to

thank Dr. Mark Ebrahim, Ms. Johanna Sotiris, and Mr. Honkit Ng at the Evelyn Gruss Lipper Cryo-EM Resource Center (CEMRC) at Rockefeller, who have made my cryo-EM data collection experiences as great as I could possibly imagine. I would also like to thank Dr. Henrik Molina at the Proteomics Resource Center (PRC) and Dr. Deena Oren at the Structural Biology Resource Center (SBRC) at Rockefeller.

I would like to thank all past and present members of the Alushin lab for their help and camaraderie over the years. I can never forget my rotation mentor Dr. Pinar S. Gurel, who introduced me to the world of TIRF microscopy and gave me honest opinions on almost everything in life. My special thanks go to Santiago Espinosa de los Reyes and Matthew Reynolds, with whom I have collaborated on multiple projects. I have always enjoyed working with and learning from Santi and Matt. I would like to thank Ayala Carl, the only other TPCB student in the lab, for all the fun and sadness we have shared together. I would like to thank Dr. Rui Gong, Dr. Xiaoyu Sun, Joseph Levin, Donovan Phua, and Carla Hachicho for all the help and discussions. I would like to thank all rotation and summer students who have worked with me, in particular, Alfred Chin, who is going to join the lab and continue working on adhesion proteins. I would like to thank new lab members Dr. Keith Hamilton and John Watters, who are great scientists and will accomplish great achievements in the lab.

At this very moment when I am prepared to embark on a new journey, to my family and my friends, to the countless others who have accompanied me and shepherded me throughout life, thank you.

TABLE OF CONTENTS

LIST OF FIGURES AND TABLES

CHAPTER 1

General introduction

Note to readers: This thesis was adapted in part from two published journal articles by the author. The two journal articles, Mei et al., 2020, and Sarker et al., 2019, have been attached to this thesis as Appendix 1 and Appendix 2, respectively.

1.1 The actin cytoskeleton is a central player in cellular mechanobiology

Sensing and responding to mechanical stimuli is one the most fundamental features of life (Iskratsch et al., 2014), which relies on converting mechanical cues into biochemical signals, a process known as mechanotransduction (Harris et al., 2018). Mechanisms for cellular mechanotransduction is a central topic of mechanobiology (Ladoux and Mege, 2017). Traditionally, mechanobiology research has been done at the cellular and tissue levels. However, at the molecular level, the mechanisms for cell to sense and transduce mechanical signals remain almost completely unknown.

Cells probe and respond to the mechanical properties of their surroundings through cytoskeletal networks composed of the actin cytoskeleton (Figure 1-1), one of the three major cytoskeletons in the cell (Jegou and Romet-Lemonne, 2021). These networks transmit forces through cell-matrix focal adhesions (Humphrey et al., 2014) and cell-cell adherens junctions (Charras and Yap, 2018), plasma membrane-associated many-protein assemblies which serve as hubs for the conversion of mechanical cues and stimuli into biochemical signaling cascades (Figure 1-1)

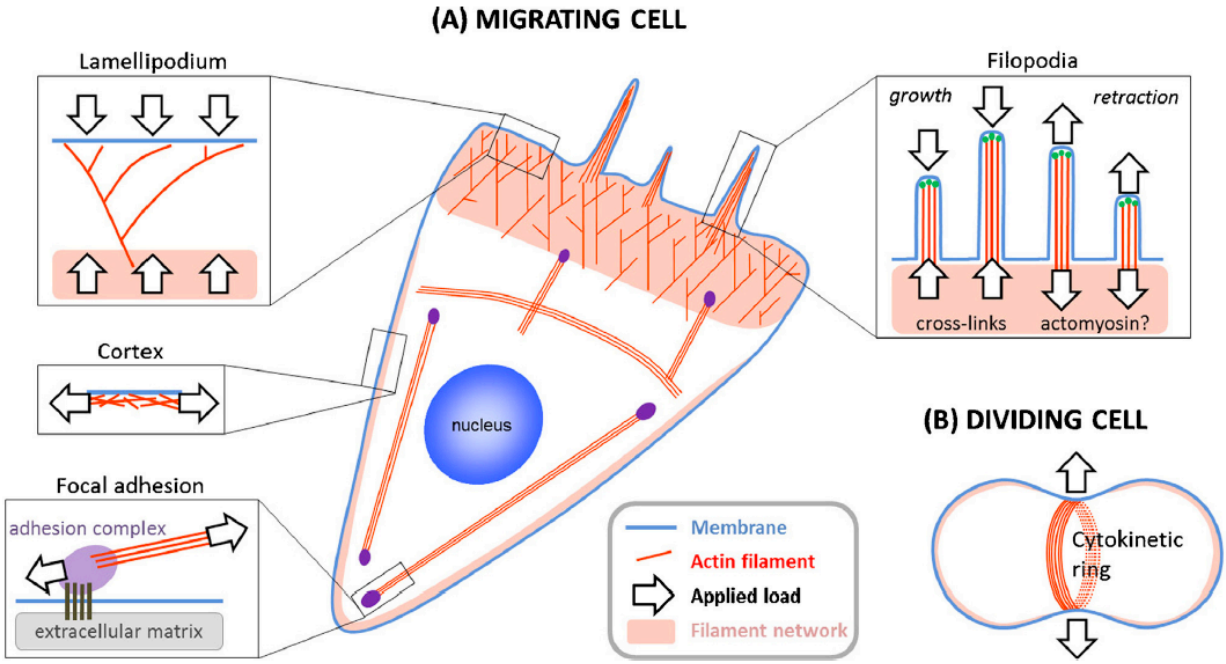

Figure 1-1. Cellular structures constructed by, and mechanical constraints applied to actin filaments. *(adapted from G. Romet-Lemonne; A. Jegou, European Journal of Cell Biology 92 (2013) 333– 338)*

Examples of cellular structures constructed by, and mechanical constraints applied to actin filaments in migrating cells (A) and dividing cells (B).

("mechanotransduction"). Defects in mechanotransduction are associated with numerous diseases (Jaalouk and Lammerding, 2009), including muscular dystrophies, cardiomyopathies, and metastatic cancer, yet therapeutics which specifically target these pathways are largely absent due to our ignorance of the mechanisms that transduce mechanical signals through the cytoskeleton.

There are 6 types of highly conserved and homologous actin isoforms in human cells, all forming flexible biopolymers 7nm in diameter with an approximately 10μm persistence length (Figure 1-2) (Blanchoin et al., 2014). Filamentous actin (F-actin) is assembled by two strands of polymerized globular actin (G-actin) through non-covalent intra-strand longitudinal interactions and inter-strand lateral interactions (von der Ecken et al., 2015). An actin filament has intrinsic structural polarity because all of its G-actin protomers must point to the same direction to polymerize. When G-actin protomers polymerize into an actin filament, its two ends have different polymerizing rates and depolymerizing rates. For F-actin, the end that grows relatively faster and depolymerizes relatively slower is named the plus end, or the barbed end according to its shape under the electron microscope, of F-actin (Blanchoin et al., 2014), and the other end is named the minus end, or the pointed end. In human cells, more than 150 actin-binding proteins (ABPs), including myosin motor proteins, actin-nucleating proteins, and actin-severing proteins, bind G-actin or F-actin with distinct families of actin-binding domains (ABDs) to regulate every single aspect of actin physiology (Pollard, 2016).

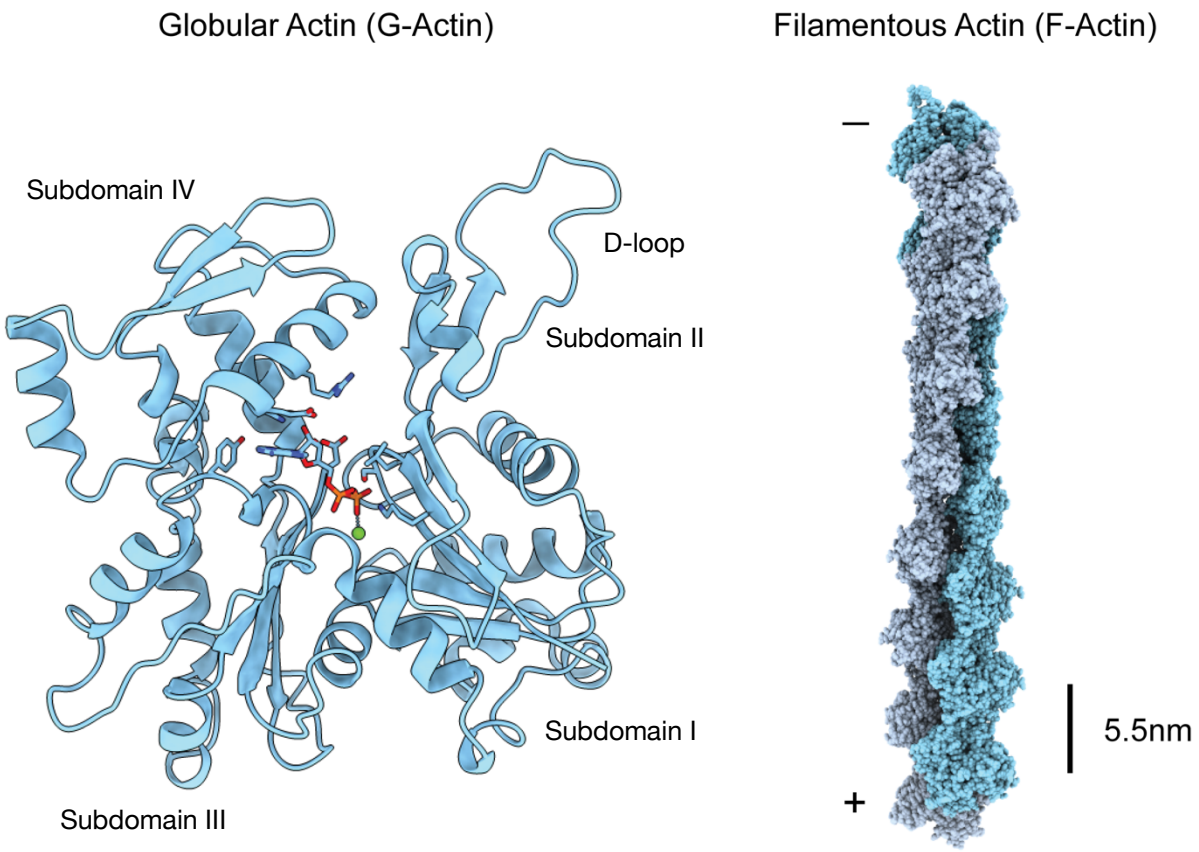

Figure 1-2. Molecular structures of globular actin (G-actin) and filamentous actin (F-actin).

G-actin subdomains 1-4, G-actin DNase I binding loop (D-loop), and the plus end and the minus end of F-actin are labeled. Scale bar, 5.5 nm.

In vivo, diverse force regimes modulate the polymerization dynamics, micron-scale architecture, and protein composition of actin assemblies by molecular mechanisms which remain unclear (Harris et al., 2018; Romet-Lemonne and Jegou, 2013). Cellular-scale pressures in the range of hundreds of pascal regulate the assembly and mechanical power of branched-actin networks generated by the actin-related protein Arp2/3 complex *in vitro* (Bieling et al., 2016) and *in vivo* (Mueller et al., 2017), tuning network geometric properties including filament length, density, and distribution of filament orientations. Live-cell imaging studies identified a subset of ABPs that preferentially localize to the cytoskeleton *in vivo* in response to this magnitude of mechanical stimulation (Schiffhauer et al., 2016), which were also postulated to recognize properties of network geometry. Molecular-scale forces in the piconewton range have also been shown to modulate the activity of F-actin polymerization (Courtemanche et al., 2013; Jegou et al., 2013; Risca et al., 2012; Zimmermann et al., 2017) and severing (Hayakawa et al., 2011) factors *in vitro*, suggesting that molecular components of actin networks could be mechanically-regulated by physiological forces. While F-actin binding by the actin-depolymerization factor cofilin was reported to be directly regulated by tension across the filament to modulate its activity (Hayakawa et al., 2011), a recent study has suggested that cofilin is tension-insensitive, instead having its severing activity regulated by filament bending (Wioland et al., 2019). For F-actin to sense and transduce mechanical signals, the first and the most fundamental step is a special subset of force-sensitive actin-binding proteins must sense mechanical forces on actin. Although whole cell stretching and micropipette aspiration assays

(Schiffhauer et al., 2016) have suggested a subset of ABPs may be responsive to mechanical forces on actin, cellular assays can hardly distinguish direct force sensing from indirect downstream effects. Well-established biophysical methods to identify ABPs that can directly sense mechanical forces applied on actin filaments at the molecular level are needed (Sun et al., 2020; Winkelman et al., 2020). To prove an ABP can directly sense force on actin, a force system has to be reconstituted *in vitro*. To date, structural mechanisms that enable some ABPs to sense force on actin remain elusive.

For decades, structural biologists have worked to elucidate molecular structures of G-actin, F-actin, and actin–ABP complexes (Dominguez and Holmes, 2011). For X-ray crystallographers, actin was a difficult target: due to the actin monomer's relatively low critical concentration, G-actin strongly tends to polymerize in the high-salt solutions used for growing protein crystals. After polymerization, the non-uniform lengths of F-actin and its filamentous nature are not compatible with crystallographic symmetry (Dominguez and Holmes, 2011). A major breakthrough happened in 1990 when K. C. Holmes and colleagues discovered G-actin binds DNase I with high affinity and this interaction prevents G-actin from polymerizing into F-actin, by which they solved the first high-resolution structure of G-actin (Kabsch et al., 1990). Since then, more than 80 G-actin crystal structures have been solved by inhibiting the polymerization of G-actin (Dominguez and Holmes, 2011). In 1990, based on their G-actin structure, K. C. Holmes and colleagues constructed the first model for F-actin by fitting the G-actin model in the observed X-ray fiber diffraction pattern (Holmes et al., 1990), but the

preliminary results did not have the sufficient resolution to explain the dynamic structural transitions accompanying polymerization and depolymerization, known as the globular (G) to fibrous (F) actin transition, at the molecular level. In 2007, Oda and colleagues, using superior X-ray fiber diffraction techniques, obtained an F-actin structure with 3.3-Å radial resolution and 5.6-Å equatorial resolution from well oriented sols of rabbit skeletal muscle, for the first time showing that the G-to-F transition entails a 20° relative re-orientation between G-actin's inner domain (containing subdomains 3, 4) and its outer domain (containing subdomains 1, 2) (Oda et al., 2009). However, a true real-space F-actin atomic model with experimental phase information was still technically prohibitive.

The rapid development and the resolution revolution of cryo-electron microscopy (Cryo-EM) (Kuhlbrandt, 2014) has fundamentally changed the field of actin structural biology. In X-ray crystallography and X-ray fiber diffraction methods, actin has to be studied under highly non-native conditions (Dominguez and Holmes, 2011). In contrast, Cryo-EM allows biological samples to be studied at near-native conditions (Cheng et al., 2015). For helical polymers like actin, a major breakthrough on the data-processing algorithms, named iterative helical real space reconstruction (IHRSR), allows near-atomic resolution 3D reconstructions (Egelman, 2007). In 2010, a 6.6-Å Cryo-EM structure, for the first time, directly visualized the secondary structures of F-actin (Fujii, et al., 2010) and validated the molecular mechanism for the G-to-F transition. In recent years, several high-resolution F-actin structures and true atomic models based on better than 4 Å data have been reported (von der Ecken et al., 2015; von der Ecken et al., 2016). By cryo-EM, the native conformation of F-actin and its highly diverse interactions

with ABPs can be studied. F-actin has been reported to adopt a structural landscape of co-existing conformations in cryo-electron microscopy (cryo-EM) studies (Egelman et al., 1982; Galkin et al., 2010b), leading to speculation that actin filaments could themselves serve as tension sensors by presenting distinct binding interfaces to ABPs in the presence of load (Galkin et al., 2012). It nevertheless remains unclear to what extent mechanical modulation of functional interactions between ABPs and F-actin occurs through direct regulation of F-actin's binding interactions by force. Furthermore, structural mechanisms enabling ABPs to detect force on F-actin, to our knowledge, are unknown.

1.2 Actin networks and high-order actin assemblies

In eukaryotic cells, G-actin monomers polymerize into F-actin cytoskeletal networks to maintain cellular shape, generate force, and support motility. This machinery relies on the organization of F-actin into a variety of high-order actin assemblies which constitute different mesoscale cellular structures (Tee et al., 2015), with the help of a diverse set of actin-binding proteins (Pollard and Cooper, 2009). Few actin-based cellular structures known are made directly from single actin filaments, which are structurally too flexible and mechanically too weak (Blanchoin et al., 2014). Higher-order actin assemblies are fundamentally composed of actin meshworks and actin bundles (Blanchoin et al., 2014): Actin meshworks, built by the only branching actin nucleator, the ARP2/3 complex, and its activator, the Wiskott-Aldrich Syndrome protein (WASP) (Higgs and Pollard, 2001), are essential for the survival of most cells,

where they serve as the mechanical support in the cell cortex (Svitkina, 2020), provide tracks for vesicle transport (Langford, 2002; Schuh, 2011), and, as discussed in Chapter 1.1, support cellular protrusion by pushing against the plasma membrane as they grow in a mechanosensitive way (Bieling et al., 2016; Mueller et al., 2017). Structural characterization of the molecular basis for ARP2/3-mediated actin branching and network formation has been a goal for structural biologists for decades. The crystal structure of the ARP2/3 complex alone has been solved (Robinson et al., 2001) and was docked into a low-resolution (32 Å) cryo-EM map of the ARP2/3–WASP–F-actin complex, the first structural analysis of actin-branching mechanism under near-native conditions (Volkmann et al., 2001). Similar to the development of the structural biology for actin filaments, structural characterization of actin branches has recently achieved remarkable progress by both single-particle cryo-EM (Shaaban et al., 2020) and cryo-electron tomography (cryo-ET) (Fäßler et al., 2020). However, 3D reconstruction of actin branches has not been obtained at near atomic resolutions, and more efforts will be necessary in the future to structurally reconstruct a full actin network.

Actin bundles constitute a variety of crucial cellular structures, such as muscle fibers, lamellipodia and filopodia (Garbett et al., 2020), stress fibers (Tojkander et al., 2012), microvilli (Sauvenet et al., 2015), the acrosome (Schmid et al., 2004), and the cytokinetic ring (Blanchoin et al., 2014). F-actin cannot bundle itself, but rather has to be crosslinked into actin bundles by a specialized subset of actin-binding proteins, hence named ‘actin-bundling proteins’. These actin crosslinkers control the composition, 3D geometrical arrangement (Shin et al., 2009), and most importantly, biochemical and

mechanical properties of actin bundles (Claessens et al., 2006; Weirich et al., 2017). Since actin filaments are polar, there are two possible orientations for a pair of neighboring single actin filaments to be assembled into a bundle: parallel, when the neighboring single filaments have the same polarity, and anti-parallel, when they have opposite polarities. Although both parallel and anti-parallel actin bundles have highly strengthened mechanical robustness compared to single actin filaments (Claessens et al., 2006), it has been speculated that different actin crosslinking proteins might preferentially induced parallel or anti-parallel actin bundles, which may have distinct functional roles in the cell, as it is well known that F-actin bundled by different actin bundlers have different biological functions (Falzone et al., 2012; Reymann et al., 2012). Dysfunction of actin-bundling proteins has been associated with numerous diseases such as cancer (Stevenson et al., 2012) and cardiomyopathy (Sarker et al., 2019). However, despite early efforts in imaging crystalline-like acrosomal bundles (Derosier et al., 1980; Schmid et al., 1993; Schmid et al., 2004; Shin et al., 2003; Shin et al., 2004), no structures of actin bundles have been reported in near-native, non-crystalline states, perpetuating a major gap in our understanding on the actin cytoskeleton. Despite recent progress in high-resolution cryo-EM structures of single actin filaments in complex with actin-binding proteins (Mei et al., 2020), to date no structural models of actin bundles have been reported by this method, which remains technically prohibitive. This is largely because the actin bundles are not stoichiometrically defined protein complexes, and the current IHRSR methods for single-filament processing, which require perfect helical symmetry, are not compatible with the geometry of actin bundles. As a result, the

questions on the structure-function relationship for actin bundles, such as whether certain actin-bundling proteins can preferentially induce parallel or anti-parallel bundles and whether this preference has a functional impact in the cell, remain unanswered because without a medium-to-high resolution structure, it is impossible to determine whether an actin bundle is parallel or anti-parallel.

1.3 Outline for this thesis

This thesis aims to address these outstanding questions by studying multimodal regulation of the actin cytoskeleton at the molecular level. In Chapter 2, the thesis describes our development of novel *in vitro* reconstituted biophysical assays to definitively identify and validate force-sensitive actin-binding proteins. In Chapter 3, the thesis describes our structural characterization of F-actin–ABP interactions by high-resolution cryo-EM. This enabled us to identify force-sensitive elements within a force-sensitive ABP by structure-guided biochemistry, facilitating dissection of the molecular mechanisms for force-sensitive actin-binding interactions. In Chapter 4, the thesis describes efforts in characterizing the structural diversity of actin filaments, actin bundles, and actin networks induced by actin-binding proteins in adhesion complexes. Finally, in Chapter 5, the thesis describes an effort to structurally characterize the actin crosslinking mechanism for the actin-bundling protein T-plastin, a key protein in cellular calcium sensing and actin network construction in filopodia. Chapter 6 summarizes the thesis, discusses general questions regarding the structure and function of actin networks, and introduces important future directions. Chapter 7 is the materials and

methods section for the entire thesis. Two published articles are attached as appendices, followed by the references section.

CHAPTER 2

Identification of Novel Force-sensitive Actin-binding Proteins

Note to readers: Part of the results discussed below arose from a collaborative effort between myself, my advisor Dr. Gregory M. Alushin, several colleagues in the Alushin Laboratory, including Mr. Santiago Espinosa de los Reyes and Mr. Matthew J. Reynolds, and several colleagues in the Liu laboratory, including Dr. Shixin Liu and Dr. Rachel Leicher, at the Rockefeller University.

2.1 Background: Actin-binding proteins in adhesion complexes

Membrane-associated cell-matrix and cell-cell adhesion complexes are the major mechanical link between cytoplasm and outside environment (Gumbiner, 1996). In multicellular organisms, cells must be held together by these junctional complexes to form organized organismal structures. The biological functions of these adhesions are intrinsically mechanical. Cells need to sense outside mechanical stimuli and respond to environmental mechanical cues. Therefore, the adhesion complexes which bind both membrane receptors and the cytoskeletal network are the natural direct mechanical linkage. For epithelial cells, there are two major kinds of cell-matrix adhesions on the basal side: focal adhesions (Burridge and Chrzanowska-Wodnicka, 1996) and hemidesmosome (Walko, 2015), as well as four major kinds of cell-cell adhesions on the lateral side: tight junctions (Otani and Furuse, 2020), gap junctions (Shimizu and Stopfer, 2013), adherens junctions (Shapiro and Weis, 2009), and desmosome (Stokes,

2007). With distinct biological functions, many of these junctional complexes are connected directly to the cytoskeleton: desmosome and hemidesmosome are connected to intermediate filaments; focal adhesion and adherens junctions are directly linked to the actin cytoskeleton by actin-binding proteins (ABPs) in the two adhesion complexes. The actin cytoskeleton is a central mediator for cellular mechanotransduction. Therefore, it is widely speculated that the major ABPs in adhesion complexes may sense mechanical forces on actin, and these potential force-sensitive actin-binding interactions serve as a major molecular basis for cells to sense environmental mechanical stimuli.

Reports have shown that ABP isoforms differentially mechanoaccumulate in cells (Schiffhauer et al., 2016), indicating that structural and biophysical analysis of closely-related ABPs could be a powerful approach for mechanistically dissecting force-sensitive F-actin binding. In this chapter, we focus our analysis on the homologous adhesion proteins α-catenin (Kobielak and Fuchs, 2004; Figure 2-1) and vinculin (Ziegler et al., 2006; Figure 2-1), major ABP components found in adherens junctions (α-catenin and vinculin) and focal adhesions (vinculin) that are critical for adhesion and cellular mechanotransduction (Dumbauld et al., 2013; Yonemura et al., 2010). Both proteins are entirely α-helical (Bakolitsa et al., 2004; Rangarajan and Izard, 2013; Figure 2-1), and are composed of a large N-terminal “head” domain, which engages in protein-protein interactions with other adhesion molecules (Kobielak and Fuchs, 2004; Ziegler et al., 2006) and a smaller C-terminal five-helix bundle F-actin binding domain (ABD) “tail” (Bakolitsa et al., 1999; Ishiyama et al., 2013) (Figure 2-2, Helix H1 to H5),

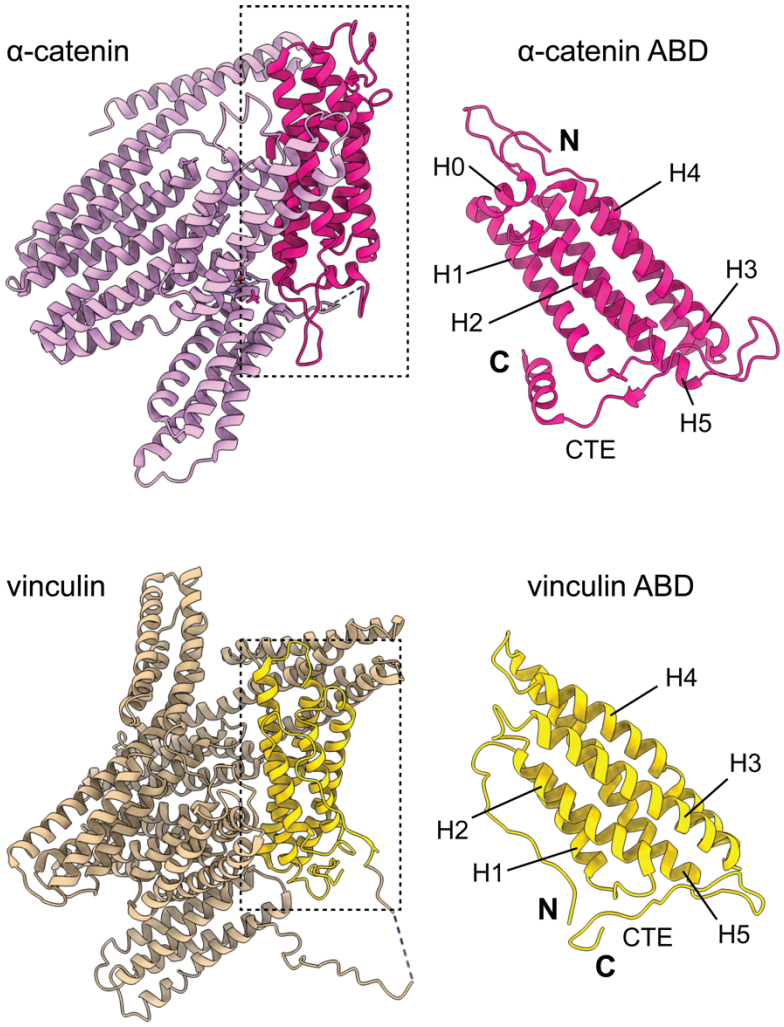

Figure 2-1. Adhesion proteins α-catenin and vinculin.

Crystal structures of human αE-catenin (PDB 4igg) and vinculin (PDB 1st6), displaying full-length proteins (left) and actin-binding domains (ABD, boxed regions on the left, zoomed in on the right).

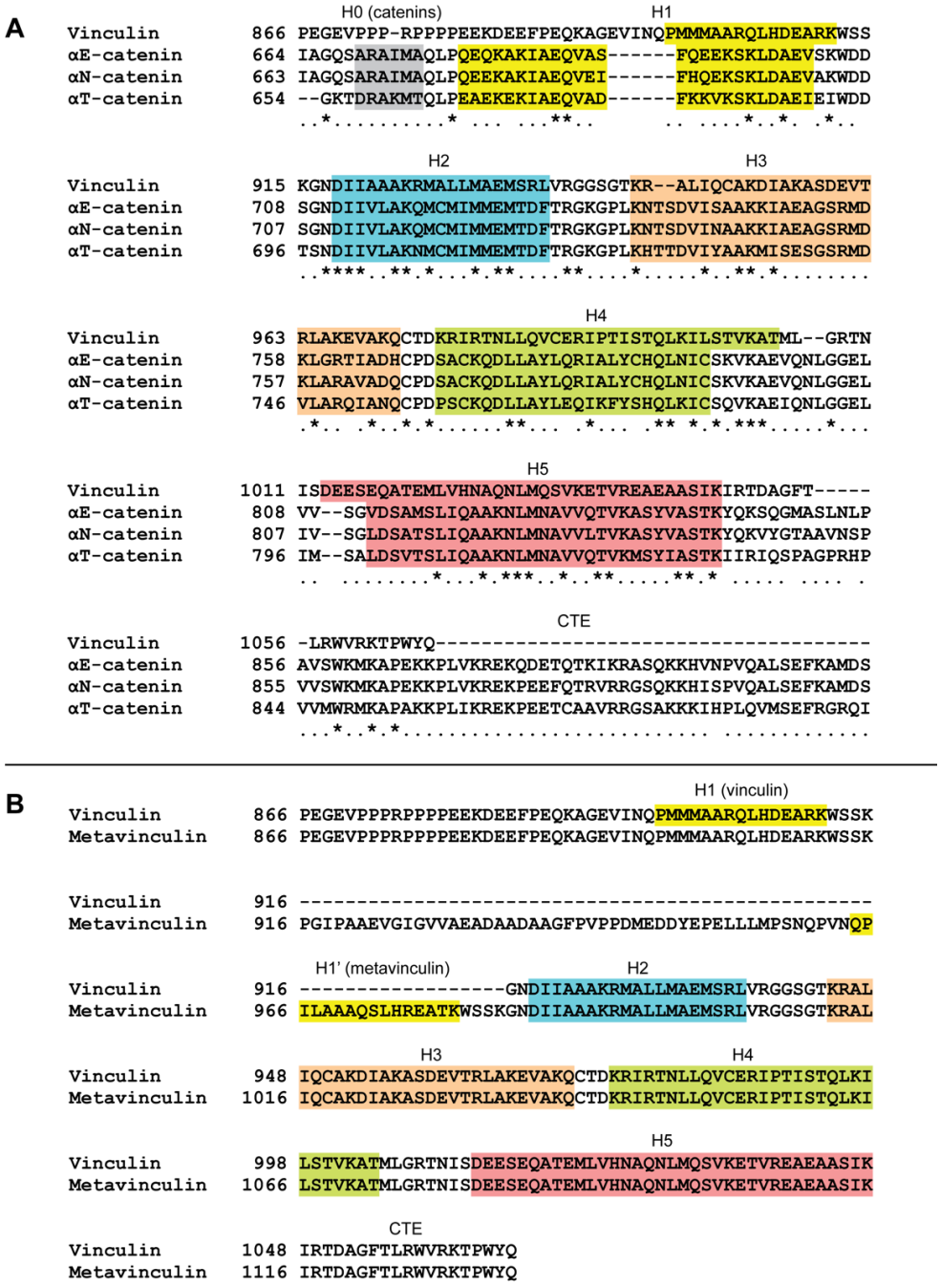

Figure 2-2. Multiple sequence alignments of human vinculin and α-catenin isoforms.

(A) Sequence alignment (see Materials and Methods) of human vinculin, αE-catenin, αN-catenin and αT-catenin. (B) Sequence alignment of human vinculin and metavinculin.

connected by a flexible proline-rich linker. The five helices in their ABDs are named H1 to H5 (Figure 2-1). Both ABDs feature a C-terminal Extension (CTE) on their very C-termini after H5 (Figure 2-1; Figure 2-2). The isolated ABDs of both vinculin and α-catenin retain the structural configurations found in their respective full-length molecules (Bakolitsa et al., 1999; Ishiyama et al., 2013; Bakolitsa et al., 2004; Rangarajan and Izard, 2013). In muscle cells, a vinculin splice variant, metavinculin, is co-expressed with vinculin, where a 68 amino-acid insert displaces the vinculin H1 helix and replaces it with helix H1', producing a protein which retains actin binding but completely loses actin bundling activity (Janssen et al., 2012; Kim et al., 2016; Oztug Durer et al., 2015) (Figure 2-1; Figure 2-2). Unlike vinculin, there are three human α-catenin isoforms, encoded by three genes (*CTNNA1-3*) (Figure 2-2), among which αE-catenin (CTNNA1) is the most abundantly and ubiquitously expressed isoform.

Full-length vinculin is a strictly auto-inhibited globular protein. In order to bind F-actin, full-length vinculin must first be activated by its binding partners (Johnson and Craig, 1995). α-catenin, on the other hand, exists in two distinct populations maintained in dynamic equilibrium in the cell (Drees et al., 2005): As a monomer, it serves as a central component of the membrane-anchored heterotrimeric α-catenin–β-catenin–cadherin complex (the "cadherin-catenin complex") at adherens junctions, which lacks F-actin-binding activity in traditional assays when isolated (Yamada et al., 2005). It also forms a soluble homodimer with constitutive modest F-actin-binding activity, thought to play a role in the generation and maintenance of actin bundles by cross-linking filaments and inhibiting Arp2/3 binding, thereby suppressing branched-actin formation

(Drees et al., 2005). The structural mechanisms by which forces transmitted through the actin cytoskeleton modulate these complex networks of actin binding interactions during adhesion maturation and adhesion maintenance remain unknown.

Recent single-molecule force-spectroscopy studies reported that both α-catenin in the cadherin-catenin complex (Buckley et al., 2014) and vinculin (Huang et al., 2017) form catch bonds with F-actin, characterized by increased bond lifetime when force is applied across the ABP-actin interface, with the vinculin-actin catch bond displaying a directional bias defined by the polarity of the actin filament (Huang et al., 2017). These studies provided one potential resolution to the apparent contradiction between biochemical studies demonstrating the cadherin-associated α-catenin population lacks F-actin binding activity (Drees et al., 2005) and cellular studies suggesting α-catenin plays a key role in linking adherens junctions to actomyosin cables (Kobielak and Fuchs, 2004). However, the geometry of these experiments, in which actin filaments suspended between two beads held in optical traps were translated across surface-tethered ABPs to probe binding events, entailed the actin filaments themselves being placed under tension prior to ABP engagement. It is not clear, in these experiments, whether it is force on actin or force on actin-binding proteins that increases binding lifetime. This leads to the hypothesis that force-activated binding to tensed F-actin, i.e., force exclusively on actin, could be a key regulatory mechanism at adhesions, promoting formation of initial attachments through membrane-anchored ABPs (e.g., the cadherin complex) prior to their coming under load, as well as serving as a mechanism to enrich soluble ABPs (e.g., the α-catenin dimer) whose binding geometry is

fundamentally incompatible with catch-bond formation. *In vivo*, both vinculin and α-catenin primarily engage contractile actomyosin bundles, whose component actin filaments are constitutively exposed to myosin-generated forces.

2.2 Novel simultaneous fluorescence microscopy and force spectroscopy assay

To determine whether the actin-binding activity of vinculin or α-catenin could be regulated solely by force across F-actin, we developed a novel correlative force spectroscopy and fluorescence microscopy assay with a commercial instrument (Hashemi Shabestari et al., 2017), which combines two cutting-edge single-molecule biophysical techniques, dual-trap optical tweezers (to detect force) and confocal fluorescence microscopy (to detect binding) (Figure 2-3). This, to our knowledge, the first assay developed to detect actin binding at the molecular level when force is exclusively exerted on actin filaments, enabled by the recent technical developments in hybrid fluorescence–optical trapping techniques (Bustamante et al., 2021).

In these experiments, Alexa-555 phalloidin-stabilized biotinylated actin filaments were captured from a laminar stream across a microfluidic flow-cell between two optically trapped streptavidin-coated beads. Tethered filaments were then transferred to a reservoir containing Halo-tagged ABD labeled with Alexa-488 and subjected to a constant velocity ramp protocol (See Materials and Methods, Chapter 7) while simultaneously recording confocal movies of both the actin and ABD fluorescence signals.

Figure 2-3. Piconewton load across individual filaments activates α-catenin binding, while vinculin is force insensitive.

(A) Top: Geometry of the microfluidic chamber. Bottom: Cartoon of correlative single-filament force and fluorescence assay.

(B and C) Representative single-filament constant velocity pulling experiments (0.1 μm / s) for vinculin ABD (B) and α-catenin ABD (C). Top: force versus time plot. Red dots, raw data; black dots, force values binned to interval of confocal frames. Middle: Montage of confocal frames of actin and ABD channels. Positions of beds are indicated with yellow circles (diameter, 4 μm). Bottom: I_{ABD}/I_{actin} ratio versus time plot. High-force: average of five intensity ratios before actin breakage; low-force: average of five intensity ratios immediately prior to high-force average. Concentration of vinculin ABD or α-catenin ABD: 2μM.

(D and E) Paired analysis of low-force and high-force averages across trials for vinculin ABD (D) (N = 6, p = 0.84) and α-catenin ABD (E) (N = 7, p = 0.0156). Wilcoxon signed rank test: *p < 0.05; n.s. (not significant), p > 0.05.

(F and G) Scatter plots of normalized fluorescence ratios versus force. Statistical comparisons are between intensity ratios divided into two bins: force below and above 1 pN or 2.2 pN (dotted lines) for vinculin ABD (F) (1 pN: below: n = 62, above: n = 20, p = 0.65; 2.2 pN: below: n = 72, above: n = 10, p = 0.74), and force below and above 1 pN or 1.8 pN (dotted lines) for α-catenin ABD (G) (1pN: below: n = 53, above: n = 15, p < 0.0001; 1.8 pN: below: n = 59, above: n = 9, p = 0.0002). KS test: ****p < 0.0001; ***p < 0.001; n.s., p > 0.05.

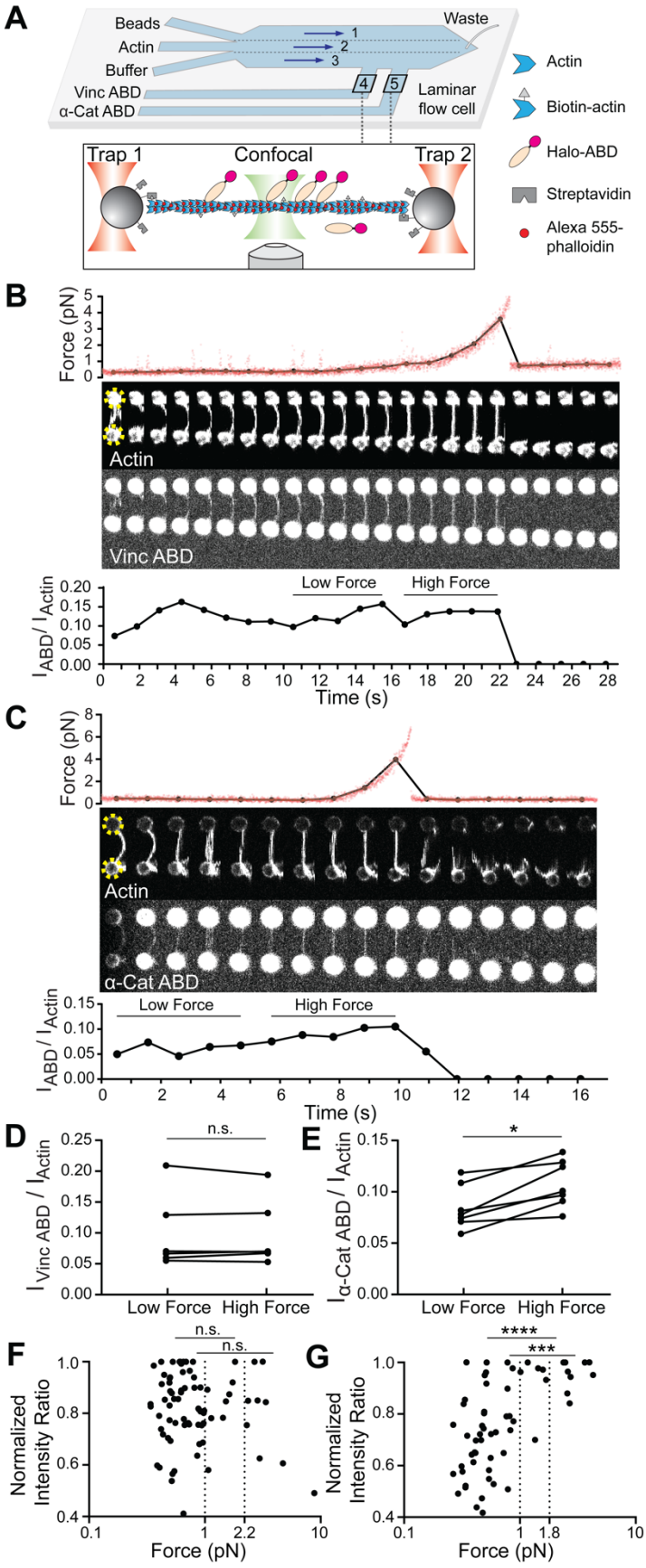
A
Beads
Actin
Buffer
Vinc ABD
α-Cat ABD
Waste
Laminar flow cell
Trap 1
Confocal
Trap 2
Actin
Biotin-actin
Halo-ABD
Streptavidin
Alexa 555-phalloidin
B
Force (pN)
Actin
Vinc ABD
Low Force
High Force
I_ABD / I_Actin
Time (s)
C
Force (pN)
Actin
α-Cat ABD
Low Force
High Force
I_ABD / I_Actin
Time (s)
D
n.s.
I_Vinc ABD / I_Actin
Low Force
High Force
E
*
I_α-Cat ABD / I_Actin
Low Force
High Force
F
n.s.
n.s.
Normalized Intensity Ratio
Force (pN)
G
****
***
Normalized Intensity Ratio
Force (pN)

We frequently observed a monotonic increase in force once a threshold extension was reached, followed by an instantaneous return to baseline (Figure 2-3; Figure 2-4), consistent with resistance from a tether composed of one or more actin filaments extended beyond their resting length (visible as straightening in the actin fluorescence channel) followed by force-induced breakage. To correlate force with ABD binding, we calculated the background-subtracted ratio of the ABD fluorescence intensity to the actin intensity (which we refer to as "I_{ABD}/I_{actin}") in each frame of the confocal movies (see Materials and Methods, Chapter 7; Figure 2-3), as well as the corresponding average force during frame acquisition (Figure 2-3 Panel B & C, top, black connected points). Apparent binding by the vinculin ABD fluctuated and did not change in response to load during individual pulling trajectories (Figure 2-3), consistent with a previous report that mechanical stimulation does not promote cytoskeletal localization of vinculin in cells (Schiffhauer et al., 2016). However, we observed an apparent steady increase in binding along individual tethers by the α-catenin ABD (Figure 2-3 Panel C), consistent with force-activated binding. To quantify this phenomenon, due to the inherent fluctuations of individual I_{ABD}/I_{actin} traces in this assay (potentially due to dynamic changes in ABD binding density along individual tethers and instability in the focus during confocal imaging), we first focused our analysis on a subset of long-lived tethers which featured at least 10 frames. We examined the difference between a "high-force" average, defined as the mean I_{ABD}/I_{actin} value from the 5 frames prior to the final tether rupture, and a "low-force" average, defined as the mean I_{ABD}/I_{actin} value from the 5 preceding frames during each recording (Figure 2-3).

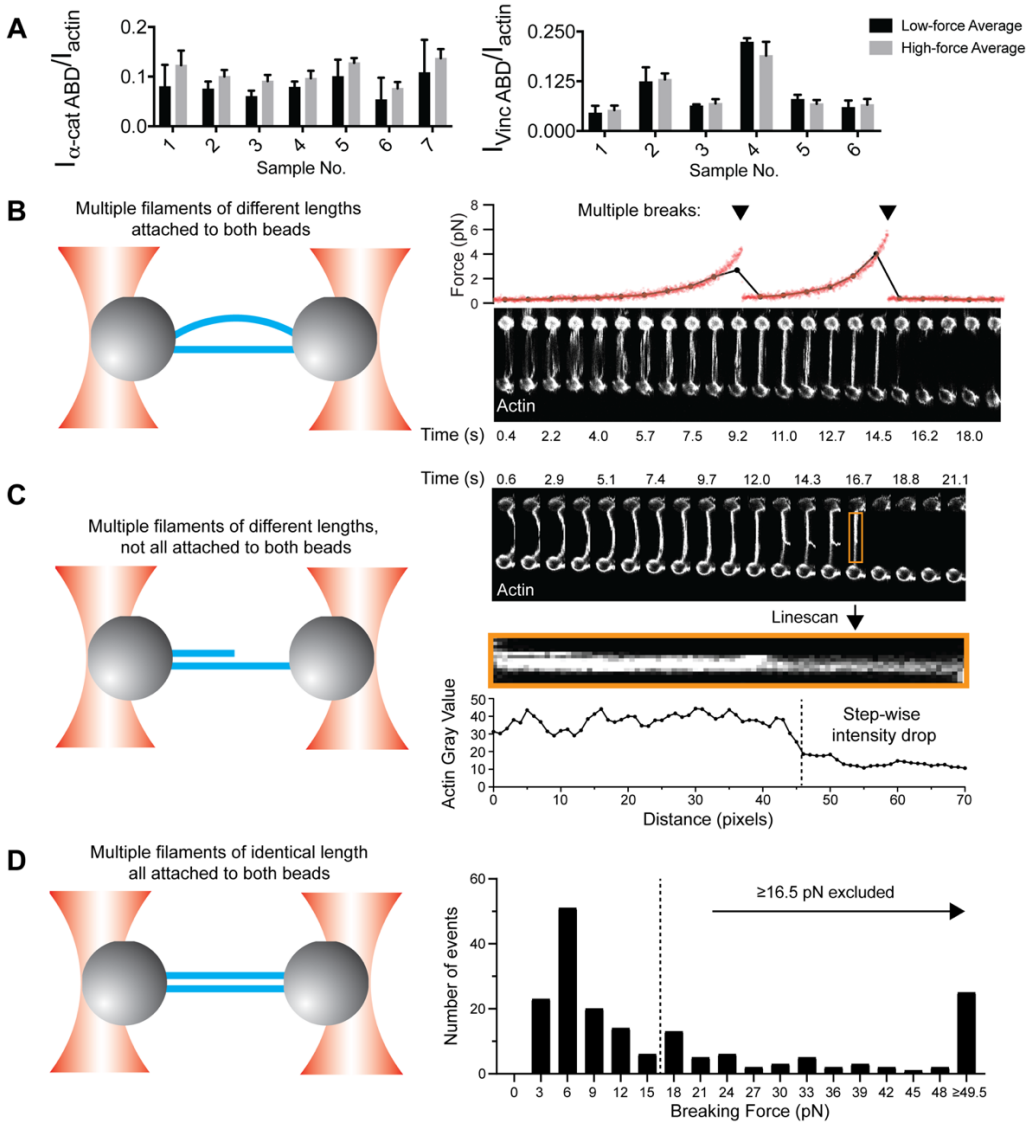

Figure 2-4. Additional analysis of single filament correlative force and fluorescence assays.

(A) Bar plots of mean ± standard deviation of high-force and low-force averages for all trials displayed in Figure 2-3 Panels D and E.

(B-D) Single-filament analysis achieved by excluding actin bundles from the dataset, including multiple actin filaments of different lengths attached to both beads (B); multiple actin filaments of different lengths not all attached to both beads (C); and multiple actin filaments of the same length attached to both beads (D).

Paired analysis of low-force / high-force averages (Materials and Methods, Chapter 7) showed a significant increase consistent with force-activated binding only by the α-catenin ABD (Figure 2-3; Figure 2-4 Panel A).

Taking advantage of the high spatial and temporal resolution of dual-bead optical trapping (Bustamante et al., 2021), we next sought to determine the impacts of force on ABD binding at the level of individual actin filaments. As our tether assembly procedure captures filaments from solution, in principle each tether could be composed of a single filament or multiple filaments. We thus elaborated the possible multi-filament tether configurations, and designed a series of criteria to identify and exclude them from analysis. The first plausible multi-filament tether configuration (1) is composed of multiple filaments of different lengths, all attached to the trapped beads at both ends (Figure 2-4), which we identified by the presence of multiple breaking peaks in the force curve, generated as the shortest remaining filament in the tether reaches full extension then ruptures (Figure 2-4 Panel B). The next plausible configuration (2) is multiple filaments of different lengths, not all of which are attached at both ends (Figure 2-4 Panel C), which we identified by fluorescence line scans of the actin intensity, where we observe step-like reductions which we interpret to correspond to the ends of non-bridging filaments (Figure 2-4 Panel C). The third and final configuration (3), composed of multiple filaments, all of essentially identical length and attached at both ends (Figure 2-4 Panel D), is the most difficult to rigorously identify. We observed significant heterogeneity in the raw actin fluorescence intensity values between tethers (potentially due to slight differences in focus), with no significant difference between configuration 1

tethers and those featuring a single rupture force peak (data not shown), suggesting raw actin intensity cannot be used as a proxy for filament number. We thus analyzed the distribution of final breaking forces for all trials (pooling data collected in the presence of both the α-catenin and vinculin ABD), reasoning that configuration 3 tethers composed of multiple fully-extended actin filaments in parallel at the final break would generally rupture at higher forces. Consistent with this prediction, we observed a single major peak in the breaking force distribution centered at ~6 pN, which is likely to primarily consist of single filaments, as well as a long tail of >16.5 pN breaking forces, which we interpret to primarily encompass configuration 3 tethers. We thus additionally excluded all tethers with >16.5 pN breaking force from further analysis.

Based on these criteria, only 21 tethers (11 vinculin ABD and 10 α-catenin ABD) out of 183 total trials were included. This subset very likely predominantly contains tethers composed of single filaments. Consistent with the expected relative fragility of single-filament tethers with low breaking forces, most of these recordings only contained a limited number of frames, precluding quantification of force-dependent binding changes in individual tethers. We thus instead examined the relationship between force magnitude and ABD binding by pooling our recordings for each protein and plotting normalized I_{ABD}/I_{actin} versus force (Figure 2-3). This analysis revealed no apparent correlation between vinculin ABD binding and force (Figure 2-3). However, the α-catenin ABD plot showed an apparent step-like transition from force-uncorrelated binding to consistent strong binding above a threshold force of approximately 1 pN (Figure 2-3).

To quantify this phenomenon, the distribution of intensity ratios above and below the subjectively identified 1 pN threshold was first examined, which found a significant difference only for the α-catenin ABD (Figure 2-3). To objectively define the threshold force, we performed K-means clustering analysis (Methods) which revealed that the α-catenin ABD force-fluorescence distribution could be optimally divided into two clusters with a threshold force of 1.8 pN. We found that the intensity ratios were also significantly different between these clusters (Figure 2-3). Although there was no obvious correlation between force and binding by the vinculin ABD, as a control we nevertheless used K-means to divide the data into two clusters, which separated at a threshold force of 2.2 pN. Consistent with the lack of a force-binding correlation for the vinculin ABD, we find no significant difference between the distribution of intensity ratios in these two clusters (Figure 2-3). In the assay we have consistently observed these behaviors across different lengths of trapped actin filaments (Figure 2-5). This analysis, which is insensitive to the exact force threshold employed, supports a force-dependent increase in F-actin binding only for the α-catenin ABD. Collectively, these data suggest that piconewton-level tensile force along individual actin filaments is sufficient to activate α-catenin's F-actin binding.

2.3 Novel *in vitro* reconstituted TIRF microscopy assay

As ~1 pN is the magnitude of force generated by individual myosin motor domains (Finer et al., 1994), we hypothesized α-catenin's F-actin binding would also be enhanced by physiological forces generated by myosins, the superfamily of motor

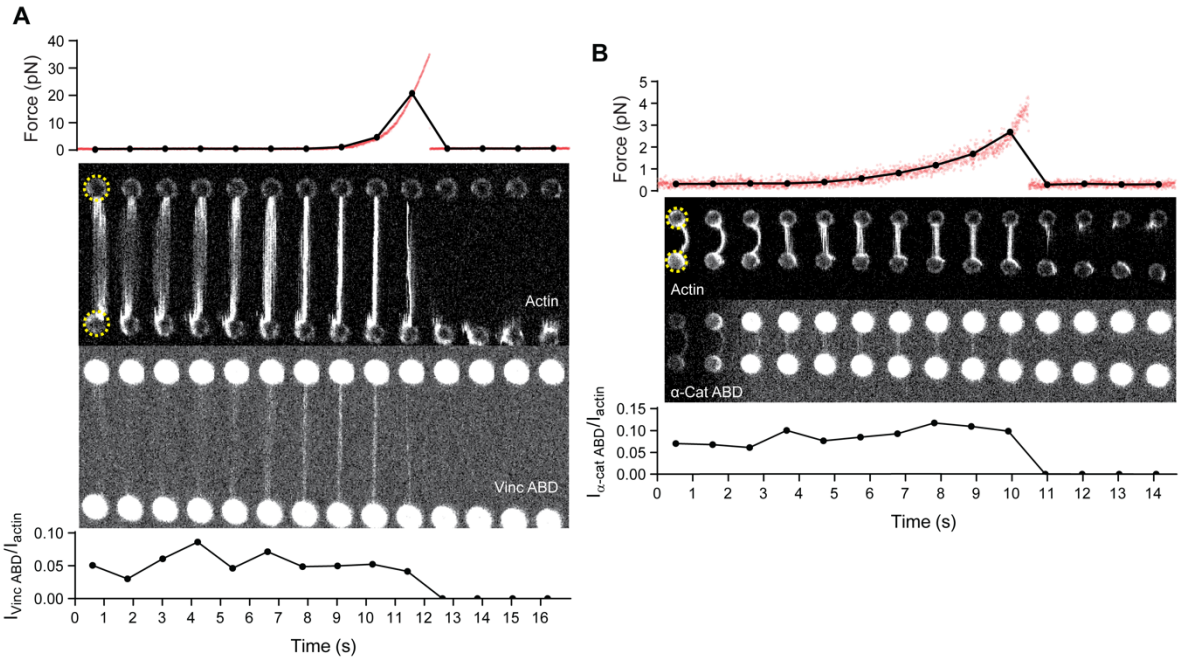

Figure 2-5. Two additional datasets of single filament correlative force and fluorescence assays.

(A and B) Additional representative traces of single-filament pulling assays as in Figure 2-3, for vinculin ABD (A) and α-catenin ABD (B). Top: force versus time plot. Red dots, raw data; black dots, force values binned to interval of confocal frames. Middle: Montage of confocal frames of actin and ABD channels. Beads are indicated with yellow circles (diameter, 4 μm). Bottom: I_{ABD}/I_{actin} ratio versus time plot.

proteins operating on the actin cytoskeleton (Sweeney and Holzbaur, 2018) in eukaryotic cells. As noted in Chapter 1, under physiological conditions essentially all cellular actin filaments are found in high-order actin networks such as actin bundles, rather than remaining as single filaments. Therefore, it is imperative to study whether the actin binding of vinculin or α-catenin can still be regulated by force in a physiologically relevant context, where myosin motors constantly exert force on actin filaments and actin filaments are bundled by ABPs (Blanchoin et al., 2014). To test this hypothesis, we developed a novel adaptation of the gliding filament assay (Kron and Spudich, 1986) to apply force to filaments mimicking actomyosin contractility *in vivo* (Figure 2-6) by utilizing Total Internal Reflection Fluorescence (TIRF) microscopy through *in vitro* reconstitution. In our preparation, plus-end directed myosin V motor proteins and minus-end directed myosin VI motor proteins are randomly surface-immobilized inside a flow chamber assembled on a cover glass for TIRF, resulting in a configuration where the motors are poised to engage in tug-of-wars along non-stabilized, rhodamine labelled actin filaments. A Halo-tagged, JF-646 (Grimm et al., 2015) labelled ABD is then flowed into the chamber in the absence of ATP, and a 2-color TIRF movie is recorded to visualize the basal level of actin-binding when filaments are anchored by the rigor-state motors. The ABD solution is then re-introduced into the same chamber in the presence of ATP to activate the motors, and a second movie recorded to visualize binding in the presence of force generation. Visual inspection of -ATP / +ATP TIRF movie pairs for the vinculin and α-catenin ABDs suggest they respond to motor-generated forces on F-actin distinctly. Actin localization of the vinculin ABD did

Figure 2-6. Forces generated by myosin motors activate α-catenin binding to F-actin.

(A) Cartoon of TIRF force reconstitution assay utilizing surface-anchored myosin motor proteins with opposing directionality.

(B and C) TIRF assays of vinculin ABD (B) and α-catenin ABD (C). Left: Representative movie frames of actin and ABD channels in the absence (top) and presence (bottom) of ATP to activate motors. Scale bar, 20μm. Right: Montages of individual filament regions. Scale bar, 5μm. Concentration of vinculin ABD or α-catenin ABD: 2μM.

(D and E) Time-averaged I_{ABD}/I_{actin} intensity ratio distributions of filament regions before and after ATP addition for vinculin ABD (D, quantification of B) and α-catenin ABD (E, quantification of C).

(F and G) Paired analysis of overall average intensity ratio change before and after ATP addition for vinculin ABD (F) ($N = 9$, $p = 0.50$) and α-catenin ABD (G) ($N = 6$, $p = 0.031$). Wilcoxon signed rank test: $^*p < 0.05$; n.s. (not significant), $p > 0.05$.

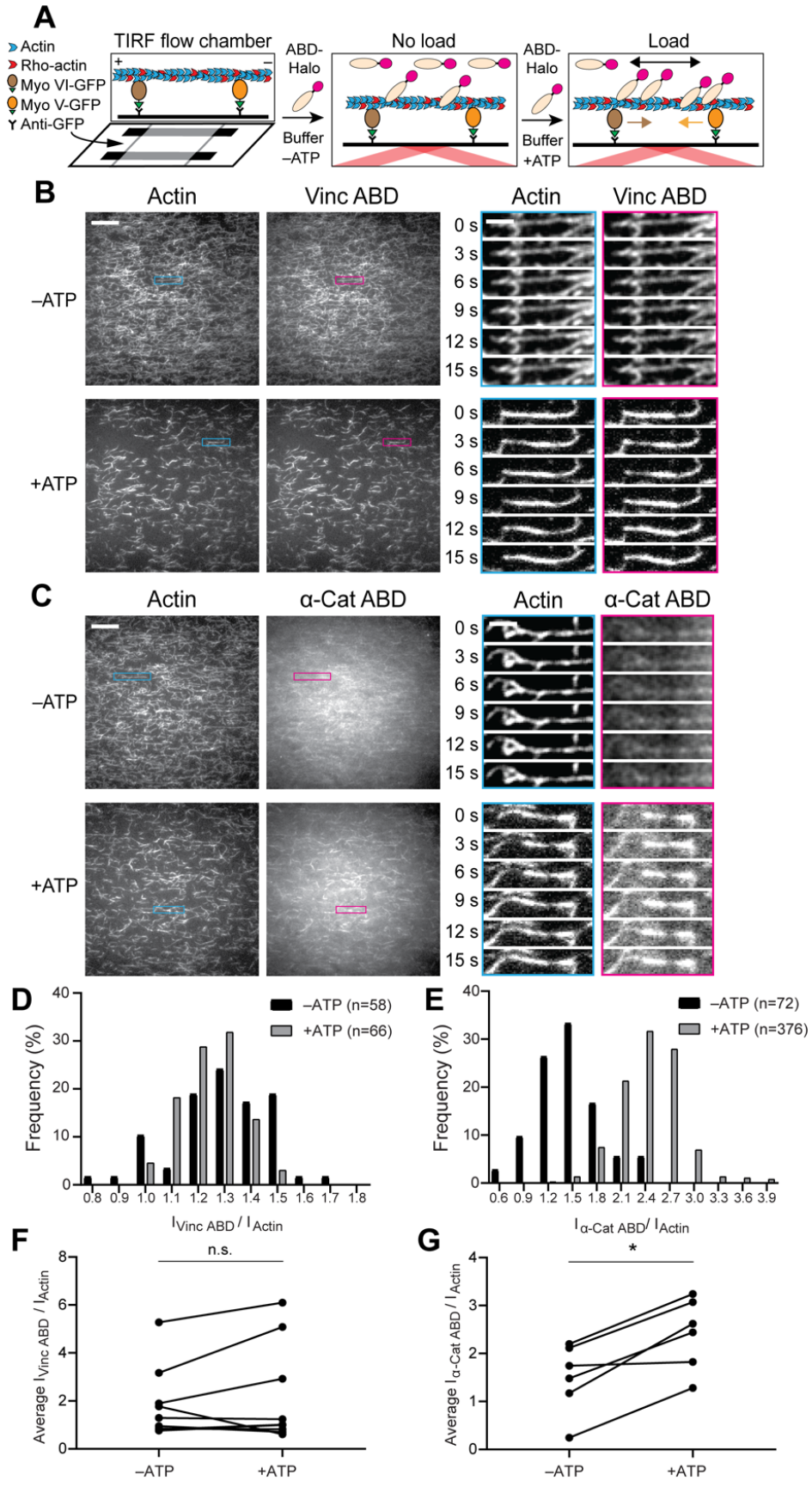
A
Actin
Rho-actin
Myo VI-GFP
Myo V-GFP
Anti-GFP
TIRF flow chamber
ABD-Halo
Buffer –ATP
No load
ABD-Halo
Buffer +ATP
Load
B
Actin
Vinc ABD
Actin
Vinc ABD
–ATP
+ATP
0 s
3 s
6 s
9 s
12 s
15 s
C
Actin
α-Cat ABD
Actin
α-Cat ABD
–ATP
+ATP
D
Frequency (%)
–ATP (n=58)
+ATP (n=66)
I Vinc ABD / I Actin
E
Frequency (%)
–ATP (n=72)
+ATP (n=376)
I α-Cat ABD/ I Actin
F
n.s.
Average I Vinc ABD / I Actin
–ATP
+ATP
G
*
Average I α-Cat ABD / I Actin
–ATP
+ATP

not change in response to motor activity (Figure 2-6); however, α-catenin ABD's actin localization was enhanced upon motor activation, indicative of force-activated actin binding (Figure 2-6).

As we expected the random deposition and inherent stochasticity of molecular motors in our assay to give rise to a distribution of forces and ABD binding states, we implemented an image analysis procedure to quantify ABD association by automatically identifying and tracking tens to hundreds of 'filament regions' in parallel through time (see Chapter 7, Materials and Methods; Figure 2-7). For each region at the size of approximately a single actin filament, a similar 'intensity ratio', representing the strength of actin binding, I_{ABD}/I_{actin}, was calculated in each frame, then averaged over time for all frames in which the region was detected. Then the distribution of 'single-filament' intensity ratios were analyzed and compared across +ATP (with force applied) and –ATP (without force applied) conditions for both ABPs. Consistent with our qualitative interpretation, histograms of I_{ABD}/I_{actin} distributions before and after ATP addition to individual flow chambers showed no shift for the vinculin ABD (Figure 2-6; Figure 2-7). However, this analysis demonstrated a clear shift towards higher values upon ATP addition for the α-catenin ABD, supporting force-activated binding (Figure 2-6; Figure 2-7). While the reported trends were consistent across experiments for both ABDs, we nevertheless observed variability between trials (Figure 2-7), potentially likely due to differences in the of background intensities in both channels resulting from inconsistencies in cover-glass surface preparation (Materials and Methods). We thus performed paired analysis of the mean I_{ABD}/I_{actin} between the -ATP / +ATP conditions

Figure 2-7. Workflow of TIRF data quantification, additional intensity ratio distributions of single-filament regions for WT α-catenin and vinculin ABDs.

(A) Workflow of quantifying and comparing single-filament region intensity ratios (I_{ABD}/I_{actin}) in the TIRF assay. Scale bar, 20μm.

(B) Time-averaged I_{ABD}/I_{actin} intensity ratio distributions of single-filament regions for before and after ATP addition for vinculin ABD (left) and α-catenin ABD (right). Along with data presented in Figure 2-6 Panels D and E, these data were used in the analysis presented in Figure 2-6 Panels F and G.

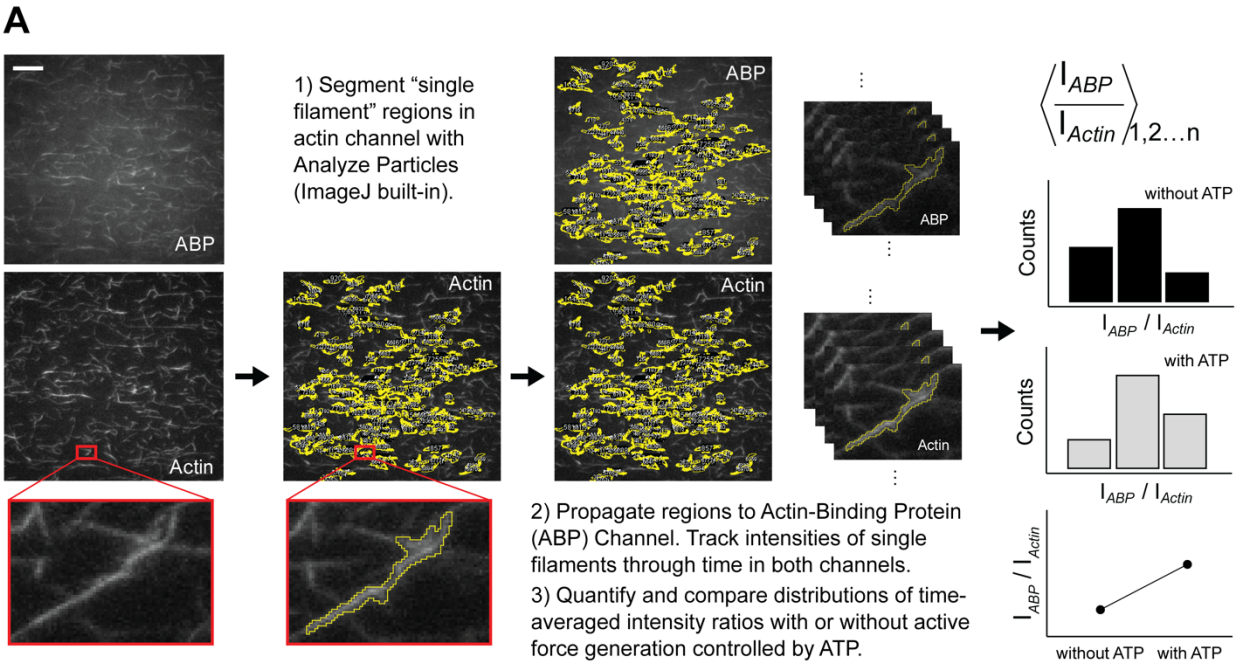
A
ABP
Actin
1) Segment “single filament” regions in actin channel with Analyze Particles (ImageJ built-in).
2) Propagate regions to Actin-Binding Protein (ABP) Channel. Track intensities of single filaments through time in both channels.
3) Quantify and compare distributions of time-averaged intensity ratios with or without active force generation controlled by ATP.
without ATP
with ATP
Counts
without ATP
with ATP

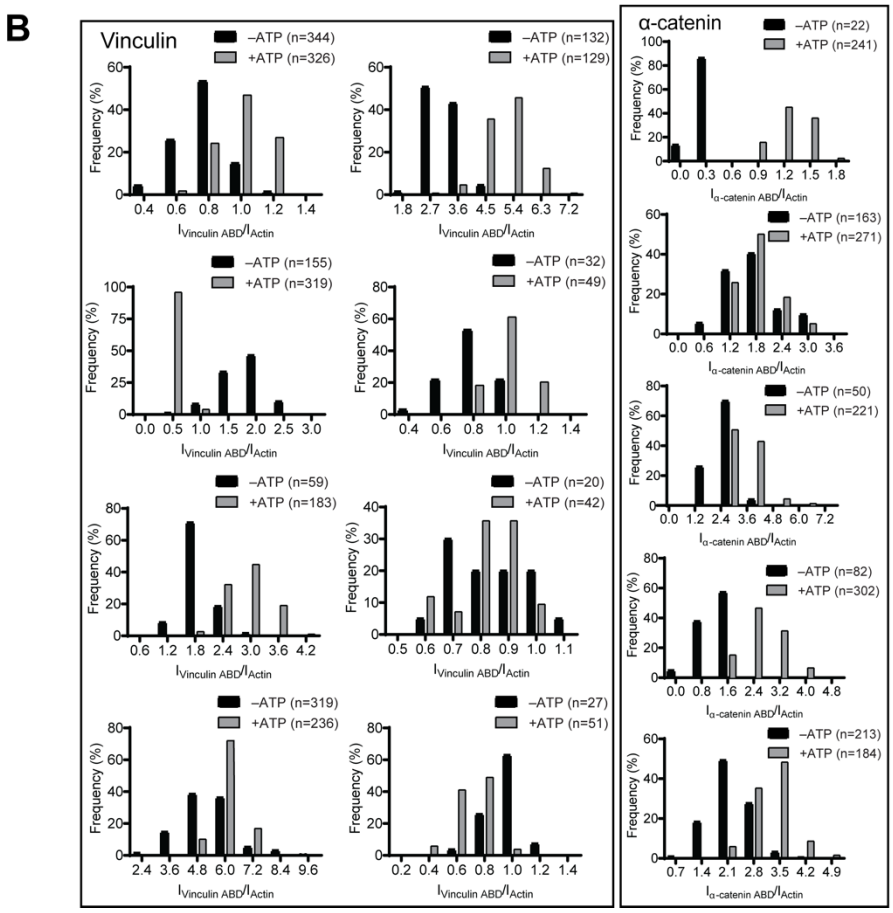
B
Vinculin
α-catenin
–ATP (n=344)
+ATP (n=326)
–ATP (n=132)
+ATP (n=129)
–ATP (n=155)
+ATP (n=319)
–ATP (n=32)
+ATP (n=49)
–ATP (n=59)
+ATP (n=183)
–ATP (n=20)
+ATP (n=42)
–ATP (n=319)
+ATP (n=236)
–ATP (n=27)
+ATP (n=51)
–ATP (n=22)
+ATP (n=241)
–ATP (n=163)
+ATP (n=271)
–ATP (n=50)
+ATP (n=221)
–ATP (n=82)
+ATP (n=302)
–ATP (n=213)
+ATP (n=184)
Frequency (%)

for each chamber (Figure 2-6), which demonstrated a significant increase only for the α-catenin ABD (Figure 2-6), but not for the vinculin ABD. To further validate the lack of force-sensing capacity for the vinculin ABD, the ABD of its splice isoform, metavinculin, was also tested by the assay (Figure 2-8). The metavinculin ABD, like the vinculin ABD, does not sense force on actin (Figure 2-8), consistent with the report that metavinculin ABD maintains a highly similar structure with vinculin ABD (Kim et al., 2016).

Our optical-trapping experiments suggest that force along individual filaments is sufficient to activate α-catenin binding. However, in the cellular context, both α-catenin and vinculin primarily engage actin-myosin bundles. In our TIRF assay, visual inspection supports increased F-actin bundling by both vinculin and α-catenin upon motor activation (Figure 2-6), presumably due to motility facilitating encounters between filaments. Although I_{ABD}/I_{actin} measurements are internally normalized for the local density of F-actin in each region, we are aware that bundling contacts could in principle enhance apparent binding. Additionally, while the ATP-dependence of this enhanced F-actin binding strongly suggests it is activated by force, allosteric remodeling of actin filament structure due to local deformations imposed by motor binding could also potentially contribute (Gurel et al., 2017). To decouple these effects, we performed assays in the presence of individual motors. In the presence of both myosin V alone (Figure 2-9) and myosin VI alone (Figure 2-9) we observe ATP-dependent formation of bundles, consistent with motor-assisted facilitated encounter between F-actin and vinculin or α-catenin. However, we observe no significant increase in apparent vinculin ABD or α-catenin ABD binding under either condition. This strongly suggests that force-

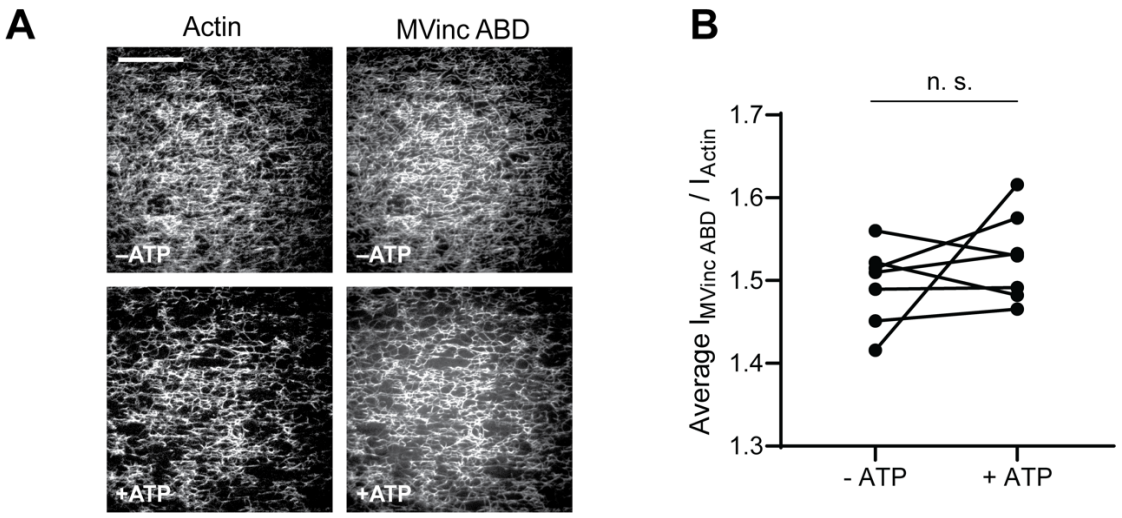

Figure 2-8. TIRF assays for metavinculin ABD.

(A) Representative TIRF-assay movie frames of actin (left) and metavinculin ABD (right) channels in the absence (top) and presence (bottom) of ATP to activate motors. Scale bar, 40μm.

(B) Paired analysis of overall average intensity ratio change before and after ATP addition for metavinculin ABD (N = 7, p = 0.47). Wilcoxon signed rank test: n.s. (not significant), $p > 0.05$.

Figure 2-9. Single motor does not activate the actin binding activities for either vinculin or α-catenin ABD.

TIRF force reconstitution assays performed with only myosin VI (first panel) or myosin V motor (second panel). Top: Representative movie frames in the presence and absence of ATP. Scale bar, 40 μm. Bottom: paired analysis of overall intensity ratio changes upon ATP addition. Wilcoxon signed rank test: n.s. (not significant), $p > 0.05$. Constructs assayed were: Vinculin ABD (myosin VI, N = 6, $p = 0.43$); Vinculin ABD (myosin V, N = 6, $p = 0.15$); α-catenin ABD (myosin VI, N = 6, $p = 0.56$); α-catenin ABD (myosin V, N = 6, $p = 0.84$).

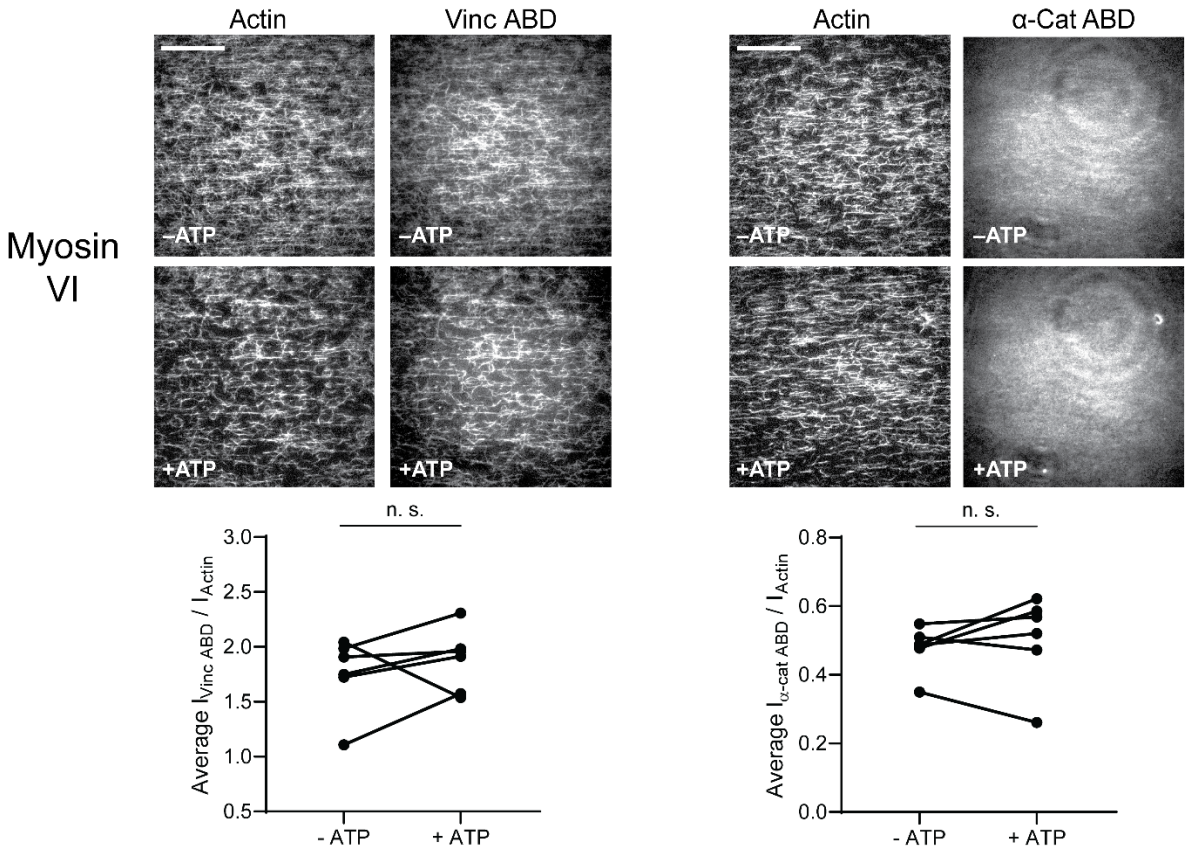
Myosin VI
Actin
Vinc ABD
α-Cat ABD
–ATP
+ATP
n. s.
Average $I_{Vinc\ ABD}$ / I_{Actin}
Average $I_{\alpha\text{-cat ABD}}$ / I_{Actin}
- ATP
+ ATP

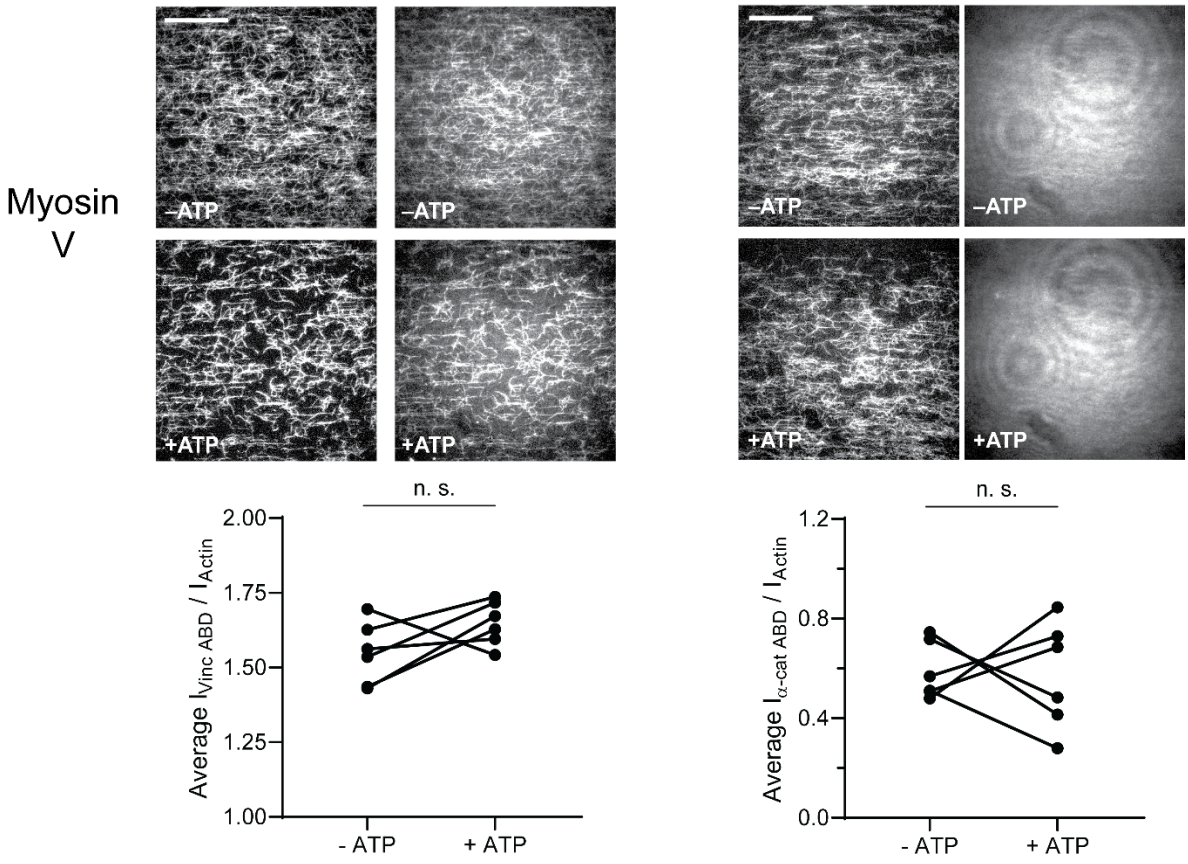
Myosin V
–ATP
+ATP
n. s.
Average $I_{Vinc\ ABD}$ / I_{Actin}
Average $I_{\alpha\text{-cat ABD}}$ / I_{Actin}
- ATP
+ ATP

activated α-catenin ABD binding is dependent upon the tug-of-war between motors of opposed directionality, mimicking the forces generated by bi-polar myosin II filaments *in vivo*. We note that forces generated by the randomly distributed force generators in the dual motor assay are complex, and can in principle include tension, compression, and torsional forces (Jegou and Romet-Lemonne, 2021; Beausang et al., 2008; Sun et al., 2007). While our optical trapping studies suggest tensile forces are sufficient to activate α-catenin ABD binding, future studies will be required to explicitly dissect the contribution of compression and torsion in the presence of myosin motors. Regardless, these studies collectively suggest physiological forces generated by myosin motor proteins in an appropriate configuration can directly activate α-catenin binding to F-actin, and that force-activated α-catenin binding also occurs in the context of actin bundles, the primary cytoskeletal architecture engaged by the protein *in vivo*.

2.4 Discussion: α-catenin, but not vinculin, directly senses force on actin

Our finding that approximately 1 pN of tension along individual filaments is sufficient for force-activated binding suggests that the actin-binding interface of α-catenin has been evolutionarily optimized to sense contractile forces generated by myosin motors (Finer et al., 1994). Despite the high-level sequence and structural homology between vinculin and α-catenin, vinculin's ABD cannot directly sense force exclusively applied on actin filaments, shown independently in our two novel biophysical assays. This unexpected functional difference in actin force sensing highlights the complex regulation that happens in junctional complexes, and the importance to dissect

the distinct roles of different force regimes in the cellular environment. Together with the report that vinculin forms a directional catch bond with F-actin, our results indicated vinculin and α-catenin might have distinct structural configurations when binding actin, and this structural difference might underlie their distinct actin-binding behavior, which will be covered in the Chapter 3 of this thesis.

It shall be noted that force-activated binding is an additional, rather than alternative, mechanism to catch-bond formation (Buckley et al., 2014) for mechanical regulation of F-actin binding. This finding that vinculin lacks this activity despite forming catch-bonds with F-actin (Huang et al., 2017) strongly suggests that these two modes of mechanical regulation operate by unique structural mechanisms, likely to fulfill distinct biological functions. Vinculin's lack of force-activated actin-binding activity is consistent with the ordered sequence of mechanically-regulated binding events underlying its coordination with α-catenin at adherens junctions, where only after preliminary attachments form through the cadherin complex and come under load is vinculin recruited and activated to bind F-actin (Yonemura et al., 2010). The lower force threshold for force-activated binding than catch-bond formation (~1 pN vs. ~10 pN) supports a model in which the formation of initial attachments to the cytoskeleton through the cadherin complex is stimulated through force-activated binding, which is subsequently strengthened by catch-bonding through both α-catenin and vinculin during adhesion maturation.

It shall also be noted that like every newly developed, single-molecule biophysical assay, quantitative results presented here should be interpreted with

caution. For the simultaneous confocal microscopy and optical trapping assays, the fluorescence intensity values were measured under the assumption that actin filaments in all frames have the same in-focus z-height (Bustamante et al., 2021), and therefore the confocal fluorescence images can be quantified and compared. Although the calculation of intensity ratios served as an internal control, the assumption might have implications, especially in the first few frames where actin filaments were not held taught between two traps. Likewise, the increased use of quantification has also been one of the major driving forces in advancing TIRF microscopy-based assays (Axelrod, 2008). However, the physical principles of evanescent wave and total internal reflection (TIR) dictate that the fluorescent intensity in TIRF microscopy can be influenced by the orientation of the fluorophore, the local change of solution refractive index, and the distance between the imaged fluorophore and the coverslip (Simon, 2009). From a physical perspective, because TIR provides a strong signal relative to noise, the quantification of TIRF images, especially on the magnitude of fluorescence signals, should be performed in a highly stringent way (Simon, 2009), which was part of the reason we have employed large-scale quantification and designed single-motor control experiments for the TIRF assay. The high variability of absolute TIRF intensity has been clearly demonstrated in the statistics of our data (Figure 2-6; Figure 2-7; Figure 2-10).

Nevertheless, the two assays described here in this Chapter are first of their kind to directly confirm the existence of force-activated binding by actin-binding proteins at both the single-filament and actomyosin bundle levels. The two assays provide strong evidence that the essential adhesion protein α-catenin directly senses force on actin,

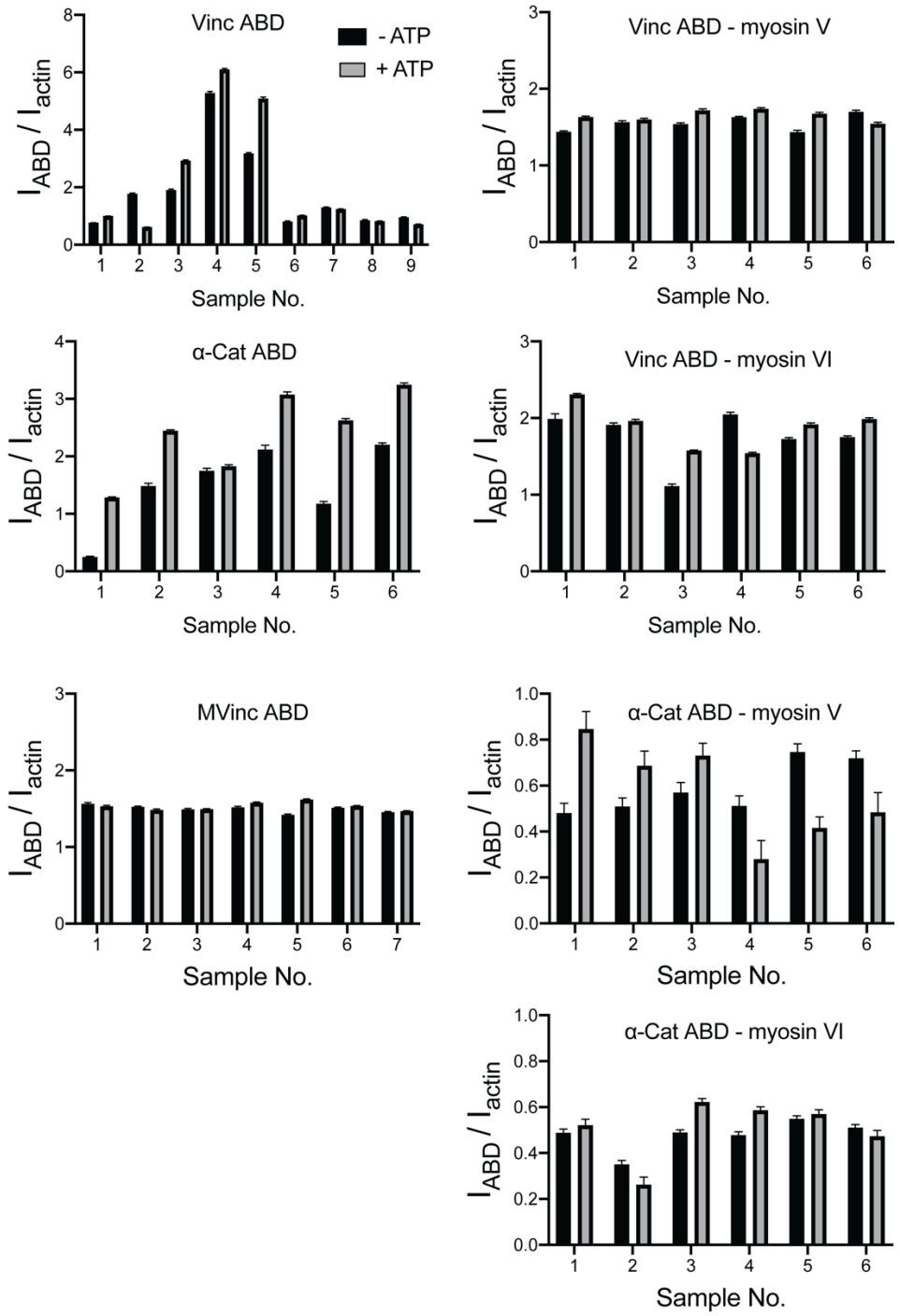

Figure 2-10. Additional analysis of TIRF assays.

Bar plots of mean ± SEM of high-force and low-force averages for all trials displayed in Figure 2-6 to Figure 2-9.

while its close homolog, another essential adhesion protein vinculin, does not. Both assays can be applied to screen, identify, and validate more novel force-sensitive actin-binding proteins, Moreover, the TIRF assay has a superior throughput and the potential to be applied in large-scale parallel screenings. Both assays are highly versatile and compatible with different buffer conditions, making them ideal choices for discovering small-molecule probes and drugs that can specifically perturb force-activated binding. It is now appreciated that specific therapeutic targeting of mechanosensitive processes may have profound implications in treating diseases like cancer metastasis, cardiomyopathy, and muscular dystrophy.

CHAPTER 3

Structure-guided biochemistry reveals the actin force-sensing mechanism of α-catenin

Note to readers: Part of the results discussed below arose from a collaborative effort between myself, my advisor Dr. Gregory M. Alushin, several colleagues in the Alushin Laboratory, including Dr. Pinar S. Gurel and Ms. Ayala G. Carl, at the Rockefeller University, and several colleagues in the Eliezer laboratory, including Dr. David Eliezer and Dr. Tapojyoti Das, at Weill Cornell Medical College.

3.1 High-resolution Cryo-EM structures of α-catenin ABD–actin and metavinculin ABD–actin complexes

Our discovery that the essential human adhesion protein α-catenin, but not its close homolog vinculin, senses force on actin prompted us to investigate the underlying molecular mechanism that enables force-sensitive actin binding by α-catenin, an uncharted territory for both force-activated binding described in Chapter 2, and for catch bond (Buckley et al., 2014; Huang et al., 2017) formation between adhesion proteins and F-actin. As discussed in Chapter 1, this lack of knowledge could be attributed to the fact that there were few high-resolution structures for F-actin–ABP complexes before the resolution revolution of cryo-electron microscopy (cryo-EM) because F-actin cannot be crystallized due to symmetry incompatibility (Fujii et al., 2010). The recent technical revolution of cryo-EM (Kuhlbrandt, 2014) has greatly expanded our understanding of F-

actin structures (von der Ecken et al., 2015), revealing that F-actin has a high degree of structural polymorphism and can adopt a structural landscape of co-existing structures in solution (Galkin et al., 2010b), which prompts the hypothesis that F-actin itself is a tension sensor and can preferentially associate with different binding partners in the presence of mechanical forces (Galkin et al., 2012). However, it remains unclear to what extent mechanical modulation of functional interactions between ABPs and F-actin occurs through direct regulation of F-actin's binding interactions by force. Structural mechanisms enabling ABPs to detect force on F-actin, to our knowledge, are unknown.

Hypothesizing that differences in the F-actin-binding interfaces of vinculin and α-catenin could underlie their differential force-activated actin binding, we pursued structural studies of both ABDs bound to F-actin with cryo-EM (Figure 3-1; Table 1). As optimizing the density of fully-decorated, well-separated individual filaments in cryo-EM images is a major bottleneck for single-particle analysis of F-actin-ABP complexes, we chose to use the ABD of the vinculin splice variant metavinculin for these studies, where a 68 amino-acid insert displaces the H1 helix and replaces it with helix H1', producing a protein which retains actin binding but completely loses actin bundling activity (Janssen et al., 2012; Kim et al., 2016; Oztug Durer et al., 2015) (see Chapter 2.1). Previous studies have suggested these isoforms engage an essentially identical site on the F-actin surface with equivalent affinity (Janssen et al., 2012; Kim et al., 2016), and we further found the metavinculin ABD lacks force-activated actin binding activity in our TIRF assay, validating its use in these studies (see Chapter 2.3). We were able to obtain fields of individual decorated filaments using this construct (Figure 3-1). After

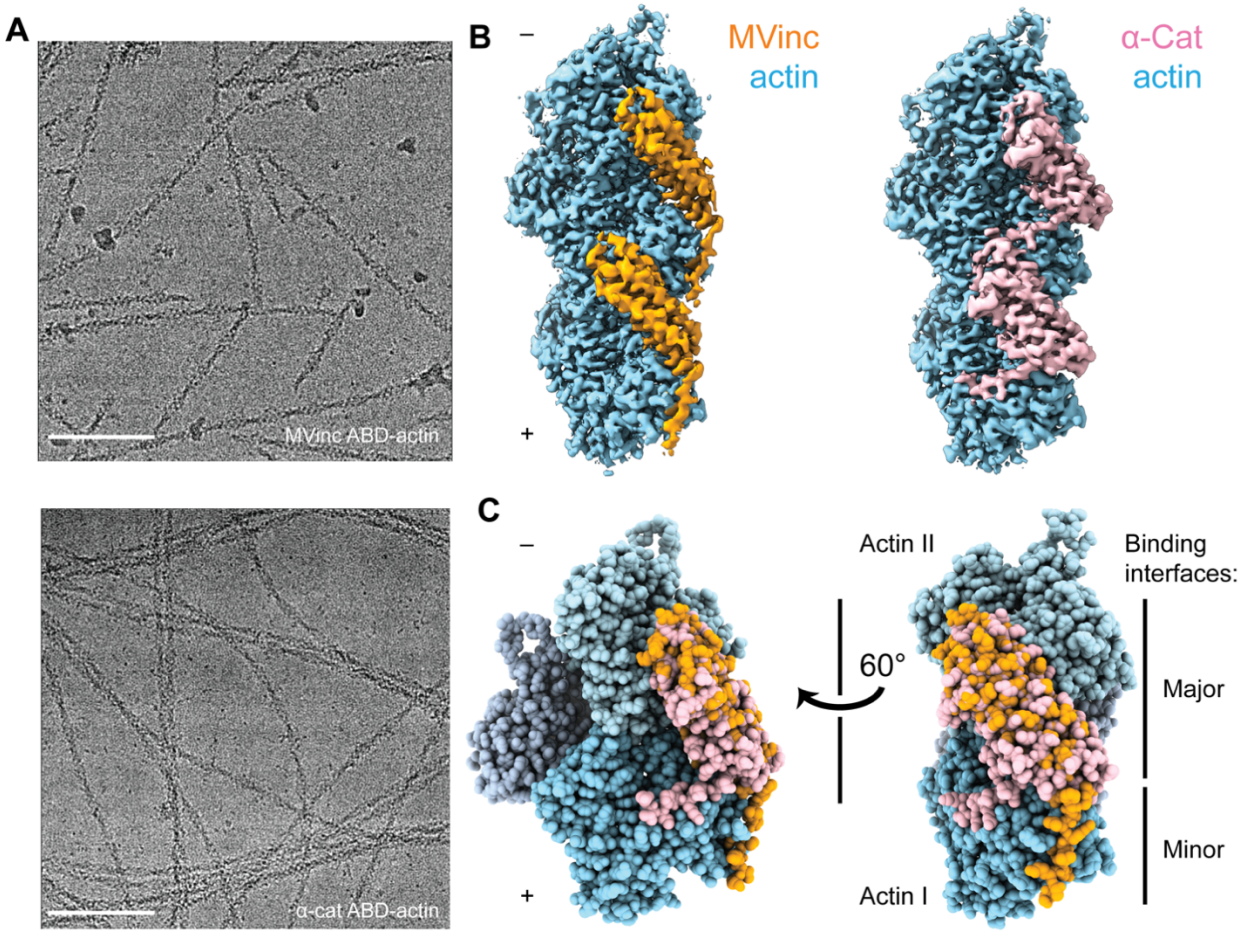

Figure 3-1. Cryo-EM structures of metavinculin and α-catenin–F-actin complexes.

(A) Representative cryo-EM micrographs of F-actin decorated with metavinculin ABD (top) and α-catenin ABD (bottom). Scale bars, 100 nm.

(B) Segmented regions of reconstructed density maps of F-actin decorated with metavinculin ABD (left) and α-catenin ABD (right), colored as indicated.

(C) Overlay of the metavinculin ABD-actin complex and α-catenin ABD-actin complex atomic models, superimposed on actin and colored as in (B). Actin subunits from the α-catenin structure are displayed in varying shades.

careful optimization (Materials and Methods), we were also able to acquire cryo-EM images of filaments decorated with the α-catenin ABD (Figure 3-1), although persistent bundling by this construct necessitated the collection of substantially more images to obtain a sufficient dataset of individual segments to obtain a high-resolution reconstruction (Table 1; Figure 3-2).

Using the Iterative Helical Real Space Reconstruction (IHRSR) approach (Egelman, 2007) as implemented in Relion 3.0 (He and Scheres, 2017; Zivanov et al., 2018) (Materials and Methods, Figure 3-2), we obtained reconstructions of the metavinculin ABD (residues 879-1134)–F-actin complex (Figure 3-1) at 2.9 Å overall resolution (Figure 3-2) and the α-catenin ABD (residues 664-906)–F-actin complex (Figure 3-1; Figure 3-2) at 3.2 Å overall resolution (Figure 3-2). As local resolutions ranged from 2.7 Å to 3.6 Å, radially decaying outward from the helical axis (Figure 3-2) for both reconstructions, atomic models for the complete sequence of Mg-ADP α-actin and continuous segments of ABD residues 981-1131 for metavinculin (Figure 3-1) and 699-871 for α-catenin (Figure 3-1) were built and refined into the maps (Figure 3-2). Contemporary with our studies (Appendix 1), Xu and colleagues also reported a 3.8 Å resolution cryo-EM reconstruction of the α-catenin ABD bound to F-actin, which shows an essentially identical conformation of the complex as presented here, providing independent validation of the interface we report (Xu et al., 2020).

Superposition of the actin-bound metavinculin ABD with the full-length vinculin crystal structure (Rangarajan et al., 2010) confirms that actin binding by both vinculin isoforms is auto-inhibited by intramolecular interactions between the N-terminal head

Figure 3-2. Cryo-EM data processing workflow for adhesion ABD-F-actin complexes.

(A and B) Cryo-EM processing workflow for metavinculin ABD–F-actin complex (A) and α-catenin ABD–F-actin complex (B) datasets. Scale bars, 100 nm.

(C and D) Left: Gold-standard Fourier Shell Correlation (FSC) between independent half maps (top, FSC 0.143) and FSC between map and model (bottom, FSC 0.5). Right: Reconstruction colored by local resolution for metavinculin ABD–F-actin reconstruction (C) and α-catenin ABD–F-actin reconstruction (D).

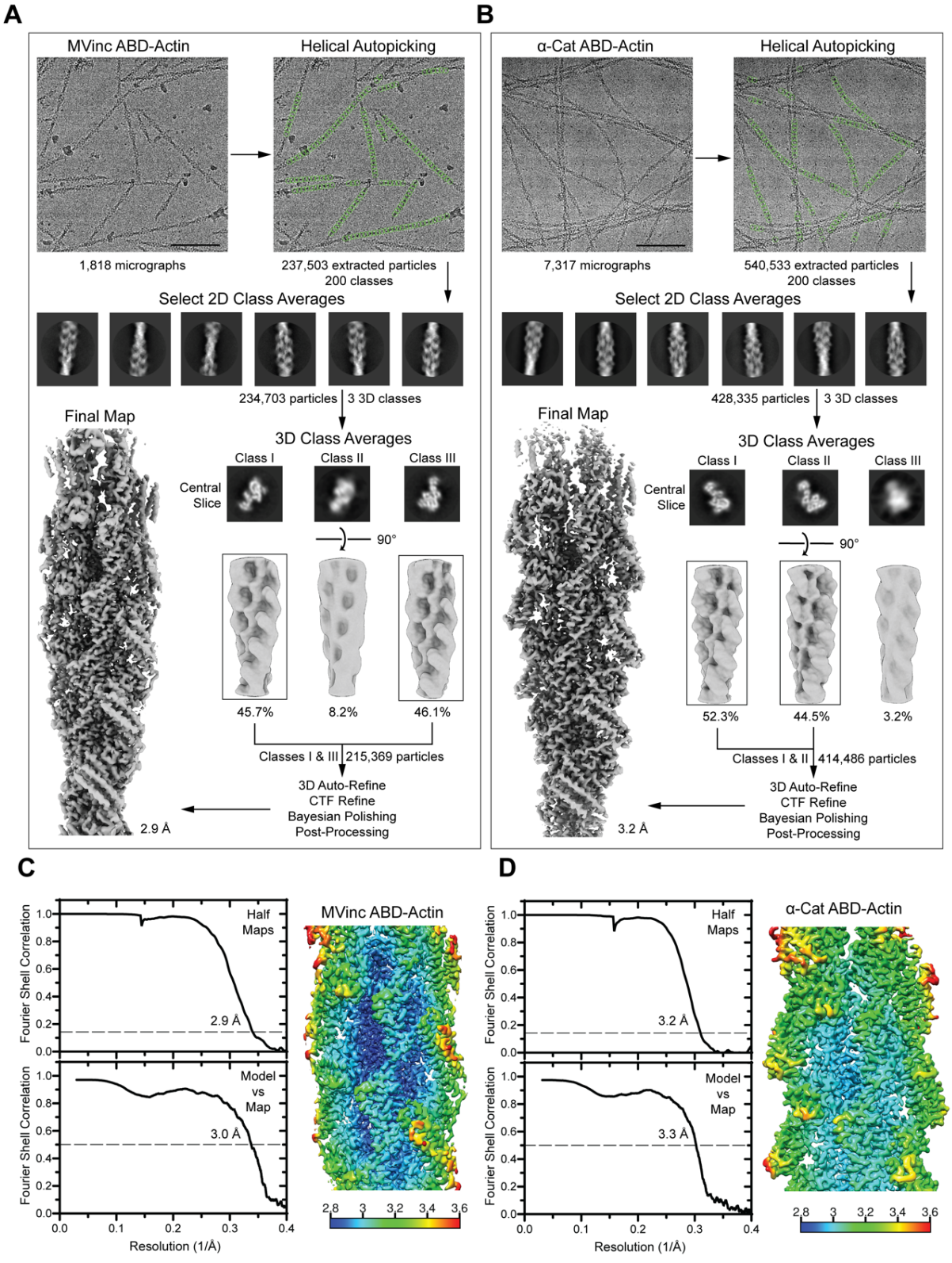
A
MVinc ABD-Actin
Helical Autopicking
1,818 micrographs
237,503 extracted particles
200 classes
Select 2D Class Averages
234,703 particles | 3 3D classes
Final Map
3D Class Averages
Class I
Class II
Class III
Central Slice
90°
45.7%
8.2%
46.1%
Classes I & III | 215,369 particles
3D Auto-Refine
CTF Refine
Bayesian Polishing
Post-Processing
2.9 Å
B
α-Cat ABD-Actin
Helical Autopicking
7,317 micrographs
540,533 extracted particles
200 classes
Select 2D Class Averages
428,335 particles | 3 3D classes
Final Map
3D Class Averages
Class I
Class II
Class III
Central Slice
90°
52.3%
44.5%
3.2%
Classes I & II | 414,486 particles
3D Auto-Refine
CTF Refine
Bayesian Polishing
Post-Processing
3.2 Å
C
Fourier Shell Correlation
Half Maps
2.9 Å
Model vs Map
3.0 Å
Resolution (1/Å)
MVinc ABD-Actin
2.8
3
3.2
3.4
3.6
D
Fourier Shell Correlation
Half Maps
3.2 Å
Model vs Map
3.3 Å
Resolution (1/Å)
α-Cat ABD-Actin
2.8
3
3.2
3.4
3.6

and C-terminal ABD tail domains (Johnson and Craig, 1995) (Figure 3-3), as the head domain clearly clashes with F-actin in the crystallized conformation. Full-length α-catenin was crystallized as an asymmetric “left-handshake dimer”, characterized by differential relative orientations between the head and tail domains of each protomer (Rangarajan and Izard, 2013). Comparing the actin-bound α-catenin ABD with both conformers in the asymmetric dimer crystal structure also reveals severe clashes between the α-catenin head domain and actin (Figure 3-3), suggesting that full-length α-catenin, despite the ability to bind actin, must also undergo substantial conformational rearrangements when actin binding actually happens.

We next compared the metavinculin ABD-F-actin and α-catenin ABD-F-actin structures (Figure 3-1), confirming previous low- and moderate-resolution studies (Janssen et al., 2006; Janssen et al., 2012; Kim et al., 2016; Thompson et al., 2014) that both ABDs engage a major site spanning the longitudinal interface of 2 actin protomers, which we term Actin I and Actin II (numbered from the plus end of the filament). In turn, each actin protomer also contacts 2 ABDs, leading to a 1:1 binding stoichiometry at saturation. Our structures establish this region is almost identical between the two ABDs, comprising 2040 $Å^2$ of buried surface area for the metavinculin ABD and 1920 $Å^2$ for the α-catenin ABD. However, our high-resolution models also reveal a previously unobserved minor interface for each ABD (confirming a recent computational prediction in the case of metavinculin (Krokhotin et al., 2019)), mediated by residues in their flexible C-terminal extensions (CTEs) on the very C-terminus of

Figure 3-3. (Meta)Vinculin and α-catenin activation mechanisms.

(A and B) Superimposed pre-bound full-length vinculin crystal structure (PDB 1st6) and post-bound metavinculin ABD cryo-EM structure in the absence of actin (A), or in the presence of actin (B).

(C, D, E, and F) Superimposed pre-bound full-length α-catenin crystal structures (PDB 4igg: C and D: Chain B; E and F: Chain A) and post-bound α-catenin ABD cryo-EM structure without (C and E) or with (D and F) actin.

(G) Superimposed pre-bound full-length vinculin crystal structure (PDB 1st6) and post-bound α-catenin ABD cryo-EM structure in the presence of actin highlights the similar orientations of their CTEs.

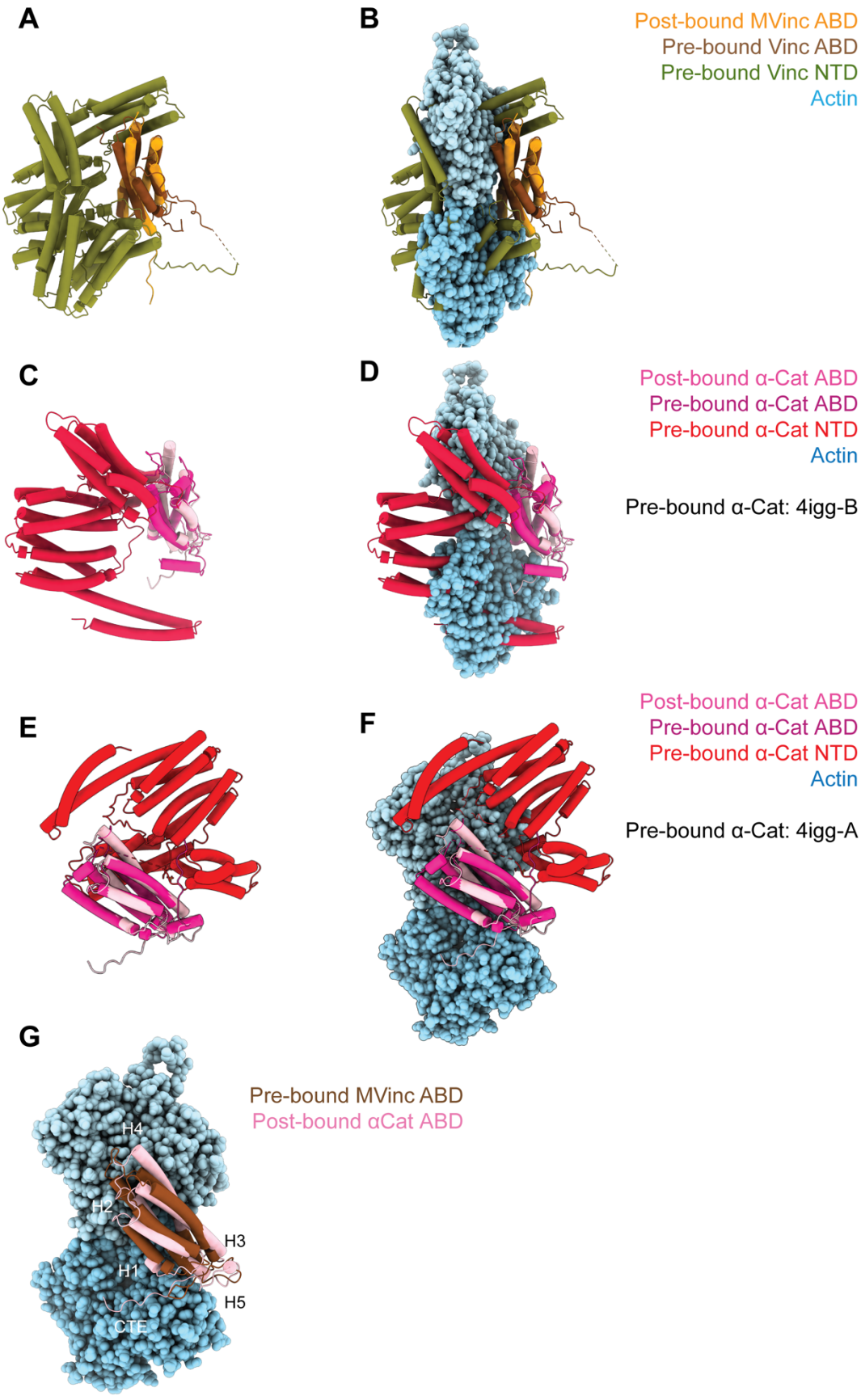
A
B
Post-bound MVinc ABD
Pre-bound Vinc ABD
Pre-bound Vinc NTD
Actin
C
D
Post-bound α-Cat ABD
Pre-bound α-Cat ABD
Pre-bound α-Cat NTD
Actin
Pre-bound α-Cat: 4igg-B
E
F
Post-bound α-Cat ABD
Pre-bound α-Cat ABD
Pre-bound α-Cat NTD
Actin
Pre-bound α-Cat: 4igg-A
G
Pre-bound MVinc ABD
Post-bound αCat ABD
H4
H2
H3
H1
H5
CTE

ABD (after all five helices), which are entirely distinct between the two proteins (see Chapter 2.1; Figure 2-2).

Consistent with our previous medium-resolution structural studies (Kim et al., 2016), we find the metavinculin ABD undergoes substantial conformational remodeling upon F-actin engagement, characterized by displacement of helix H1' from the 5 helix bundle to license a rearrangement of helices H2-H5 to relieve clashes with F-actin (Figure 3-4). N-terminal residues 879-980 are not visible in the map (Figure 3-4 Panel A, transparent brown), and are presumably disordered in the actin-bound state, while residues 981-985 (Figure 3-4 Panel A, brown) undergo a slight rearrangement, extending helix H2 by 1.5 turns (5 residues). Our high-resolution map reveals this contact to be mediated by the (meta)vinculin CTE (Figure 3-4). The CTE is released from its pre-bound position, extending helix H5 by 2 turns (6 residues), then undergoing an approximately 60° swing to engage a site along actin subdomain 1 proximal to H5 (Figure 3-4). Coupled to this transition, helices H2-H5 slightly rearrange to accommodate actin binding and avoid steric clashes (Figure 3-4).

The α-catenin ABD also undergoes an order-to-disorder transition at its N-terminus upon actin binding (Figure 3-4 Panel B), as no density for residues 664-698, the majority of H0-H1, is present in our map (Figure 3-4 Panel B), confirming a recent report that this region is important for activating α-catenin's actin engagement (Ishiyama et al., 2018). This is accompanied by a twisting rearrangement of helices H2-H4 reminiscent of that found in (meta)vinculin (Figure 3-4), as well as extension of H4 by 3 turns (9 residues) through folding of the H3-H4 loop, to sculpt a major actin-binding

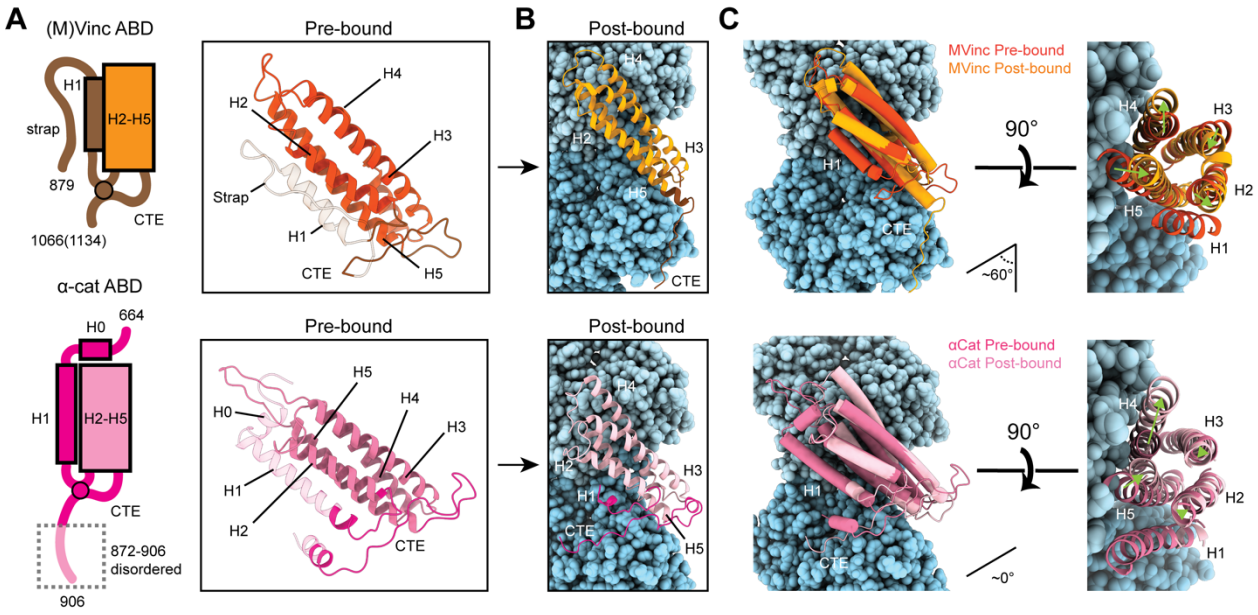

Figure 3-4. Major ABD conformational rearrangements upon actin binding.

(A) Cartoons and crystal structures of pre-bound (meta)vinculin ABD (PDB 1st6, dark orange, top) and α-catenin ABD (PDB 4igg chain B, dark pink, bottom). Regions that undergo major rearrangements are highlighted in brown (metavinculin) or magenta (α-catenin); regions not resolved in the actin-bound cryo-EM structures are transparent.

(B) Cryo-EM structures of metavinculin ABD (orange, top) and α-catenin ABD (pink, bottom). Flexible regions colored as in (A); actin, shades of blue.

(C) Superimposed pre-bound and post-bound structures of metavinculin ABD (top) and α-catenin ABD (bottom). Green arrows indicate displacement of helices; rotation angles indicate repositioning of C-terminal extensions (CTEs).

interface sterically compatible with the filament (Figure 3-4). This suggests that N-terminal helix release allosterically coupled to ABD helical-bundle rearrangement is a fundamentally conserved mechanistic feature of actin binding by members of the vinculin / α-catenin family. However, we observe distinct rearrangements in the α-catenin CTE, which undergoes a slight lateral shift and helical unfurling, rather than a swing, to engage a site spanning a different surface of actin subdomain 1 (Figure 3-4).

Metavinculin H5 extension is facilitated by binding interactions with Actin I (Figure 3-5), notably a hydrophobic interaction between metavinculin I1114 and Actin Y91, and a salt bridge between metavinculin R1117 and actin E100. This positions the CTE to form an extended interface with actin subdomain 1, contiguous with that mediated by H5, with metavinculin W1126 buried in a proximal hydrophobic pocket formed by actin residues A7, P102, P130, A131 and W356, bolstered by a distal salt bridge between metavinculin R1128 and actin E361 (Figure 3-5 Panel B) after the 60° swing. In contrast, the α-catenin CTE retains an overall conformation similar to its pre-bound state (Figure 3-5 Panels A and C) consistent with the slight lateral shift of its CTE. An extensive hydrophobic network we term a ‘tryptophan latch’ embraces CTE residue W859 in both pre-bound and post-bound states, preventing α-catenin CTE unfurling (Figure 3-5 Panel C, right). A single turn of helix H1 on the N-terminal side of the ABD remains folded, with H1 residue W705 packing against CTE residue M861, encircling W859 along with CTE residues L852 and L854, as well as residues W705, I712, I763, L776, P768, V833, and Y837 from neighboring regions of the helical bundle, facilitating coordinated conformational transitions between the N- and C-terminal flexible regions of

Figure 3-5. The actin-binding interfaces of metavinculin and α-catenin.

(A) Overlay of the metavinculin ABD-actin complex and α-catenin ABD-actin complex atomic models highlighting C-terminal extensions (CTEs) of metavinculin ABD and α-catenin ABD, superimposed on Actin I and colored as in Figure 3-4. Actins from α-catenin structure are displayed.

(B and C) Detailed views of key contacts at minor interfaces: metavinculin CTE and actin (B); within the α-catenin tryptophan latch (right) and between its CTE and actin (left) (C).

(D) Overlay of the metavinculin ABD-actin complex and α-catenin ABD-actin complex atomic models highlighting helical binding interfaces of metavinculin ABD and α-catenin ABD, superimposed and colored as in (A). Actins from α-catenin structure are displayed.

(E, F and G) Detailed views of key contacts at major interface between metavinculin / α-catenin helices H4–H5 and Actin I (E); Actin II (F); Actin II D-loop (G).

(H) Actin C_α traces colored by per-residue RMSD from the indicated comparisons. For superposition, segmented actin density from the cryo-EM maps was first aligned, followed by fitting the atomic models into their corresponding maps.

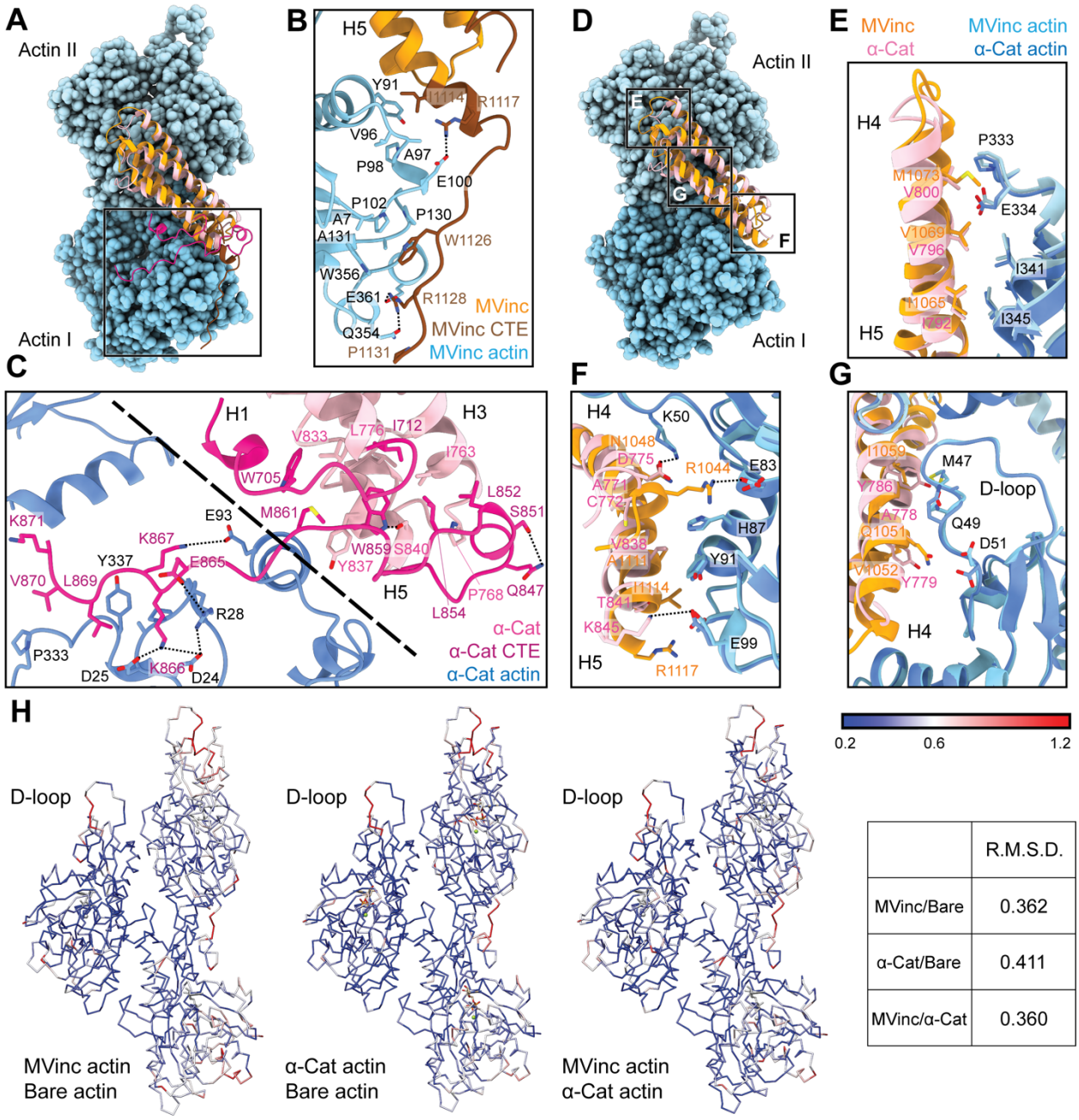

	R.M.S.D.
MVinc/Bare	0.362
α-Cat/Bare	0.411
MVinc/α-Cat	0.360

the α-catenin ABD upon actin binding. A putative hydrogen bond is also maintained between S840 and the single nitrogen atom in W859's indole ring, maximizing the binding potential of this residue.

The latch positions the neighboring region of the α-catenin CTE to bind a distinct site on Actin I's subdomain 1 (Figure 3-5 Panel C, left) mediated by proximal salt bridges (α-catenin E865 – actin R28, α-catenin K866 – actin D24/D25, α-catenin K867 – actin E93) and distal hydrophobic interactions (α-catenin L869/V870 – actin P333/Y337). Superposition of the actin-bound conformation of the α-catenin ABD with the pre-bound conformation of the (meta)vinculin ABD (Figure 3-3) reveals a striking positional overlap between α-catenin W859 and metavinculin W1126 (vinculin W1058 is identically positioned, not shown), which is also engaged by a sparser latch in the pre-bound conformation. We thus speculate the extensive latch of α-catenin prevents W859 release and the extension of its CTE to engage the same site as metavinculin W1126.

3.2 Discovery of α-catenin force sensor by structure-guided protein engineering

The complete non-overlap and lack of homology of the (meta)vinculin and α-catenin minor actin-binding interfaces mediated by their CTEs lead us to hypothesize that the CTEs could be involved in differential force-activated actin binding. To identify other potential contributing structural elements, we first undertook a detailed comparison of their major actin-binding interfaces mediated by helices H4-H5 in both proteins (Figure 3-5 Panel D). The Actin II binding interface is almost identical between the two ABDs (Figure 3-5 Panel E), mediated by an extensive series of conserved

hydrophobic contacts: α-catenin I792/metavinculin I1065 – actin I345, α-catenin V796/metavinculin V1069 – actin I341, and α-catenin V800/metavinculin M1073 – actin P333/E334. The Actin I interface, on the other hand, is more variable and characterized by few clear residue-level binding interactions (Figure 3-5 Panel F), notably likely weak long-distance salt bridges (metavinculin R1044 – actin E83 and α-catenin K845 – actin E99) specific to each protein, despite the overall shape complementarity across the interface. Each ABD also features a unique hydrophobic interaction with actin Y91 (metavinculin I1114 / α-catenin V838).

The Actin I interface extends into contacts with the actin D-loop (Figure 3-5 Panel G), a flexible region of actin which mediates structurally polymorphic longitudinal interactions between protomers (Galkin et al., 2010b) reported to be modulated by actin nucleotide state (Chou and Pollard, 2019; Merino et al., 2018) and ABPs (Dominguez and Holmes, 2011; Oda et al., 2019). Both ABDs form a potential weak long-distance interaction with actin D-loop residue K50: in metavinculin, a hydrogen bond through N1048, and in α-catenin, a salt bridge through D775. The D-loop then adopts subtly different conformations between the two interfaces centered at M47. Although clear residue-level binding interactions are not readily apparent, the conformation of M47 at the metavinculin interface would clash with α-catenin Y786, a position occupied by the smaller residue I1059 in metavinculin, suggesting local sterics unique to each ABD determine compatibility with a distinct D-loop conformation. Comparison of the actin conformation observed in a similar-resolution structure of ADP F-actin in isolation (“F-actin alone”, M.S. in preparation) versus when bound to metavinculin or α-catenin, as

well as comparison of the metavinculin-bound and α-catenin-bound conformations reveals minimal rearrangements throughout the majority of the structure (Figure 3-5), in contrast to a previous report of α-catenin-induced structural changes in F-actin inferred from low-resolution cryo-EM analysis (Hansen et al., 2013). The sole region featuring rearrangements greater than 1 Å RMSD is a 3-4 residue stretch of the D-loop centered on M47. As force across the filament could feasibly modulate D-loop structure to regulate ABP binding, we hypothesized ABD residues mediating D-loop interactions could also mediate differential force-activated actin binding.

To investigate whether D-loop interactions contribute to α-catenin force-activated binding, we designed a triple point-mutant α-catenin ABD construct where 3 residues in close proximity to the D-loop were replaced by those in vinculin: α-catenin ABD$^{A778Q\ Y779V\ Y786I}$. In force reconstitution assays, this construct did not visibly associate with actin in either the –ATP or +ATP condition in the concentration regime accessible by TIRF (Figure 3-6 Panel A). While these data suggest that the α-catenin D-loop interactions contribute to overall affinity for F-actin, the complete lack of binding is refractory to determining whether this interface has a separable role in force-activated actin binding.

We thus returned to our initial hypothesis that differential force-activated binding could be mediated by the CTEs. Although we were unable to accurately model the final three residues of the metavinculin CTE, weak density is clearly present (Figure 3-6 Panel B, red), suggesting the entire CTE engages F-actin. By contrast, density for the α-catenin CTE is only present until K871 (Figure 3-5 Panel C; Figure 3-6 Panel C).

Figure 3-6. TIRF assays for the α-catenin ABD triple mutant which does not bind actin, and putative ABD-ABD contacts along F-actin.

(A) Representative TIRF-assay movie frames of actin (left) and α-catenin ABD "triple mutant" (α-cat ABD-tm) (right) channels in the absence (top) and presence (bottom) of ATP to activate motors. As the ABD did not visibly associate with F-actin in either condition, these data were not quantified. Scale bar, 20 μm.

(B and C) Views of potential contacts between longitudinally adjacent actin-bound ABDs mediated by CTEs for metavinculin (B) and α-catenin (C). Left: segmented density maps highlighting contact regions (boxes). Right: Detailed view of putative contacts, with density map shown in grey transparent representation. The distal end of the metavinculin CTE (residues W1132, Y1133, Q1134), which is positioned to mediate inter-ABD contacts, was not modeled due to weak electron density (red).

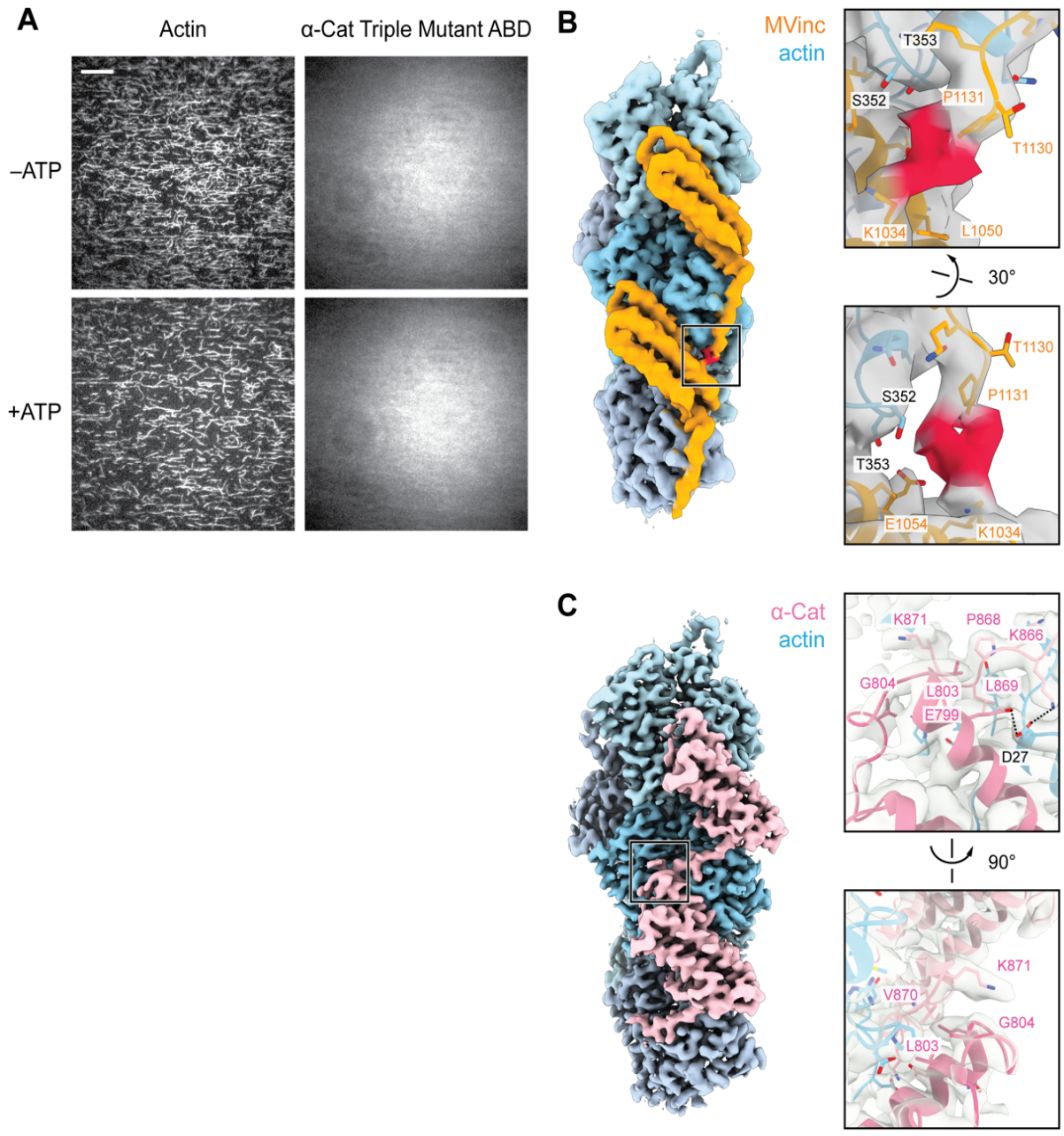
A
Actin
α-Cat Triple Mutant ABD
–ATP
+ATP
B
MVinc
actin
T353
S352
P1131
T1130
K1034
L1050
30°
T1130
S352
P1131
T353
E1054
K1034
C
α-Cat
actin
K871
P868
K866
G804
L803
L869
E799
D27
90°
K871
V870
G804
L803

Notably, all three human α-catenin isoforms have highly homologous CTEs that extend an additional 35 amino acids (Figure 2-2, see Chapter 2), diverging in sequence and length from the vinculin CTE. Consistent with previous primary-structure-function analysis (Pokutta et al., 2002) showing that residues after P864, which bear no homology to vinculin, are necessary for actin binding, our structure shows that residues 865-871 are in direct contact with actin (Figure 3-5 Panel C), forming an extensive interface. We therefore hypothesized that distal residues 872-906, a 35-residue element within CTE unique to αE-catenin (Figure 2-2, see Chapter 2) that was not resolved in our cryo-EM analysis and is thus presumably conformationally flexible, could uniquely contribute to force-activated actin binding.

To test whether distal residues 872-906 have a separable role in force-activated binding, i.e., as a “force detector”, we first truncated these residues from the α-catenin ABD (α-cat ABDΔC, the truncated product) by site-directed mutagenesis (Materials and Methods, see Chapter 7). The mutant was then subjected to the novel TIRF assay we developed (see Chapter 2.3) to test whether α-cat ABDΔC could still sense mechanical force on actin. Consistent with a regulatory role for this segment, α-cat ABDΔC constitutively associated with F-actin in TIRF assays (Figure 3-7 Panel A; Figure 3-8), with no significant increase in actin binding upon ATP addition, suggesting that this distal region (residues 872-906) is necessary for force-activated binding by negatively-regulating low-force binding.

To investigate the sufficiency of distal residues 872-906, we generated chimeric ABDs featuring the H2-H5 bundle region of vinculin and the flexible termini of α-catenin.

Figure 3-7. The distal tip of α-catenin's C-terminus is a force detector.

(A, B and C) TIRF force reconstitution assays. Left: Representative movie frames in the presence and absence of ATP. Scale bar, 30 μm. Right: Cartoon of ABD construct (left) and paired analysis of overall intensity ratio change upon ATP addition (right). Wilcoxon signed rank test: *$p < 0.05$; n.s. (not significant), $p > 0.05$. Constructs assayed were: α-cat ABDΔC (A) (αE-catenin$_{664\text{-}871}$, N = 5, p = 0.81); Vinc ABD-NCSwap (B) (αE-catenin$_{664\text{-}708}$-vinculin$_{916\text{-}1041}$-αE-catenin$_{837\text{-}906}$, N = 6, p = 0.031); Vinc ABD-NCSwapΔC (C) (αE-catenin$_{664\text{-}708}$-vinculin$_{916\text{-}1041}$-αE-catenin$_{837\text{-}871}$, N = 5, p = 0.63).

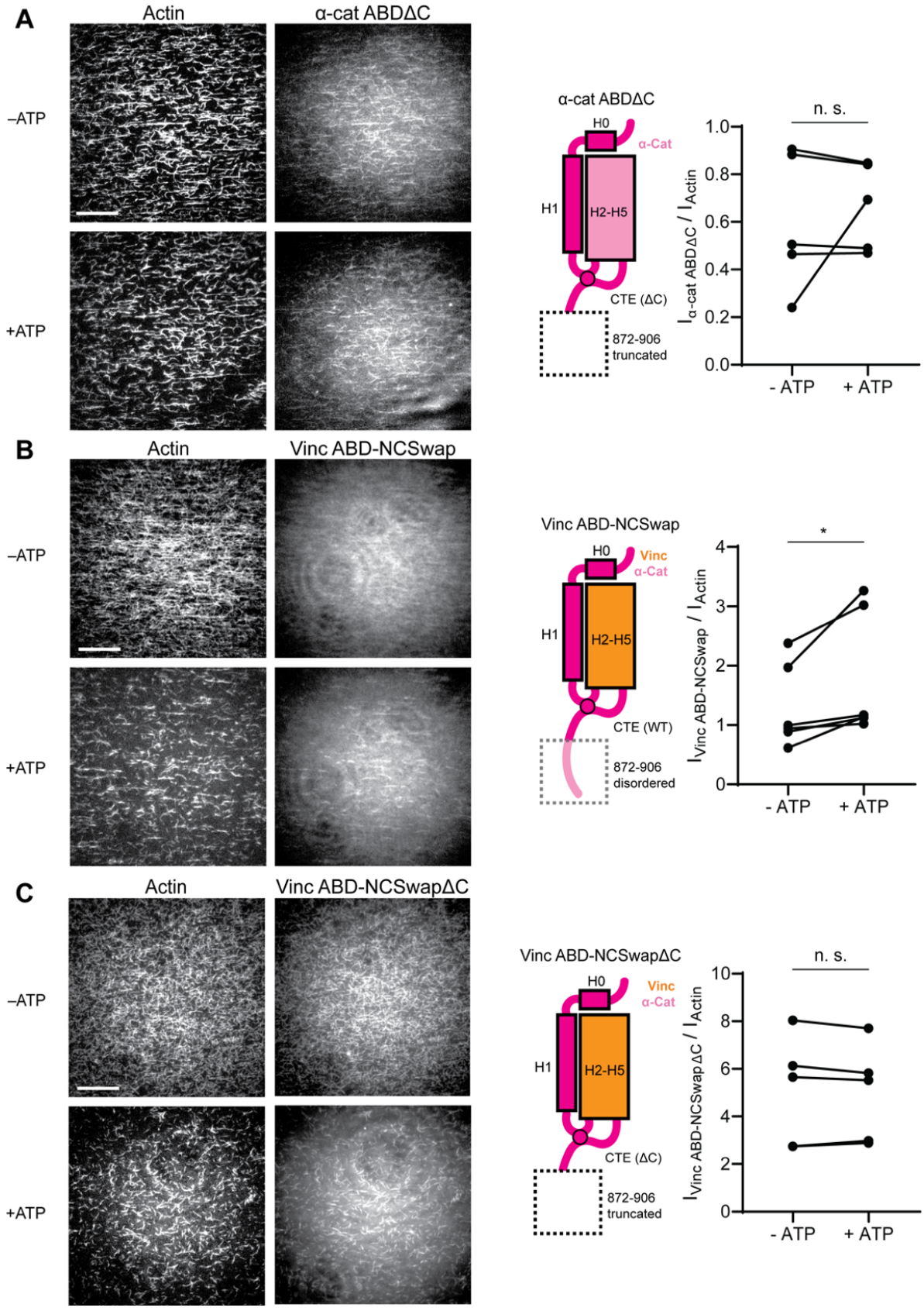
A
Actin
α-cat ABDΔC
–ATP
+ATP
α-cat ABDΔC
H0
α-Cat
H1
H2-H5
CTE (ΔC)
872-906
truncated
n. s.
1.0
0.8
0.6
0.4
0.2
0.0
$I_{\alpha\text{-cat ABD}\Delta C} / I_{Actin}$
- ATP
+ ATP
B
Actin
Vinc ABD-NCSwap
–ATP
+ATP
Vinc ABD-NCSwap
H0
Vinc
α-Cat
H1
H2-H5
CTE (WT)
872-906
disordered
*
4
3
2
1
0
$I_{Vinc\ ABD\text{-}NCSwap} / I_{Actin}$
- ATP
+ ATP
C
Actin
Vinc ABD-NCSwapΔC
–ATP
+ATP
Vinc ABD-NCSwapΔC
H0
Vinc
α-Cat
H1
H2-H5
CTE (ΔC)
872-906
truncated
n. s.
10
8
6
4
2
0
$I_{Vinc\ ABD\text{-}NCSwap\Delta C} / I_{Actin}$
- ATP
+ ATP

A vinculin ABD construct where only the CTE was substituted was non-functional (data not shown). However, consistent with close proximity and structural coordination between the α-catenin N-terminal segment and the CTE through the tryptophan latch (Figure 3-5 Panel C), a vinculin ABD construct featuring both the α-catenin N-terminal segment and the CTE (vinc ABD-NCSwap, Materials and Methods) gained force-activated binding activity in TIRF assays, with diminished low-force binding observed (Figure 3-7 Panel B; Figure 3-8 Panel B) in contrast to the wild-type vinculin ABD (see Chapter 2). A C-terminal truncation of this construct (vinc ABD-NCSwapΔC) equivalent to α-cat ABDΔC reverted to constitutive binding insensitive to force in TIRF assays (Figure 3-7 Panel C; Figure 3-8 Panel C), supporting the α-catenin CTE as the key determinant of force-activated binding, in which the distal residues 872-906 serves as the direct force-detector. We thus conclude that the distal C-terminus (residues 872-906) of α-catenin is necessary and sufficient for force-activated actin binding through negative regulation of low-force binding.

3.3 The molecular mechanism for the force-sensitive actin binding by α-catenin

While our studies pinpoint the final 35 amino acids of α-catenin as a force-detector, the exact molecular mechanism by which this segment negatively regulates low-force binding to F-actin remains to be elucidated. To reveal this mechanism, it is necessary to characterize the structural and conformational landscape of the α-catenin CTD, especially the 35-residue force sensor, in solution. Subsequently, direct structural characterization of α-catenin ABD binding to tensed F-actin has to be performed under

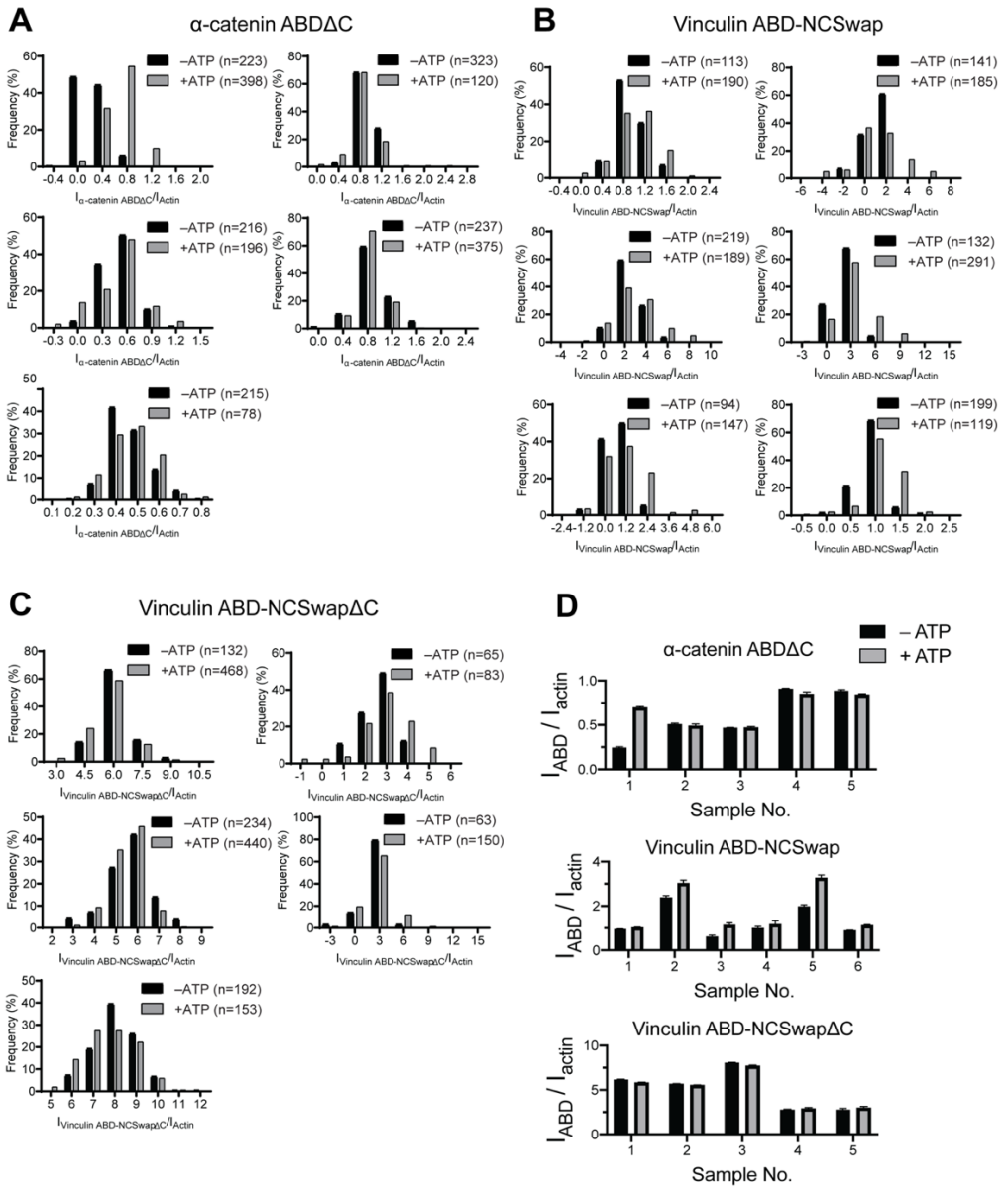

Figure 3-8. Intensity ratio distributions of single-filament regions for α-catenin and vinculin CTE mutants.

(A, B and C) Time-averaged I_{ABD}/I_{actin} intensity ratio distributions of single-filament regions before and after ATP addition for α-catenin ABDΔC (A); Vinc ABD-NCSwap (B); Vinc ABD-NCSwapΔC (C). These data were used for the analysis presented in Figure 3-7 A-C. (D) Bar plots of mean ± SEM of high-force and low-force averages for all trials displayed in Figure 3-7.

active force generation. However, the solution structure of the α-catenin force sensor is currently unknown. Existing techniques in structural biology are not compatible with direct mechanical manipulation on actin. Therefore, developing novel cryo-EM methods to study mechanically modulated actin filaments is imperative.

We propose two potential, non-exclusive conceptual models for this modulation. As we observe the distal tip of the ordered region of the CTE to be in close apposition to the next ABD binding site along the actin filament, with potential contacts between CTE residues V870 and K871 with the H4-H5 loop and the N-terminal tip of H5 in longitudinally adjacent ABD (Figure 3-6 Panel C), the first model invokes steric exclusion (Figure 3-9 Panel A). In the absence of force, the force-detector physically blocks the adjacent binding site through steric hindrance, which can be relieved by an increase in protomer axial spacing in the presence of tension, consistent with prior truncation studies suggesting residues 884-906 may inhibit α-catenin's actin binding (Pappas and Rimm, 2006). As the force-detector likely represents a flexibly tethered conformational ensemble, in the presence of thermal fluctuations we envision this would manifest as a tension-dependent increase of the binding on-rate at the site due to its increased fractional availability. Although saturating the filament for structural studies could lead to non-physiological inter-ABD interactions, cooperative F-actin binding by the α-catenin ABD has previously been reported under non-saturating conditions (Hansen et al., 2013), and supplemental soluble ABD enhanced catch-bonding by the cadherin complex (Buckley et al., 2014), suggesting communication between actin-bound ABDs is likely to be physiologically relevant. We note that cooperative and

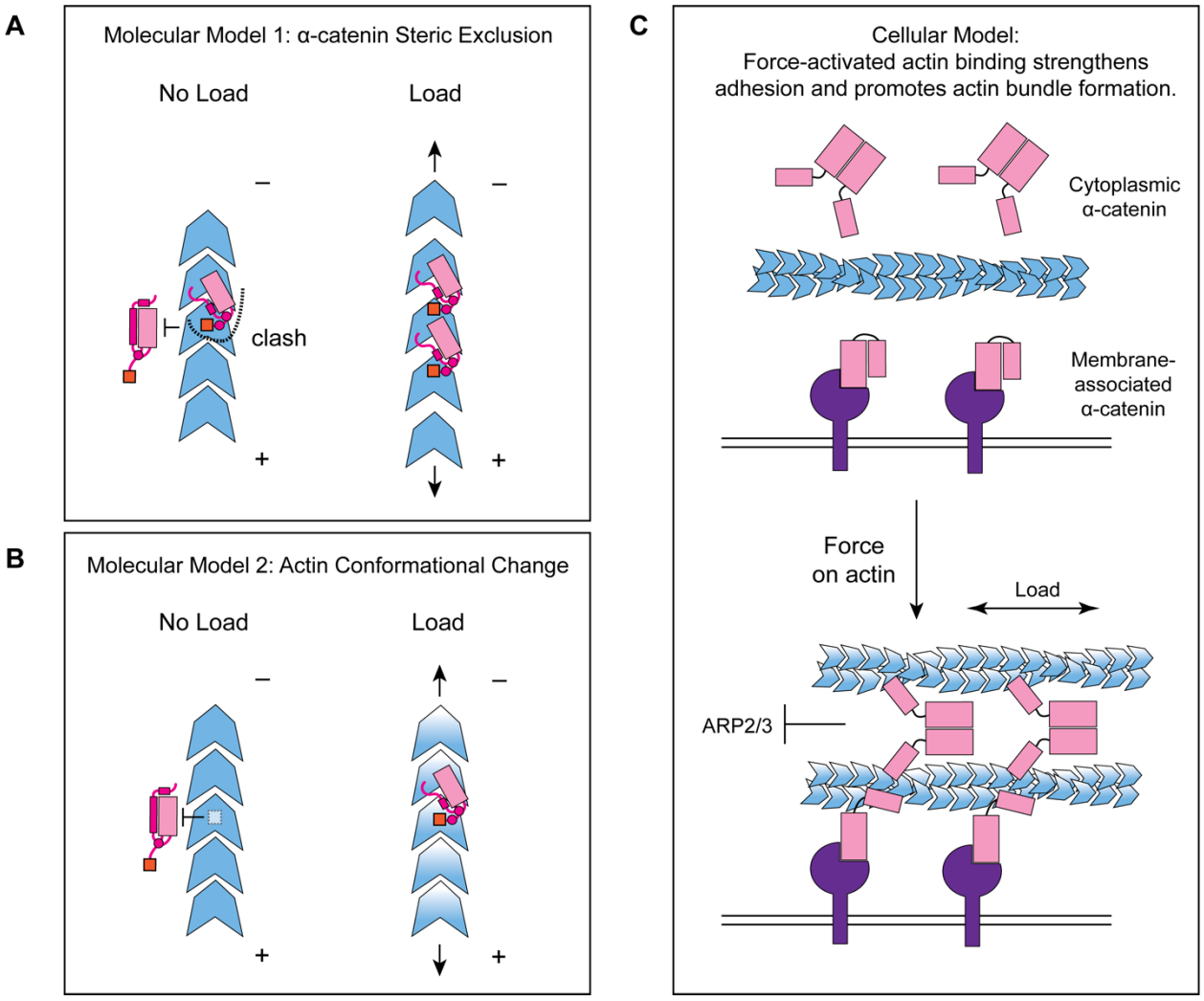

Figure 3-9. Molecular and cellular mechanisms for force-activated binding by α-catenin.

(A and B) Cartoons of two conceptual mechanistic models for force-activated actin binding by the α-catenin ABD. Orange box represents the force detector (residues 872-906) at the distal tip of the CTE. Blue gradient represents a force-induced conformational transition in the actin protomer.

(C) Cartoon of proposed biological functions for force-activated actin binding by the two cellular populations of α-catenin. Membrane-associated cadherin-catenin complexes are illustrated in purple.

inhibitory inter-ABD communication are not *a priori* mutually exclusive, and the interplay of these opposing effects could produce differential outcomes as a function of ABD concentration and filament load, an important subject for future studies.

The second model invokes a conformational change in the actin protomer which specifically occurs in the presence of mechanical load, which is recognized and preferentially bound by the force-detector, relieving inhibition (Figure 3-9 Panel B). Although our studies suggest only minor actin conformational changes when binding is driven by mass action (Figure 3-5 Panel H), they do not rule out as yet unobserved actin conformations specifically evoked by force. Furthermore, while for simplicity we have framed both models in terms of discrete transitions between structural states, low piconewton forces could also modulate the intrinsic structural fluctuations of F-actin to control α-catenin engagement through either mechanism, as has previously been speculated for cofilin (Galkin et al., 2012; Hayakawa et al., 2011; Wioland et al., 2019).

As mentioned above, the solution structure of the α-catenin force sensor, as well as structural studies of the α-catenin ABD–F-actin interface in the presence of active force generation, will be necessary to dissect the interplay of these models. The ongoing efforts, which was started by me and will be continued by future lab members, have laid the foundation for both questions. First, in a collaboration with the lab of Dr. David Eliezer, we have started to study the solution structure of α-catenin ABD, especially its 35-residue tension sensor, by nuclear magnetic resonance (NMR) spectroscopy (Figure 3-10). A pilot study was performed using purified ^{15}N-labeled α-catenin ABD in solution in the absence of F-actin, in which distinct chemical shifts have

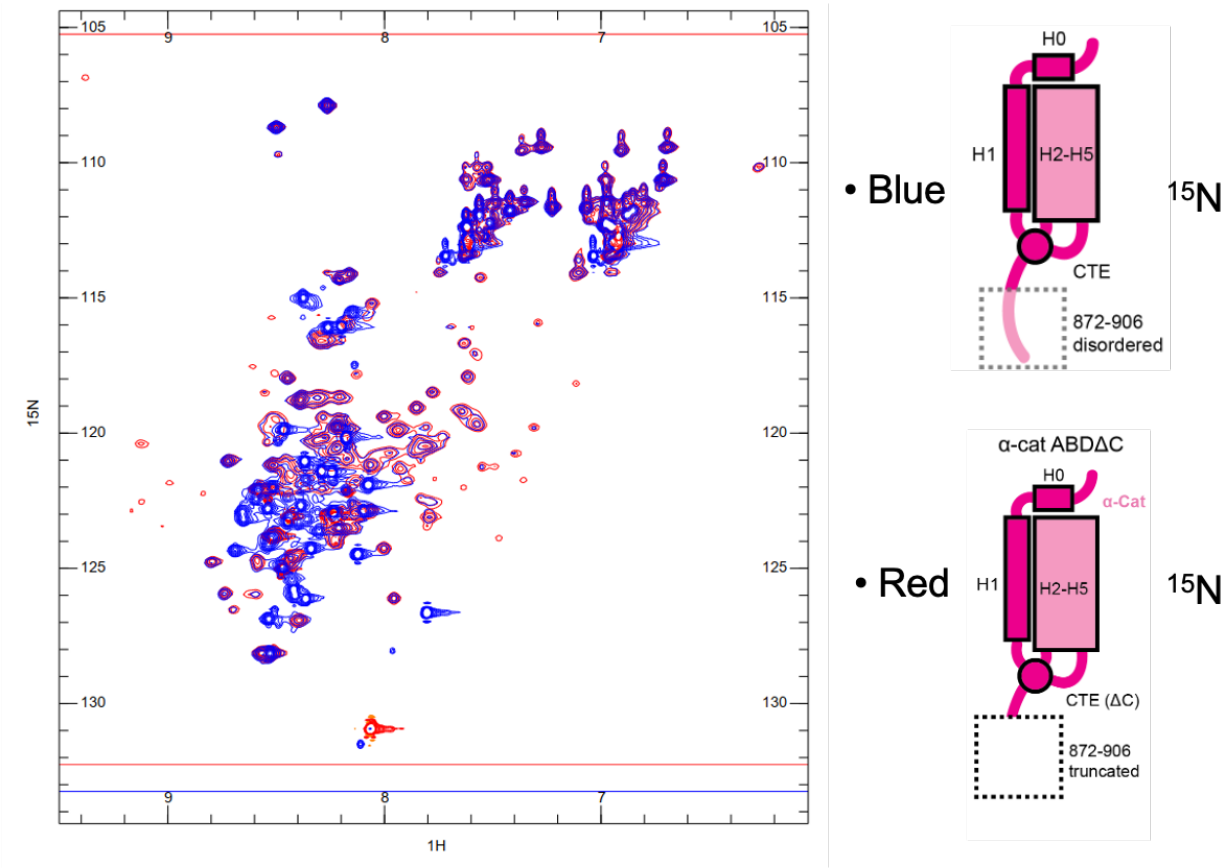

Figure 3-10. Pilot study on the solution structure of α-catenin mechanosensor.

Two-dimensional nuclear magnetic resonance (NMR) spectrum of α-catenin ABD (residue 664-906, blue chemical shift peaks) and α-catenin ABDΔC (residue 664-871, red chemical shift peaks).

been observed for its C-terminal extension (CTE) when the spectra of the untruncated and the CTE-truncated α-catenin ABD are compared (Figure 3-10). Ongoing work to study and compare the chemical shifts of the CTE residues have been performed in the presence of actin filaments. By analyzing these NMR spectra, we hope to know whether CTE, especially the 35-residue force sensor, is itself an ordered domain in solution, whether it can fold into an ordered domain upon actin binding, and if so, whether the structure of the force sensor changes in the absence and the presence of F-actin. In the experiments F-actin was not labeled with the ^{15}N isotope, and therefore did not contribute to the NMR signal. At 27kD, the α-catenin ABD is a small enough protein to be studied by NMR. Our pilot study has shown that the 35-residue force sensor can be pinpointed by comparing the NMR spectra of untruncated and truncated α-catenin ABD.

Second, in order to structurally characterize the actin-binding conformation of α-catenin ABD under active force generation, my colleagues Pinar Gurel and Ayala Carl in the Alushin lab are developing a novel cryo-EM method. Protein samples for Cryo-EM are prepared by plunge-freezing a thin layer of a protein solution on a metal support grid, the 'EM grid', which is usually coated with a thin layer of holey carbon (Figure 3-11 Panel A). The holey carbon layer on EM grids can be randomly surface-decorated with a mixture of myosin V and myosin VI, which essentially replicates the force system for the TIRF assay (Chapter 2.3) on EM grids: when the plunge-frozen protein solution contains F-actin and ATP, the two oppositely directed motors will stretch actin filaments spanning the holes (Figure 3-11 Panel A), which we anticipate will activate actin binding by α-catenin. This high-energy conformational state of actin will be preserved by rapid

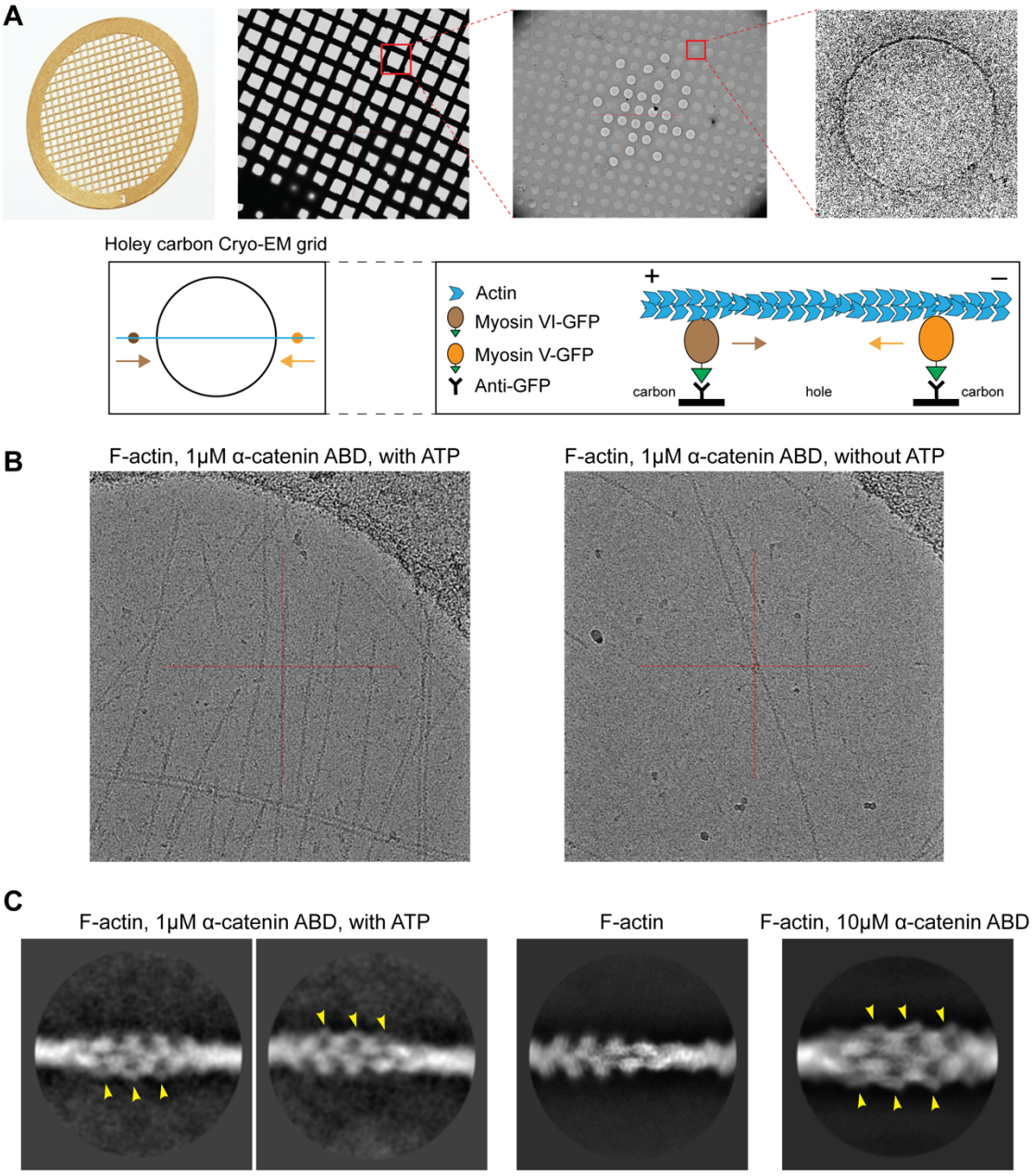

Figure 3-11. Direct structural characterization of force-activated asymmetrical actin binding by α-catenin ABD.

(A) An illustration of a Cryo-EM grid and cartoon for the novel surface-immobilized myosin motor method for active force generation on F-actin imaged by Cryo-EM. (B) Representative Cryo-EM micrographs under –/+ force conditions. (C) Representative 2D class averages indicating force-induced asymmetrical actin binding by α-catenin.

plunge freezing. Because only the protein solution that covers the holes is imaged by Cryo-EM, the images would not contain myosin motors decorating the carbon surface. Therefore, our strategy provides a unique way to introduce force on actin filament and capture the high-energy conformations of tensed actin filaments without adding interfering background signals. To our knowledge, this is currently represents the only method for protein structure characterization in the presence of active force generation. Cryo-EM micrographs under the –/+ force conditions show that the α-catenin ABD, at a concentration of 1μM, preferentially binds to tensed F-actin when ATP was included in the sample compared to the F-actin sample when ATP was excluded (Figure 3-11 Panel B). In our previous high-resolution α-catenin structure, 10μM α-catenin was used to fully decorate F-actin (Figure 3-11 Panel C, bare F-actin and fully decorated F-actin). However, in this study it is imperative to pick an α-catenin concentration at which α-catenin's preferential actin binding can be distinguished from background binding in the absence of force. To achieve this goal multiple α-catenin concentrations were screened, and 1 μM produced the optimal results after the first round of screening. Preliminary Cryo-EM data processing of the +ATP dataset revealed unexpected results: the 2D class averages showed an asymmetrical actin binding by α-catenin in which the α-catenin molecules preferentially bind to one side of F-actin, while the other side remain undecorated (Figure 3-11 Panel C). Although further high-resolution characterization is not trivial and will be required to prove this asymmetrical side binding mechanism, the preliminary results presented here point to an unanticipated molecular mechanism that α-catenin's force-activated binding might derive from tension-induced, transient actin

local deformation and curvature sensing by α-catenin. Ongoing effort in solving the high-resolution force-activated α-catenin–F-actin structures will, hopefully, reveal the full structural mechanism of the force-sensitive actin binding by α-catenin ABD.

3.4 Discussion: A general mechanism for detecting force on actin through a flexible element

Our studies reveal that α-catenin preferentially binds tensed F-actin, using its flexible C-terminus to detect piconewton load which can be generated by myosin motors. We propose this force-activated F-actin binding could play an important role in the formation and reinforcement of cell-cell adhesion complexes, facilitating mechanically regulated interactions between α-catenin and actomyosin cables tuned for high sensitivity to motor-generated forces.

The approximately 3 Å resolution cryo-EM structures of both proteins bound to F-actin (to our knowledge, the highest-resolution structures of ABP-F-actin complexes reported to date) reveal they share an overlapping major actin binding site. However, they undergo markedly different rearrangements at their flexible N- and C-termini upon binding, resulting in distinct contacts mediated by their C-terminal extensions (CTEs) which re-fold on the actin surface. Truncating α-catenin's CTE results in constitutive strong F-actin binding regardless of force, and a chimeric construct of vinculin featuring α-catenin's CTE gains force-activated binding, demonstrating the α-catenin CTE to be a modular "force-detector" which negatively regulates low-force binding. Together, our studies indicate piconewton force on F-actin can be discriminated by flexible elements

in ABPs to mediate direct force-activated binding. This provides direct evidence that actin filaments are themselves tension sensors which can transduce mechanical force into regulated partner binding. Future studies pursuing NMR solution structures of α-catenin's flexible CTE, as well as reconstituting myosin force generation on the surface of cryo-EM girds, should fully reveal the structural mechanism of force-activated actin binding by α-catenin, guided by the preliminary results we present here.

The finding that the force-detector element of α-catenin can be functionally transplanted to vinculin demonstrates that force-activated F-actin binding is a modular activity which can be conferred by short sequence motifs. We thus speculate there are likely to be other actin-binding proteins with functionally analogous force-detectors, and that force-activated actin binding could serve as a general cellular mechanism to mediate mechanotransduction through the cytoskeleton, as a fundamental process in converting mechanical signals to downstream biochemical signals.

Table 1. Cryo-EM data collection, refinement and validation statistics.

	Metavinculin ABD–F-actin (EMDB-20844, PDB 6UPW)	**α-catenin ABD–F-actin** (EMDB-20843, PDB 6UPV)
Data collection and processing		
Microscope	Titan Krios	Titan Krios
Voltage (kV)	300	300
Detector	K2 Summit	K2 Summit
Magnification	29,000	29,000
Electron exposure (e^{-} / Å^2)	60	60
Exposure rate (e^{-} / pixel / s)	6	6
Calibrated pixel size (Å)	1.03	1.03
Defocus range (μm)	–1.5 to –3.5	–1.5 to –3.5
Helical symmetry	C1	C1
	27.06 Å rise	27.03 Å rise
	-167.07° twist	-166.88° twist
Initial filament segments (no.)	237,503	540,533
Final filament segments (no.)	215,369	414,486
Map resolution (Å)	2.94	3.24
FSC threshold	0.143	0.143
Refinement		
Initial model (PDB ID)	3JBK, 3J8A	4IGG, 3J8A
Model resolution (Å)	2.98	3.28
FSC threshold	0.5	0.5
Map sharpening B factor (Å^2)	–58	–85
Model composition	5 actin protomers, 2 actin-binding domains	
Non-hydrogen atoms	16,896	17,233
Protein residues	2,152	2,201
Ligands	5 Mg.ADP	
B factors (Å^2)		
Protein	53.41	71.59
Ligand	47.29	56.65
R.M.S. deviations		
Bond lengths (Å)	0.012	0.012
Bond angles (°)	0.860	0.833
Validation		
MolProbity score	1.23	1.33
Clash score	3.32	4.63
Poor rotamers (%)	0.06	0.05
Ramachandran plot		
Favored (%)	97.46	97.56
Allowed (%)	2.54	2.44
Disallowed (%)	0.00	0.00
EMRinger Score	4.40	3.87

CHAPTER 4

Structural mechanisms for actin binding and bundling by adhesion proteins

Note to readers: Part of the results discussed below arose from a collaborative effort between myself, my advisor Dr. Gregory M. Alushin, several colleagues in the Alushin Laboratory, including Mr. Santiago Espinosa de los Reyes and Ms. Ayala G. Carl, at the Rockefeller University, colleagues in the Sharon Campbell laboratory at University of North Carolina, Chapel Hill, and colleagues in the Alexander Dunn laboratory, including Dr. Alexander Dunn and Dr. Leanna Owen, at Stanford University.

4.1 Actin bundling by vinculin is regulated by metavinculin

As a functionally critical adhesion protein, vinculin is ubiquitously expressed (Ziegler et al., 2006) in human tissues. However, metavinculin, the larger splice isoform, is selectively expressed in smooth and cardiac muscle cells (Byrne et al., 1992), where it is always co-expressed with vinculin (Feramisco et al., 1982). Metavinculin expression is tightly controlled at substoichiometric levels relative to vinculin (9-42%), which correlates with the contractile needs of muscle cells (Burridge and Feramisco, 1980). Reduced metavinculin expression level is associated with cardiomyopathy (CM) and disorganized intercalated disc structures (Maeda et al., 1997), suggesting that metavinculin is necessary for the maintenance of muscle actin-membrane adhesion sites, playing an important role in force generation and transmission through its interaction with the actin cytoskeleton. Although both vinculin and metavinculin use their

tail domains (Vt and MVt) to bind actin (Ziegler et al., 2006), MVt, unlike Vt, does not bundle actin in vitro (Janssen et al., 2012). Moreover, playing a dominant negative role, metavinculin can fine-tune the architecture of vinculin-induced actin bundles (Oztug Durer et al., 2015). Point mutations identified within the MVt 68-residue insert cause altered actin organization and heart disease, notably dilated cardiomyopathy (DCM) and hypertrophic cardiomyopathy (HCM) (Maeda et al., 1997; Olson et al., 2002; Vasile et al., 2006). While A934V and ΔL954 metavinculin mutations are associated with DCM (Olson et al., 2002), an R975W mutation has been identified in patients with both DCM and HCM (Vasile et al., 2006). Both DCM and HCM are diseases of myocardium that prevent normal blood flow within the heart resulting from disruption in force transmission, suggesting a key role of the metavinculin-actin interaction in altering the properties of vinculin-associated actin network. However, the details of how MVt and its cardiomyopathy-associated mutants alter the vinculin-actin network have never been systematically examined by electron microscopy, and the molecular mechanisms by which metavinculin CM-associated mutants cause HCM and DCM are unknown.

To better understand the role of metavinculin in actin filament assembly and consequences of cardiomyopathy-related mutations, in a collaboration project with the laboratory of Dr. Sharon Campbell (Sarker et al., 2019), we conducted a series of negative stain EM experiments in the absence and presence of vinculin. The Vt and MVt protein constructs used in this study are shown by schematics (Figure 4-1 Panel A). The Vt domain encompasses 188 C-terminal residues of vinculin and consists of five α-helices (H1-H5) flanked by an N-terminal strap (NtS) and a C-terminal hairpin (CtHP).

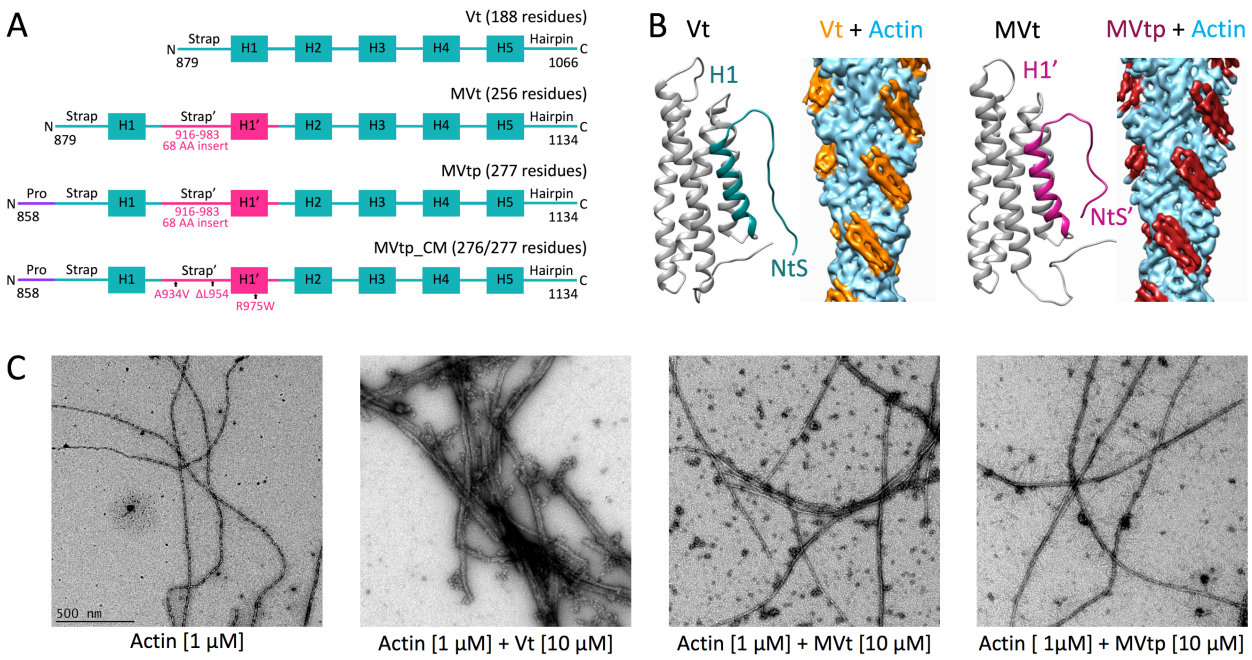

Figure 4-1. Actin binding by vinculin and metavinculin tail.

(A) Schematic representation of vinculin tail (Vt) and metavinculin tail (MVt) domain constructs. (B) Crystal structures of Vt (PDB ID 1TR2) and MVt (PDB ID 3MYI); and Cryo-EM reconstruction of Vt-actin (PDB ID 3JBI) and MVt-actin (PDB IDs 3JBK) complexes. (C) Negative stain EM images of actin filaments. Micrographs are acquired at the same magnification (scale bar = 500 nm, shown in the left panel). Crosslinking or bundling of actin filaments by Vt generates thick fibers whereas MVt and MVtp do not promote actin filament bundling.

MVt contains an extra 68-residue insert between helices H1 and H2 of Vt's sequence that displaces its 37 N-terminal residues and replaces its original H1 and NtS by similarly structured H1' and NtS'. MVtp contains additional 21-residue proline-rich linker preceding the NtS of MVt. Single point mutations specific to the metavinculin insert region, namely A934V, ΔL954 and R975W, have been implicated in cardiomyopathies and atherosclerosis. Our previous cryo-EM reconstructions showed similar mode of actin binding by both Vt and MVt through the compactly folded H2-H5 region which is identical in sequence (Kim et al., 2016) (Figure 4-1 Panel B). We have acquired negative stain EM images of actin filaments in the absence and presence of wild type Vt, MVt and MVtp (Figure 4-1 Panel C). The actin-alone sample showed structured single actin filaments. Vt induced crosslinking, or bundling, of these actin filaments and resulted in formation of thick fibers. However, when MVt or MVtp was added to actin instead of Vt, actin bundling was dramatically reduced and almost no thick fibers were observed. This is consistent with previously reported observation that MVt is incapable of F-actin bundling, indicating that the MVt insert region negatively regulates actin-induced MVt dimerization.

To quantify differences in actin filament organization in more detail in the presence of Vt, Mvt, and MVt cardiomyopathy mutants, we developed a quantitative negative-stain EM assay (Figure 4-2; see Materials and Methods, Chapter 7). The quantitative power of traditional negative stain EM imaging of F-actin assemblies is limited by selection bias, as choosing which part of the grid to image is dependent on input of an experienced user. Additionally, the frequently irregular structure of these

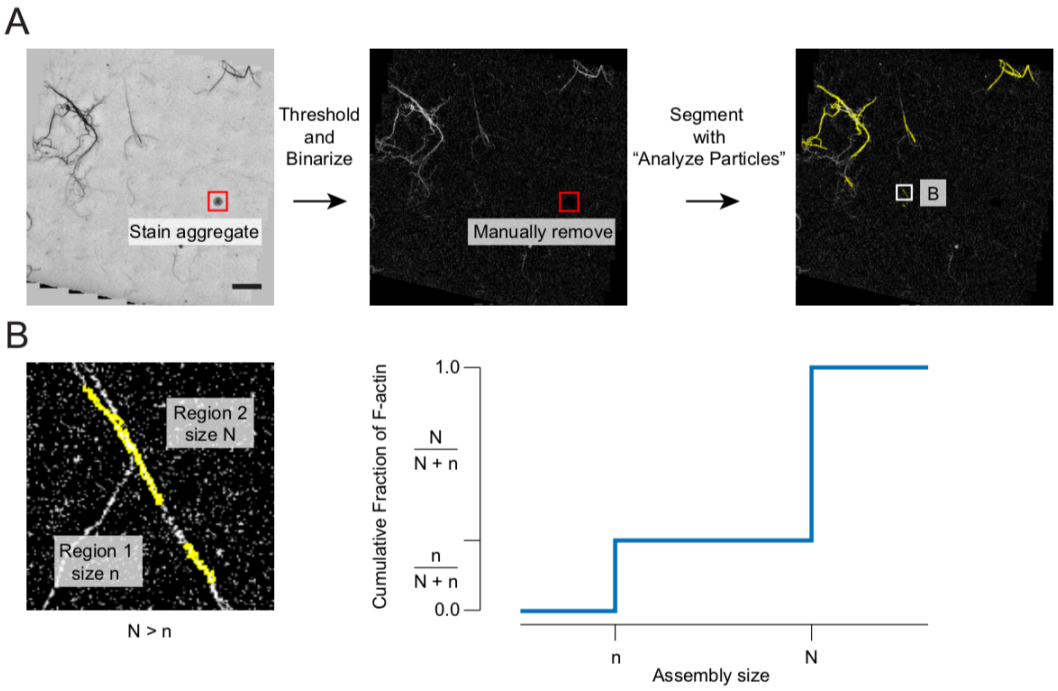

Figure 4-2. Quantification of actin assemblies from negative stain EM images.

(A) Flow-chart of quantification procedure. Images are thresholded and binarized with ImageJ, and obvious stain aggregates/crystals removed (red box). The binarized image is then segmented with "Analyze Particles", which detects regions of contiguous pixels (yellow outlines). Bar corresponds to 10µm. (B) Left - zoomed area corresponding to white box in A, which contains two regions. Region 2 is larger than region 1. Right - cumulative plot of a dataset composed only of region 1 and region 2 for illustration purposes. Each region contributes to the normalized cumulative sum proportionally to its size. Actual datasets contain hundreds to thousands of regions, and thus plots appear smoother at smaller sizes, but discrete jumps are visible for rare, large regions.

assemblies, compounded by their inherently variable contrast after negative staining, is refractory to image analysis methodology which depends on classification or averaging. To overcome selection bias, we targeted grid squares at low magnification where their contents were invisible. We then imaged the entirety of each targeted square at a magnification sufficient to resolve individual actin filaments, tiling it with overlapping fields of view which were subsequently stitched together (Figure 4-3 Panel A). We next implemented an image analysis procedure to detect and quantify higher order assemblies. Images were thresholded (the only step requiring user input due to stain variability) and binarized, then automatically segmented into contiguous regions using the “Analyze Particles” procedure in ImageJ. To analyze these data, we plot the cumulative fraction of F-actin + bound proteins detected in all regions vs. region size (Figure 4-2; Figure 4-3), which we find to be a sensitive metric of higher order assembly state that is robust against variations in background noise between different datasets (see Chapter 7). The actin bundling activities of Vt and MVt were first validated (Figure 4-3). As expected, we find the presence of Vt shifts the distribution towards larger assemblies versus actin alone, while the presence of wild-type MVt produced a modest effect, with substantially fewer large assemblies than for Vt.

The effects of MVt cardiomyopathy mutants were then examined by the assay, in which we observed a significant increase in assemblies in the presence of MVt cardiomyopathy mutants A934V, ΔL954, and R975W, with R975W having the most dramatic effect, consistent with the severity of disease caused by this mutation in patients. Examination of the images shows an irregular, mesh-like organization of

Figure 4-3. MVt cardiomyopathy mutants promote formation of actin assemblies. (A) Stitched negative-stain EM images of F-actin alone and in the presence of wild type Vt and MVt proteins (bars = 10μm). Zoomed views of the boxed regions are shown in the bottom panel (bars = 1μm). (B) Stitched negative-stain EM images of F-actin in the presence of MVt constructs featuring cardiomyopathy mutations (bars = 10 μm). Zoomed views of the boxed regions are shown in the bottom panel (bars = 1 μm). (C) Cumulative plots of F-actin assemblies from the indicated conditions. Pair-wise comparisons show all distributions to be significantly different (KS test, $p < 0.01$). $N \geqslant 10$ fields and $n \geqslant 764$ regions were quantified for each condition. F-actin, 0.5 μM; Vt/MVt constructs, 2.0 μM.

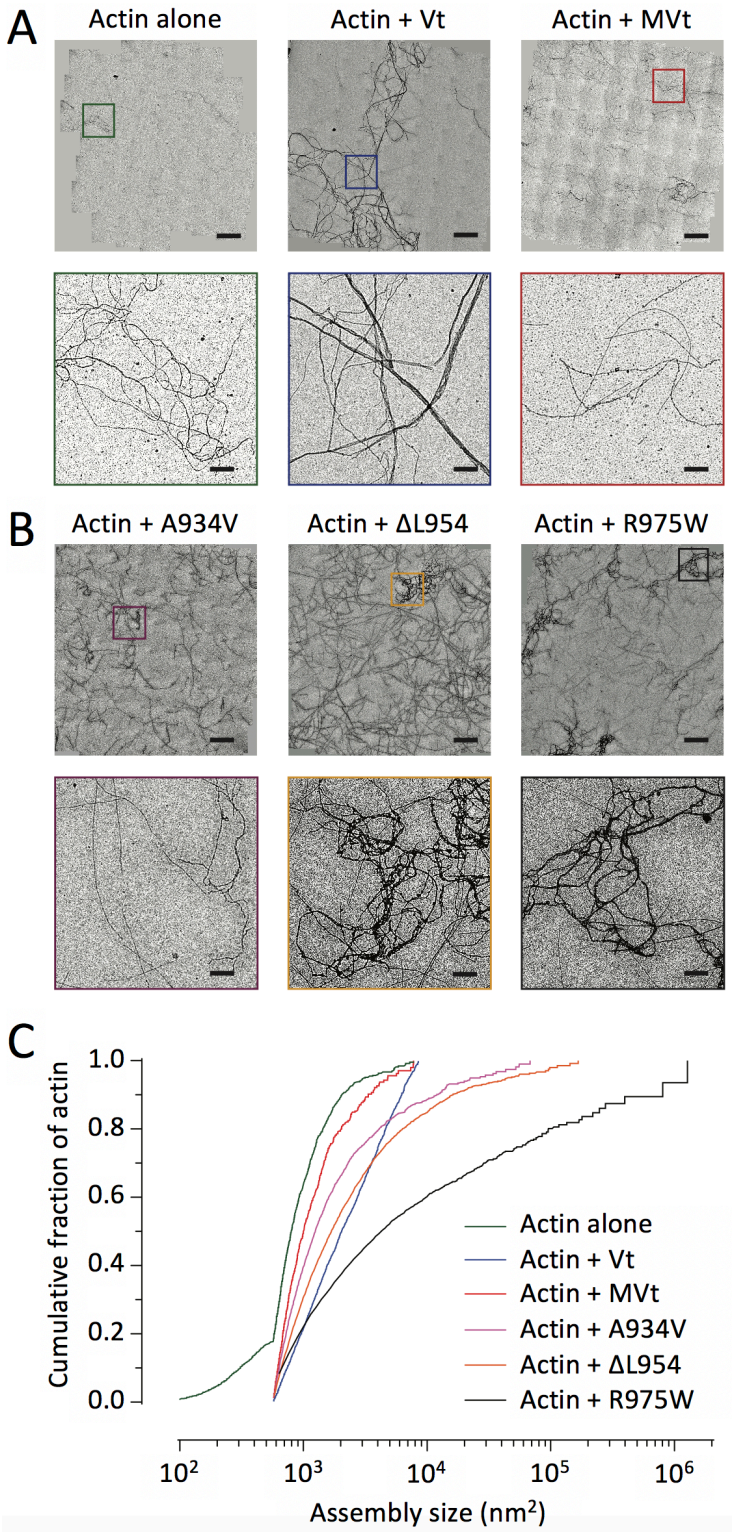
A
Actin alone
Actin + Vt
Actin + MVt
B
Actin + A934V
Actin + ΔL954
Actin + R975W
C
Cumulative fraction of actin
1.0
0.8
0.6
0.4
0.2
0.0
Actin alone
Actin + Vt
Actin + MVt
Actin + A934V
Actin + ΔL954
Actin + R975W
10²
10³
10⁴
10⁵
10⁶
Assembly size (nm²)

filaments (Figure 4-3 Panel B), unlike the linear bundles formed in the presence of Vt. The distributions of assembly sizes of the MVt cardiomyopathy-associated mutants are also distinct from Vt (Figure 4-3 Panel C), suggesting they may form higher order actin-based structures by different mechanisms.

To study how metavinculin and its cardiomyopathy-associated mutants can fine-tune vinculin-actin structures, the negative stain EM assay was employed to visualize the high-order actin structures formed in the presence of both Vt and MVt, modelling the normal physiological scenario where vinculin and metavinculin are co-expressed in smooth muscle. Consistent with previous reports, the presence of wild-type MVt inhibits the bundling activity of Vt at both a physiologically relevant substoichiometric 1:3 ratio (Figure 4-4), and a stoichiometric 1:1 ratio (Figure 4-4). Importantly, all MVt mutants dramatically stimulate, rather than inhibit, Vt mediated actin high-order assemblies at both ratios (Figure 4-4). On the one hand, the morphology of these assemblies is consistent with Vt-mediated actin bundling, as linear bundles are clearly visible. However, on the other hand, these bundles are frequently coated with unusually large, amorphous aggregates, which are rarely observed *in vitro* in the presence of Vt alone, MVt alone, or Vt + wild-type MVt (Figure 4-3; Figure 4-4) or *in vivo* in any cellular actin structures, suggesting that the structures observed here might be non-physiological and pathogenic. These observations indicate while metavinculin possesses the capacity to fine-tune vinculin-induced actin bundling at both stoichiometric and substoichiometric levels, its cardiomyopathy-associated mutants lose this capacity, and can form potentially pathogenic high-order actin assemblies. Our study revealed a potential

Figure 4-4. MVt cardiomyopathy mutants stimulate, rather than inhibit, F-actin bundling activity of Vt.

(A) Stitched negative-stain EM images of F-actin in the presence of Vt + wild type or cardiomyopathy mutant MVt at Vt to MVt ratio of 3:1 (bars = 10μm). Zommed views of the boxed regions are shown in the bottom panel (bars = 1μm). F-actin 0.5μM, Vt 3.75μM and MVt 1.25 μM. (B) Stiched negative-stain EM images of F-actin in the presence of Vt + wild type or cardiomyopathy mutant MVt at Vt to MVt ratio of 1:1 (bars = 10μm). Zommed views of the boxed regions are shown in the bottom panel (bars = 1μm). F-actin 0.5μM, Vt 2.5μM and MVt 2.5μM. (C) Cumulative plots of F-actin assemblies in the presence of Vt to MVt at ratio of 3:1. (D) Cumulative plots of F-actin assemblies in the presence of Vt to MVt at ratio of 1:1. Pair-wise comparisons show all distributions to be significantly different (KS test, $p < 0.0001$) in panels C and D. $N > 10$ fields and $n > 655$ regions were quantified for each condition in panel C and $N > 10$ fields and $n > 2241$ regions were quantified for each condition in panel D. Vt alone data are replotted from Figure 4-3.

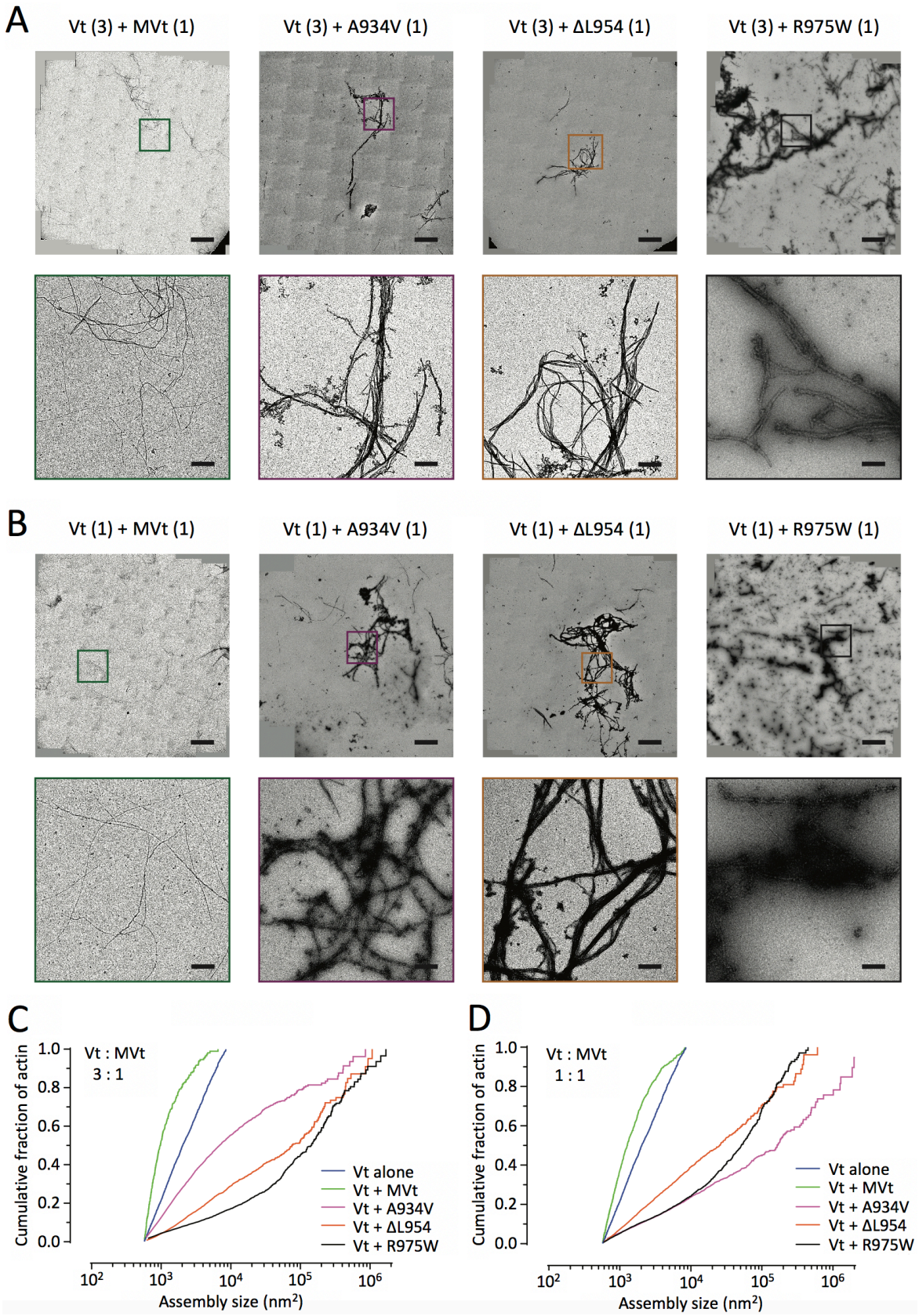
A
Vt (3) + MVt (1)
Vt (3) + A934V (1)
Vt (3) + ΔL954 (1)
Vt (3) + R975W (1)
B
Vt (1) + MVt (1)
Vt (1) + A934V (1)
Vt (1) + ΔL954 (1)
Vt (1) + R975W (1)
C
Vt : MVt
3 : 1
Cumulative fraction of actin
1.0
0.8
0.6
0.4
0.2
0.0
10^2
10^3
10^4
10^5
10^6
Assembly size (nm^2)
Vt alone
Vt + MVt
Vt + A934V
Vt + ΔL954
Vt + R975W
D
Vt : MVt
1 : 1
Cumulative fraction of actin
Assembly size (nm^2)
Vt alone
Vt + MVt
Vt + A934V
Vt + ΔL954
Vt + R975W

molecular mechanism for the pathogenesis of human hypertrophic and dilated cardiomyopathies.

In summary, consistent with previous findings, MVt is unable to induce actin bundling by itself, and the presence of sub-stoichiometric amounts MVt relative to Vt inhibits the assembly of actin filaments into parallel bundles. In contrast to wild type MVt, MVt cardiomyopathy (CM)-associated mutants induce the formation of disordered higher-order F-actin assemblies rather than the parallel actin bundles formed in the presence of Vt. Consistent with previous reports on the severity of these CM-associated metavinculin mutations, we found that different mutants have distinct abilities in inducing the formation of high-order actin assemblies on its own, or in enhancing the formation of higher order actin assemblies by Vt, with A934V as the mildest mutation and R975W as the most severe one.

4.2 Structural characterization of actin bundles induced by vinculin and α-catenin

Although both vinculin and α-catenin bundle actin filaments *in vitro* and *in vivo*, and vinculin and α-catenin have high sequence and structural homology, the proposed actin bundling mechanisms by full-length vinculin and α-catenin are distinct (Rangarajan et al., 2013; Kim et al., 2016). Full-length α-catenin dimerizes through its head domain (Pokutta and Weis, 2000) and this dimerization site overlaps with its β-catenin binding site (Pokutta and Weis, 2000). Full-length α-catenin also maintains actin-binding capacity in solution (Yamada et al., 2005) and its C-terminal ABD is therefore not entirely sterically inhibited by its head domain. It is widely believed that due these

dimerization and actin binding properties, the soluble population of α-catenin cross links actin filaments. At 100 kDa, full-length α-catenin is a large actin crosslinker (Pollard, 2016), suggesting that actin bundles induced by α-catenin could have large interfilament spacing and a highly flexible structure. On the contrary, full-length vinculin is a strictly auto-inhibited protein: full-length vinculin cannot bind F-actin in solution before its activation disrupts the strong interaction between the vinculin head and the actin-binding vinculin tail, nor can it dimerize in solution when not binding to F-actin (Ziegler et al., 2006). Since neither the vinculin head domain, unlike the head domain of α-catenin, nor the vinculin tail domain can dimerize on its own in solution, it has been proposed that the reason why vinculin can bundle F-actin is solely because of its actin-binding tail domain (Kim et al., 2016). It has been shown that actin binding triggers a major conformational change of vinculin tail, in which helix H1 becomes disordered, and the C-terminal extension undergoes a 60° swing to engage a novel site on F-actin (see Chapter 3.1). Therefore, the only plausible explanation for vinculin-induced actin bundling is its actin binding-associated conformational change exposing a cryptic dimerization site within vinculin tail (Huehn and Sindelar, 2016). At 21kD, the size of vinculin tail is in line with most ABPs. A compact actin crosslinker inevitably restricts the movement between different actin filaments in a bundle. To confirm these hypotheses, medium-to-high resolution Cryo-EM structures of vinculin- and α-catenin-induced actin bundles will be necessary, which is still technically prohibitive. Currently, there is no method to solve structures of actin bundles directly under near-native conditions.

As discussed above, unlike vinculin, α-catenin homodimers formed in solution (Rangarajan et al., 2013) which are widely thought to be the structural unit for its actin bundling. Although the structure of the α-catenin dimer has been solved by X-ray crystallography (Rangarajan et al., 2013), a structure of full-length, dimeric α-catenin–F-actin complex has never been obtained. In our previous efforts to solve the high-resolution structure of F-actin decorated by α-catenin ABD (see Chapter 3.1), robust bundling has also been observed (Figure 4-5 Panel A), indicating α-catenin ABD might be able to bundle actin as well, likely by a mechanism similar to that of vinculin tail considering its compact size and lack of dimerization potential in solution. It is also possible that in human cells, the two actin-bundling mechanisms co-exist. Therefore, structurally characterizing both the α-catenin ABD–F-actin bundles and the full-length α-catenin–F-actin bundles is crucial for elucidating the actin bundling mechanism by α-catenin.

In Chapter 3, we avoided analyzing actin bundles in order to solve high-resolution structures of single actin filaments decorated by metavinculin and α-catenin ABDs as we were focusing on actin-binding interface and actin-induced conformational change of vinculin and α-catenin. To study the actin filaments bundled by α-catenin ABD, micrographs from the same dataset were re-examined and the F-actin bundles, rather than single filaments, were highlighted (Figure 4-5 Panel A). Avoiding actin bundling was also the reason why we used metavinculin, which does not bundle F-actin, for the vinculin–actin structural characterization. Therefore, to study the structures of vinculin-induced actin bundles by cryo-EM, a new dataset of vinculin ABD (vinculin tail)-

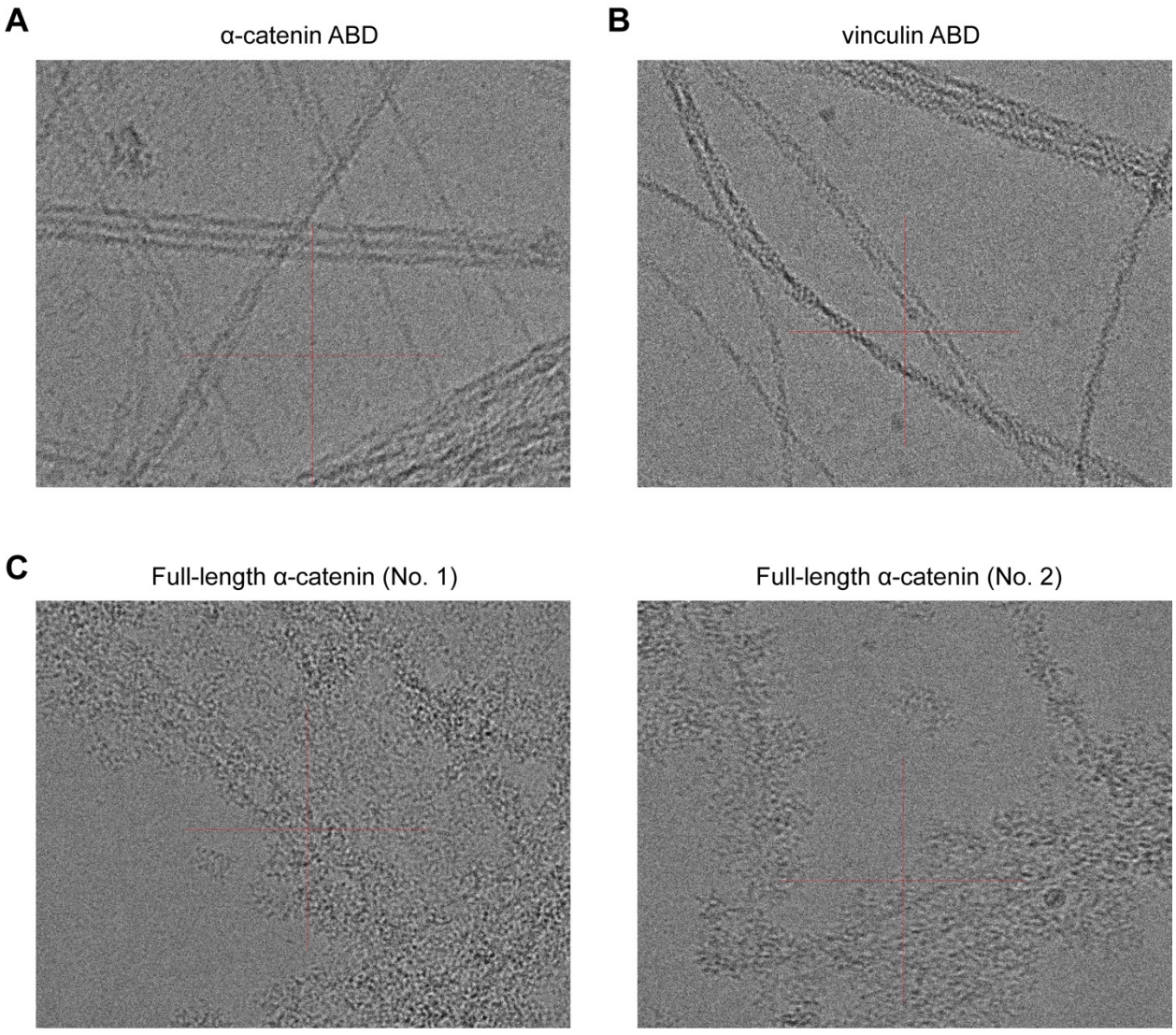

Figure 4-5. Actin bundles induced by α-catenin and vinculin.

(A) A representative cryo-EM micrograph of F-actin bundles decorated with α-catenin ABD (664-906). (B) A representative cryo-EM micrograph of F-actin bundles decorated with vinculin ABD (vinculin tail, Vt) (879-1066). (C) Two representative cryo-EM micrographs of F-actin bundles decorated with full-length human αE-catenin.

decorated F-actin was collected (Figure 4-5 Panel B). In contrast to the metavinculin ABD (Figure 3-1), the vinculin ABD clearly bundles F-actin. To study the actin filaments bundled by full-length α-catenin, full-length human αE-catenin was expressed in *E. coli*, subsequently purified, and subjected to Cryo-EM structural characterization in complex with F-actin (Figure 4-5 Panels C, D). Unlike uniformly decorated, relatively thin actin bundles induced by vinculin tail or α-catenin ABD, consistently with theoretical hypothesis, actin filaments bundled by full-length α-catenin have significantly larger protein mass between individual actin filaments and are more irregularly decorated, comparable to actin filaments bundled by myosin motor proteins (Gurel et al., 2017) (Figure 4-5 Panels C, D). In the cryo-EM images, a significant part of actin filaments is completely covered by a layer of protein, presumably dimeric α-catenin (Figure 4-5 Panels C, D). We conclude, for vinculin/α-catenin ABD-induced actin bundles, novel single-particle cryo-EM algorithms in addition to existing IHRSR methods for single-filament analysis will be required to solve medium-to-high resolution structures of actin bundles; for full-length α-catenin-induced actin bundles, single-particle and helical reconstruction methods are less likely to be effective. Alternative methods for 3D reconstruction, such as cryo-electron tomography, are likely necessary to dissect the structural details of full-length α-catenin-induced actin bundles.

4.3 Structural characterization of talin ABS3-decorated actin filaments

Besides vinculin, another major adaptor protein in the cell-matrix focal adhesion is the protein talin, a 270kD modular protein that directly connects membrane-

associated integrin receptors and actin filaments, acting as a cellular mechanosensitive signaling hub (Goult et al., 2018) that physically spans a linear path of force transmission, enabling it to integrate extracellular and intracellular inputs. Talin contains a globular N-terminal integrin-binding FERM domain, and a long rod on the C-terminal side that contains 13 consecutive rod domains (R1 to R13), connected by a flexible linker (Goult et al., 2018). The talin rod domains are a series of amphipathic α-helical bundles. Although 9 out of 13 rod domains have a vinculin-binding site (VBS) and vinculin can be sequentially recruited to talin rods when different scales of mechanical forces are applied on talin and expose the cryptic VBS in different rod domains (del Rio et al., 2009), talin is also an actin-binding protein in its own right, containing three actin-binding sites (ABS1, 2, and 3). Despite the various ways for talin to engage actin (directly through its ABS or indirectly by recruiting vinculin), it has been shown that the talin ABS3–actin interaction is singularly essential for focal adhesion formation and function (Goult et al., 2018). ABS3 is the C-terminal ABS of talin, immediately N-terminal to its final dimerization helix (Gingras et al., 2008). It has furthermore recently been reported that talin ABS3 can form a directional catch bond with F-actin (Owen et al., 2020). However, the structure of talin ABS3–F-actin complex remains unknown. Therefore, the molecular basis for the catch bond formation between talin ABS3 and F-actin remains a mystery.

In a collaboration with the laboratory of Prof. Alexander Dunn at Stanford University, we have begun examining the structural basis for actin binding by talin ABS3. Besides its functional importance for force transmission and catch bond

formation, the actin binding mechanism of talin ABS3 (residues 2300-2482, talin 1 rod domain 13) is anticipated to be structurally unique because of its close proximity to the C-terminal dimerization helix (residues 2494-2541). This suggests that when one ABS3 in a talin dimer binds actin, it is highly likely for the other ABS3 to bind the same actin filament, a highly unusual ABD actin-binding mode supported by low-resolution negative stain EM (Gingras et al., 2008) in which a talin dimer spans across three actin protomers in the same actin filament. Because of the low actin-binding affinity for talin ABS3, this dimerization helix is crucial for its actin binding (Gingras et al., 2008; Goult et al., 2018). The low affinity, and the symmetry incompatibility with F-actin caused by forced dimerization by the C-terminal helix, makes cryo-EM structural characterization of talin ABS3–F-actin complex particularly challenging.

In our experiments, utilizing purified GFP- and Halo-tagged talin 1 rod domain 13 plus the dimerization helix (from the Dunn Lab), we attempted to study its actin binding at two different pH (6.5 and 7.0) by Cryo-EM. The talin construct shows weak to non-existent actin binding at both pH (Figure 4-6 Panel A and B). 2D classification with or without helical symmetry confirmed weak binding, as the 2D class averages resemble undecorated actin segments (Figure 4-6 Panel C). This result served as another good example demonstrating the current technical limit for the cryo-EM methods to study actin binding interactions: actin helical symmetry can complicate the structural analysis of some actin-binding proteins. It is technically challenging to obtain a high-resolution reconstruction of an actin-binding protein that does not share the helical symmetry of F-actin, as demonstrated previously for tropomyosin (von der Ecken et al., 2015).

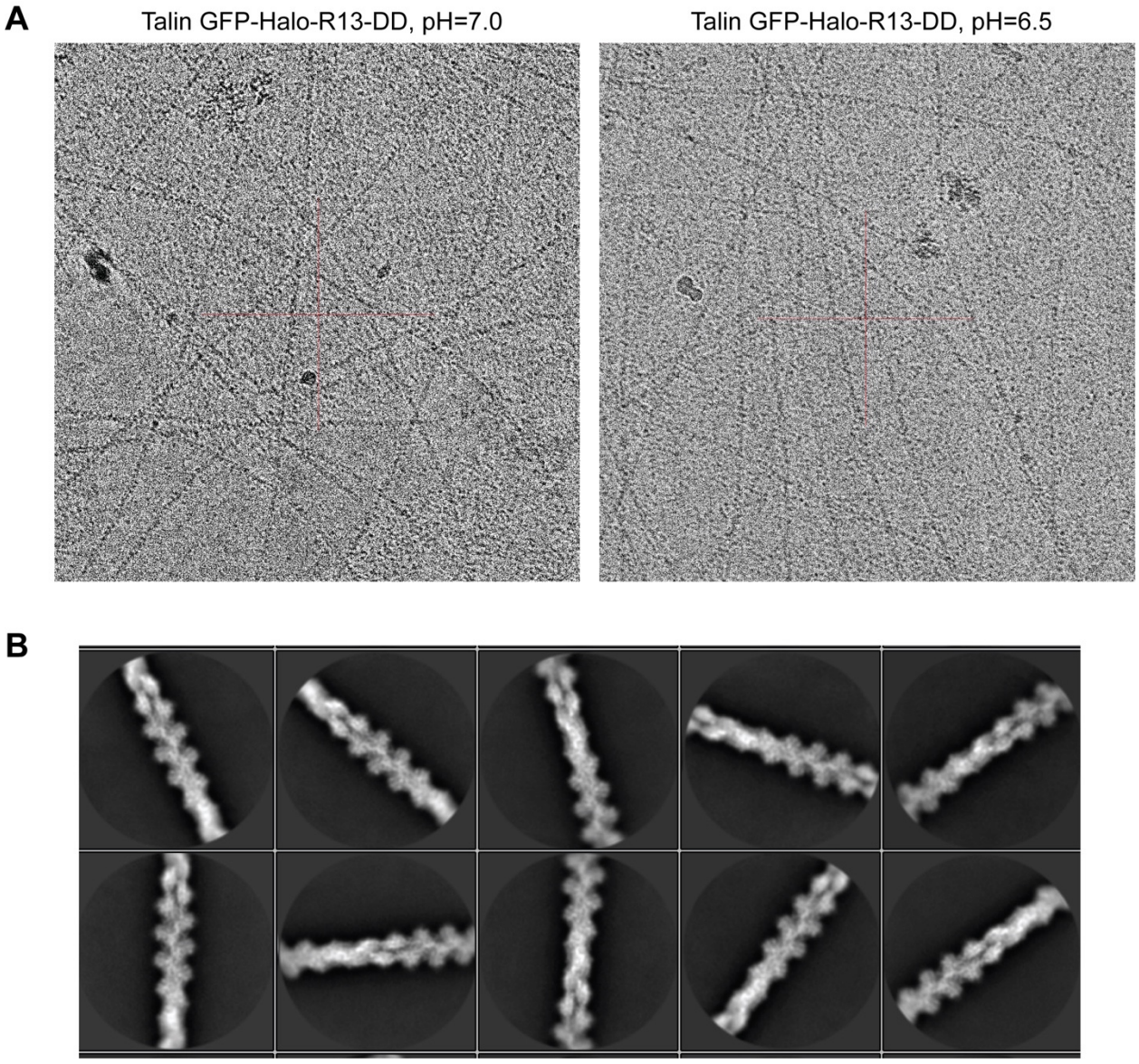

Figure 4-6. Structural studies on talin ABS3–F-actin complex.

(A) Representative cryo-EM micrographs of F-actin decorated with GFP- and Halo-tagged talin ABS3 (rod domain 13, R13) plus dimerization domain (DD) under two different pH values. (B) Representative 2D class averages showed minimal decoration on actin filaments.

4.4 Discussion: complex interactions between F-actin and adhesion proteins

The experiments in this Chapter investigate the complex actin-binding and actin-bundling interactions by three essential adhesion ABPs, α-catenin, (meta)vinculin, and talin. Among them, α-catenin and vinculin can bind and bundle actin filaments, with potentially distinct mechanisms *in vivo*, while the truncated α-catenin and vinculin ABDs likely share similar actin-bundling mechanisms with full-length vinculin both *in vitro* and *in vivo*. Talin has multiple actin-binding sites, and this Chapter focuses on its essential ABS3, which binds actin through an obligate dimer induced by talin's C-terminal dimerization domain (DD). Current structural techniques, especially the IHRSR-based helical reconstruction cryo-EM, cannot meet the challenges in structurally characterizing these diverse modes of actin engagement. Novel cryo-EM methods need to be developed to solve high-resolution structures of actin bundles and symmetry-incompatible actin-binding proteins.

This complex interplay of actin engagement by adhesion proteins likely has profound biological implications. Talin and vinculin are the two most important proteins closely interacting with each other while underlying the 'molecular clutch' in focal adhesion (Kanchanawong et al., 2010) in the path of force transmission from integrin to F-actin. Similarly, α-catenin interacts with vinculin in adherens junction (Shapiro and Weis, 2009) to reinforce the F-actin–adherens junction engagement. Our observations suggest that these ABPs engage actin network in distinct ways, and our studies pave the way for an *in vitro* reconstituted platform for structurally dissecting mechanisms for cellular force transmission and actin network formation. Our preliminary cryo-EM work

reported in this Chapter provided an important starting point for future high-resolution structural work on high-order actin assemblies frequently observed in cells. Our work also demonstrated possible molecular mechanisms by which mutations in adhesion proteins can contribute to human diseases, laying the foundation for future mechanistic studies on the pathogenesis of a variety of human diseases involved in the actin cytoskeleton and cellular mechanotransduction.

CHAPTER 5

Structural mechanisms for actin bundling by T-plastin

Note to readers: Part of the results discussed below arose from a collaborative effort between myself, my advisor Dr. Gregory M. Alushin, several colleagues in the Alushin Laboratory, including Mr. Matthew J. Reynolds and Dr. Rui Gong, at the Rockefeller University, and colleagues in the Tobias Meyer laboratory, including Dr. Tobias Meyer and Dr. Damien Garbett, at Stanford University.

5.1 Plastins/Fimbrins are unique Calponin Homology (CH)-domain actin-bundling proteins.

To crosslink actin filaments, actin-bundling proteins need more than one actin-binding domain. In most cases this is accomplished by dimerization: some actin-bundling proteins are themselves obligate homodimers, like α-actinin (de Almeida Ribeiro et al., 2014), or obligate heterodimers, like spectrin (Liem, 2016). Other actin-bundling proteins can form homodimers before actin-binding, like α-catenin (see Chapter 2, 3, 4), or, like vinculin (see Chapter 2, 3, 4), after they first engage F-actin. It is also possible that two distinct actin-binding proteins, when interacting with each other, can bundle actin (Yang et al., 2021). One major exception known for this dimerization requirement is the family of plastin/fimbrin proteins. Plastins are obligate monomeric actin-bundling proteins that have two actin-binding domains (ABDs) in a single polypeptide chain (Figure 5-1 Panel A). Because of the presence of an N-terminal

Figure 5-1. Cryo-EM structures of a human T-plastin–F-actin complex.

(A) Schematics for the domain structure of human T-plastin.

(B) Homology model of the actin-binding ‘core’ of human T-plastin.

(C) Representative Cryo-EM micrographs of F-actin decorated with full-length human T-plastin in the absence (left) or the presence of (right) calcium. Scale bars, 100 nm.

(D) Segmented regions of reconstructed density map of F-actin decorated with full-length human T-plastin, colored as indicated.

(E) The T-plastin–F-actin complex atomic model, colored as in (D). Actin subunits are displayed in varying shades of blue. The inter ABD CH2-3 linker, highlighted with lime color is displayed as a cartoon (box). CH3: olive; CH4: dark green.

(F) The actin-binding interface of T-plastin ABD2 is constituted of helices H1, H3, and H4 within CH3.

(G) Superimposed T-plastin ‘pre-bound’ homology model and ‘post-bound’ cryo-EM model. The conformational change of the CH2-3 linker is highlighted (box). Rotation angles indicate repositioning of the CH2-3 linker and CH4.

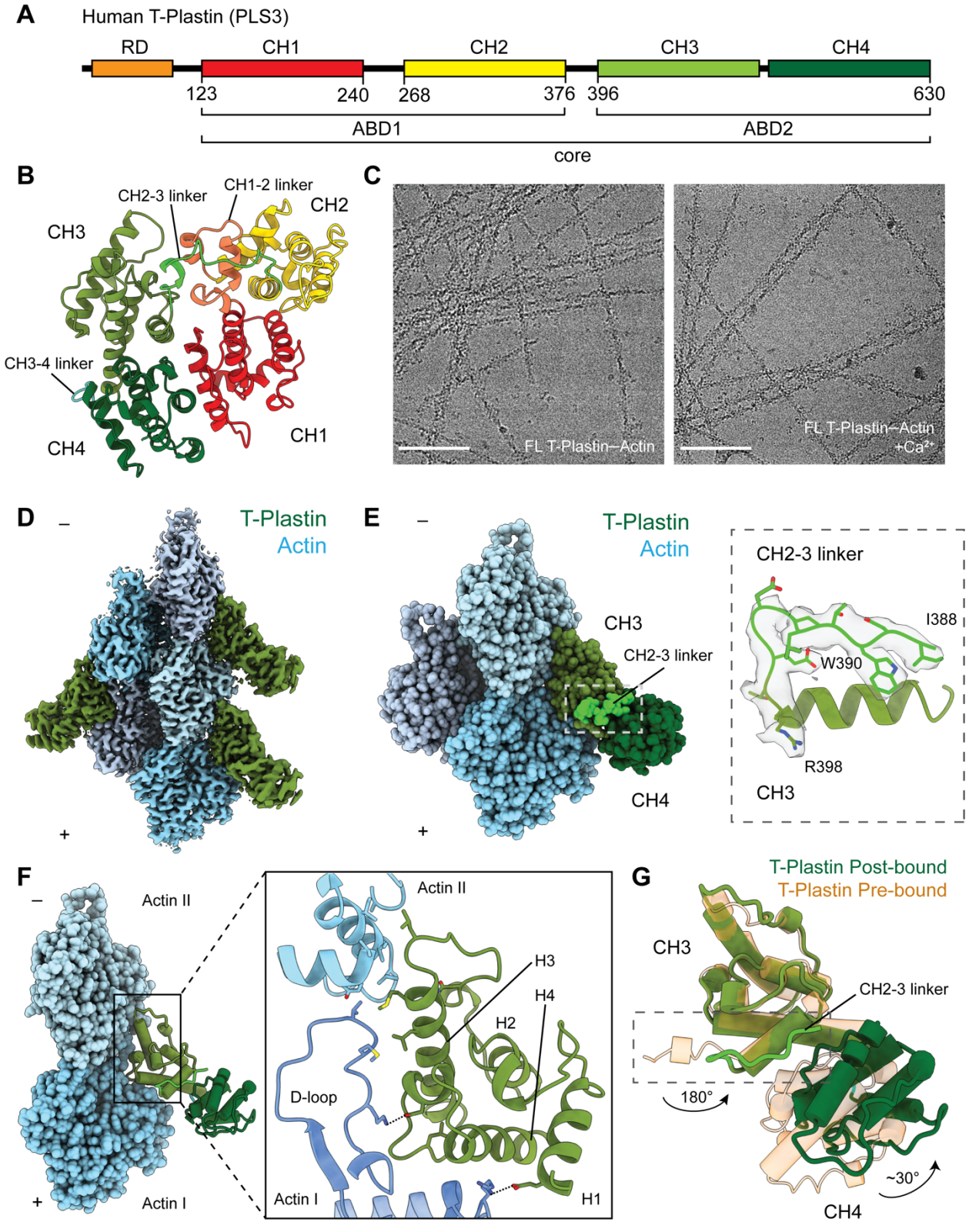
A
Human T-Plastin (PLS3)
RD
CH1
CH2
CH3
CH4
123
240
268
376
396
630
ABD1
ABD2
core
B
CH2-3 linker
CH1-2 linker
CH2
CH3
CH3-4 linker
CH4
CH1
C
FL T-Plastin–Actin
FL T-Plastin–Actin +Ca²⁺
D
–
T-Plastin
Actin
+
E
–
T-Plastin
Actin
CH3
CH2-3 linker
CH4
+
CH2-3 linker
I388
W390
R398
CH3
F
–
Actin II
+
Actin I
Actin II
H3
H4
H2
D-loop
Actin I
H1
G
T-Plastin Post-bound
T-Plastin Pre-bound
CH3
CH2-3 linker
180°
~30°
CH4

regulatory domain (RD) that contains two calcium-binding EF-hand motifs (Ishida et al., 2017), the two ABDs in plastin are not symmetrical. Discovered independently as fimbrin/I-plastin (PLS1), a major protein in microvilli (Bretscher and Weber, 1980), and L-plastin (LCP1/PLS2), an actin-associated biomarker overexpressed in cancer cells (Goldstein et al., 1985), plastins are the evolutionary most ancient known family of actin-bundling proteins and are highly conserved throughout eukaryotic evolution (Adams et al., 1991; Lin et al., 1993). Among the three tissue-specific human plastin isoforms, it is T-plastin (PLS3) that is ubiquitously expressed in solid tissues and is the most abundant isoform (Shinomiya, 2012). T-plastin has recently been identified as a key actin stabilizer that strengthens and promotes cell protrusions: it is in fact the only major known actin crosslinker localized to lamellipodia and filopodia in endothelial cells (Garbett et al., 2020). Actin-bundling is the only established cellular activity for T-plastin, and Ca^{2+} can suppress its bundling activity by an unknown mechanism (Schwebach et al., 2017). As a result, T-plastin is involved in many cellular processes involved in calcium sensing, including cell migration, endocytosis, and membrane trafficking, and mutations in T-plastin has recently been reported as a cause of congenital osteoporosis (Schwebach et al., 2017; Schwebach et al., 2020). Although the calcium-regulated actin bundling by T-plastin has been studied *in vitro* (Schwebach et al., 2017; Schwebach et al., 2020), to date we do not know the structural mechanism by which full-length T-plastin can engage actin filaments with its two asymmetrical ABDs. It is yet to be discovered whether T-plastin's unique structure leads to a unique way of actin bundling, and if so, how its unique way of actin bundling can contribute to its function and implied

dysfunction in pathogenesis. To address these questions, direct structural characterization of the full-length T-plastin–F-actin complex is needed.

As discussed above, human T-plastin (PLS3) is a 70.8kD monomeric protein that consists of an N-terminal Ca^{2+}-sensing regulatory domain (RD) and an actin-binding 'core' (Figure 5-1 Panel A). The core consists of two calponin homology (CH) domain actin-binding domains, ABD1 and ABD2. CH domain ABD is one of the largest actin-binding domain families, including the ABDs in dystrophin/utrophin, α-actinin, spectrin, and filamin, in which two adjacent CH domains constitute an ABD (Liem, 2016; Gimona et al., 2002). CH-domain actin-binding proteins share a highly conserved structural fold for actin binding, while maintaining a high degree of sequence variability and functional diversity (Gimona et al., 2002; Moores and Kendrick-Jones 2000). It is worth noting not every CH domain protein can bind or is associated with the actin cytoskeleton (Gimona and Mital, 1998). A general rule is if a protein harbors two immediately adjacent CH domains, known as a tandem CH domain, it is likely these two CH domains constitute an actin-binding domain (Gimona et al., 2002).

We refer to the first tandem T-plastin CH domain (CH1 and CH2) as ABD1. Similarly, the second tandem CH domain, CH3 and CH4, constitutes ABD2. Although to our knowledge no crystal structures of human plastins have been solved, structures of the 'core' of the Arabidopsis (PDB 1pxy) and the fission yeast (PDB 1rt8) fimbrins have been reported (Klein et al., 2004). Despite evolutionary distance, human T-plastin has 41.4% and 43.6% protein sequence identity, respectively, to these two fimbrins. This allowed us to construct a reliable homology model of the actin-binding 'core' of T-plastin

(Figure 5-1 Panel B), which we refer to as the 'pre-bound' structure of T-plastin (i.e. yet to bind F-actin). Similar to the domain organization reported in the crystal structures, the pre-bound T-plastin core adopts a closed horseshoe conformation with the N-terminal CH1 in close contact with the C-terminal CH4 (Figure 5-1 Panel B). The two ABDs adopt a quasi-anti-parallel orientation, connected by a 20-residue linker (Figure 5-1, light green), the CH2-3 linker. Notably, two intra-ABD linkers, the CH1-2 linker in ABD1, and the CH3-4 linker in ABD2, are very different in length (28 residues and 7 residues, respectively).

5.2 High-resolution cryo-EM structure of the human T-plastin–F-actin complex

We then pursued structural studies of full-length human T-plastin bound to F-actin with cryo-EM. After careful optimization (see Chapter 7, Materials and Methods), we were able to acquire cryo-EM images both in the absence and in the presence of Ca^{2+} (Figure 5-1 Panel C; Figure 5-2). Cryo-EM images clearly showed that although actin filaments are bundled under both conditions, bundling is significantly suppressed by Ca^{2+} (Figure 5-1 Panel C). Because the conventional Iterative Helical Real Space Reconstruction (IHRSR) approach can only be applied to single filaments, we decided to characterize the initial binding of T-plastin to actin before it bundles actin filaments by analyzing single filaments in the $+Ca^{2+}$ dataset (Figure 5-1 Panel C, right) using a conventional helical reconstruction approach. We obtained a 3D reconstruction of the full-length T-plastin–F-actin complex (Figure 5-1 Panel D) at 2.6 Å overall resolution (Figure 5-2), a substantial improvement over the α-catenin / metavinculin structures

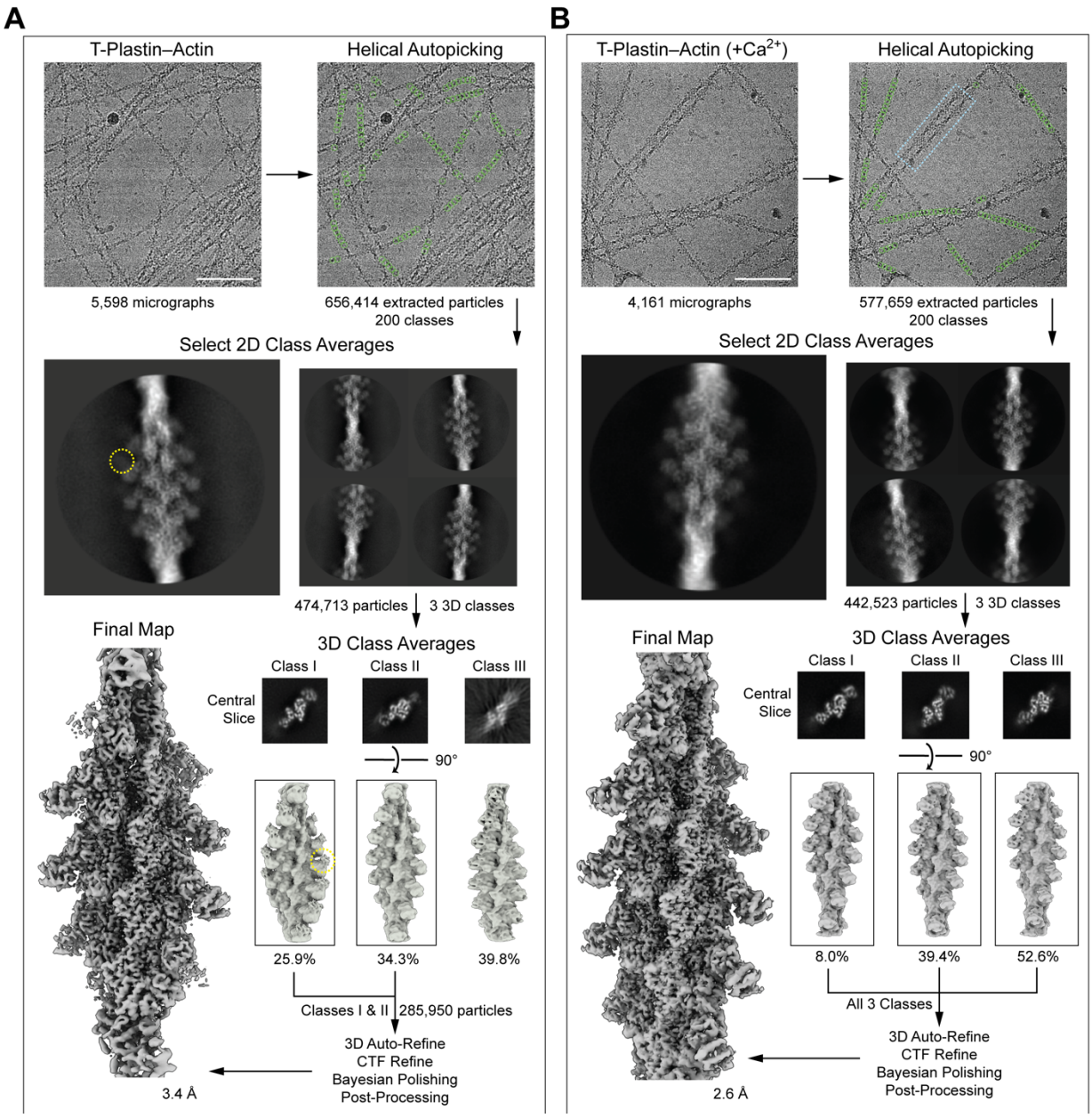

Figure 5-2. Cryo-EM data processing workflow for the T-plastin–F-actin complexes.

(A and B) Cryo-EM processing workflow for full-length T-plastin–F-actin complex datasets in the absence (A) and the presence (B) of calcium. Scale bars, 100 nm. Yellow circle: weak signal for a domain. Blue square: a representative actin bundle.

presented in Chapter 3. As local resolutions ranged from 2.4 Å to 3.9 Å, radially decaying outward from the helical axis (Figure 5-2), an atomic model for the complete sequence of Mg-ADP α-actin and continuous segments of T-plastin was built and refined directly into the map (Figure 5-1 Panel D). We only resolved two CH domains, i.e., one ABD, in the actin-bound full-length T-plastin cryo-EM density map (Figure 5-1 Panel D). The map resolution allowed us to unambiguously identify them as CH3 (olive) and CH4 (dark green), i.e., ABD2, plus a short segment in CH2-3 linker (lime) on the N-terminus of CH3 (Figure 5-1 Panel E). Human T-plastin residues 388-630 was built into the map with high confidence. The near-uniform ABD2 decoration in the dataset strongly indicates that when T-plastin engages F-actin, ABD2 is the first one to bind. The data also indicate that Ca^{2+} suppresses T-plastin-mediated actin bundling by inhibiting the subsequent actin binding of ABD1 after ABD2 has engaged, rather than downregulated initial F-actin binding, consistent with the previous biochemical studies suggesting calcium only inhibits T-plastin's actin bundling, but does not inhibit T-plastin's actin binding (Namba et al., 1992).

Like many other ABPs, T-plastin's CH3 domain of ABD2 engages a major site spanning the longitudinal interface of two adjacent actin protomers (Figure 5-1 Panels E and F), which we term Actin I and Actin II (numbered from the plus end of the filament), while CH4 does not engage actin directly. The architecture of a CH domain is dominated by four major α-helices (Gimona et al., 2002), here we named H1 to H4 (Figure 5-1 Panel F) from N-terminus to C-terminus. The four major helices are connected by loops and relatively short, irregular helices. We find helices H1, H3, and

H4 constitute the actin-binding site of T-plastin ABD2, mediated by an extensive hydrophobic interface among H3, Actin II, and Actin I D-loop, as well as salt bridges between H1/H4 and Actin I (Figure 5-1 Panel F). Comparison of the actin conformation observed in a similar-resolution structure of ADP F-actin in isolation ("bare actin", M.S. in preparation) versus when bound to T-plastin reveals minimal rearrangements throughout the majority of the actin structure (Figure 5-3). Compared to the 'pre-bound' structure, CH3 maintains the overall pre-bound conformation, featuring only slight conformational changes in the loop region. The four major constituting helices in CH3 maintain their respective positions. However, CH4 undergoes an approximately 30° swing around the CH3-4 linker to avoid steric clash with actin (Figure 5-1 Panel G). Notably, the short stretch of CH2-3 linker resolved in the cryo-EM map undergoes a major conformational rearrangement, a 180° degree flip pointing away from the actin filament (Figure 5-1 Panels E and G), upon binding actin, indicating after ABD2 first binds actin, the positions of its N-terminal RD and ABD1 may undergo a significant conformational change.

Intriguingly, both the CH3 and CH4 domains undergo minimal structural changes (Figure 5-3 Panel D) upon actin binding when analyzed individually, suggesting that despite the overall conformational change observed for CH4, it is the inter-domain movement through flexible linkers, rather than the intra-domain rearrangement of the major α-helices, that dominates the conformational changes of T-plastin upon actin binding. Despite tissue specific expression, the three human plastin isoforms share highly similar sequences (Figure 5-4) with at least 74% identity. Our actin-bound full-

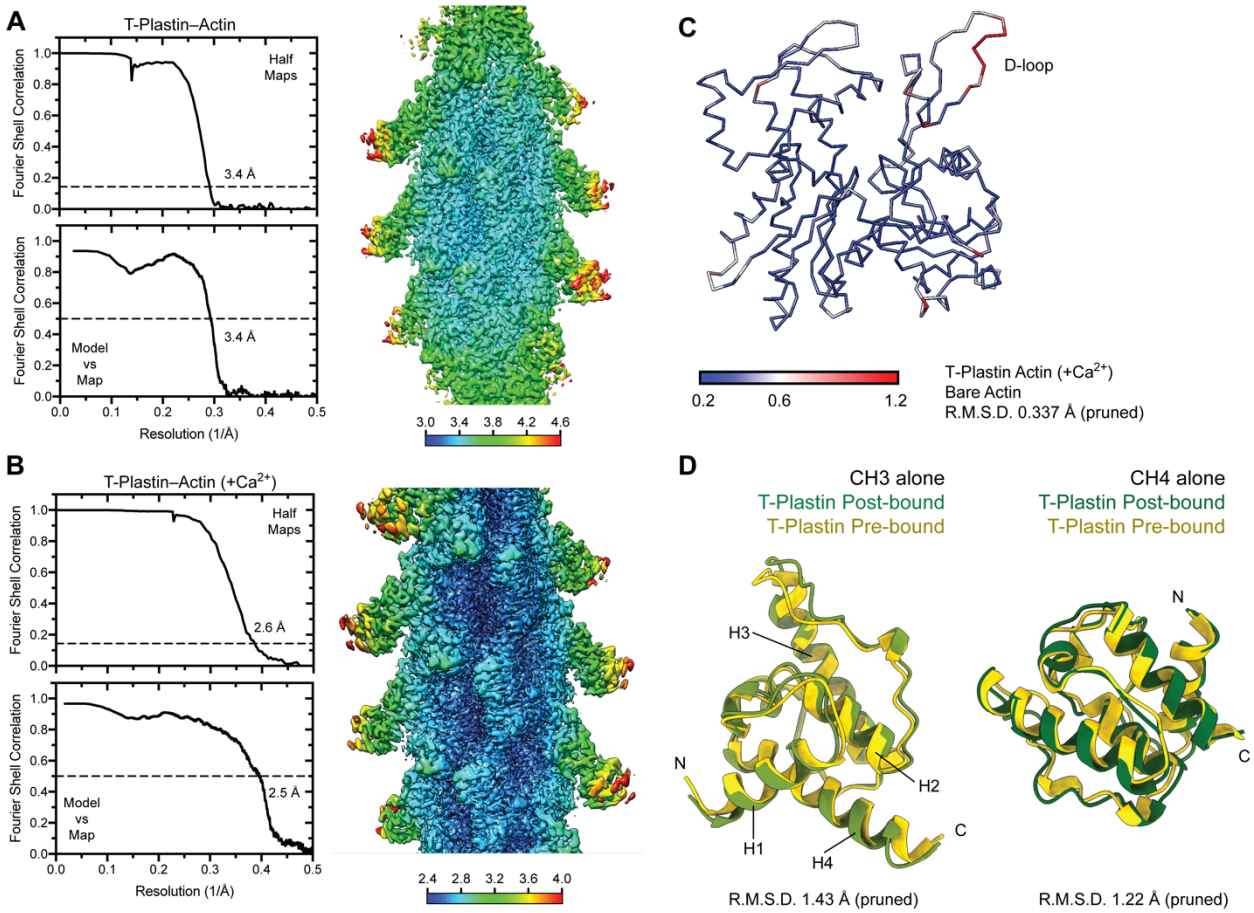

Figure 5-3. Resolution analysis and actin / CH domain comparisons.

(A and B) 3D reconstruction analyses (map FSC, map-to-model FSC, and local resolution) for full-length T-plastin–F-actin complex datasets in the absence (A) and the presence (B) of calcium.

(C) Actin C_α traces colored by per-residue RMSD from the indicated comparisons.

(D) Structural alignments of the pre-bound and the post-bound conformations for segmented individual CH3 and CH4.

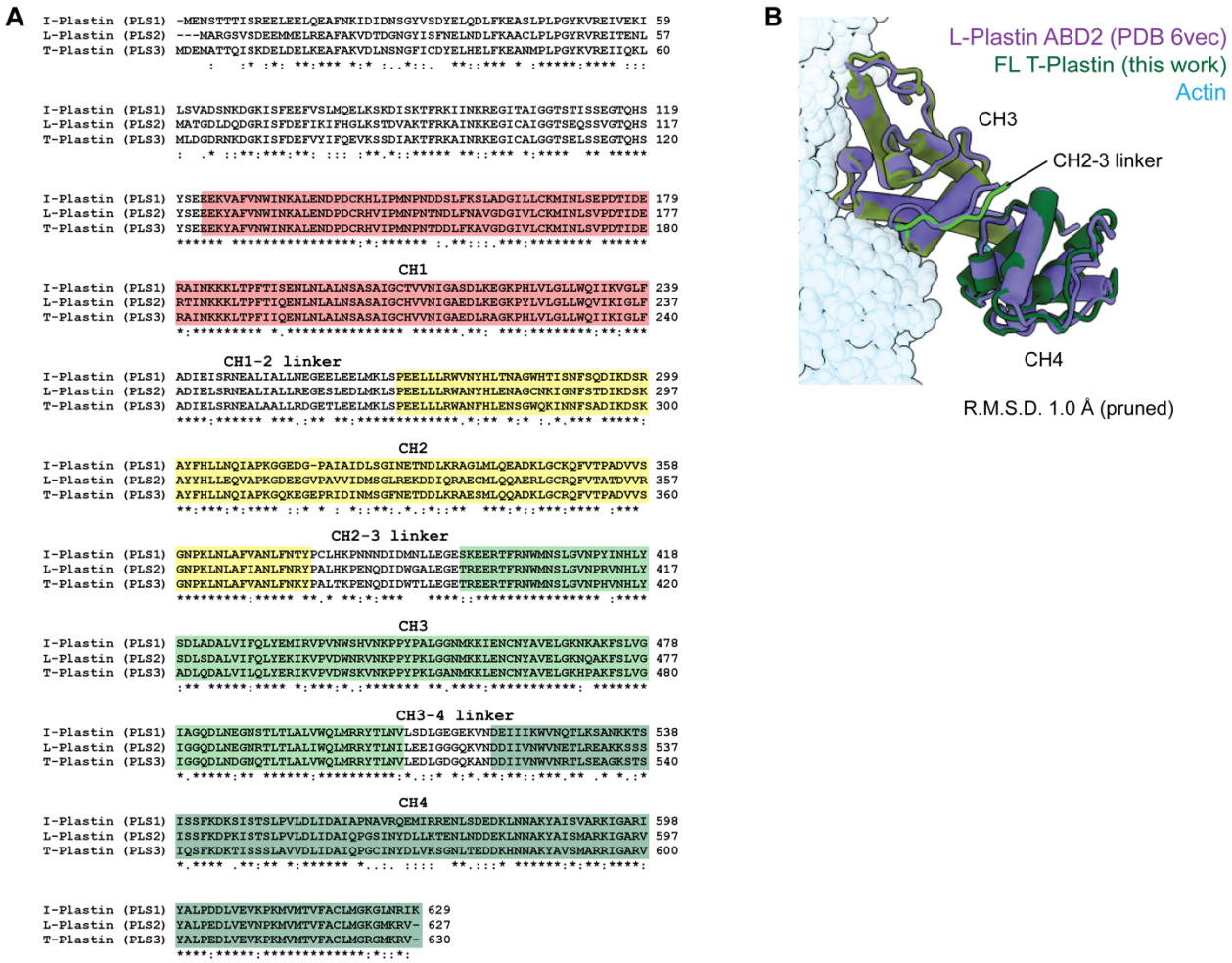

Figure 5-4. Multiple sequence alignments and structural comparison of human plastin isoforms.

(A) Sequence alignment (see Materials and Methods) of human I-plastin (PLS1), L-plastin (LCP1/PLS2), and T-plastin (PLS3). (B) Structural alignment (see Materials and Methods) of L-Plastin ABD2 (PDB 6vec) and full-length T-plastin (this work).

length T-plastin structure is highly similar to the actin-bound structure of truncated L-plastin ABD2 which as recently been reported (Figure 5-4) (Schwebach et al., 2020), consistent with a model in which T-plastin's two ABDs can operate independently once auto-inhibtion is released. As discussed in Chapter 5.1, CH domain ABPs, a highly diverse family in both protein sequence and biological function (Figure 5-5 Panel A), maintain a high-degree structural homology. So far, only plastin ABD's second CH domains could be resolved by Cryo-EM (Figure 5-4; Figure 5-5), while the second CH domains of the utrophin, spectrin, and filamin A ABDs were not observed in cryo-EM density maps when bound to F-actin, likely because plastin ABD2 has the shortest inter-CH domain linker (Figure 5-5), reducing the conformational flexibility of their actin-bound states (Galkin et al., 2010). Upon actin binding, most CH domain ABDs, except for plastin's ABD, form an additional minor actin-binding site with a short N-terminal stretch folding on F-actin (Figure 5-5). The uniqueness of the plastin ABD2 likely derives from its relative position in the protein sequence: unlike the ABDs of utrophin, spectrin or filamin, plastin's ABD2 is on the C-terminal side of the entire protein (Figure 5-1 Panel A). The preceding element N-terminal to the CH3, especially the CH2-3 linker which adopts a novel conformation upon actin binding, prevents T-plastin from forming this extended N-terminal actin-binding tail. For the ABDs of plastin (ABD2), utrophin, β-spectrin, and filamin A, it is always the first CH domain within the ABD that forms the actin-binding site (ABS), and the structures of these first CH domains are strikingly similar (Figure 5-5), directly demonstrating sequence variations do not perturb a

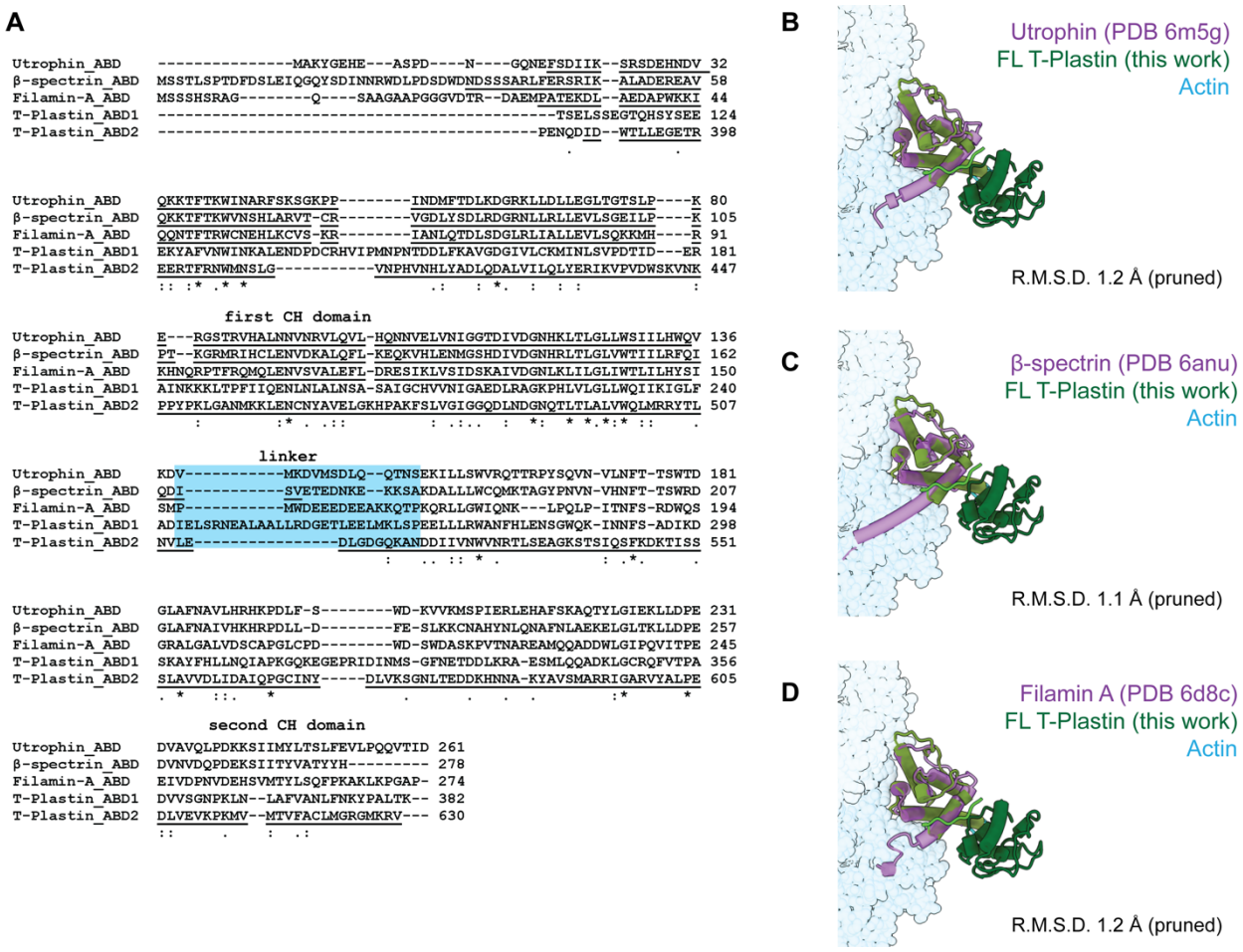

Figure 5-5. Multiple sequence alignments and structural comparison of CH domain actin-binding proteins.

(A) Sequence alignment (see Materials and Methods) of the ABDs of human utrophin, β-spectrin, filamin A, and T-plastin.

(B, C, and D) Structural alignments (see Materials and Methods) of utrophin ABD (PDB 6m5g) (B), β-spectrin ABD (PDB 6anu), or filamin A ABD (PDB 6d8c) with T-plastin ABD2 (this work).

common conserved mechanism for CH domain ABPs to construct their actin binding sites.

5.3 Single actin filaments decorated by T-plastin reveals a frustrated state for actin bundling

Inspired by the structural homology of CH domain ABPs in general, the pre-bound conformations of T-plastin's ABD1 and ABD2 were compared. Despite modest sequence identity (Figure 5-5), especially the length difference between CH1-2 linker and CH3-4 linker, pre-bound ABD1 and ABD2 share an almost identical structure (Figure 5-6 Panel A). With a structural homology at this level, it is almost certain that when binding to F-actin, both ABDs will share a highly similar ABS (Figure 5-6 Panel A), here annotated as ABS1 and ABS2 (Figure 5-6 Panel B).

However, the positioning of the pre-bound ABD1 is clearly incompatible with actin bundling because the ABS1 is buried within the core of pre-bound T-plastin (Figure 5-6 Panel B), preventing its access to F-actin. This incompatibility indicates a stepwise, sequential actin-bundling mechanism by which the initial actin binding by ABD2 triggers a conformational change of T-plastin which releases ABD1, and therefore exposes its ABS1 for the second actin-binding event, resulting in actin bundling. To study this mechanism, we reasoned that the full-length T-plastin–F-actin complex should be studied in the absence of calcium, without bundling suppression. We therefore turned to the $-Ca^{2+}$ dataset in which actin filaments are heavily bundled by T-plastin, using the similar method in which we studied the single actin filaments decorated by T-plastin in

Figure 5-6. Cryo-EM structure of human T-plastin–F-actin complex in the absence of calcium reveals a frustrated T-plastin conformational state.

(A) Superimposed pre-bound T-plastin ABD1 and ABD2 from the homology modeling. ABS, actin-binding site. Actin from the post-bound model is displayed.

(B) Actin-binding sites (ABS1 and ABS2) within the pre-bound T-plastin structure.

(C) Representative 2D class average after focused 3D classification. Signal from an extra domain is highlighted in the yellow circle.

(D) Segmented regions from the reconstructed density map of F-actin decorated with full-length human T-plastin after focused classification, colored as indicated.

(E) The T-plastin–F-actin complex pseudo-atomic model refined into the density map in (D), colored as in (D). Actin subunits are displayed in varying shades of blue. CH2: yellow; inter-ABD CH2-3 linker: lime; CH3: olive; CH4: dark green.

(F, G) Superimposed pre-bound and post-bound structures of T-plastin, from CH2 helix 2 to the C-terminus. Rotation angles indicate repositioning of CH2 and the CH2-3 linker.

(H) Predicted position of T-plastin CH1 based on CH2 helices 2, 3, 4.

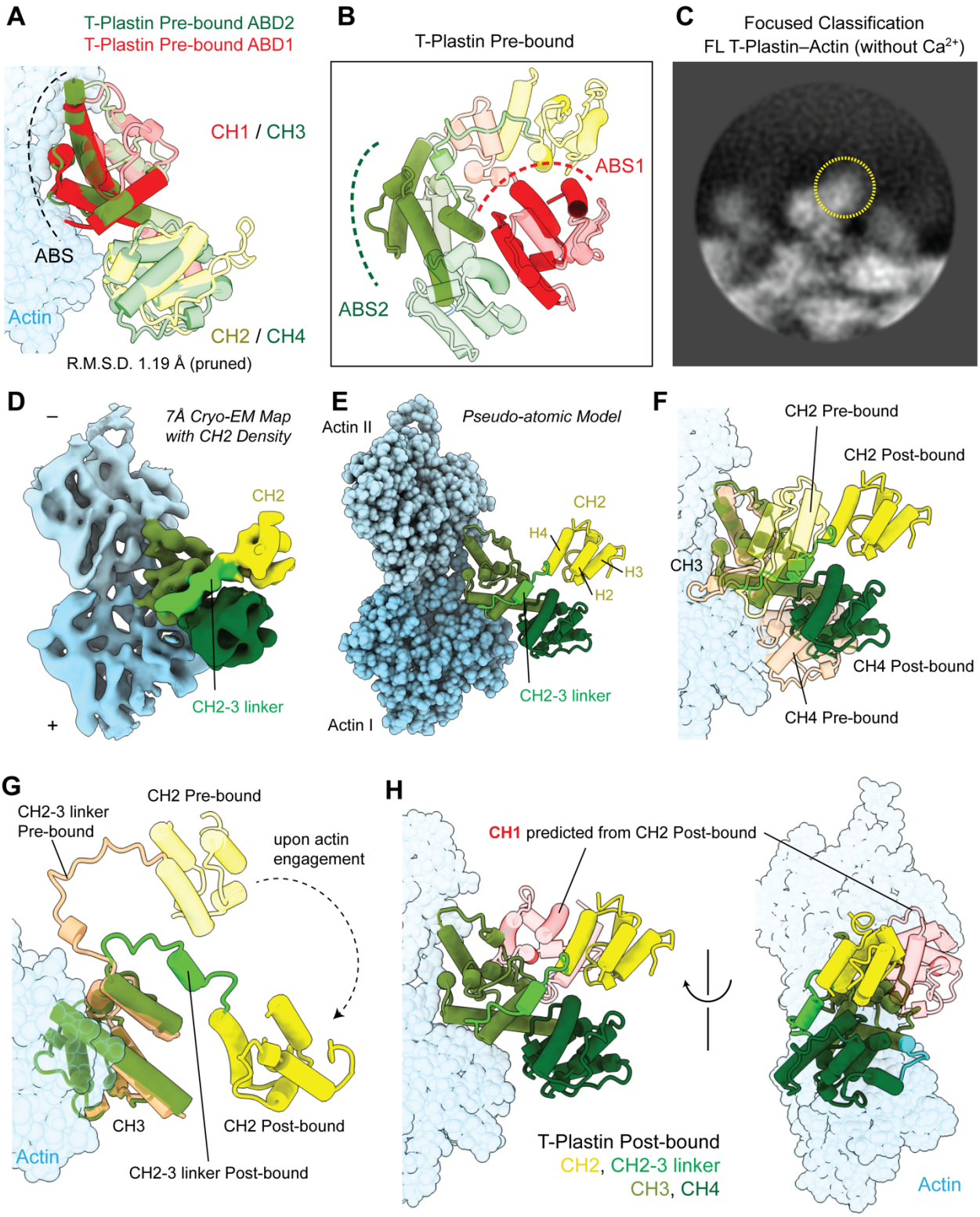
A
T-Plastin Pre-bound ABD2
T-Plastin Pre-bound ABD1
CH1 / CH3
ABS
Actin
CH2 / CH4
R.M.S.D. 1.19 Å (pruned)
B
T-Plastin Pre-bound
ABS1
ABS2
C
Focused Classification
FL T-Plastin–Actin (without Ca2+)
D
–
7Å Cryo-EM Map
with CH2 Density
CH2
CH2-3 linker
+
E
Actin II
Pseudo-atomic Model
CH2
H4
H3
H2
CH2-3 linker
Actin I
F
CH2 Pre-bound
CH2 Post-bound
CH3
CH4 Post-bound
CH4 Pre-bound
G
CH2-3 linker
Pre-bound
CH2 Pre-bound
upon actin
engagement
CH3
CH2 Post-bound
Actin
CH2-3 linker Post-bound
H
CH1 predicted from CH2 Post-bound
T-Plastin Post-bound
CH2, CH2-3 linker
CH3, CH4
Actin

the absence of calcium by the conventional IHRSR helical reconstruction approach. Since heavy actin bundling reduces the quality of single particles extracted from single actin filaments, unsurprisingly the cryo-EM 3D reconstruction generated a lower-resolution map at 3.4 Å overall resolution (Figure 5-2). The model derived from this map is almost identical to the previous model built from the $+Ca^{2+}$ dataset (Figure 5-3). However, unlike the $+Ca^{2+}$ dataset, in the 3D classification of $–Ca^{2+}$ dataset we noticed vague signals for a new domain (Figure 5-2, yellow circles). In a collaboration with my colleague Matthew Reynolds in the laboratory, the dataset was further processed by focused classification which strengthened signals for the new domain (Figure 5-6 Panel C) and generated a 7-Å Cryo-EM 3D reconstruction (Figure 5-6 Panel D; Figure 5-7 Panel A; local resolution: Figure 5-7 Panel B), allowing us to unambiguously confirm the density for the newly observed domain belongs to the entire CH2-3 linker and the final three helices, H2, H3, and H4, of T-plastin CH2 (Figure 5-6 Panels D, E), within ABD1. Aligning the pre-bound and post-bound states revealed a major conformational change of the CH2 and the CH2-3 linker upon actin engagement (Figure 5-6 Panels F, G), in which the CH2-3 linker swings approximately 120° (Figure 5-6 Panel G).

If we assume the actin-binding-induced conformational change for T-plastin happens at the inter-ABD linker, i.e., the CH2-3 linker, and the ABD itself does not undergo major conformational change given the high degree structural homology between ABD1 and ABD2, it is possible to predict the position of the entire T-plastin ABD1 by the three α-helices resolved. Intriguingly, the CH1 position predicted from the CH2 post-bound (Figure 5-6 Panel H) or from the entire CH2-4 post-bound (Figure 5-7

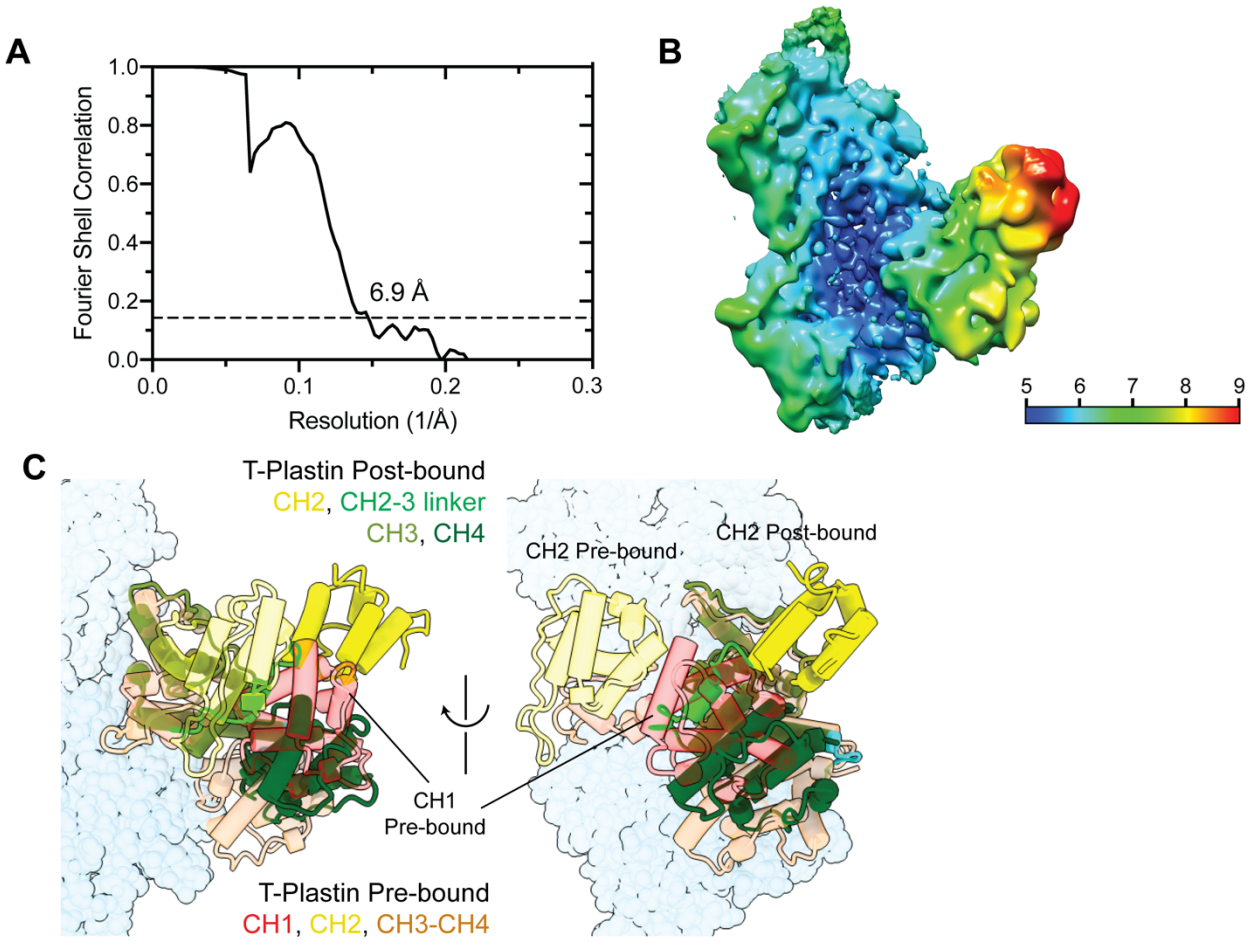

Figure 5-7. Focused refinement resolution assessment and analysis.

(A and B) FSC (A) and local resolution (B) analyses for the 3D cryo-EM reconstruction in (A).

(C) Positioning of CH1 and CH2 when aligning the pre-bound and the entire post-bound (the structure in Figure 5-6 Panel E) structures.

Panel C) conformation is still incompatible with actin bundling due to steric clash. This result strongly suggests the post-bound CH2 conformation revealed in this reconstruction is a frustrated, intermediate T-plastin conformational state binding to single filaments that is poised for subsequent actin bundling, rather than a fully opened, actin bundling state. The results shown here strongly suggest that T-plastin ABD1, like the ABD2, does undergo a further structural rearrangement when binding actin, after the ABD2–actin engagement releases its actin-binding site. Our 7-Å Cryo-EM structure captures an intermediate conformation between ABD2 actin binding and ABD1 actin binding, and provides a strong evidence for an asymmetrical, stepwise, sequential actin bundling mechanism by human T-plastin.

5.4 Co-sedimentation assays support a sequential actin-bundling mechanism

To validate whether human T-plastin bundles actin in a sequential mechanism, several point mutants for T-plastin have been designed guided by our high-resolution post-bound cryo-EM structure (Figure 5-1). We first focused on the CH2-3 linker, in which residue W390 is docked in a hydrophobic pocket on the interface between the CH2-3 linker and the CH3 H1 (Figure 5-1 Panel E; Figure 5-8 Panel A, Box (a)). We reasoned the interaction mediated by W390 facilitates the 180° swing of the CH2-3 linker (Figure 5-1 Panel G), and plays an important role in releasing ABD1 after ABD2 first binds F-actin. To test this hypothesis, we mutated W390 to alanine, and performed a two-step actin co-sedimentation assay (Kim et al., 2016) to dissect the effects of W390A on actin binding and actin bundling by T-plastin. In the assay (see Chapter 7 for

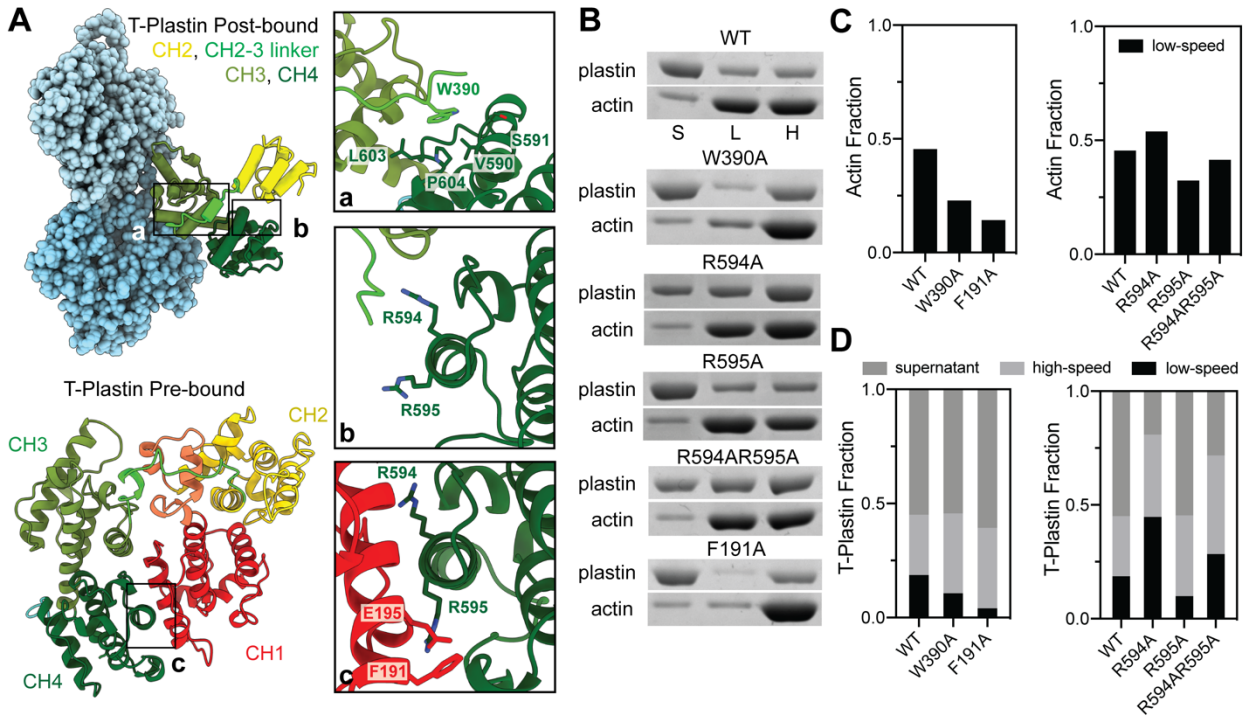

Figure 5-8. Mutational analysis supports a sequential bundling model.

(A) Key residues potentially regulating T-plastin-mediated actin bundling identified within the CH2-3 linker (a); the pre-bound CH1-4 binding interface (b, c); and T-plastin ABS1 (c).

(B) Representative SDS-PAGE analysis of low-speed and high-speed actin co-sedimentation assays of WT human T-plastin and T-plastin point mutants. S, supernatant; L, low-speed pellet; H, high-speed pellet.

(C and D) Quantification of (B).

details), after mixing and incubating WT or mutant T-plastin with F-actin, a first centrifugation was performed at low speed to pellet bundled F-actin together with bound proteins. At this low speed, single actin filaments would remain in the supernatant. Subsequently, a second centrifugation was performed at low speed to pellet all remaining actin filaments. The effects of T-plastin mutations can be analyzed by (1) the relative distribution of F-actin in the low-speed pellet vs the high-speed pellet; (2) the distribution of T-plastin in the low-speed pellet, the high-speed pellet, and the supernatant (Kim et al., 2016). The assay reveals that the W390A mutation suppresses actin bundling by T-plastin but has minimal effects on actin binding (Figure 5-8 Panels B, C, and D). The results strongly support a sequential actin bundling model.

In the pre-bound conformation, T-plastin's CH1 and CH4 form an extensive binding interface. Invoking a sequential actin bundling model, we reasoned disrupting this binding interface would facilitate T-plastin's actin bundling. To test this hypothesis, we mutated two arginine residues on the CH1–CH4 interface, R594 and R595, to alanine (Figure 5-8 Panel A, Box (b)). As discussed in the previous chapters, T-plastin's ABD1 and ABD2 share a high-degree structural homology, from which we could pinpoint key residues that potentially constitute the ABD1–actin binding interface. We reasoned that correctly disrupting the ABD1–actin binding interface would reduce actin bundling, supporting our prediction of the ABD1 actin-binding interface and further support a sequential actin bundling mechanism. To test this hypothesis, we mutated F191 of CH1 to alanine (Figure 5-8 Panel A, Box (c)), a key residue predicted to be on the ABD1–actin binding interface. In the experiments, we discovered the R594A single

mutant and the R594A/R595A double mutant bundle actin much stronger than the WT T-plastin, while the R595A does not have a pronounced effect on actin bundling (Figure 5-8 Panels B, C, and D). We also discovered F191A strongly inhibits actin bundling by T-plastin (Figure 5-8 Panels B, C, and D). In summary, the *in vitro* actin co-sedimentation assays collectively support a stepwise and sequential actin bundling mechanism by T-plastin: T-plastin ABD2 first engage actin, which triggers an internal conformational change that releases ABD1 for actin bundling.

5.5 Discussion: towards a Ca^{2+}-regulated actin-bundling mechanism by human T-plastin

In this chapter, we systematically characterized the actin-binding and actin-bundling mechanism of human T-plastin. By suppressing the actin-bunding activity with Ca^{2+}, we first obtained a 2.6-Å Cryo-EM reconstruction of full-length T-plastin–actin complex with T-plastin decorated on single actin filaments. Subsequently, in the absence of Ca^{2+}, we solved a 6.9-Å Cryo-EM structure of full-length T-plastin–actin complex by focused classification, which reveals a frustrated, intermediate state poised for actin bundling after ABD2 engages actin. The structures reveal T-plastin binds and bundles F-actin in a stepwise and asymmetrical fashion: ABD2 binds an actin filament first and the binding triggers an internal conformational change in T-plastin that releases ABD1, which can only bind another actin filament after ABD2 binds. Structure-guided mutagenesis and actin co-sedimentation assays strongly support this bundling mechanism.

Despite the progress reported in this chapter, structural mechanism for the actin bundling by T-plastin is only partially revealed. To understand how T-plastin can crosslink actin filaments *in vivo*, two hurdles must be cleared:

(1) A structure of T-plastin-crosslinked actin bundle is necessary. To date, direct structural characterization of actin bundles is still technically prohibitive. Actin bundles are not constructed in a stoichiometrically defined manner, as seen in Chapter 4. Component heterogeneity, lack of symmetry, and the large box size required for the analysis are likely the major issues that need to be addressed in Cryo-EM studies. Careful *in vitro* reconstitution of biochemically defined actin bundles and novel data-processing cryo-EM algorithms will be crucial in this effort. A structure of T-plastin-crosslinked actin bundle can provide invaluable information on the relative orientation (parallel or anti-parallel), the inter-filamentous distance, the T-plastin conformation, and the binding stoichiometry of actin bundles.

(2) The calcium regulatory mechanism of T-plastin-induced actin bundling remains a mystery. The presence of the EF-hand-based regulatory domain (RD) affords T-plastin the unique property of sensing calcium signals. The regulatory domain is extremely flexible (Ishida et al., 2017), making it refractory to structural characterization as a domain within full-length T-plastin. It is likely that when calcium is not present and T-plastin bundles actin, as ABD1 becomes more ordered, the RD also becomes ordered and more amenable to structural characterization. Therefore, a structure of T-plastin-crosslinked actin bundle may also be the key to reveal the calcium regulation mechanism.

The answer to these two questions will likely reveal the full picture of T-plastin's calcium-sensitive actin-bundling mechanism. Subsequent cell biology studies based on the molecular-level information can further reveal the functional impacts of disease-associated mutations found in T-plastin and potentially facilitate the development of targeted therapeutics.

CHAPTER 6

Conclusions, overall discussion, and future directions

6.1 Conclusions

In eukaryotic cells, the actin cytoskeleton is a central regulator of cellular mechanics, and intricate interactions between the actin cytoskeleton and its binding proteins regulates every aspect of actin physiology. This thesis sought to investigate two aspects of actin physiology of particular importance: how actin can sense mechanical forces and mediate cellular mechanotransduction, and how cellular actin networks and high-order actin structures are constructed from single actin filaments. We addressed these two questions by studying key actin-binding proteins and dissecting structural mechanisms at the molecular level. In Chapter 2, the thesis described the development of two novel *in vitro* reconstituted biophysical assays to independently and unambiguously identify and validate novel force-sensitive actin binding proteins. A case study on a homologous pair of ABPs in cellular adhesions, α-catenin and vinculin, revealed α-catenin directly senses force on actin, while vinculin does not. In Chapter 3, the thesis described near-atomic-resolution cryo-EM structures of the α-catenin ABD–F-actin and vinculin ABD–F-actin complexes, structure-guided discovery of α-catenin's force sensor, and ongoing efforts to elucidate α-catenin's force sensing mechanism. In Chapter 4, the thesis further described structural characterization of adhesion ABP–F-actin complexes, introduced how adhesion proteins can construct F-actin networks, and explored potential molecular mechanisms by which mutations in adhesion proteins can

lead to diseases involved in actin network structures and actin-mediated mechanotransduction. Besides the adhesion ABPs, another large ABP family is the calponin-homology (CH) domain ABP family. In Chapter 5, using a unique CH domain ABP, T-plastin, as an example, the thesis revealed the structural mechanism by which T-plastin crosslinks F-actin. In summary, with state-of-the-art biochemical, biophysical, and structural methods, this thesis systematically studied the molecular mechanisms for the multi-modal regulation of actin networks by actin binding proteins.

6.2 Discussion and future directions

Studies at the cellular and the tissue levels have suggested mechanical properties of cellular actin networks rely on F-actin's ability as a force sensor which transduces mechanical signals to force-sensitive ABPs, such as α-catenin (Romet-Lemonne and Jegou, 2013; Jegou and Romet-Lemonne, 2021). Recent work has also revealed force-sensitive behaviors of *in vitro* reconstituted actin networks (Bieling et al., 2016). Ongoing technical developments, particularly innovations in single-molecule biophysical techniques and structural techniques, enabled us to reveal the molecular mechanisms for actin force sensing at single-filament level, which is the topic of this thesis. In the future, better *in vitro* and *in vivo* biophysical assays, together with more powerful *in situ* structural reconstruction methods, such as cryo-electron tomography, will help elucidate the molecular mechanisms by which *in vitro* and *in vivo* cellular actin network senses and transduces mechanical stimuli.

From single filaments to actin network, a signaling web for cellular mechanosensing and mechanotransduction is constructed with the help of myriad actin-binding, and more generally, actin-associated proteins. Current studies have mostly focused on a handful of representative proteins, which substantially limits our understanding on the complexity of cellular actin networks. To understand how cells sense forces, it is imperative for us to better understand structures and functions of these actin-associated proteins. This effort continues to depend on ongoing technical innovations, including protein biochemistry and the development of biochemically controlled actin networks.

This thesis describes one of the first efforts to apply force on single molecules and single polymers in structural characterization, a major technical challenge in structural biology yet to be conquered. From the very beginning, structural biological methods have focused on solving ground-state-energy structures for biomolecules because they represent the abundantly populated conformational states that are much easier to be characterized. However, it is increasingly appreciated that biomolecules are usually dynamic. Sparsely and transiently populated, high-energy-state protein conformational states are often key functional states for proteins and protein complexes. Force-activated protein conformational states, which were studied in this thesis, fall into this category. In addition, there are light-activated, heat-activated, and ligand-activated high-energy protein conformational states, for which structural characterization is nearly impossible because of their dynamic and transient nature. Furthermore, using existing knowledge to trap mimics of those states without knowing whether a trapped state is an

actual functional state can misdirect a field. A future generation of structural biologists will have to address how to characterize high-energy protein conformational states, and specifically for this thesis, how to get a protein structure when it is under active force generation, with the help of an ever-progressing biochemical toolbox and ever-developing computational power.

Actin is an exemplary demonstration for the complexity and the dynamics of a single protein. Actin is one of the most abundant and most conserved protein on earth (Blanchoin et al., 2014), yet it has remarkable conformational flexibility and a highly diverse network of protein-protein interactions, a focus of this thesis. In fact, theories have claimed that it is precisely this flexibility and diversity that drive and maintain its conservation (Galkin et al., 2012b). This deep understanding for a single protein illustrates the power of protein biochemistry. Among the 20,000-strong human proteome (Pertea et al., 2018), the vast majority have not been studied at all. Protein biochemistry will continue to push the boundary of scientific discovery in the years to come.

CHAPTER 7

Materials and Methods

F-Actin preparation

Filamentous actin (F-actin) was polymerized fresh for each experiment from actin monomers in G-Mg (G buffer supplemented with 0.1 mM $MgCl_2$) and KMEI (50 mM KCl, 1 mM $MgCl_2$, 1 mM EGTA, 10 mM imidazole pH 7.0, 1mM DTT) buffers as described previously (Gurel et al., 2017). 30% rhodamine-labeled actin filaments used in TIRF microscopy assays were prepared by co-polymerizing unlabeled actin monomers and rhodamine-labeled actin monomers (Cytoskeleton catalogue # AR05) at a 7:3 molar ratio (total actin concentration 1µM) at room temperature for 2 hours in the dark. For optical trapping/confocal microscopy assays, 10% biotinylated actin filaments were prepared by co-polymerizing purified unlabeled actin monomers and biotinylated actin monomers (Cytoskeleton catalogue # AB07) at a 9:1 molar ratio (total actin concentration 1µM) at room temperature for 2 hours. The biotinylated F-actin was subsequently stabilized and fluorescently labeled by adding 1.2 molar equivalents of Alexa Fluor 555 Phalloidin (ThermoFisher catalogue # A34055).

Expression cloning

Vectors for expression of WT H. sapiens vinculin ABD (879-1066), H. sapiens metavinculin ABD (879-1134), H. sapiens α-catenin ABD (αE-catenin 664-906), α-catenin ABDΔC (αE-catenin 664-871), vinculin ABD-NCSwap (αE-catenin 664-708-

vinculin 916-1041-αE-catenin 837-906), vinculin ABD-NCSwapΔC (αE-catenin 664-708-vinculin 916-1041-αE-catenin 837-871), and WT full-length human αE-catenin (1-906) were constructed by inserting the corresponding cDNA sequence into a pET bacterial expression vector with an N-terminal His6-tag, strep-tag, TEV cleavage site, and, for proteins used in fluorescence imaging experiments, a subsequent C-terminal Halo-tag by Gibson assembly (Gibson et al., 2009). Constructs for proteins used in Cryo-EM structural studies are not Halo-tagged. Three WT α-catenin TIRF trials were performed with a previously reported Halo-tagged α-catenin ABD construct (αE-catenin 671-906), and no difference was observed.

WT human T-plastin (1-630), as well as T-plastin mutants F191A, W390A, R594A, R595A, R594/R595A was expressed in a pE-SUMO vector obtained from Dr. Damien Garbett in the Meyer Lab at Stanford University.

Expression and purification of actin binding proteins

C-terminally GFP-tagged mouse myosin V HMM and myosin VI S1 were purified from SF9 cells using published protocols (Wang et al., 2000). Human calmodulin (CaM) was purified from Rosetta2(DE3) E. coli cells using a published protocol (Putkey et al., 1985) and stored in Gel Filtration Buffer (20mM Tris-Cl pH 8.0, 100mM NaCl, 2 mM β-mercaptoethanol) supplemented with 5% v/v glycerol.

All other ABPs were expressed in Rosetta2(DE3) E. coli cells (Novagen) grown in LB media at 37°C to an optical density of 0.8-1.0 and induced with 0.7 mM IPTG. After induction, the cells were grown for 16 hours at 16°C, then cell pellets were

collected and stored at -80°C until use. To purify halo-tagged ABPs for fluorescent labelling, cells pellets were resuspended in Lysis Buffer (50 mM Tris-Cl pH 8.0, 150 mM NaCl, 5% v/v glycerol, 2 mM β-mercaptoethanol, 20 mM imidazole) and lysed with an Avestin Emulsiflex C5 homogenizer, after which the lysate was clarified at 15,000 g for 30 minutes. Cleared lysate was incubated with Ni-NTA resin (Qiagen) for 1 hour on a rotator at 4°C, after which the flow-through was discarded and the resin was washed with 5 bed volumes of lysis buffer. Proteins were subsequently eluted in Elution Buffer (50 mM Tris-Cl pH 8.0, 150 mM NaCl, 5% v/v glycerol, 2 mM β-mercaptoethanol, 300 mM imidazole). Purified His-tagged TEV protease (prepared according to a published protocol (Tropea et al., 2009)) or SUMO protease Ulp1 was added at 0.05 mg / ml working concentration, then the eluate was dialyzed against Dialysis Buffer (20 mM Tris-Cl pH 8.0, 300 mM NaCl, 5% v/v glycerol, 2 mM β-mercaptoethanol) for 16 hours. The protein solution was then reapplied to Ni-NTA resin, and the flow-through was collected.

Protein was then sequentially purified by a HiTrapQ HP anion exchange column (GE Healthcare) followed by size exclusion chromatography on a Superdex 200 Increase column in Gel Filtration Buffer supplemented with 10% v/v glycerol, and then snap-frozen in liquid Nitrogen and stored at -80°C. Non-halo-tagged proteins prepared for cryo-EM studies were purified identically, except glycerol was omitted from all buffers. Purified talin ABS3 (GFP-Halo-R13-DD) protein was obtained from Dr. Leanna Owen in the Dunn Lab at Stanford University.

To isotopically label the α-catenin used in the NMR studies, α-catenin was over-expressed by growing Rosetta2 (DE3) *E. coli* in the N^{15} labeled minimal medium. First, 5x M9 salt were prepared by adding 34 g of Na_2HPO_4, 15 g of KH_2PO_4, and 2.5 g NaCl to 1L dH_2O. N^{15} labeled minimal medium was then prepared by adding 200ml 5x M9 salt solution, 100 µl 1M $CaCl_2$, and 1 ml of 1M $MgSO_4$ to 700µl dH_2O, and subsequently after autoclaving, 1.0 g labeled N^{15} ammonium chloride, 4.0 g of unlabeled dextrose, and 100x Gibco MEM vitamin solution (cat. No. 11120052) were added. The total volume of the medium was brought to 1L.

After rapid thawing prior to use, all proteins were clarified by ultracentrifugation at 45,000 rpm in a TLA100 rotor for 10 minutes at 4°C. All protein concentrations were estimated using the Bradford colorimetric assay (Pierce), calibrated with BSA.

Synthesis of Halo-JF-646 and labelling of ABPs

Fluorescent dye JF-646 (Grimm et al., 2015) NHS-ester building block (TOCRIS) was conjugated with Halo-tag ligand amine O4 (Promega) by synthetic chemistry according to published protocols (Grimm et al., 2017). Briefly, 1.5 equivalents of amine O4 ligand was added to one equivalent of the JF-646 NHS-ester in DMF followed by adding 5% triethylamine. The reaction was vigorously stirred for 16 hours at room temperature and the product was purified by silica gel chromatography, dried by SpeedVac (ThermoFisher), and reconstituted in DMSO.

For optical trapping/confocal microscopy assays, HaloTag Alexa Fluor 488 Ligand (Promega) was utilized as described above, followed by desalting through a PD

SpinTrap G-25 column (GE Healthcare) according to the manufacturer's protocol to remove unreacted dye prior to use. To label the Halo-tagged actin-binding proteins with Halo-JF-646 for TIRF microscopy assays, two equivalents of synthesized Halo-JF-646 dye was added to the protein solution, followed by incubation for at least two hours in the dark at 4°C prior to use. Subsequent removal of excess dye was not required, as JF-646 is a fluorogenic dye (Grimm et al., 2015).

Correlative force spectroscopy and confocal microscopy assays

Experiments were performed at room temperature (approximately 25°C) on a LUMICKS C-Trap instrument combining confocal fluorescence with dual-trap optical tweezers (Hashemi Shabestari et al., 2017) (Wasserman et al. 2019). The optical traps were cycled through pre-set positions in the five channels of a microfluidic flow cell by an automated stage (Figure 2-3 Panel A). Channels 1–3 were separated from each other by laminar flow, which we utilized to form actin filament tethers between two 4 µm-diameter streptavidin-coated polystyrene beads (Spherotech) held in optical traps with a stiffness of 0.3 pN / nm. We first captured a single bead in each trap in channel 1. The traps were then transferred to channel 2, containing 5-20 nM Alexa 555 phalloidin-stabilized, 10% biotinylated F-actin in MB supplemented with 1 µM dark phalloidin, where tethers were formed by briefly moving 1 of the 2 traps towards the other trap against the direction of flow, followed by rapidly moving the traps to channel 3, which contained only buffer (MB + 1 µM dark phalloidin). The presence of a tether was verified by carefully separating the traps and observing an associated increase in force when

monitoring the force-extension curve, applying the minimum extension feasible to avoid prematurely rupturing the tether.

The traps were then moved to orthogonal channel 4 or 5, which contained 2 μM fluorescently labeled vinculin ABD or α-catenin ABD (diluted in MB supplemented with 1μM dark phalloidin), respectively, and flow was ceased during data acquisition. Force data were acquired at 200 Hz during constant velocity (0.1 μm / s) pulling experiments while simultaneously acquiring 2-color confocal fluorescence scans at 33 ms line scan time, exciting Alexa Fluor 488 HaloTag ligand and Alexa Fluor 555 phalloidin fluorophores with laser lines at 488 nm and 532 nm, respectively.

Data analysis was performed using ImageJ and custom software provided by LUMICKS. Force data from the 2 traps were averaged and binned to the confocal frame interval. The intensity values are measured by drawing a box in imageJ to measure the fluorescence intensities of actin and ABP in both channels with background subtraction, calculating the background from an equal-sized box from that frame in an area devoid of filaments or beads. For paired analysis, the “high-force” and “low-force” averages were calculated only from the final tether to rupture, as long as the entire force trace has at least 10 quantifiable confocal image frames. For fluorescence-force correlation plots, only single-filament tethers selected based on Figure 2-4 Panels A-C were used. I_{ABP}/I_{Actin} values were normalized by dividing the values in each recording by the largest value observed during that recording. K-means clustering analysis was performed to identify the cutoff force in the correlation plots for each ABP. Briefly, the force-fluorescence data were grouped into two clusters using scikit-learn (Pedregosa et al.,

2011). For both α-catenin and vinculin, the data separated along the force axis, providing a threshold force for each ABP. Furthermore, a silhouette analysis for both ABPs confirmed that the data should not be clustered into more than two clusters (Kaufman and Rousseeuw, 2009).

TIRF force reconstitution assays

Glass coverslips (Rectangular: Corning 22 x 50 mm #1½ Cover Glass; Square: Fisherbrand 22 x 22 mm #1½ Microscope Cover Glass) were cleaned by 30 minute 100% acetone wash, 10 minute 100% ethanol wash, and 2 hour 2% Hellmanex III liquid cleaning concentrate (HellmaAnalytics) wash in a bath sonicator followed by rinsing with water. The cleaned glass coverslips were coated with 1 mg/ml mPEG5K-Silane (Sigma) in a 96% ethanol, 10 mM HCl solution for at least 16 hours. After coating, the coverslips were rinsed with 96% ethanol and water, then air-dried and stored at 4°C until use. Flow cells were prepared with one square and one rectangular coverslip, both coated with mPEG-Silane. Double-sided adhesive tape (3M) was used to make ~4 mm-wide flow chambers between the coverslips, which were open on both sides to facilitate buffer exchange when adding components for imaging.

For each assay, 6 mg/ml anti-GFP antibody (Sigma #G1546) solution reconstituted in water was first introduced into the flow chamber and incubated for 2 minutes. Subsequently, Motility Buffer ("MB": 20 mM MOPS pH7.4, 5 mM MgCl2, 0.1 mM EGTA, 1 mM DTT) containing 0.075 μM GFP-myosin V S1 and 0.15 μM GFP-myosin VI S1 were flowed into the chamber and incubated for another 2 minutes. A

solution of 1 mg / ml bovine serum albumin (BSA) in MB was then flowed into the flow chamber and incubated for at least 2 minutes, after which 1 μM rhodamine-labeled F-actin in MB was flowed into the chamber and incubated for 20-30 s. The flow chamber was rinsed with MB buffer to remove F-actin not bound to the rigor-state motors, then Imaging Buffer (MB without ATP, supplemented with 0.01% Nonidet P-40 subsitute (Roche), 1 μM calmodulin, 15 mM glucose (Sigma), 1 μg / ml glucose oxidase (Sigma), and 0.05 μg/ml catalase (Sigma)) containing 2 μM fluorescently labeled ABP was flowed into the chamber. The first movie (-ATP, no force) was then recorded. A second Imaging Buffer, identical to the first but now including 100 μM ATP, was then introduced into the same chamber, and a second movie (+ATP, with force) was recorded. For each solution that was introduced, complete buffer exchange was facilitated by applying a filter paper at the other end of the flow chamber while pipetting.

Dual-color TIRF image series (“movies”) were recorded at room temperature (approximately 25°C) using a Nikon TiE inverted microscope equipped with an H-TIRF module and an Agilent laser launch, driven by Nikon Elements software. Images were taken every 2 seconds with an Apo TIRF 60X 1.49 NA objective (Nikon) on an Andor iXon EMCCD camera; Rhodamine and JF646 fluorophores were excited by laser lines at 561 nm and 640 nm, respectively.

Filament region quantification

To quantify ABP association with individual “filament regions” of TIRF movies, we developed a custom ImageJ (Schneider et al., 2012) plugin (Figure 2-7 Panel A) which

features a graphical user interface (GUI). The plugin takes as input two movie files, the actin channel and the ABP channel from a dual-color TIRF experiment, as well as an adjustable set of parameters (set by default in the GUI to the optimized values used in this study).

To identify regions of interest (ROIs) in each frame, the actin channel image series was preprocessed (unsharp mask, median filter, rolling ball subtraction), binarized, then segmented into contiguous regions of pixels using the built-in ImageJ plugin “Analyze Particles”. ROIs whose centroids were fewer than 30 pixels from the edge of the field-of-view were excluded from further analysis due to incompatibility with downstream background subtraction procedures. The ROIs were then tracked through the image series and sorted into filament regions (representing individual filaments or small groups of filaments) by shortest Euclidean distance between ROI centroids in neighboring frames, with a maximum distance cutoff of 24 pixels. ROIs that were not matched with a pre-existing filament region by this criterion (i.e. whose centroid was greater than 24 pixels away from any ROI in the previous frame) were considered to represent a newly appeared filament region. Although this may result in overcounting the absolute number of filaments (should this be of interest; we do not believe this caveat impacts the conclusions of the present study), we find this procedure reliably handles events such as filament breakages and desultory motion in a completely automated fashion. To account for poorly tethered filaments fluctuating in and out of the evanescent field, only filament regions detected in at least 10 consecutive frames were included in the analysis.

Intensity in both the actin channel and the ABP channel were then quantified for each region. For each channel, the local background for each filament region in each frame was calculated as the mean grey value of the pixels from a 60 by 60 pixel box centered on the region's centroid, excluding pixels belonging to the region itself or any other filament region detected in the frame. Background-subtracted mean grey values were then calculated, followed by the ratio of these values across all frames in which the filament region was detected and their average, which we here report as the overall I_{ABP}/I_{Actin} for that filament region. The program then outputs all frame and average I_{ABP}/I_{Actin} values of the tracked filaments sorted by filament number for analysis, as well as a file containing all tracked regions.

Cryo-EM sample preparation and data collection

F-actin was polymerized in G-Mg and KMEI from 5μM unlabeled actin monomers at R.T for 1hr and then diluted to 0.6 μM in KMEI prior to use. Purified vinculin (879-1066) or metavinculin ABD (879-1134) was diluted in KMEI to 10 μM prior to use. After screening grids prepared with finely sampled ABP concentrations, we found diluting purified α-catenin ABD (664-906) to 20 μM in KMEI prior to use gave an optimal balance between filament decoration and bundling. Full-length human T-plastin was buffer exchanged into KMEI or Ca-KMEI (KMEI buffer + 2mM $CaCl_2$) by desalting column (GE PD SpinTrap G-25) and was maintained at a concentration of 20 μM. For the full-length α-catenin, the optimal concentration was screened and 6 μM was the optimal concentration used in data collection. For talin ABS3, purified protein was

received as 50µl aliquots at 63 µM concentration in 20mM Tris-Cl pH 8, 50 mM KCl, and 1 mM DTT. Prior to grid preparation experiments, talin solution was buffer-exchanged twice and diluted to 30 µM in KMEI plus 5 mM MOPS, at pH 6.5 or pH 7. All KMEI buffer was supplemented with 1 mM DTT and 0.05% NP-40.

Immediately prior to sample preparation, CF-1.2/1.3-3Au 300-mesh gold C-flat holey carbon cryo-TEM grids (Protochips) were plasma cleaned with a Hydrogen / Oxygen mixture for 5 seconds in a Gatan Solarus. Actin (3 µl) was first applied to the grid in the humidified chamber of a Leica EM GP plunge freezer and incubated for 60 s at 25°C. Actin binding protein (3 µl) was then applied and incubated for 30 s. Solution (3 µl) was then removed and an additional 3 µl of the same actin-binding solution was applied. After an additional 30 s, 3 µl of solution was removed, then the grid was back-blotted for 5 s, plunge-frozen in ethane slush, and stored in liquid Nitrogen until imaging.

To reconstitute the myosin V and VI force system on cryo-EM grids, no plasma cleaning was performed. Grids were first incubated with anti-GFP solution (prepared according to the TIRF assay protocol) on both sides, each side for 1 minute. Myosin V and myosin VI solutions were mixed according to the TIRF assay protocol, and the mixed solution was then applied to both sides of the grid and incubated for 1 minute on each side. Subsequently, the front side of the grid was blocked by MB-PVP solution, which contains 1mg/ml polyvinylpyrrolidone (Sigma, PVP10) polymer in 1x motility buffer, for 2 minutes. The front side of the grid was then blotted with an actin solution containing 0.6 µM F-actin for 30 seconds, washed twice in a tube with motility buffer, then mounted onto a Leica EM-GP. Solutions containing MB, ATP, and α-catenin were

then applied and incubated for 30 s. Solution (3 µl) was then removed and an additional 3 µl of the same actin-binding solution was applied. After an additional 30 s, 3 µl of solution was removed, then the grid was back-blotted for 5 s, plunge-frozen in ethane slush, and stored in liquid Nitrogen until imaging.

Cryo-EM data for metavinculin ABD–actin, α-catenin ABD–actin, full-length α-catenin-actin, vinculin ABD–actin, and T-plastin–actin (–Ca^{2+}) were recorded on a Titan Krios (ThermoFisher/FEI) operated at 300 kV equipped with a Gatan K2 Summit camera at the Rockefeller University (Rockefeller Krios I). SerialEM (Mastronarde, 2005) was used for automated data collection. Movies were collected at a nominal magnification of 29,000X in super-resolution mode resulting in a calibrated pixel size of 1.03 Å / pixel (superresolution pixel size of 0.515 Å / pixel), over a defocus range of -1.5 to -3.5 µm. 40 frames were recorded over 10 s of exposure at a dose rate of 6 electrons per pixel per second (1.5 electrons per $Å^2$ per second) for a cumulative dose of 60 electrons per $Å^2$. The T-plastin–actin (+Ca^{2+}) dataset was recorded at the New York Structural Biology Center (NYSBC) on a Titan Krios (ThermoFisher/FEI) operated at 300 kV equipped with a Gatan K2 Summit camera. Movies were collected in counting mode resulting in a calibrated pixel size of 1.06 Å / pixel, over a defocus range of -1.5 to -3.5 µm. 50 frames were recorded over 10 s of exposure at a dose rate of 1.34 electrons per pixel per second (1.4204 electrons per $Å^2$ per second) for a cumulative dose of 71.02 electrons per $Å^2$.

Cryo-EM image processing

Unless otherwise noted, all image processing was performed within the RELION-3.0 package (Zivanov et al., 2018). Movie frames were aligned and summed with 2 x 2 binning using the MotionCor2 algorithm (Zheng et al., 2017) as implemented in RELION (Zivanov et al., 2019), utilizing subframe motion correction with 5 × 5 patches. Contrast transfer function (CTF) parameters were estimated from non-doseweighted summed images with CTFFIND4 (Rohou and Grigorieff, 2015). Bimodal angular searches around psi angle priors were utilized in all subsequent 2D and 3D alignment / classification procedures. Around 2,000 segments were initially manually picked, extracted, and subjected to 2D classification to generate templates for auto-picking. Helical auto-picking was then performed utilizing a step-size of 3 asymmetric units with a 27 Å helical rise. Segments were extracted from dose-weighted (Grant and Grigorieff, 2015) sum images in 512 x 512 pixel boxes which were not further down-sampled, then a second round of 2D classification followed by auto-picking with featureful class averages was performed. Particles were then extracted and subjected to whole-dataset 2D classification using a 200 Å tube diameter and 300 Å mask diameter. Segments from the dataset that contributed to featureful class averages were selected for 3D analysis.

All subsequent 3D classification and 3D auto-refine steps were primed with estimates of helical rise and twist of 27.0 Å and -167.0°, respectively, utilizing an initial reference low-pass filtered to 35 Å resolution, with the outer tube diameter set to 200 Å, inner tube diameter set to -1, and the mask diameter set to 300 Å. The first round of 3D

classification into 3 classes was performed utilizing a reconstruction of a bare actin filament (EMBD-7115) as the initial reference. A second iteration of 3D classification was then performed as above, utilizing a featureful class with clear ABP density produced by the first round as the initial reference. For datasets except for T-plastin–actin ($+Ca^{2+}$), this second round of 3D classification yielded two classes with helical parameters similar to the initial estimates and well-resolved 3D features, and one junk class with aberrant helical parameters and distorted features. For T-plastin–actin ($+Ca^{2+}$) dataset, all three classes were good, featureful 3D classes, indicating the high quality of this dataset. Segments contributing to the two good classes were then pooled for 3D auto-refinement.

The first round of auto-refinement was then performed using one of the two good 3D averages as an initial reference. All masks for subsequent post-processing steps were calculated with 0 pixel extension and a 6 pixel soft edge from the converged reconstruction produced by that round of refinement, low-pass filtered to 15 Å and thresholded to fully encompass the density map. First-round post-processing was performed with a 50 % z length mask, followed by CTF refinement without beam-tilt estimation and Bayesian polishing (Zivanov et al., 2019). A second round of auto-refinement was then performed using the converged reconstruction from the first round as the initial reference. Second-round post-processing was performed with a 30 % z length mask, followed by a second round of CTF refinement with beam-tilt estimation and Bayesian polishing. A final round of auto-refinement was then performed using the converged reconstruction from the second round as the initial reference. We found that

this iterative procedure of tightening the mask for polishing resulted in substantial resolution improvements, potentially by mitigating the effects of medium-range disorder in F-actin previously speculated to limit the resolution of reconstructions of this filament (Galkin et al., 2012; Merino et al., 2018).

The final reconstructions converged with helical rise of 27.1 Å and twist of -167.1° for the metavinculin ABD–F-actin complex, a helical rise of 27.0 Å and twist of -166.9° for the α-catenin ABD-F-actin complex, a helical rise of 27.0 Å and twist of -166.8° for the T-plastin–F-actin ABD-F-actin complex ($–Ca^{2+}$), and a helical rise of 27.4 Å and twist of -166.8° for the T-plastin–F-actin ABD-F-actin complex ($+Ca^{2+}$), consistent with our finding that actin rearrangements evoked by these ABPs are minimal (Figure 3-5 Panel H; Figure 5-3 Panel C). Final post-processing was performed with a 30% z length mask, leading to global resolution estimates of 2.9 Å for the metavinculin ABD–F-actin complex, 3.2 Å for the α-catenin ABD–F-actin complex, 3.4 Å for the full-length T-plastin–F-actin complex ($–Ca^{2+}$), and 2.6 Å for the full-length T-plastin–F-actin complex ($+Ca^{2+}$), by the gold-standard Fourier shell correlation (FSC) 0.143 criterion. B-factors of both datasets estimated during post-processing were then used to generate sharpened, local-resolution filtered maps with RELION. Key statistics summarizing cryo-EM image processing are reported in Table 1.

For the metavinculin ABD–actin and the α-catenin ABD–actin datasets, asymmetric focused classification (without alignment) utilizing masks isolating the ABD region showed no evidence of segments with unoccupied binding sites (data not shown), suggesting that decoration of actin filaments by both 10 μM metavinculin ABD

and 20 μM α-catenin ABD was essentially complete, with 100% occupancy at the limit of detection of current methods. For the T-plastin–actin datasets, focused classification with a binary mask around the decorated T-plastin identified signals of an extra domain within T-plastin (see Chapter 5.3), indicating T-plastin is flexible and adopts multiple conformations when binding to actin. The segments that contain the signal of an extra domain were selected and subjected to 3D reconstruction, leading to a 6.9-Å Cryo-EM structure that features 3 helices (H2, H3, and H4) of T-plastin CH2.

Model building and refinement

To generate homology models of the actin-binding 'core' (Figure 5-1) of plastin, the Robetta server was used (Kim et al., 2004). The selected homology model for 'pre-bound' T-plastin was the model that had the highest score. Sharpened, local-resolution-filtered maps as described above were used for model building. The density maps were of sufficient quality for *de novo* atomic model building. As structures of components were available, initial models of actin (PDB 3j8a), metavinculin ABD (PDB 3jbk) truncated to residues 981-1131, α-catenin ABD (PDB 4igg chain B) truncated to residues 699-871, and the 'pre-bound' T-plastin homology model were fit into the density map using Rosetta (Wang et al., 2016). Models were subsequently inspected and adjusted with Coot (Brown et al., 2015; Emsley et al., 2010), and regions that underwent significant conformational rearrangements were manually rebuilt. The models were then subjected to several rounds of simulated annealing followed by real-space refinement in Phenix (Adams et al., 2010; Afonine et al., 2018) alternating with

manual adjustment in Coot. A final round of real-space refinement was performed without simulated annealing. The pseudo-atomic model for T-plastin was generated by rigid-body docking of T-plastin CH2 and ISOLDE flexible fitting (Croll, 2018). Key statistics summarizing model building, refinement, and validation are reported in Table S1.

Molecular graphics and structure analysis

Structural figures and movies were prepared with ChimeraX (Goddard et al., 2018). Per-residue RMSD analysis was performed with UCSF Chimera (Pettersen et al., 2004) as previously described (Zhang et al., 2015). The surface area of actin-binding interfaces was calculated with PDBePISA (Krissinel and Henrick, 2007) (EMBL-EBI). Model quality was assessed with EMRinger (Barad et al., 2015) and MolProbity (Chen et al., 2010) as implemented in Phenix.

Sequence alignments

Protein sequences of human vinculin (UniProt Accession Code P18206-2), human metavinculin (P18206-1), human αE-catenin (P35221), human αN-catenin (P26232), human αT-catenin (Q9UI47), human I-plastin (Q14651), human L-plastin (P13796), human T-plastin (P13797), human utrophin (P46939), human β-spectrin (O15020), and human filamin A (P21333), were aligned with ClustalOmega (Sievers and Higgins, 2014) (EMBL-EBI).

Negative stain EM

For the negative stain EM experiments in Figure 4-1, an aliquot of actin (1 µM) without or with Vt, MVt, or MVtp (10 µM), or was incubated in actin polymerization buffer (10 mM Tris, 200 mM KCl, 10 mM imidazole, 2.5 mM $MgCl_2$, 1 mM EGTA, 2 mM DTT (pH 7.5)) for 15 min and absorbed directly onto glow-discharged carbon-coated 400 mesh copper grids for 3 min, and then stained with 2% (w/v) uranyl acetate in water. TEM images were obtained using a FEI Tecnai 12 electron microscope at 80 kV and captured on a Gatan First Light CCD camera using Gatan Digital Micrograph software (Gatan, Pleasanton, CA).

For the experiments displayed in Figure 4-3 and Figure 4-4, F-actin and the indicated Vt ± MVt constructs were mixed in KMEI and incubated at room temperature for 15 min. Sample (4 µl) was then applied to a glow-discharged continuous carbon grid (Ted Pella) and incubated for 60 s. After incubation, the grid was washed with three 100 µl drops of 1% uranyl acetate, then blotted to dryness. Images were acquired with the SerialEM package on a Tecnai F20 operating at 120 kV with a Gatan Ultrascan 4000 CCD camera. Tiled images with 20% overlap were acquired at 7800× magnification, 3 µm underfocus, and 4-fold camera binning, corresponding to a calibrated pixel size of 5.7 nm at the specimen level. Stitched images were assembled with the “blendmont” program from the IMOD software package.

F-actin assembly quantification

Images were thresholded and binarized using ImageJ, then segmented into continuous regions of pixels using the built-in “Analyze Particles” plugin, including regions 100–500,000 pixels in size and with a circularity of 0–0.3. This procedure does not always capture every region that an expert user would designate to contain F-actin in every image (e.g., areas which are not outlined in yellow in Figure 4-2). However, we find its performance superior to both manual segmentation of the images, which requires user decisions on region boundaries and the minimum size of regions, as well as a sliding box quantification (a measure of local density), which is extremely sensitive to noise introduced by slight differences in thresholding (data not shown). Size measurements of regions were pooled from all images for a given condition, then divided into 10,000 equal sized bins per data set and plotted via a normalized cumulative histogram. Data were binned and cumulative sums calculated with a python script (available at www.github.com/alushinlab/FactinAssemblyQuant) using the function “binned_statistic” implemented in SciPy (www.scipy.org). Plots were generated and statistical tests were conducted with GraphPad Prism.

Actin co-sedimentation assays

Briefly, mixtures of F-actin and T-plastin WT or mutants were generated at the concentrations reported and were incubated at room temperature for 30 min in co-sedimentation buffer (10 mM Tris (pH 7.5), 100 mM KCl, 2.5 mM $MgCl_2$, and 2 mM DTT). The samples were then spun for 30 min. at 8,000 rpm (low-speed) in a TLA-100

rotor. This pellet was the ‘low-speed’ pellet. The supernatant was taken out from the spinning tube and then spun for 30 min. at 80,000 rpm (high-speed). This pellet was the ‘high-speed’ pellet, and the supernatant was also collected. All three fractions were subject to SDS-PAGE and Coomassie staining. The gels were scanned and quantified with ImageJ. Plots were generated with GraphPad Prism.

APPENDIX 1

Mei, L., Espinosa de los Reyes, S., Reynolds, M.J., Leicher, R., Liu, S., and Alushin, G.M. (2020). Molecular mechanism for direct actin force-sensing by α-catenin. ELife 9, e62514.

RESEARCH ARTICLE

Molecular mechanism for direct actin force-sensing by α-catenin

Lin Mei[1,2], Santiago Espinosa de los Reyes[1], Matthew J Reynolds[1], Rachel Leicher[2,3], Shixin Liu[3], Gregory M Alushin[1]*

[1]Laboratory of Structural Biophysics and Mechanobiology, The Rockefeller University, New York, United States; [2]Tri-Institutional PhD Program in Chemical Biology, The Rockefeller University, New York, United States; [3]Laboratory of Nanoscale Biophysics and Biochemistry, The Rockefeller University, New York, United States

Abstract The actin cytoskeleton mediates mechanical coupling between cells and their tissue microenvironments. The architecture and composition of actin networks are modulated by force; however, it is unclear how interactions between actin filaments (F-actin) and associated proteins are mechanically regulated. Here we employ both optical trapping and biochemical reconstitution with myosin motor proteins to show single piconewton forces applied solely to F-actin enhance binding by the human version of the essential cell-cell adhesion protein αE-catenin but not its homolog vinculin. Cryo-electron microscopy structures of both proteins bound to F-actin reveal unique rearrangements that facilitate their flexible C-termini refolding to engage distinct interfaces. Truncating α-catenin's C-terminus eliminates force-activated F-actin binding, and addition of this motif to vinculin confers force-activated binding, demonstrating that α-catenin's C-terminus is a modular detector of F-actin tension. Our studies establish that piconewton force on F-actin can enhance partner binding, which we propose mechanically regulates cellular adhesion through α-catenin.

***For correspondence:** galushin@rockefeller.edu

Competing interests: The authors declare that no competing interests exist.

Funding: See page 28

Received: 27 August 2020
Accepted: 21 September 2020
Published: 24 September 2020

Reviewing editor: Andrew P Carter, MRC Laboratory of Molecular Biology, United Kingdom

Introduction

Cells probe and respond to the mechanical properties of their surroundings through cytoskeletal networks composed of actin filaments (F-actin), myosin motor proteins, and dozens of actin-binding proteins (ABPs). These networks transmit forces through cell-matrix focal adhesions (***Humphrey et al., 2014***) and cell-cell adherens junctions (***Charras and Yap, 2018***), plasma membrane-associated many-protein assemblies which serve as hubs for the conversion of mechanical cues and stimuli into biochemical signaling cascades (mechanotransduction). Defects in mechanotransduction are associated with numerous diseases (***Jaalouk and Lammerding, 2009***), including muscular dystrophies, cardiomyopathies, and metastatic cancer, yet therapeutics which specifically target these pathways are largely absent due to our ignorance of the mechanisms that transduce mechanical signals through the cytoskeleton.

Diverse force regimes modulate the polymerization dynamics, micron-scale architecture, and protein composition of actin assemblies by molecular mechanisms that remain unclear (***Harris et al., 2018***; ***Romet-Lemonne and Jégou, 2013***). Cellular-scale pressures in the range of hundreds of pascal regulate the assembly and mechanical power of branched-actin networks generated by the ARP2/3 complex in vitro (***Bieling et al., 2016***) and in vivo (***Mueller et al., 2017***), tuning network geometric properties including filament length, density, and distribution of filament orientations. Live-cell imaging studies identified a subset of ABPs that preferentially localize to the cytoskeleton in vivo in response to this magnitude of mechanical stimulation (***Schiffhauer et al., 2016***), which were also postulated to recognize properties of network geometry. Molecular-scale forces in the

eLife digest All of the cells in our bodies rely on cues from their surrounding environment to alter their behavior. As well sending each other chemical signals, such as hormones, cells can also detect pressure and physical forces applied by the cells around them. These physical interactions are coordinated by a network of proteins called the cytoskeleton, which provide the internal scaffold that maintains a cell's shape. However, it is not well understood how forces transmitted through the cytoskeleton are converted into mechanical signals that control cell behavior.

The cytoskeleton is primarily made up protein filaments called actin, which are frequently under tension from external and internal forces that push and pull on the cell. Many proteins bind directly to actin, including adhesion proteins that allow the cell to 'stick' to its surroundings. One possibility is that when actin filaments feel tension, they convert this into a mechanical signal by altering how they bind to other proteins.

To test this theory, Mei et al. isolated and studied an adhesion protein called α-catenin which is known to interact with actin. This revealed that when tiny forces – similar to the amount cells experience in the body – were applied to actin filaments, this caused α-catenin and actin to bind together more strongly. However, applying the same level of physical force did not alter how well actin bound to a similar adhesion protein called vinculin. Further experiments showed that this was due to differences in a small, flexible region found on both proteins. Manipulating this region revealed that it helps α-catenin attach to actin when a force is present, and was thus named a 'force detector'.

Proteins that bind to actin are essential in all animals, making it likely that force detectors are a common mechanism. Scientists can now use this discovery to identify and manipulate force detectors in other proteins across different cells and animals. This may help to develop drugs that target the mechanical signaling process, although this will require further understanding of how force detectors work at the molecular level.

piconewton range have also been shown to modulate the activity of F-actin polymerization (***Courtemanche et al., 2013***; ***Jégou et al., 2013***; ***Risca et al., 2012***; ***Zimmermann et al., 2017***) and severing (***Hayakawa et al., 2011***) factors in vitro, suggesting that molecular components of actin networks could be mechanically regulated by physiological forces. While F-actin binding by the actin-depolymerization factor cofilin was reported to be directly regulated by tension across the filament to modulate its activity (***Hayakawa et al., 2011***), a recent study has suggested that cofilin is tension-insensitive, instead having its severing activity regulated by filament bending (***Wioland et al., 2019***). F-actin has been reported to adopt a structural landscape of co-existing conformations in cryo-electron microscopy (cryo-EM) studies (***Galkin et al., 2010b***), leading to speculation that actin filaments could themselves serve as tension sensors by presenting distinct binding interfaces to ABPs in the presence of load (***Galkin et al., 2012***). It nevertheless remains unclear to what extent mechanical modulation of functional interactions between ABPs and F-actin occurs through direct regulation of F-actin's binding interactions by force. Furthermore, structural mechanisms enabling ABPs to detect force on F-actin, to our knowledge, are unknown.

Inspired by the report that the enhanced cytoskeletal localization response of ABP isoforms differed substantially when cells were mechanically stimulated (***Schiffhauer et al., 2016***), we reasoned that biophysical and structural analysis of closely-related ABPs would be a powerful approach for mechanistically dissecting mechanically regulated F-actin binding. Here we specifically investigate enhanced binding to F-actin when the load is applied solely to the filament, which we refer to as 'force-activated binding'. Our studies focus on the homologous adhesion proteins α-catenin (***Kobielak and Fuchs, 2004***) and vinculin (***Ziegler et al., 2006***), which are major ABP components found in adherens junctions (α-catenin and vinculin) and focal adhesions (vinculin) that are critical for the force-dependent strengthening of cellular adhesion and mechanotransduction (***Dumbauld et al., 2013***; ***Yonemura et al., 2010***). Vinculin is a strictly auto-inhibited globular protein that must engage with multiple adhesion partners to be activated and bind F-actin (***Johnson and Craig, 1995***), stabilizing adhesion through incompletely defined mechanisms. On the other hand, α-catenin exists in two distinct populations maintained in dynamic equilibrium in the cell (***Drees et al., 2005***). It serves as a

central component of the membrane-anchored heterotrimeric α-catenin–β-catenin–cadherin complex (the 'cadherin-catenin complex') at adherens junctions, which lacks F-actin-binding activity in traditional assays when isolated (**Yamada et al., 2005**). It also forms a soluble homodimer with constitutive modest F-actin-binding activity, thought to play a role in the generation and maintenance of actin bundles by cross-linking filaments and inhibiting ARP2/3 binding, thereby suppressing branched-actin formation (**Drees et al., 2005**). The structural mechanisms by which forces transmitted through the actin cytoskeleton modulate the complex networks of binding interactions formed by α-catenin and vinculin during adhesion maturation remain unknown.

Both proteins are entirely α-helical (**Bakolitsa et al., 2004**; **Rangarajan and Izard, 2013**) and are composed of a large N-terminal 'head' domain, which engages in protein-protein interactions with other adhesion molecules (**Kobielak and Fuchs, 2004**; **Ziegler et al., 2006**) and a smaller C-terminal 5-helix bundle F-actin binding 'tail' domain (**Bakolitsa et al., 1999**; **Ishiyama et al., 2013**; **Figure 1—figure supplement 1**, Helices H1–H5), connected by a flexible linker. The isolated actin-binding domains (ABDs), which we utilize in our study, retain their structures and actin-binding activities (**Bakolitsa et al., 1999**; **Ishiyama et al., 2013**), engaging a similar site on the filament surface (**Hansen et al., 2013**; **Janssen et al., 2006**; **Kim et al., 2016**; **Thompson et al., 2014**). Recent single-molecule force-spectroscopy studies reported that both α-catenin in the cadherin-catenin complex (**Buckley et al., 2014**) and vinculin (**Huang et al., 2017**) form catch bonds with F-actin, characterized by increased bond lifetime when moderate forces around 10 pN are applied across the ABP-actin interface. These studies provided one potential resolution to the apparent contradiction between biochemical studies demonstrating the cadherin-associated α-catenin population lacks F-actin binding activity (**Drees et al., 2005**) and cellular studies suggesting α-catenin plays a key role in linking adherens junctions to the cytoskeleton (**Kobielak and Fuchs, 2004**). However, in vivo both vinculin and α-catenin primarily engage contractile actomyosin bundles, whose component actin filaments are constitutively exposed to myosin-generated forces. This led us to hypothesize that force-activated binding to tensed F-actin could also be a key regulatory mechanism at adhesions, suitable for promoting the formation of initial attachments to actomyosin through membrane-anchored ABPs (e.g. the cadherin complex) before the ABP-F-actin interface itself coming under load. Furthermore, it could also serve as a mechanism to enrich soluble ABPs (e.g. the α-catenin dimer) whose binding geometry is fundamentally incompatible with catch-bond formation.

Here using simultaneous optical trapping and confocal fluorescence microscopy, we show that tension on the order of 1 pN across actin filaments directly enhances F-actin binding by human αE-catenin, but not vinculin. Utilizing a novel Total Internal Reflection Fluorescence (TIRF) microscopy in vitro reconstitution assay, we further show that physiological forces generated by myosin motor proteins activate α-catenin F-actin binding. Approximately 3 Å resolution cryo-EM structures of both proteins bound to F-actin (to our knowledge, the highest-resolution structures of ABP-F-actin complexes reported to date) reveal they share an overlapping major actin-binding site. However, they undergo markedly different rearrangements at their flexible N- and C-termini upon binding, resulting in distinct contacts mediated by their C-terminal extensions (CTEs) which re-fold on the actin surface. Truncating α-catenin's CTE results in constitutive strong F-actin binding regardless of force, and a chimeric construct of vinculin featuring α-catenin's CTE gains force-activated binding, demonstrating the α-catenin CTE to be a modular 'force-detector' which negatively regulates low-force binding. Together, our studies indicate piconewton force on F-actin can be discriminated by flexible elements in ABPs to mediate direct force-activated binding.

Results

Piconewton tension across individual actin filaments directly activates binding by α-catenin

To determine whether the actin-binding activity of vinculin or α-catenin could be regulated solely by force across F-actin, we performed correlative force and fluorescence measurements with a commercial instrument (**Hashemi Shabestari et al., 2017**) that combines dual-trap optical tweezers and confocal fluorescence microscopy (**Figure 1A**). In these experiments, Alexa-555 phalloidin-stabilized biotinylated actin filaments were captured from a laminar stream across a microfluidic flow-cell between two optically trapped streptavidin-coated beads. Tethered filaments were then transferred

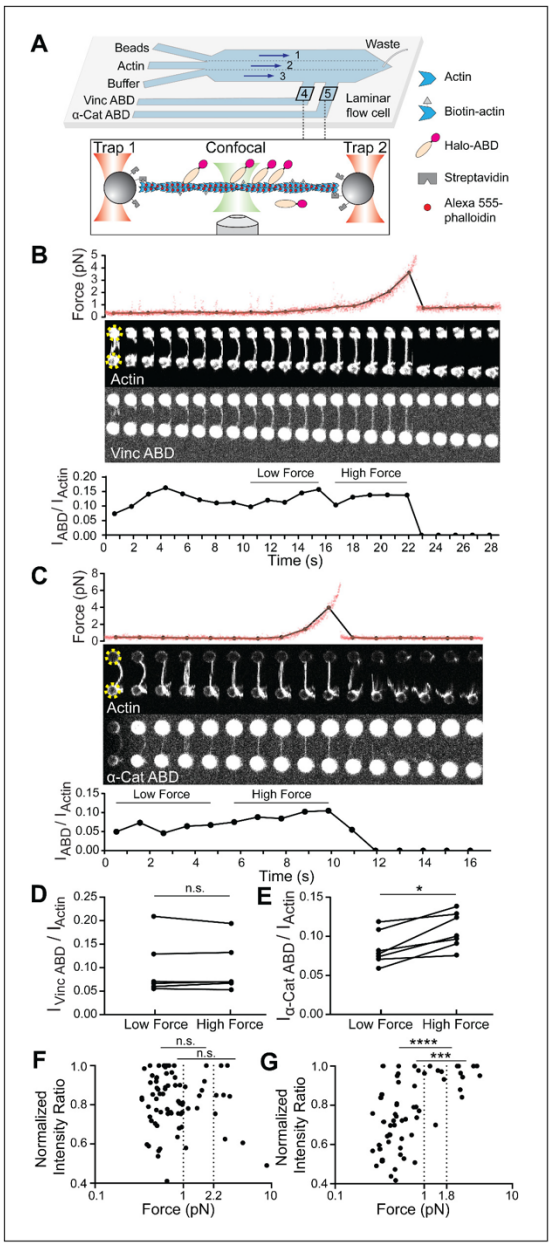

Figure 1. Piconewton load across individual filaments activates α-catenin binding, while vinculin is force insensitive. (**A**) Top: Geometry of the microfluidic chamber. Bottom: Cartoon of correlative single-filament force and fluorescence assay. (**B and C**) Representative single-filament constant velocity pulling experiments (0.1 μm/s) for vinculin ABD (**B**) and α-catenin ABD (**C**). Top: Force versus time plot. Red dots, raw data; black dots, force

Figure 1 continued on next page

Figure 1 continued

values binned to an interval of confocal frames. Middle: Montage of confocal frames of actin and ABD channels. Positions of beads are indicated with yellow circles (diameter, 4 μm). Bottom: I_{ABD}/I_{actin} ratio versus time plot. High-force: Average of five intensity ratios before actin breakage; low-force: average of five intensity ratios immediately before high-force average. Concentration of vinculin ABD or α-catenin ABD: 2 μM. (**D and E**) Paired analysis of low-force and high-force averages across trials for vinculin ABD (**D**) (N = 6, p=0.84) and α-catenin ABD (**E**) (N = 7, p=0.0156). Wilcoxon signed-rank test: *p<0.05; n.s. (not significant), p>0.05. (**F and G**) Scatter plots of normalized fluorescence ratios versus force. Statistical comparisons are between intensity ratios divided into two bins: force below and above 1 pN or 2.2 pN (dotted lines) for vinculin ABD (**F**) (1 pN: below: n = 62, above: n = 20, p=0.65; 2.2 pN: below: n = 72, above: n = 10, p=0.74), and force below and above 1 pN or 1.8 pN (dotted lines) for α-catenin ABD (**G**) (1pN: below: n = 53, above: n = 15, p<0.0001; 1.8 pN: below: n = 59, above: n = 9, p=0.0002). KS test: ****p<0.0001; ***p<0.001; n.s., p>0.05.

The online version of this article includes the following figure supplement(s) for figure 1:

Figure supplement 1. Multiple sequence alignments of human vinculin and α-catenin isoforms.

Figure supplement 2. Additional analysis of single filament correlative force and fluorescence assays.

to a reservoir containing Halo-tagged ABD labeled with Alexa-488 and subjected to a constant velocity pulling protocol while simultaneously recording confocal movies of both the actin and ABD fluorescence signals.

We frequently observed a monotonic increase in force once a threshold extension was reached, followed by an instantaneous return to baseline (***Figure 1B,C***; ***Figure 1—figure supplement 2A,B***), consistent with resistance from a tether composed of one or more actin filaments extended beyond their resting length (visible as straightening in the actin fluorescence channel) followed by force-induced breakage. To correlate force with ABD binding, we calculated the background-subtracted ratio of the ABD fluorescence intensity to the actin intensity (which we refer to as 'I_{ABD}/I_{actin}') in each frame of the confocal movies (Materials and methods; ***Figure 1B,C***, bottom), as well as the corresponding average force during frame acquisition (***Figure 1B,C***, top, black connected points). Apparent binding by the vinculin ABD fluctuated and did not change in response to load during individual pulling trajectories (***Figure 1B***), consistent with a previous report that mechanical stimulation does not promote cytoskeletal localization of vinculin in cells (***Schiffhauer et al., 2016***). However, we observed an apparent steady increase in binding along individual tethers by the α-catenin ABD (***Figure 1C***), consistent with force-activated binding. To quantify this phenomenon, due to the inherent fluctuations of individual I_{ABD}/I_{actin} traces in this assay (potentially due to dynamic changes in ABD binding density along individual tethers and instability in the focus during confocal imaging), we first focused our analysis on a subset of long-lived tethers which featured at least 10 frames. We examined the difference between a 'high-force' average, defined as the mean I_{ABD}/I_{actin} value from the five frames before the final tether rupture, and a 'low-force' average, defined as the mean I_{ABD}/I_{actin} value from the five preceding frames during each recording (***Figure 1B,C***). Paired analysis of low-force/high force averages (Materials and methods) showed a significant increase consistent with force-activated binding only by the α-catenin ABD (***Figure 1D and E***; ***Figure 1—figure supplement 2A***).

Next, we sought to determine the impacts of force on ABD binding at the level of individual actin filaments. As our tether assembly procedure captures filaments from solution, in principle each tether could be composed of a single filament or multiple filaments. We thus elaborated the possible multi-filament tether configurations and designed a series of criteria to identify and exclude them from the analysis. The first plausible multi-filament tether configuration (1) is composed of multiple filaments of different lengths, all attached to the trapped beads at both ends (***Figure 1—figure supplement 2B***), which we identified by the presence of multiple breaking peaks in the force curve, generated as the shortest remaining filament in the tether reaches full extension then ruptures (***Figure 1—figure supplement 2B***). The next plausible configuration (2) is multiple filaments of different lengths, not all of which are attached at both ends (***Figure 1—figure supplement 2C***), which we identified by fluorescence line scans of the actin intensity, where we observe step-like reductions which we interpret to correspond to the ends of non-bridging filaments (***Figure 1—figure supplement 2C***). The third and final configuration (3), composed of multiple filaments, all of essentially

identical length and attached at both ends (***Figure 1—figure supplement 2D***), is the most difficult to rigorously identify. We observed significant heterogeneity in the raw actin fluorescence intensity values between tethers (potentially due to slight differences in focus), with no significant difference between configuration one tethers and those featuring a single rupture force peak (data not shown), suggesting raw actin intensity cannot be used as a proxy for filament number. We thus analyzed the distribution of final breaking forces for all trials (pooling data collected in the presence of both the α-catenin and vinculin ABD), reasoning that configuration three tethers composed of multiple fully-extended actin filaments in parallel at the final break would generally rupture at higher forces. Consistent with this prediction, we observed a single major peak in the breaking force distribution centered at ~6 pN, which is likely to primarily consist of single filaments, as well as a long tail of ≥16.5 pN breaking forces, which we interpret to primarily encompass configuration three tethers. We thus additionally excluded all tethers with ≥16.5 pN breaking force from further analysis.

Based on these criteria, only 21 tethers (11 vinculin ABD and 10 α-catenin ABD) out of 183 total trials were included. This subset very likely predominantly contains tethers composed of single filaments. Consistent with the expected relative fragility of single-filament tethers with low breaking forces, most of these recordings only contained a limited number of frames, precluding quantification of force-dependent binding changes in individual tethers. We thus instead examined the relationship between force magnitude and ABD binding by pooling our recordings for each protein and plotting normalized I_{ABD}/I_{actin} versus force (***Figure 1F,G***). This analysis revealed no apparent correlation between vinculin ABD binding and force (***Figure 1F***). However, the α-catenin ABD plot showed an apparent step-like transition from force-uncorrelated binding to consistent strong binding above a threshold force of approximately 1 pN (***Figure 1G***).

To quantify this phenomenon, we initially examined the distribution of intensity ratios above and below the subjectively identified 1 pN threshold, finding a significant difference only for the α-catenin ABD (***Figure 1F,G***). To objectively define the threshold force, we performed K-means clustering analysis (Materials and methods) which revealed that the α-catenin ABD force-fluorescence distribution could be optimally divided into two clusters with a threshold force of 1.8 pN. We found that the intensity ratios were also significantly different between these clusters (***Figure 1G***). Although there was no obvious correlation between force and binding by the vinculin ABD, as a control we nevertheless used K-means to divide the data into two clusters, which separated at a threshold force of 2.2 pN. Consistent with the lack of a force-binding correlation for the vinculin ABD, we find no significant difference between the distribution of intensity ratios in these two clusters (***Figure 1F***). This analysis, which is insensitive to the exact force threshold employed, supports a force-dependent increase in F-actin binding only for the α-catenin ABD. Collectively, these data suggest that piconewton-level tensile force along individual actin filaments is sufficient to activate α-catenin's F-actin binding.

Physiological forces generated by myosin motors activate F-actin binding by α-catenin

As ~1 pN is the magnitude of force generated by individual myosin motor domains (***Finer et al., 1994***), we hypothesized α-catenin's F-actin binding would also be enhanced by physiological forces generated by myosins. To test this hypothesis, we developed a novel adaptation of the gliding filament assay (***Kron and Spudich, 1986***) to apply force to filaments mimicking actomyosin contractility in vivo (***Figure 2A***). In our preparation, plus-end directed myosin V motor proteins and minus-end directed myosin VI motor proteins are randomly surface-immobilized inside a flow chamber assembled on a cover glass for TIRF, resulting in a configuration where the motors are poised to engage in tug-of-war along non-stabilized, rhodamine-labeled actin filaments. A Halo-tagged, JF-646 (***Grimm et al., 2015***) labeled ABD is then flowed into the chamber in the absence of ATP, and a 2-color TIRF movie is recorded to visualize the basal level of actin binding when filaments are anchored by the rigor-state motors. The ABD is then re-introduced into the same chamber in the presence of ATP to activate the motors, and a second movie is recorded to visualize binding in the presence of force generation. Visual inspection of -ATP/+ATP TIRF movie pairs for the vinculin and α-catenin ABDs suggest they respond to motor-generated forces on F-actin distinctly. Actin localization of the vinculin ABD did not change in response to motor activity (***Figure 2B***; ***Figure 2—video 1***); however, α-catenin ABD's actin localization was enhanced upon motor activation, indicative of force-activated actin binding (***Figure 2C***; ***Figure 2—video 2***).

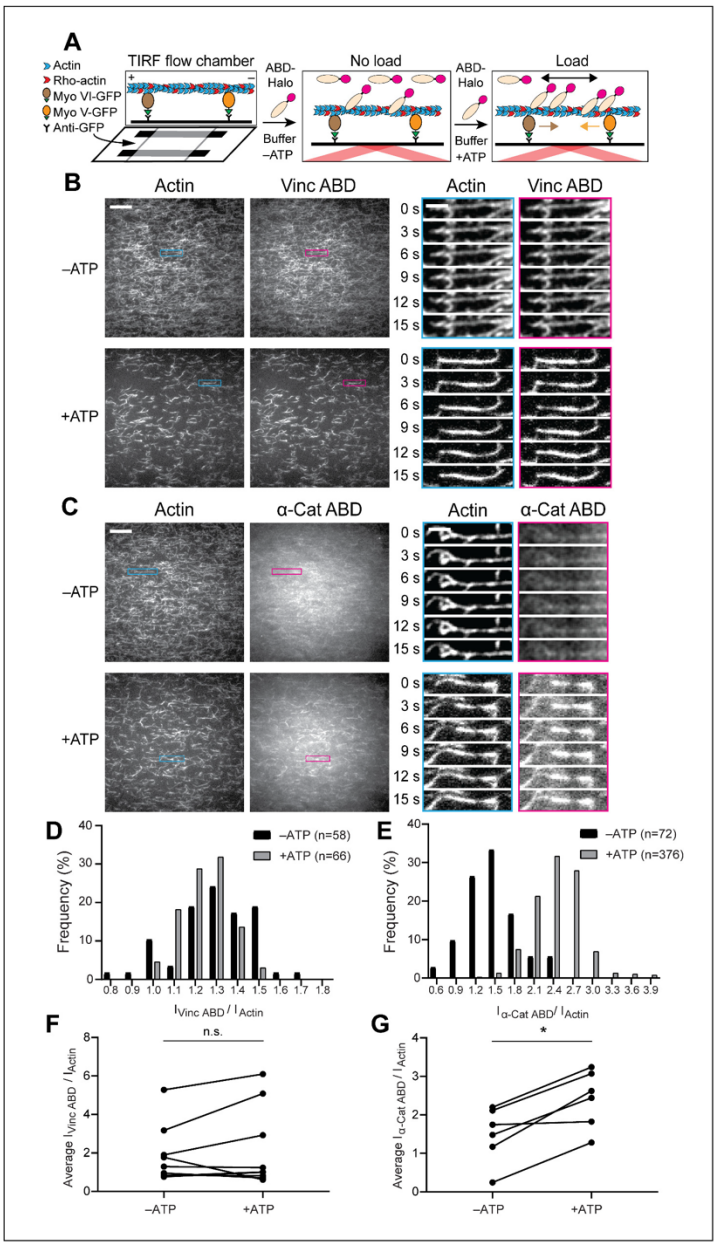

Figure 2. Forces generated by myosin motors activate α-catenin binding to F-actin. (**A**) Cartoon of TIRF force reconstitution assay utilizing surface-anchored myosin motor proteins with opposing directionality. (**B and C**) TIRF assays of vinculin ABD (**B**) and α-catenin ABD (**C**). Left: Representative movie frames of actin and ABD channels in the absence (top) and presence (bottom) of ATP to activate motors. Scale bar, 20 µm. Right: Montages of individual filament regions. Scale bar, 5 µm. Concentration of vinculin ABD or α-catenin ABD: 2 µM. (**D and E**) Time-averaged I_{ABD}/I_{actin} intensity ratio

Figure 2 continued on next page

Figure 2 continued

distributions of filament regions before and after ATP addition for vinculin ABD (D, quantification of (**B**)) and α-catenin ABD (**E**, quantification of (**C**)). (**F and G**) Paired analysis of the overall average intensity ratio change before and after ATP addition for vinculin ABD (**F**) (N = 9, p=0.50) and α-catenin ABD (**G**) (N = 6, p=0.031). Wilcoxon signed-rank test: *p<0.05; n.s. (not significant), p>0.05.

The online version of this article includes the following video and figure supplement(s) for figure 2:

Figure supplement 1. Workflow of TIRF data quantification, additional intensity ratio distributions of single-filament regions for WT α-catenin and vinculin ABDs, and TIRF assays with the metavinculin ABD.

Figure supplement 2. Single motors do not activate actin binding by the vinculin or α-catenin ABD.

Figure supplement 3. Additional analysis of TIRF assays.

Figure 2—video 1. TIRF force reconstitution assay of wild-type vinculin ABD.
https://elifesciences.org/articles/62514#fig2video1

Figure 2—video 2. TIRF force reconstitution assay of wild-type α-catenin ABD.
https://elifesciences.org/articles/62514#fig2video2

Figure 2—video 3. TIRF force reconstitution assay (myosin V only) of wild-type vinculin ABD.
https://elifesciences.org/articles/62514#fig2video3

Figure 2—video 4. TIRF force reconstitution assay (myosin V only) of wild-type α-catenin ABD.
https://elifesciences.org/articles/62514#fig2video4

Figure 2—video 5. TIRF force reconstitution assay (myosin VI only) of wild-type vinculin ABD.
https://elifesciences.org/articles/62514#fig2video5

Figure 2—video 6. TIRF force reconstitution assay (myosin VI only) of wild-type α-catenin ABD.
https://elifesciences.org/articles/62514#fig2video6

As we expected the random deposition and inherent stochasticity of molecular motors in our assay to give rise to a distribution of forces and ABD binding states, we implemented an image analysis procedure to quantify ABD association by automatically identifying and tracking tens to hundreds of 'filament regions' through time (Materials and methods, ***Figure 2—figure supplement 1A***). For each region, I_{ABD}/I_{actin} was calculated in each frame, then averaged over all frames in which the region was detected. Consistent with our qualitative interpretation, histograms of I_{ABD}/I_{actin} distributions before and after ATP addition to individual flow chambers showed no shift for the vinculin ABD (***Figure 2D***, ***Figure 2—figure supplement 1B***). However, this analysis demonstrated a clear shift toward higher values upon ATP addition for the α-catenin ABD, supporting force-activated binding (***Figure 1E***, ***Figure 2—figure supplement 1B***). While the reported trends were consistent across experiments for both ABDs, we nevertheless observed variability between trials (***Figure 2—figure supplement 1B***), potentially due to differences in the background intensities in both channels resulting from inconsistencies in cover-glass surface preparation (Materials and methods). We thus performed paired analysis of the mean I_{ABD}/I_{actin} between the -ATP/+ATP conditions for each chamber (***Figure 2F and G***), which demonstrated a significant increase only for the α-catenin ABD (***Figure 2G***).

Our optical-trapping experiments suggest that force along individual filaments is sufficient to activate α-catenin binding. However, in the cellular context, both α-catenin and vinculin primarily engage actin-myosin bundles. In our TIRF assay, visual inspection supports increased F-actin bundling by both vinculin and α-catenin upon motor activation (***Figure 2B and C***), presumably due to motility facilitating encounters between filaments. Although I_{ABD}/I_{actin} measurements are internally normalized for the local density of F-actin in each region, we are aware that inter-filament ABD bundling contacts could in principle enhance apparent binding. Additionally, while the ATP-dependence of this enhanced F-actin binding strongly suggests it is activated by force, allosteric remodeling of actin filament structure due to local deformations imposed by motor binding could also potentially contribute (***Gurel et al., 2017***). To decouple these effects, we performed assays in the presence of individual motors. In the presence of both myosin V alone (***Figure 2—figure supplement 2***, ***Figure 2—video 3*** and ***Figure 2—video 4***) and myosin VI alone (***Figure 2—figure supplement 2***, ***Figure 2—video 5*** and ***Figure 2—video 6***) we observe ATP-dependent formation of bundles. However, we observe no significant increase in apparent vinculin ABD or α-catenin ABD binding in either condition. This strongly suggests that force-activated

α-catenin ABD binding is dependent upon the tug-of-war between motors of opposed directionality, mimicking the forces generated by bi-polar myosin II filaments in vivo.

We note that forces generated by the randomly distributed force generators in the dual-motor assay are complex, and can in principle include tension, compression, and torsional forces (***Beausang et al., 2008***; ***Sun et al., 2007***). While our optical trapping studies suggest tensile forces are sufficient to activate α-catenin ABD binding (***Figure 1***), future studies will be required to explicitly dissect the contribution of compression and torsion in the presence of myosin motors.

Additionally, we note that there are caveats associated with our TIRF experiments. First, the relatively low apparent affinity of our α-catenin ABD construct in this assay necessitates utilizing a high working concentration. The commensurate high fluorescence background is refractory to definitively measuring the intensity level constituting F-actin binding saturation in the absence or presence of force generation. This limits our ability to establish the binding stoichiometry range in which force-activated actin binding occurs, which has the potential to constrain or discriminate between plausible molecular mechanisms (see Discussion). In contemporary studies, Xu and colleagues have reported a series of α-catenin ABD N-terminal deletion constructs with substantially increased F-actin affinity in the absence of force, notably a construct consisting of residues 698–906, which boosts affinity ~18-fold (***Xu et al., 2020***). Presuming this construct maintains force-activated binding activity, it may be a useful tool to dissect the impact of α-catenin's binding stoichiometry. Second, due to the strong propensity of the α-catenin ABD to bundle actin filaments in our TIRF experiments, it remains to be conclusively determined if myosin motor activity can also activate α-catenin binding along single filaments. It may be possible to achieve a sufficiently low surface density of actin filaments to avoid bundling in the dual-motor assay in presence of the actin stabilizing drug phalloidin, which would enable probing α-catenin's association with individual actin filaments in the presence of active force generation. We will pursue these studies, and their outcome will be presented in a follow-up report.

Regardless, the data we present here collectively suggest physiological forces generated by myosin motor proteins in an appropriate configuration can directly activate α-catenin binding to F-actin, and that force-activated α-catenin binding also occurs in the context of actin bundles, the primary cytoskeletal architecture engaged by the protein in vivo.

Cryo-EM structures of the metavinculin ABD-F-actin and α-catenin ABD-F-actin complexes

Hypothesizing that differences in the F-actin-binding interfaces of vinculin and α-catenin could underlie their differential force-activated actin binding, we pursued structural studies of both ABDs bound to F-actin with cryo-EM (***Figure 3***; ***Figure 3—figure supplement 1***; ***Table 1***). As optimizing the density of fully-decorated, well-separated individual filaments in cryo-EM images is a major bottleneck for single-particle analysis of F-actin-ABP complexes, we chose to use the ABD of the vinculin splice variant metavinculin for these studies, where a 68 amino-acid insert displaces the H1 helix and replaces it with helix H1′, producing a protein which retains actin binding but completely loses actin bundling activity (***Janssen et al., 2012***; ***Kim et al., 2016***; ***Oztug Durer et al., 2015***; ***Figure 1—figure supplement 1B***). Previous studies have suggested these isoforms engage an essentially identical site on the F-actin surface with equivalent affinity (***Janssen et al., 2012***; ***Kim et al., 2016***), and we further found the metavinculin ABD lacks force-activated actin-binding activity in our TIRF assay, validating its use in these studies (***Figure 2—figure supplement 1C,D***). We were able to obtain fields of individual decorated filaments using this construct (***Figure 3A***, top). After careful optimization (Materials and methods), we were also able to acquire cryo-EM images of filaments decorated with the α-catenin ABD (***Figure 3A***, bottom), although persistent bundling by this construct necessitated the collection of substantially more images to obtain a sufficient dataset of individual segments to obtain a high-resolution reconstruction (***Table 1***; ***Figure 3—figure supplement 1***).

Using the Iterative Helical Real Space Reconstruction (IHRSR) approach (***Egelman, 2007***) as implemented in Relion 3.0 (***He and Scheres, 2017***; ***Zivanov et al., 2018***; Materials and methods, ***Figure 3—figure supplement 1***), we obtained reconstructions of the metavinculin ABD (residues 879–1134)–F-actin complex (***Figure 3B***, left) at 2.9 Å overall resolution (***Figure 3—figure supplement 1***) and the α-catenin ABD (residues 664–906)–F-actin complex (***Figure 3B***, right) at 3.2 Å overall resolution (***Figure 3—figure supplement 1***). As local resolutions ranged from 2.7 Å to 3.6 Å,

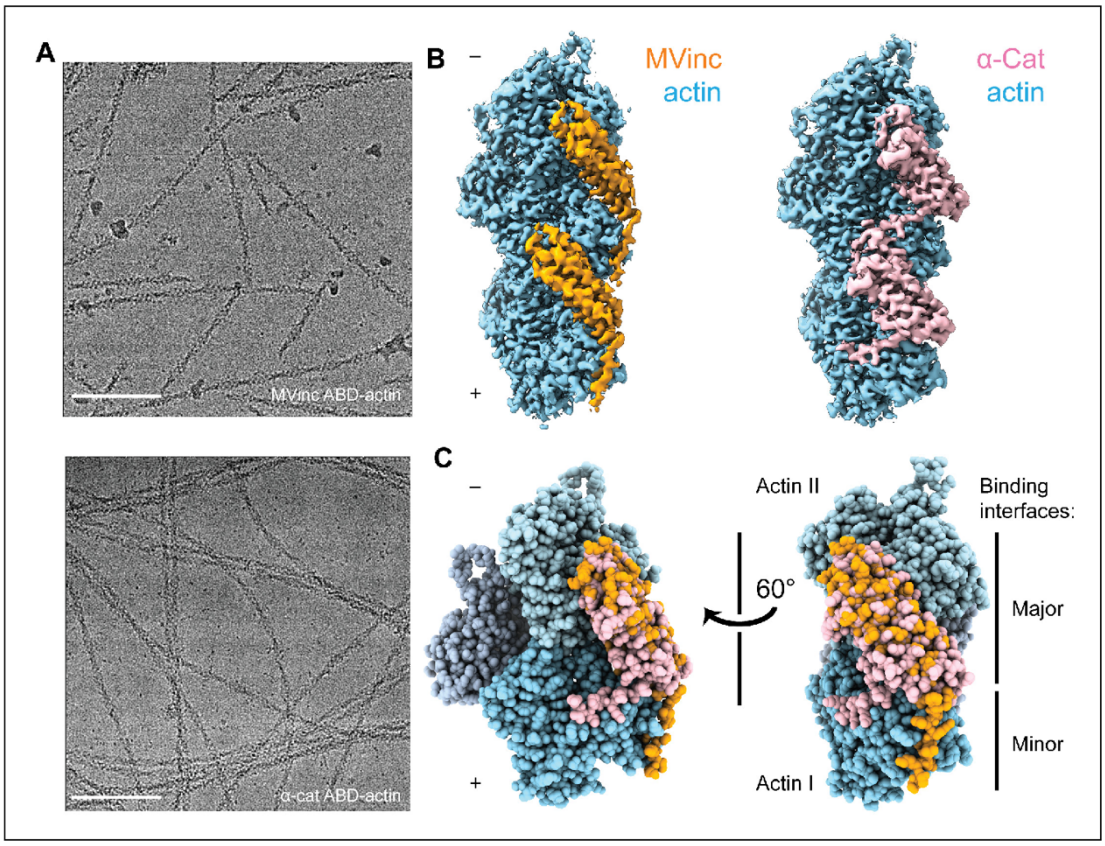

Figure 3. Cryo-EM structures of metavinculin and α-catenin–F-actin complexes. (**A**) Representative cryo-EM micrographs of F-actin decorated with metavinculin ABD (top) and α-catenin ABD (bottom). Scale bars, 100 nm. (**B**) Segmented regions of reconstructed density maps of F-actin decorated with metavinculin ABD (left) and α-catenin ABD (right), colored as indicated. (**C**) Overlay of the metavinculin ABD-actin complex and α-catenin ABD-actin complex atomic models, superimposed on actin and colored as in (**B**). Actin subunits from the α-catenin structure are displayed in varying shades.
The online version of this article includes the following figure supplement(s) for figure 3:

Figure supplement 1. Cryo-EM data processing workflow and 3D reconstruction analysis.

radially decaying outward from the helical axis (***Figure 3—figure supplement 1C,D***) for both reconstructions, atomic models for the complete sequence of Mg-ADP α-actin and continuous segments of ABD residues 981–1131 for metavinculin (***Figure 3C***) and 699–871 for α-catenin (***Figure 3C***) were built and refined into the maps (***Figure 3—figure supplement 1***). In their contemporary work, Xu and colleagues also reported a 3.6 Å resolution cryo-EM reconstruction of the α-catenin ABD bound to F-actin (***Xu et al., 2020***), which shows a highly similar conformation of the complex to that presented here (actin, 0.5 Å RMSD; α-catenin residues 711–842, corresponding to helices H2–H5, 1.0 Å RMSD).

Superposition of the actin-bound metavinculin ABD with the full-length vinculin crystal structure (***Bakolitsa et al., 2004***) confirms that actin binding by both vinculin isoforms is auto-inhibited by intramolecular interactions between the N-terminal head and C-terminal ABD tail

Table 1. Cryo-EM data collection, refinement, and validation statistics.

	Metavinculin ABD–F-actin (EMDB-20844, PDB 6UPW)	α-catenin ABD–F-actin (EMDB-20843, PDB 6UPV)
Data collection and processing		
Microscope	Titan Krios	Titan Krios
Voltage (kV)	300	300
Detector	K2 Summit	K2 Summit
Magnification	29,000	29,000
Electron exposure ($e^-/Å^2$)	60	60
Exposure rate (e^-/pixel/ s)	6	6
Calibrated pixel size (Å)	1.03	1.03
Defocus range (μm)	–1.5 to –3.5	–1.5 to –3.5
Helical symmetry	C1	C1
	27.06 Å rise	27.03 Å rise
	−167.07° twist	−166.88° twist
Initial filament segments (no.)	237,503	540,533
Final filament segments (no.)	215,369	414,486
Map resolution (Å)	2.94	3.24
FSC threshold	0.143	0.143
Refinement		
Initial model (PDB ID)	3JBK, 3J8A	4IGG, 3J8A
Model resolution (Å)	2.98	3.28
FSC threshold	0.5	0.5
Map sharpening B factor ($Å^2$)	–58	–85
Model composition	5 actin protomers, 2 actin-binding domains	
Non-hydrogen atoms	16,896	17,233
Protein residues	2152	2201
Ligands	5 Mg.ADP	
B factors ($Å^2$)		
Protein	53.41	71.59
Ligand	47.29	56.65
R.M.S. deviations		
Bond lengths (Å)	0.012	0.012
Bond angles (°)	0.860	0.833
Validation		
MolProbity score	1.23	1.33
Clash score	3.32	4.63
Poor rotamers (%)	0.06	0.05
Ramachandran plot		
Favored (%)	97.46	97.56
Allowed (%)	2.54	2.44
Disallowed (%)	0.00	0.00
EMRinger Score	4.40	3.87

domains (*Johnson and Craig, 1995*; *Figure 4—figure supplement 1A,B*), as the head domain clearly clashes with F-actin in the crystallized conformation. Full-length α-catenin was crystallized as an asymmetric 'left-handshake dimer', characterized by differential relative orientations between the head and tail domains of each protomer (*Rangarajan and Izard, 2013*). Comparing the actin-bound α-catenin ABD with both conformers in the asymmetric dimer crystal structure also reveals severe clashes between the α-catenin head and actin (*Figure 4—figure supplement 1C–F*), suggesting that full-length α-catenin must also undergo substantial conformational rearrangements to bind F-actin.

Next, we compared the metavinculin ABD-F-actin and α-catenin ABD-F-actin structures (*Figure 3C*), confirming previous low- and moderate-resolution studies (*Janssen et al., 2006*; *Janssen et al., 2012*; *Kim et al., 2016*; *Thompson et al., 2014*) that both ABDs engage a major site spanning the longitudinal interface of 2 actin protomers, which we term Actin I and Actin II (numbered from the plus end of the filament). In turn, each actin protomer also contacts 2 ABDs, leading to a 1:1 binding stoichiometry at saturation. Our structures establish this region is almost identical between the two ABDs, comprising 2040 Å^2 of buried surface area for the metavinculin ABD and 1920 Å^2 for the α-catenin ABD. However, our high-resolution models also reveal a previously unobserved minor interface for each ABD (confirming a recent computational prediction in the case of metavinculin [*Krokhotin et al., 2019*]), mediated by residues in their flexible C-terminal extensions (CTEs), which are entirely distinct between the two proteins (*Figure 1—figure supplement 1A*).

Differential conformational remodeling is linked to unique features of actin binding

Consistent with our previous medium-resolution structural studies (*Kim et al., 2016*), we find the metavinculin ABD undergoes substantial conformational remodeling upon F-actin engagement, characterized by displacement of helix H1′ from the 5-helix bundle to license a rearrangement of helices H2–H5 to relieve clashes with F-actin (*Figure 4A,B*; *Figure 4—video 1* and *Figure 4—video 2*). N-terminal residues 879–980 are not visible in the map (*Figure 4A*, transparent brown), and are presumably disordered in the actin-bound state, while residues 981–985 (*Figure 4A*, brown) undergo a slight rearrangement, extending helix H2 by 1.5 turns (five residues). Our high-resolution map reveals this contact to be mediated by the (meta)vinculin CTE (*Figure 4*). The CTE is released from its pre-bound position, extending helix H5 by two turns (six residues), then undergoing an approximately 60˚ swing to engage a site along actin subdomain one proximal to H5 (*Figure 4A and B*; *Figure 5—video 1*). Coupled to this transition, helices H2–H5 slightly rearrange to accommodate actin binding and avoid steric clashes (*Figure 4B and C*; *Figure 4—video 2*).

We find that the α-catenin ABD also undergoes an order-to-disorder transition at its N-terminus upon actin binding (*Figure 4A,B*; *Figure 4—video 1*), as no density for residues 664–698, the majority of H0-H1, is present in our map (*Figure 3D*; *Figure 4A,B*; *Figure 4—video 1*), confirming recent reports that this region is important for activating α-catenin's actin engagement (*Ishiyama et al., 2018*; *Xu et al., 2020*). This is accompanied by a twisting rearrangement of helices H2–H4 reminiscent of that found in (meta)vinculin (*Figure 4B*; *Figure 4—video 2*), as well as the extension of H4 by three turns (nine residues) through folding of the H3-H4 loop, to sculpt a major actin-binding interface sterically compatible with the filament (*Figure 4B*; *Figure 4—video 1*). This suggests that N-terminal helix release allosterically coupled to ABD helical-bundle rearrangement is a fundamentally conserved mechanistic feature of actin binding by members of the vinculin/α-catenin family. However, we observe distinct rearrangements in the α-catenin CTE, which undergoes a slight lateral shift and helical unfurling, rather than a swing, to engage a site spanning a different surface of actin subdomain 1 (*Figure 4A and B*; *Figure 5—video 1*).

Metavinculin H5 extension is facilitated by binding interactions with Actin I (*Figure 5A,B*; *Figure 5—video 1*), notably a hydrophobic interaction between metavinculin I1114 and Actin Y91, and a salt bridge between metavinculin R1117 and actin E100. This positions the CTE to form an extended interface with actin subdomain 1, contiguous with that mediated by H5, with metavinculin W1126 buried in a proximal hydrophobic pocket formed by actin residues A7, P102, P130, A131, and W356, bolstered by a distal salt bridge between metavinculin R1128 and actin E361 (*Figure 5B*). By contrast, the α-catenin CTE retains an overall conformation similar to its pre-bound state (*Figure 5A and C*; *Figure 5—video 1*). An extensive hydrophobic network we term a

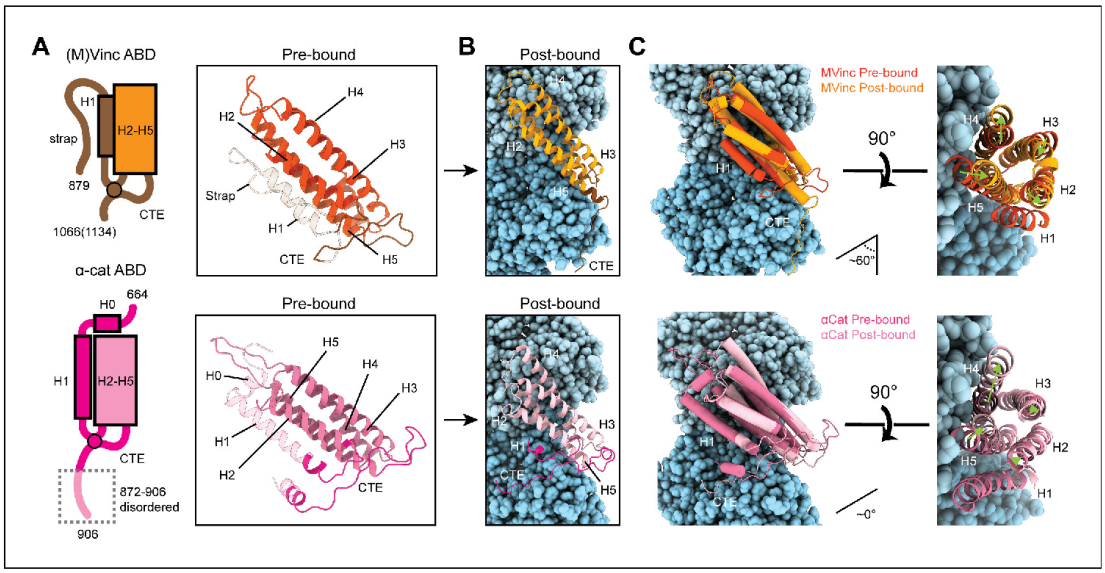

Figure 4. Major ABD conformational rearrangements upon actin binding. (**A**) Cartoons and crystal structures of pre-bound (meta)vinculin ABD (PDB 1st6, dark orange, top) and α-catenin ABD (PDB 4igg chain B, dark pink, bottom). Regions that undergo major rearrangements are highlighted in brown (metavinculin) or magenta (α-catenin); regions not resolved in the actin-bound cryo-EM structures are transparent. (**B**) Cryo-EM structures of metavinculin ABD (orange, top) and α-catenin ABD (pink, bottom). Flexible regions colored as in (**A**); actin, shades of blue. (**C**) Superimposed pre-bound and post-bound structures of metavinculin ABD (top) and α-catenin ABD (bottom). Green arrows indicate displacement of helices; rotation angles indicate repositioning of C-terminal extensions (CTEs).

The online version of this article includes the following video and figure supplement(s) for figure 4:

Figure supplement 1. (Meta)vinculin and α-catenin activation mechanisms.

Figure 4—video 1. Overall conformational changes in ABDs upon actin binding.

https://elifesciences.org/articles/62514#fig4video1

Figure 4—video 2. Rearrangements in the helical bundle regions of ABDs upon actin binding.

https://elifesciences.org/articles/62514#fig4video2

'tryptophan latch' embraces CTE residue W859 in both pre-bound and post-bound states, preventing α-catenin CTE unfurling (***Figure 5C***, right; ***Figure 5—video 1***). A single turn of helix H1 on the N-terminal side of the ABD remains folded, with H1 residue W705 packing against CTE residue M861, encircling W859 along with CTE residues L852 and L854, as well as residues W705, I712, I763, L776, P768, V833, and Y837 from neighboring regions of the helical bundle, facilitating coordinated conformational transitions between the N- and C-terminal flexible regions of the α-catenin ABD upon actin binding. A putative hydrogen bond is also maintained between S840 and the single nitrogen atom in W859's indole ring, maximizing the binding potential of this residue.

The latch positions the neighboring region of the CTE to bind a distinct site on Actin I's subdomain 1 (***Figure 5C***, left; ***Figure 5—video 1***) mediated by proximal salt bridges (α-catenin E865 – actin R28, α-catenin K866 – actin D24/D25, α-catenin K867 – actin E93) and distal hydrophobic interactions (α-catenin L869/V870 – actin P333/Y337). Consistent with a key role for the latch in coordinating conformational transitions that enable F-actin binding, Xu et al. report that mutating W859 to alanine reduces α-catenin's F-actin-binding affinity 10-fold (***Xu et al., 2020***). Superposition of the actin-bound conformation of the α-catenin ABD with the pre-bound conformation of the (meta)vinculin ABD (***Figure 4—figure supplement 1G***) reveals a striking positional overlap between α-catenin W859 and metavinculin W1126 (vinculin W1058 is identically positioned, not shown), which is also

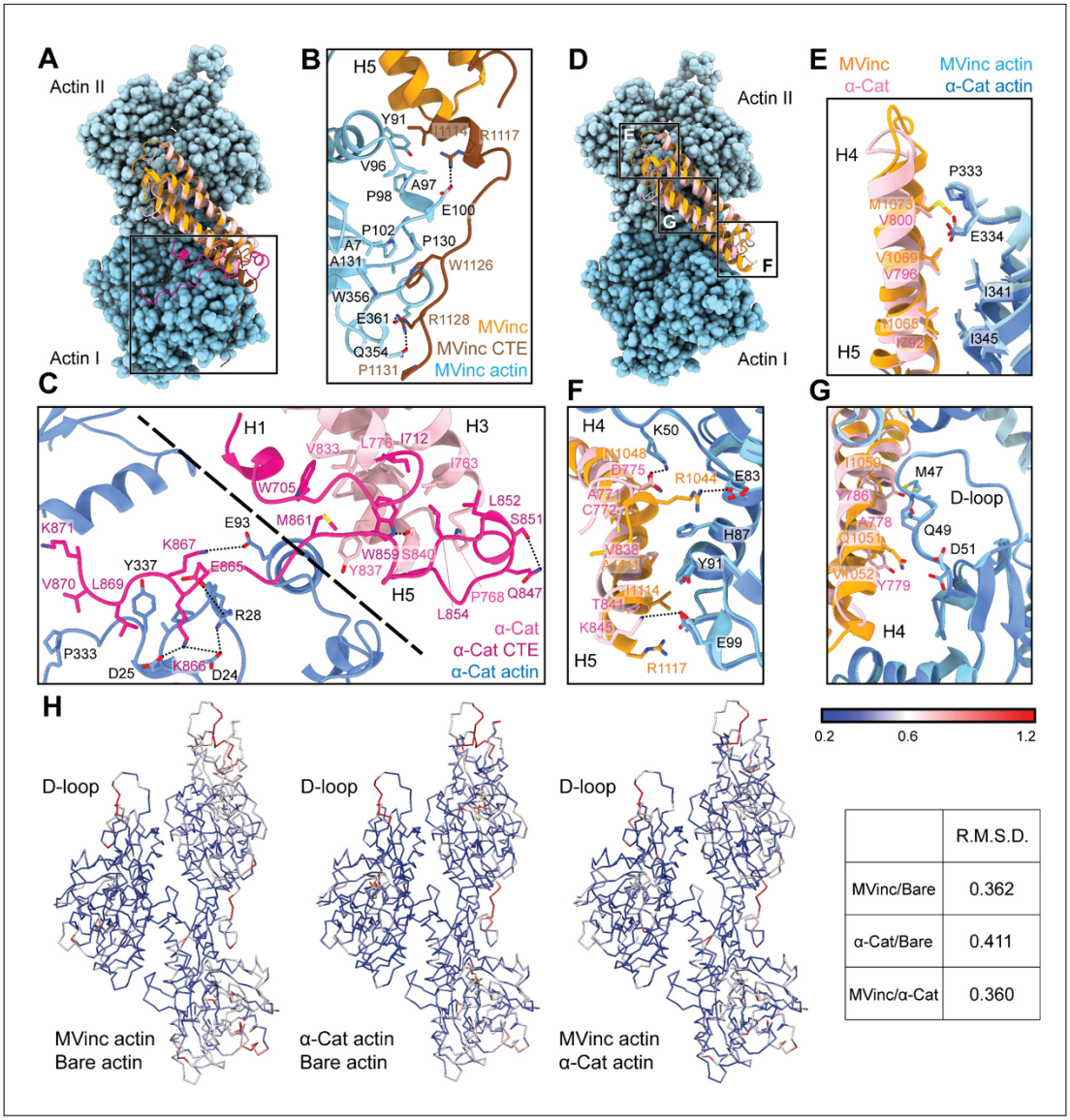

	R.M.S.D.
MVinc/Bare	0.362
α-Cat/Bare	0.411
MVinc/α-Cat	0.360

Figure 5. The actin-binding interfaces of metavinculin and α-catenin. (**A**) Overlay of the metavinculin ABD-actin complex and α-catenin ABD-actin complex atomic models highlighting C-terminal extensions (CTEs) of metavinculin ABD and α-catenin ABD, superimposed on Actin I and colored as in ***Figure 4***. Actins from α-catenin structure are displayed. (**B and C**) Detailed views of key contacts at minor interfaces: metavinculin CTE and actin (**B**); within the α-catenin tryptophan latch (right) and between its CTE and actin (left) (**C**). (**D**) Overlay of the metavinculin ABD-actin complex and α-catenin ABD-actin complex atomic models highlighting helical binding interfaces of metavinculin ABD and α-catenin ABD, superimposed and colored as in (**A**). Actins from α-catenin structure are displayed. (**E, F, and G**) Detailed views of key contacts at the major interface between metavinculin/α-catenin helices H4–H5 and Actin I (**E**); Actin II (**F**); Actin II D-loop (**G**). (**H**) Actin C_α traces colored by per-residue RMSD from the indicated comparisons. For superposition, segmented actin density from the cryo-EM maps was first aligned, followed by fitting the atomic models into their corresponding maps.

Figure 5 continued on next page

Figure 5 continued

The online version of this article includes the following video and figure supplement(s) for figure 5:

Figure supplement 1. TIRF assays for the α-catenin ABD triple mutant which does not bind actin, and putative ABD-ABD contacts along F-actin.
Figure 5—video 1. Detailed views of distinct conformational changes in CTEs.
https://elifesciences.org/articles/62514#fig5video1

engaged by a sparser latch in the pre-bound conformation (***Figure 5—video 1***). We thus speculate the extensive latch of α-catenin prevents W859 release and the extension of its CTE to engage the same site as metavinculin W1126.

Major filament binding interfaces discriminate actin D-loop conformations

The complete non-overlap of the (meta)vinculin and α-catenin minor actin-binding interfaces mediated by their CTEs lead us to hypothesize that the CTEs could be involved in differential force-activated actin binding. To identify other potential contributing structural elements, we undertook a detailed comparison of their major actin-binding interfaces mediated by helices H4–H5 in both proteins (***Figure 5D***). The Actin II binding interface is almost identical between the two ABDs (***Figure 5E***), mediated by an extensive series of conserved hydrophobic contacts: α-catenin I792/metavinculin I1065 – actin I345, α-catenin V796/metavinculin V1069 – actin I341, and α-catenin V800/metavinculin M1073 – actin P333/E334. The Actin I interface, on the other hand, is more variable and characterized by few clear residue-level binding interactions (***Figure 5F***), notably likely weak long-distance salt bridges (metavinculin R1044 – actin E83 and α-catenin K845 – actin E99) specific to each protein, despite the overall shape complementarity across the interface. Each ABD also features a unique hydrophobic interaction with actin Y91 (metavinculin I1114/α-catenin V838).

The Actin I interface extends into contacts with the actin D-loop (***Figure 5G***), a flexible region of actin which mediates structurally polymorphic longitudinal interactions between protomers (***Galkin et al., 2010b***) reported to be modulated by actin nucleotide state (***Chou and Pollard, 2019***; ***Merino et al., 2018***) and ABPs (***Dominguez and Holmes, 2011***; ***Oda et al., 2019***). Both ABDs form a potential weak long-distance interaction with actin D-loop residue K50: in metavinculin, a hydrogen bond through N1048, and in α-catenin, a salt bridge through D775. The D-loop then adopts subtly different conformations between the two interfaces centered at M47. Although clear residue-level binding interactions are not readily apparent, the conformation of M47 at the metavinculin interface would clash with α-catenin Y786, a position occupied by the smaller residue I1059 in metavinculin, suggesting local sterics unique to each ABD determine compatibility with a distinct D-loop conformation. Comparison of the actin conformation observed in a similar-resolution structure of ADP F-actin in isolation ('F-actin alone', M.S. in preparation) versus when bound to metavinculin or α-catenin, as well as comparison of the metavinculin-bound and α-catenin-bound conformations reveals minimal rearrangements throughout the majority of the structure (***Figure 5H***). This contrasts with a previous report of α-catenin-induced structural changes in F-actin inferred from low-resolution cryo-EM analysis (***Hansen et al., 2013***), but it is consistent with the high-resolution studies of ***Xu et al., 2020***. The sole region featuring rearrangements greater than 1 Å RMSD is a 3–4 residue stretch of the D-loop centered on M47. As force across the filament could feasibly modulate D-loop structure to regulate ABP binding, we hypothesized ABD residues mediating D-loop interactions could also mediate differential force-activated actin binding.

The α-catenin C-terminal extension is a force-detector element

To investigate whether D-loop interactions contribute to α-catenin force-activated binding, we designed a triple point-mutant α-catenin ABD construct where three residues in close proximity to the D-loop were replaced by those in vinculin: α-cat ABD$^{A778Q\ Y779V\ Y786I}$. In force reconstitution assays, this construct did not visibly associate with actin in either the –ATP or +ATP condition in the concentration regime accessible by TIRF (***Figure 5—figure supplement 1A***). While these data

suggest that the α-catenin D-loop interactions contribute to overall affinity for F-actin, the complete lack of binding is refractory to determining whether this interface has a separable role in force-activated actin binding.

We thus returned to our initial hypothesis that differential force-activated binding could be mediated by the CTEs. Although we were unable to accurately model the final three residues of the metavinculin CTE, weak density is clearly present (***Figure 5—figure supplement 1B***, red), suggesting the entire CTE engages F-actin. By contrast, density for the α-catenin CTE is only present until K871 (***Figure 5C***; ***Figure 5—figure supplement 1C***). Notably, all three human α-catenin isoforms have highly homologous CTEs that extend an additional 35 amino acids (***Figure 1—figure supplement 1A***), diverging in sequence and length from the vinculin CTE. Consistent with previous primary-structure-function analysis (***Pokutta et al., 2002***) showing that residues after P864, which bear no homology to vinculin, are necessary for actin binding, our structure shows that residues 865–871 are in direct contact with actin (***Figure 5C***; ***Figure 5—video 1***), forming an extensive interface. We therefore hypothesized that distal residues 872–906, a 35-residue element unique to α-catenin (***Figure 1—figure supplement 1A***) that was not resolved in our cryo-EM analysis and is thus presumably conformationally flexible, could uniquely contribute to force-activated actin binding.

To test whether distal residues 872–906 have a separable role in force-activated binding, that is as a 'force detector', we first truncated them from the α-catenin ABD (α-cat ABDΔC). Consistent with a regulatory role for this segment, α-cat ABDΔC constitutively associated with F-actin in TIRF assays (***Figure 6A***; ***Figure 6—figure supplement 1A***; ***Figure 6—video 1***), with no significant increase in binding upon ATP addition, suggesting that this region is necessary for force-activated binding by negatively-regulating low-force binding. This contrasts with the observations of Xu et al., who report a modest (~2-fold) reduction in F-actin-binding affinity when this region is truncated in solution co-sedimentation assays, notably in the background of a construct where H0 has also been truncated in order to boost affinity overall (***Xu et al., 2020***). Possible sources of this discrepancy include differences in α-catenin binding behavior between solution assays and our TIRF assays, where filaments are immobilized. Additionally, coordination between rearrangements in the CTE and H0–H1 (potentially through allosteric mechanisms) may be necessary to mediate the force-detector's negative regulatory effects.

To investigate the sufficiency of the force-detector, we generated chimeric ABDs featuring the H2–H5 bundle region of vinculin and the flexible termini of α-catenin. A vinculin ABD construct where only the CTE was substituted was non-functional (data not shown). However, consistent with structural coordination between the α-catenin N-terminal segment and the CTE through the tryptophan latch (***Figure 5C***; ***Figure 5—video 1***), a construct featuring both the α-catenin N-terminal segment and the CTE (vinc ABD-NCSwap, Materials and methods) gained force-activated binding activity, with diminished low-force binding observed (***Figure 6B***; ***Figure 6—figure supplement 1B***; ***Figure 6—video 2***) in contrast to the wild-type vinculin ABD (***Figure 1B***). A C-terminal truncation of this construct (vinc ABD-NCSwapΔC) equivalent to α-cat ABDΔC reverted to constitutive binding regardless of force (***Figure 6C***; ***Figure 6—figure supplement 1C***; ***Figure 6—video 3***), supporting the α-catenin CTE as the key determinant of force-activated binding, in which 872–906 serves as the force-detector. We thus conclude that the distal C-terminus (residues 872–906) of α-catenin is necessary and sufficient for force-activated actin binding through negative regulation of low-force binding.

Discussion

Our studies reveal that α-catenin preferentially binds tensed F-actin, using its flexible C-terminus to detect piconewton load that can be generated by myosin motors. We propose this force-activated F-actin binding could play an important role in the formation and reinforcement of cell-cell adhesion complexes, facilitating mechanically regulated interactions between α-catenin and actomyosin cables tuned for high sensitivity to motor-generated forces.

We further provide evidence that actin filaments are themselves tension sensors that can transduce mechanical force into regulated partner binding. Our finding that the force-detector element of α-catenin can be functionally transplanted to vinculin demonstrates that force-activated F-actin binding is a modular activity that can be conferred by short sequence motifs. We thus speculate

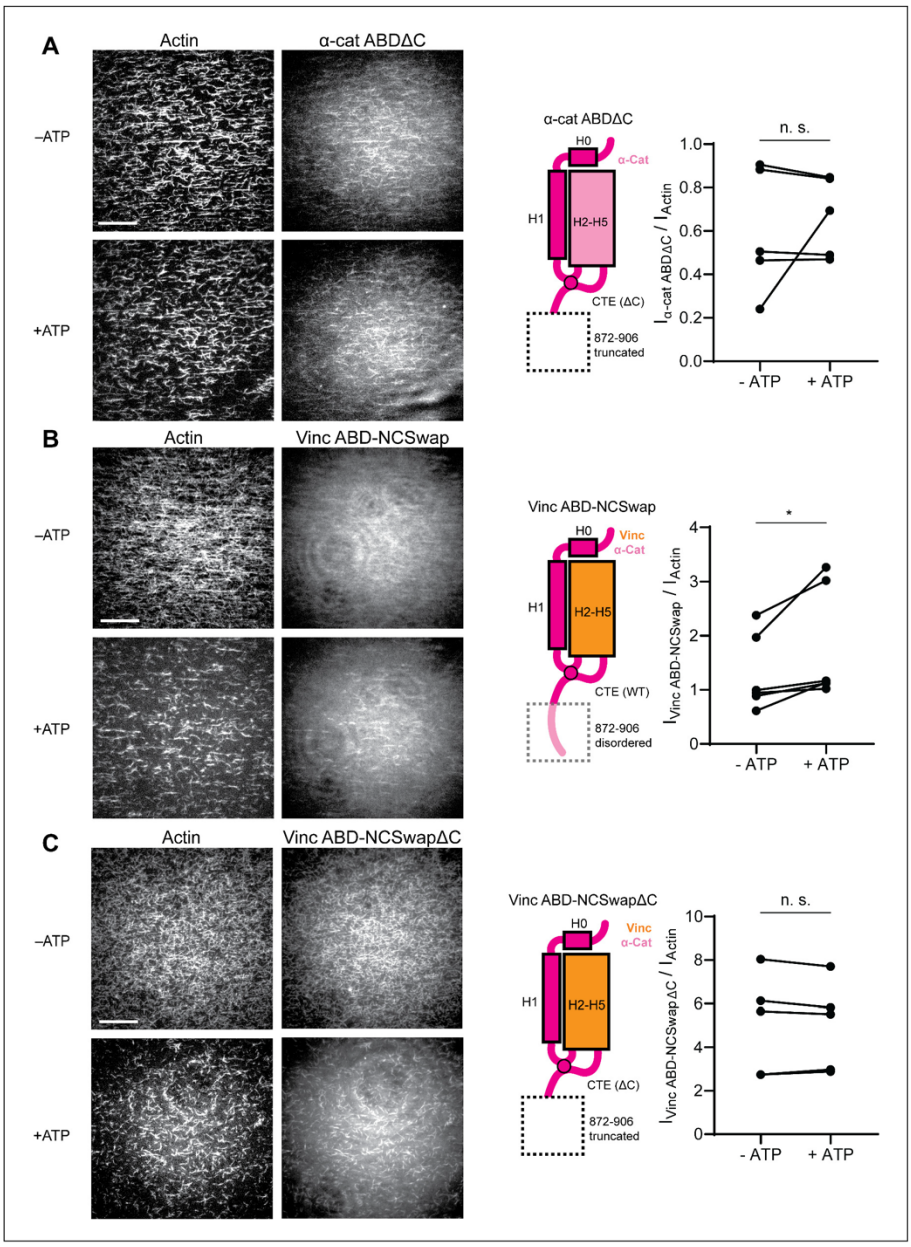

Figure 6. The distal tip of α-catenin's C-terminus is a force detector. (**A, B, and C**) TIRF force reconstitution assays. Left: Representative movie frames in the presence and absence of ATP. Scale bar, 30 μm. Right: Cartoon of ABD construct (left) and paired analysis of the overall intensity ratio change upon ATP addition (right). Wilcoxon signed-rank test: *p<0.05; n.s. (not significant), p>0.05. Constructs assayed were: α-cat ABDΔC (**A**) (αE-catenin$_{664\text{-}871}$,

Figure 6 continued on next page

Figure 6 continued

N = 5, p=0.81); Vinc ABD-NCSwap (**B**) (αE-catenin$_{664-708}$-vinculin$_{916-1041}$-αE-catenin$_{837-906}$, N = 6, p=0.031); Vinc ABD-NCSwapΔC (**C**) (αE-catenin$_{664-708}$-vinculin$_{916-1041}$-αE-catenin$_{837-871}$, N = 5, p=0.63). Concentration of ABD constructs: 2 μM.

The online version of this article includes the following video and figure supplement(s) for figure 6:

Figure supplement 1. Intensity ratio distributions of single-filament regions for α-catenin and vinculin CTE mutants.

Figure 6—video 1. TIRF force reconstitution assay of α-catenin ABDΔC truncation mutant.
https://elifesciences.org/articles/62514#fig6video1

Figure 6—video 2. TIRF force reconstitution assay of Vinc ABD-NCSwap chimera.
https://elifesciences.org/articles/62514#fig6video2

Figure 6—video 3. TIRF force reconstitution assay of Vinc ABD-NCSwapΔC chimera truncation mutant.
https://elifesciences.org/articles/62514#fig6video3

there may be other actin-binding proteins with functionally analogous force-detectors, which could broadly mediate mechanotransduction through the cytoskeleton.

Molecular mechanism for detecting force on actin through a flexible structural element

While our studies pinpoint the final 35 amino acids of α-catenin as a force-detector, the exact molecular mechanism by which this segment negatively regulates low-force binding to F-actin remains to be elucidated. Here we propose two potential, non-exclusive conceptual models for this modulation. As we observe the distal tip of the ordered region of the CTE to be in close apposition to the next ABD binding site along the actin filament, with potential contacts between CTE residues V870 and K871 with the H4–H5 loop and the N-terminal tip of H5 in longitudinally adjacent ABD (***Figure 5—figure supplement 1C***), the first model invokes steric exclusion (***Figure 7A***). In the absence of force, the force-detector (***Figure 6***; ***Figure 7***) physically blocks the adjacent binding site through steric hindrance, which can be relieved by an increase in protomer axial spacing in the presence of tension, consistent with prior truncation studies suggesting residues 884–906 may inhibit α-catenin's actin binding (***Pappas and Rimm, 2006***). As the force-detector likely represents a flexibly tethered conformational ensemble, in the presence of thermal fluctuations we envision this would manifest as a tension-dependent increase of the binding on-rate at the site due to its increased fractional availability. Although saturating the filament for structural studies could lead to non-physiological inter-ABD interactions, cooperative F-actin binding by the α-catenin ABD has previously been reported under non-saturating conditions (***Hansen et al., 2013***), and supplemental soluble ABD enhanced catch-bonding by the cadherin complex (***Buckley et al., 2014***), suggesting communication between actin-bound ABDs is likely to be physiologically relevant. We note that cooperative and inhibitory inter-ABD communication are not a priori mutually exclusive, and the interplay of these opposing effects could produce differential outcomes as a function of ABD concentration and filament load, an important subject for future studies.

The second model invokes a conformational change in the actin protomer that specifically occurs in the presence of mechanical load, which is recognized and preferentially bound by the force-detector, relieving inhibition (***Figure 7B***). Although our studies suggest only minor actin conformational changes when the binding is driven by mass action (***Figure 5H***), they do not rule out as yet unobserved actin conformations specifically evoked by force. Furthermore, while for simplicity we have framed both models in terms of discrete transitions between structural states, low piconewton forces could also modulate the intrinsic structural fluctuations of F-actin to control α-catenin engagement through either mechanism, as has previously been speculated for cofilin (***Galkin et al., 2012***; ***Hayakawa et al., 2011***; ***Wioland et al., 2019***). Although currently technically prohibitive, structural studies of the α-catenin ABD–F-actin interface in the presence of active force generation, as well as supporting functional experiments, will be necessary to dissect the interplay of these models.

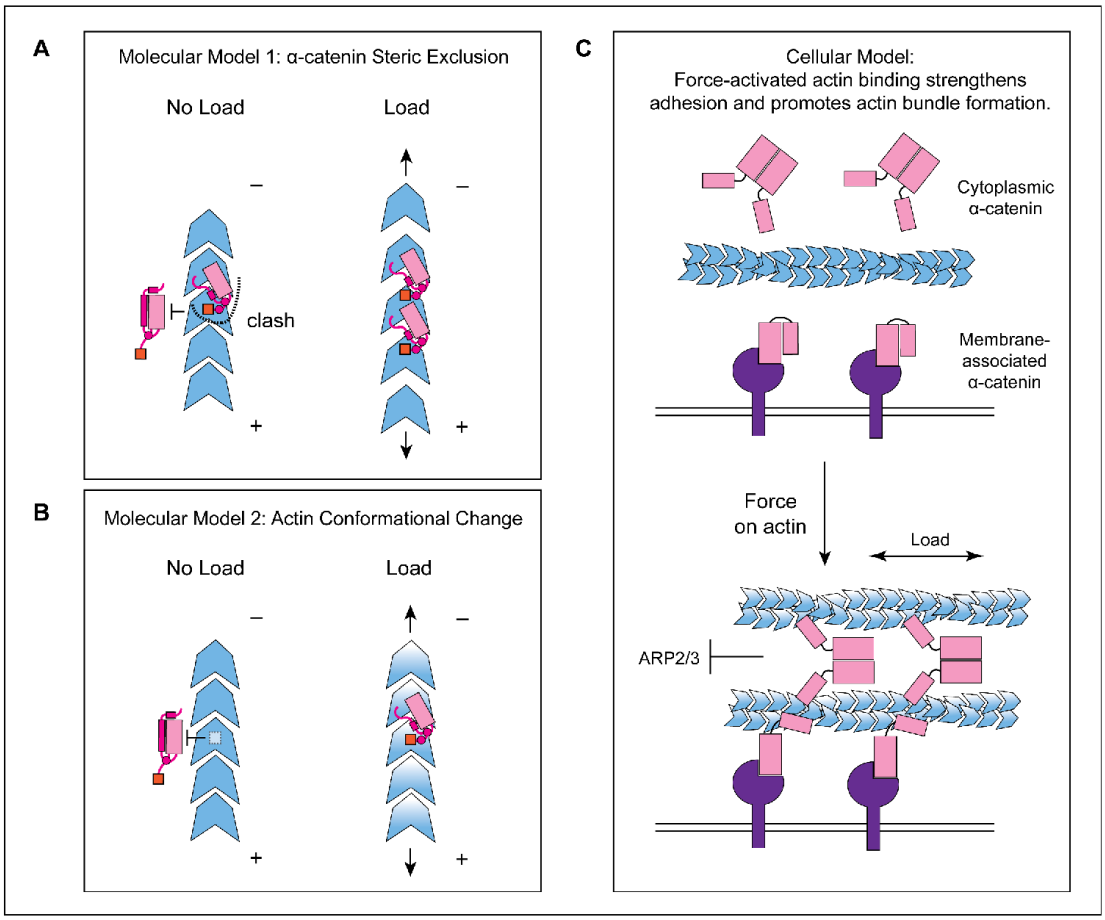

Figure 7. Molecular and cellular mechanisms for force-activated binding by α-catenin. (**A and B**) Cartoons of two conceptual mechanistic models for force-activated actin binding by the α-catenin ABD. Orange box represents the force detector (residues 872–906) at the distal tip of the CTE. Blue gradient represents a force-induced conformational transition in the actin protomer. (**C**) Cartoon of proposed biological functions for force-activated actin binding by the two cellular populations of α-catenin. Membrane-associated cadherin-catenin complexes are illustrated in purple.

Mechanically-regulated adhesion through α-catenin and vinculin

Our finding that approximately 1 pN of tension along individual filaments is sufficient for force-activated binding suggests that the actin-binding interface of α-catenin has been evolutionarily optimized to sense contractile forces generated by myosin motors (***Finer et al., 1994***). We speculate force-activated binding enables the cadherin-catenin complex to recognize and preferentially engage pre-stressed actomyosin cables adjacent to the plasma membrane at adherens junctions (***Figure 7C***), providing a mechanism for initial engagement between actin and the cadherin-associated population of α-catenin, as well as rapidly strengthening adhesion after preliminary attachments are formed. This could facilitate the transition from nascent cell-cell contacts to mature adherens junctions, as punctate nascent adhesions associated with radial actin cables

coalesce and spread along a developing circumferential band of tensed actomyosin bundles (**Vaezi et al., 2002**), as well as support dynamic adherens junction remodeling during epithelial morphodynamics (**Lecuit and Yap, 2015**). It also provides a mechanism for concentrating the soluble, cytoplasmic α-catenin population at sites of cytoskeletal tension (**Figure 7C**). Previous studies have demonstrated this population is enriched on actomyosin bundles linked to adherens junctions, where it suppresses lamellipodium activity and promotes adhesion maturation (**Drees et al., 2005**). While enrichment has been speculated to occur via local release from the cadherin complex, this model is difficult to reconcile with its low cellular concentration and the high concentration of soluble α-catenin required to inhibit Arp2/3-mediated actin branching in vitro (**Drees et al., 2005**). Force-activated binding provides a feasible cellular mechanism for this enrichment of the homodimeric cytoplasmic α-catenin population, driven by enhanced affinity for tensed F-actin rather than mass action effects due to local concentration. Our identification of a functionally separable force-detector in α-catenin with amino-acid level precision will facilitate a detailed examination of these models in cell lines and in vivo.

We note that force-activated binding is an additional, rather than alternative, mechanism to catch-bond formation (**Buckley et al., 2014**) for mechanical regulation of F-actin binding. Our finding that vinculin lacks this activity despite forming catch-bonds with F-actin (**Huang et al., 2017**) strongly suggests that these two modes of mechanical regulation operate by unique structural mechanisms, likely to fulfill distinct biological functions. Vinculin's lack of force-activated actin-binding activity is consistent with the ordered sequence of mechanically-regulated binding events underlying its coordination with α-catenin at adherens junctions, where only after preliminary attachments form through the cadherin complex and come under load is vinculin recruited and activated to bind F-actin (**Yonemura et al., 2010**). The lower force threshold for force-activated binding than catch-bond formation (~1 pN vs. ~10 pN) supports a model in which the formation of initial attachments to the cytoskeleton through the cadherin complex is stimulated through force-activated binding, which is subsequently strengthened by catch-bonding through both α-catenin and vinculin during adhesion maturation.

In their parallel work, Xu et al. speculate that the displacement of H1 from the α-catenin ABD upon actin binding could be stabilized or induced by force (**Xu et al., 2020**), providing a possible structural mechanism for catch-bond formation which we have previously proposed could also be employed by vinculin (**Kim et al., 2016**; **Swaminathan et al., 2017**). This model predicts that the force required to dissociate H1 from the α-catenin ABD should be lower than the force required to displace the ABD in the mechanically-reinforced, strongly bound state from F-actin. It furthermore predicts that the constitutive high F-actin affinity α-catenin ABD construct (residues 711–842) lacking H0-H1 reported by Xu et al., which they propose mimics the strongly-bound state (**Xu et al., 2020**), should no longer form catch bonds with F-actin due to its anticipated inability to switch between weakly and strongly bound states. Thus, this proposed structural mechanistic framework is now well-positioned to be subjected to explicit experimental scrutiny. We believe dissecting the interplay between force-activated binding and catch-bond formation in vitro and in vivo, as well as the structural basis for coordinated actin catch-bonding by α-catenin and vinculin, are important subjects for future studies.

Implications for cytoskeletal mechanotransduction

Our direct observation of force-activated binding to F-actin mediated by a short, flexible sequence element suggests this mechanism could feasibly be employed by other ABPs. Proteins from the large Calponin Homology (CH) domain ABP superfamily have diverse functions as cytoskeletal cross-linkers and plasma membrane/organelle tethers (**Liem, 2016**; **Razinia et al., 2012**). Their ABDs have also been reported to have sequence elements that undergo folding transitions associated with filament engagement (**Avery et al., 2017**; **Galkin et al., 2010a**; **Iwamoto et al., 2018**) which can sterically regulate their actin binding (**Harris et al., 2019**). This suggests members of this family could plausibly employ force-activated binding mechanisms similar to α-catenin to coordinate diverse mechanotransduction pathways throughout the cell, as could other ABPs with similar properties. The experimental strategy established here should be broadly useful for identifying force-sensitive ABPs and defining their force-detector-F-actin interfaces, such as the α-catenin CTE-F-actin interaction, in atomistic detail. This will facilitate elucidating the

molecular and cellular mechanisms of cytoskeletal mechanotransduction with sufficient precision for guiding inhibitor development.

Materials and methods

Key resources table

Reagent type (species) or resource	Designation	Source or reference	Identifiers	Additional information
Recombinant DNA Reagent	pET His-Strep-TEV and pET His-Strep-TEV-Halo vectors	This paper		Ampicillin resistance; expression vectors for *E. coli* Contact Alushin Lab for distribution
Recombinant DNA Reagent	pFastBac Dual Expression Vector	ThermoFisher	10712024	Expression vectors for sf9 insect cells
Gene (*H. sapiens*)	Vinculin; *Hs*VCL isoform 1	Synthesized by Genewiz	UniProt:P18206-2	
Gene (*H. sapiens*)	Metavinculin; *Hs*VCL isoform 2	Synthesized by Genewiz	UniProt:P18206-1	
Gene (*H. sapiens*)	αE-catenin; *Hs*CTNNA1	Addgene # 24194	UniProt:P35221	
Strain, strain background (*E. coli*)	Rosetta2 (DE3)	Novagen	71400–4	*E. coli* strain for protein expression
Cell line (*S. frugiperda*)	Gibco Sf9 insect cell	ThermoFisher	11496015	Insect cell line for protein expression
Transfected construct (*S. frugiperda*)	Gibco Bac-to-Bac Baculovirus Expression System	ThermoFisher	10359016	Insect cell line transfection kit for protein expression
Chemical compound, drug	Halo-tag ligand amine O4	Promega	P6741	Synthetic precursor for the fluorescent dye JF-646-Halo
Chemical compound, drug	JF-646 NHS-ester building block	TOCRIS	6148	Synthetic precursor for the fluorescent dye JF-646-Halo
Chemical compound, drug	HaloTag Alexa Fluor 488 Ligand	Promega	G1001	
Chemical compound, drug	Alexa Fluor 555-Phalloidin	ThermoFisher	A34055	
Biological sample (*O. cuniculus*)	Actin Protein (Rhodamine): Rabbit Skeletal Muscle	Cytoskeleton, Inc	AR05-C	
Biological sample (*O. cuniculus*)	Actin Protein (Biotin): Rabbit Skeletal Muscle	Cytoskeleton, Inc	AB07-C	
Other	Streptavidin Coated Polystyrene Particles	Spherotech	SVP-40–5	Used in optical trapping experiments
Other	C-flat Holey Carbon Grids for TEM - Gold Only	EMS	CF313-100-Au	Used in cryo-EM experiments
Software, algorithm	C-trap viewer	LUMICKS		http://www.nat.vu.nl/~iheller/download.html
Software, algorithm	TWOM viewer	LUMICKS		http://www.nat.vu.nl/~iheller/download.html
Software, algorithm	ImageJ 1.5	***Schneider et al., 2012*** https://doi.org/10.1038/nmeth.2089	RRID:SCR_003070	ImageJ plugin for TIRF image analysis: https://github.com/alushinlab/ActinEnrichment

Continued on next page

Continued

Reagent type (species) or resource	Designation	Source or reference	Identifiers	Additional information
Software, algorithm	RELION 3.0	***He and Scheres, 2017*** https://doi.org/10.1016/j.jsb.2017.02.003 ***Schneider et al., 2012*** https://doi.org/10.1016/j.jmb.2011.11.010 ***Zivanov et al., 2018*** https://doi.org/10.7554/eLife.42166	RRID:SCR_016274	
Software, algorithm	CTFFIND 4.1.5	***Rohou and Grigorieff, 2015*** https://doi.org/10.1016/j.jsb.2015.08.008	RRID:SCR_016732	
Software, algorithm	Phenix 1.17.1	***Afonine et al., 2018*** https://doi.org/10.1107/S2059798318006551	RRID:SCR_014224	
Software, algorithm	Coot 0.8.9	***Emsley et al., 2010*** https://doi.org/10.1107/S0907444910007493	RRID:SCR_014222	
Software, algorithm	UCSF Chimera 1.14	***Pettersen et al., 2004*** https://doi.org/10.1002/jcc.20084	RRID:SCR_004097	
Software, algorithm	UCSF ChimeraX 1.0	***Goddard et al., 2018*** https://doi.org/10.1002/pro.3235	RRID:SCR_015872	
Software, algorithm	GraphPad Prism 8	GraphPad Software, Inc	RRID:SCR_002798	

Contact and materials availability

Further information and requests for resources and reagents should be directed to the corresponding author, Gregory M. Alushin (galushin@rockefeller.edu). All reagents generated in this study are available from the corresponding author without restriction.

Experimental model and subject details

Globular actin (G-actin) monomers were purified from chicken skeletal muscle as described previously (***Pardee and Spudich, 1982***) and maintained in G-Ca buffer: G buffer (2 mM Tris-Cl pH 8, 0.5 mM DTT, 0.2M ATP, 0.01% NaN_3) supplemented with 0.1 mM $CaCl_2$, at 4˚C before use. C-terminally GFP-tagged mouse myosin V HMM and myosin VI S1 were purified from SF9 insect cells using published protocols (***Wang et al., 2000***). All other proteins were heterologously expressed in Rosetta2(DE3) *E. coli* cells (Novagen) grown in LB media as described in Method details.

Method details

F-actin preparation

Filamentous actin (F-actin) was polymerized fresh for each experiment from actin monomers in G-Mg (G buffer supplemented with 0.1 mM $MgCl_2$) and KMEI (50 mM KCl, 1 mM $MgCl_2$, 1 mM EGTA, 10 mM imidazole pH 7.0, 1 mM DTT) buffers as described previously (***Gurel et al., 2017***); 30% rhodamine-labeled actin filaments used in TIRF microscopy assays were prepared by copolymerizing unlabeled actin monomers and rhodamine-labeled actin monomers (Cytoskeleton catalog # AR05) at a 7:3 molar ratio (total actin concentration 1 µM) at room temperature for 2 hr in the dark. For optical trapping/confocal microscopy assays, 10% biotinylated actin filaments were prepared by copolymerizing purified unlabeled actin monomers and biotinylated actin monomers (Cytoskeleton catalog # AB07) at a 9:1 molar ratio (total actin concentration 1 µM) at room temperature for 2 hr. The biotinylated F-actin was subsequently stabilized and fluorescently labeled by adding 1.2 molar equivalents of Alexa Fluor 555 Phalloidin (ThermoFisher catalog # A34055).

Expression cloning

Vectors for expression of WT *H. sapiens* vinculin ABD (879–1066), *H. sapiens* metavinculin ABD (879–1134), *H. sapiens* α-catenin ABD (αE-catenin$_{664-906}$), α-catenin ABDΔC (αE-catenin$_{664-871}$), vinculin ABD-NCSwap (αE-catenin$_{664-708}$-vinculin$_{916-1041}$-αE-catenin$_{837-906}$), and vinculin ABD-NCSwapΔC (αE-catenin$_{664-708}$-vinculin$_{916-1041}$-αE-catenin$_{837-871}$) were constructed by inserting the corresponding cDNA sequence into a pET bacterial expression vector with an N-terminal His6-tag, Strep-tag, TEV cleavage site, and, for proteins used in fluorescence imaging experiments, a subsequent C-terminal Halo-tag by Gibson assembly (***Gibson et al., 2009***). Constructs for proteins used in Cryo-EM structural studies are not Halo-tagged. Three WT α-catenin TIRF trials were performed with a previously reported Halo-tagged α-catenin ABD construct (αE-catenin$_{671-906}$), and no difference was observed.

Expression and purification of actin-binding proteins

C-terminally GFP-tagged mouse myosin V HMM and myosin VI S1 were purified from SF9 cells using published protocols (***Wang et al., 2000***). Human calmodulin (CaM) was purified from Rosetta2(DE3) *E. coli* cells using a published protocol (***Putkey et al., 1985***) and stored in gel filtration buffer (20 mM Tris-Cl pH 8.0, 100 mM NaCl, 2 mM β-mercaptoethanol) supplemented with 5% v/v glycerol.

All other ABPs were expressed in Rosetta2(DE3) *E. coli* cells (Novagen) grown in LB media at 37˚C to an optical density of 0.8–1.0 and induced with 0.7 mM IPTG. After induction, the cells were grown for 16 hr at 16˚C, then cell pellets were collected and stored at −80˚C until use. To purify Halo-tagged ABPs for fluorescent labeling, cells pellets were resuspended in lysis buffer (50 mM Tris-Cl pH 8.0, 150 mM NaCl, 5% v/v glycerol, 2 mM β-mercaptoethanol, 20 mM imidazole) and lysed with an Avestin Emulsiflex C5 homogenizer, after which the lysate was clarified at 15,000 g for 30 min. Cleared lysate was incubated with Ni-NTA resin (Qiagen) for 1 hr on a rotator at 4˚C, after which the flow-through was discarded and the resin was washed with five bed volumes of lysis buffer. Proteins were subsequently eluted in elution buffer (50 mM Tris-Cl pH 8.0, 150 mM NaCl, 5% v/v glycerol, 2 mM β-mercaptoethanol, 300 mM imidazole). Purified His-tagged TEV protease (prepared according to a published protocol [***Tropea et al., 2009***]) was added at 0.05 mg/mL working concentration, then the eluate was dialyzed against dialysis buffer (20 mM Tris-Cl pH 8.0, 300 mM NaCl, 5% v/v glycerol, 2 mM β-mercaptoethanol) for 16 hr. The protein solution was then reapplied to Ni-NTA resin, and the flow-through was collected.

Protein was then sequentially purified by a HiTrapQ HP anion exchange column (GE Healthcare) followed by size exclusion chromatography on a Superdex 200 Increase column in gel filtration buffer supplemented with 10% v/v glycerol, and then snap-frozen in liquid nitrogen and stored at −80˚C. Non-Halo-tagged proteins prepared for cryo-EM studies were purified identically, except glycerol was omitted from all buffers.

After rapid thawing before use, proteins were clarified by ultracentrifugation at 45,000 rpm in a TLA100 rotor for 10 min at 4˚C. All protein concentrations were estimated using the Bradford colorimetric assay (Pierce), calibrated with BSA.

Synthesis of Halo-JF-646 and labeling of ABPs

Fluorescent dye JF-646 (***Grimm et al., 2015***) NHS-ester building block (TOCRIS) was conjugated with Halo-tag ligand amine O4 (Promega) by synthetic chemistry according to published protocols (***Grimm et al., 2017***). Briefly, 1.5 equivalents of amine O4 ligand were added to one equivalent of the JF-646 NHS-ester in DMF followed by adding 5% triethylamine. The reaction was vigorously stirred for 16 hr at room temperature and the product was purified by silica gel chromatography, dried by SpeedVac (ThermoFisher), and reconstituted in DMSO.

For optical trapping/confocal microscopy assays, HaloTag Alexa Fluor 488 Ligand (Promega) was utilized as described above, followed by desalting through a PD SpinTrap G-25 column (GE Healthcare) according to the manufacturer's protocol to remove unreacted dye before use. To label the Halo-tagged actin-binding proteins with Halo-JF-646 for TIRF microscopy assays, two equivalents of synthesized Halo-JF-646 dye was added to the protein solution, followed by incubation for at least 2 hr in the dark at 4˚C before use. Subsequent removal of excess dye was not required, as JF-646 is a fluorogenic dye (***Grimm et al., 2015***).

Correlative force spectroscopy and confocal microscopy assays

Experiments were performed at room temperature (approximately 25˚C) on a LUMICKS C-Trap instrument combining confocal fluorescence with dual-trap optical tweezers (***Hashemi Shabestari et al., 2017***; ***Wasserman et al., 2019***). The optical traps were cycled through pre-set positions in the five channels of a microfluidic flow cell by an automated stage (***Figure 1A***). Channels 1–3 were separated from each other by laminar flow, which we utilized to form actin filament tethers between two 4 μm-diameter streptavidin-coated polystyrene beads (Spherotech) held in optical traps with a stiffness of 0.3 pN/nm. We first captured a single bead in each trap in channel 1. The traps were then transferred to channel 2, containing 5–20 nM Alexa 555 phalloidin-stabilized, 10% biotinylated F-actin in motility buffer ('MB': 20 mM MOPS pH7.4, 5 mM $MgCl_2$, 0.1 mM EGTA, 1 mM DTT) supplemented with 1 μM dark phalloidin, where tethers were formed by briefly moving 1 of the two traps toward the other trap against the direction of flow, followed by rapidly moving the traps to channel 3, which contained only buffer (MB + 1 μM dark phalloidin). The presence of a tether was verified by carefully separating the traps and observing an associated increase in force when monitoring the force-extension curve, applying the minimum extension feasible to avoid prematurely rupturing the tether.

The traps were then moved to orthogonal channel 4 or 5, which contained 2 μM fluorescently labeled vinculin ABD or α-catenin ABD (diluted in MB supplemented with 1 μM dark phalloidin), respectively, and flow was ceased during data acquisition. Force data were acquired at 200 Hz during constant velocity (0.1 μm/s) pulling experiments while simultaneously acquiring 2-color confocal fluorescence scans at 33 ms line scan time, exciting Alexa Fluor 488 HaloTag ligand and Alexa Fluor 555 phalloidin fluorophores with laser lines at 488 nm and 532 nm, respectively.

Data analysis was performed using ImageJ and custom software provided by LUMICKS. Force data from the two traps were averaged and binned to the confocal frame interval. The intensity values are measured by drawing a box in ImageJ to measure the fluorescence intensities of actin and ABP in both channels with background subtraction, calculating the background from an equal-sized box from that frame in an area devoid of filaments or beads. For paired analysis, the 'high-force' and 'low-force' averages were calculated only from the final tether to rupture, as long as the entire force trace has at least 10 quantifiable confocal image frames. For fluorescence-force correlation plots, only single-filament tethers selected based on ***Figure 1—figure supplement 2A–C*** were used. I_{ABP}/I_{Actin} values were normalized by dividing the values in each recording by the largest value observed during that recording. K-means clustering analysis was performed to identify the cutoff force in the correlation plots for each ABP. Briefly, the force-fluorescence data were grouped into two clusters using scikit-learn (***Pedregosa et al., 2011***). For both α-catenin and vinculin, the data separated along the force axis, providing a threshold force for each ABP. Furthermore, a silhouette analysis for both ABPs confirmed that the data should not be clustered into more than two clusters (***Kaufman and Rousseeuw, 2009***).

TIRF force reconstitution assays

Glass coverslips (Rectangular: Corning 22 × 50 mm #1½ Cover Glass; Square: Fisherbrand 22 × 22 mm #1½ Microscope Cover Glass) were cleaned by 30 min 100% acetone wash, 10 min 100% ethanol wash, and 2 hr 2% Hellmanex III liquid cleaning concentrate (HellmaAnalytics) wash in a bath sonicator followed by rinsing with water. The cleaned glass coverslips were coated with 1 mg/mL mPEG5K-Silane (Sigma) in a 96% ethanol, 10 mM HCl solution for at least 16 hr. After coating, the coverslips were rinsed with 96% ethanol and water, then air-dried and stored at 4˚C until use. Flow cells were prepared with one square and one rectangular coverslip, both coated with mPEG-Silane. Double-sided adhesive tape (3M) was used to make ~4 mm-wide flow chambers between the coverslips, which were open on both sides to facilitate buffer exchange when adding components for imaging.

For each assay, 6 mg/mL anti-GFP antibody (Sigma #G1546) solution reconstituted in water was first introduced into the flow chamber and incubated for 2 min. Subsequently, MB containing 0.075 μM GFP-myosin V S1 and 0.15 μM GFP-myosin VI S1 were flowed into the chamber and incubated for another 2 min. A solution of 1 mg/mL bovine serum albumin (BSA) in MB was then flowed into the flow chamber and incubated for at least 2 min, after which 1 μM rhodamine-labeled F-actin in MB was flowed into the chamber and incubated for 20–30 s. The flow chamber was rinsed with MB

buffer to remove F-actin not bound to the rigor-state motors, then imaging buffer (MB without ATP, supplemented with 0.01% Nonidet P-40 substitute [Roche], 1 μM calmodulin, 15 mM glucose [Sigma], 1 μg/mL glucose oxidase [Sigma], and 0.05 μg/mL catalase [Sigma]) containing 2 μM fluorescently labeled ABP was flowed into the chamber. The first movie (-ATP, no force) was then recorded. A second imaging buffer, identical to the first but now including 100 μM ATP, was then introduced into the same chamber, and a second movie (+ATP, with force) was recorded. For each solution that was introduced, complete buffer exchange was facilitated by applying a filter paper at the other end of the flow chamber while pipetting.

Dual-color TIRF image sequences (movies) were recorded at room temperature (approximately 25˚C) using a Nikon TiE inverted microscope equipped with an H-TIRF module and an Agilent laser launch, driven by Nikon Elements software. Images were taken every 2 s with an Apo TIRF 60 × 1.49 NA objective (Nikon) on an Andor iXon EMCCD camera; Rhodamine and JF646 fluorophores were excited by laser lines at 561 nm and 640 nm, respectively.

Filament region quantification

To quantify ABP association with individual 'filament regions' of TIRF movies, we developed a custom ImageJ (***Schneider et al., 2012***) plugin (***Figure 2—figure supplement 1A***) which features a graphical user interface (GUI). The plugin takes as input two movie files, the actin channel and the ABP channel from a dual-color TIRF experiment, as well as an adjustable set of parameters (set by default in the GUI to the optimized values used in this study).

To identify regions of interest (ROIs) in each frame, the actin channel image series was preprocessed (unsharp mask, median filter, rolling ball subtraction), binarized, then segmented into contiguous regions of pixels using the built-in ImageJ plugin 'Analyze Particles'. ROIs whose centroids were fewer than 30 pixels from the edge of the field-of-view were excluded from further analysis due to incompatibility with downstream background subtraction procedures. The ROIs were then tracked through the image series and sorted into filament regions (representing individual filaments or small groups of filaments) by shortest Euclidean distance between ROI centroids in neighboring frames, with a maximum distance cutoff of 24 pixels. ROIs that were not matched with a pre-existing filament region by this criterion (i.e. whose centroid was greater than 24 pixels away from any ROI in the previous frame) were considered to represent a newly appeared filament region. Although this may result in overcounting the absolute number of filaments (should this be of interest; we do not believe this caveat impacts the conclusions of the present study), we find this procedure reliably handles events such as filament breakages and desultory motion in a completely automated fashion. To account for poorly tethered filaments fluctuating in and out of the evanescent field, only filament regions detected in at least 10 consecutive frames were included in the analysis.

Intensity in both the actin channel and the ABP channel were then quantified for each region. For each channel, the local background for each filament region in each frame was calculated as the mean gray value of the pixels from a 60 by 60 pixel box centered on the region's centroid, excluding pixels belonging to the region itself or any other filament region detected in the frame. Background-subtracted mean gray values were then calculated, followed by the ratio of these values across all frames in which the filament region was detected and their average, which we here report as the overall I_{ABP}/I_{Actin} for that filament region. The program then outputs all frame and average I_{ABP}/I_{Actin} values of the tracked filaments sorted by filament number for analysis, as well as a file containing all tracked regions.

Cryo-EM sample preparation and data collection

F-actin was polymerized in G-Mg and KMEI from 5 μM unlabeled actin monomers at room temperature for 1 hr and then diluted to 0.6 μM in KMEI before use. Purified metavinculin ABD (879–1134) was diluted in KMEI to 10 μM before use. After screening grids prepared with finely sampled ABP concentrations, we found diluting purified α-catenin ABD (664-906) to 20 μM in KMEI before use gave an optimal balance between filament decoration and bundling.

Immediately before sample preparation, CF-1.2/1.3-3Au 300-mesh gold C-flat holey carbon cryo-TEM grids (Protochips) were plasma cleaned with a Hydrogen/Oxygen mixture for 5 s in a Gatan Solarus. Actin (3 μL) was first applied to the grid in the humidified chamber of a Leica EM GP plunge freezer and incubated for 60 s at 25˚C. Actin-binding protein (3 μL) was then applied and incubated

for 30 s. Solution (3 µL) was then removed and an additional 3 µL of the same actin-binding protein solution was applied. After an additional 30 s, 3 µL of solution was removed, then the grid was back-blotted for 5 s, plunge-frozen in ethane slush, and stored in liquid nitrogen until imaging.

Cryo-EM data were recorded on a Titan Krios (ThermoFisher/FEI) operated at 300 kV equipped with a Gatan K2 Summit camera. SerialEM (***Mastronarde, 2005***) was used for automated data collection. Movies were collected at a nominal magnification of 29,000X in super-resolution mode resulting in a calibrated pixel size of 1.03 Å/pixel (superresolution pixel size of 0.515 Å/pixel), over a defocus range of −1.5 to −3.5 µm; 40 frames were recorded over 10 s of exposure at a dose rate of 6 electrons per pixel per second (1.5 electrons per $Å^2$ per second) for a cumulative dose of 60 electrons per $Å^2$.

Cryo-EM image processing

Unless otherwise noted, all image processing was performed within the RELION-3.0 package (***Zivanov et al., 2018***). Movie frames were aligned and summed with 2 × 2 binning using the MotionCor2 algorithm (***Zheng et al., 2017***) as implemented in RELION (***Zivanov et al., 2019***), utilizing subframe motion correction with 5 × 5 patches. Contrast transfer function (CTF) parameters were estimated from non-doseweighted summed images with CTFFIND4 (***Rohou and Grigorieff, 2015***). Bimodal angular searches around psi angle priors were utilized in all subsequent 2D and 3D alignment/classification procedures. Around 2000 segments were initially manually picked, extracted, and subjected to 2D classification to generate templates for auto-picking. Helical auto-picking was then performed utilizing a step-size of 3 asymmetric units with a 27 Å helical rise. Segments were extracted from dose-weighted (***Grant and Grigorieff, 2015***) sum images in 512 × 512 pixel boxes which were not further down-sampled, then a second round of 2D classification followed by auto-picking with featureful class averages was performed.

A total of 237,503 particles from 1708 images (for the metavinculin ABD-actin dataset) and 540,553 particles from 7317 images (for the α-catenin ABD-actin dataset) were then extracted and subjected to whole-dataset 2D classification (***Figure 3—figure supplement 1***) using a 200 Å tube diameter and 300 Å mask diameter. 234,703 segments from the metavinculin ABD-actin dataset and 428,335 particles from the α-catenin ABD-actin dataset contributed to featureful class averages and were selected for 3D analysis.

All subsequent 3D classification and 3D auto-refine steps were primed with estimates of helical rise and twist of 27.0 Å and −167.0˚, respectively, utilizing an initial reference low-pass filtered to 35 Å resolution, with the outer tube diameter set to 200 Å, inner tube diameter set to −1, and the mask diameter set to 300 Å. The first round of 3D classification into three classes was performed utilizing a reconstruction of a bare actin filament (EMBD-7115) as the initial reference. A second iteration of 3D classification was then performed as above, utilizing a featureful class with clear ABP density produced by the first round as the initial reference. For both datasets, this second round of 3D classification yielded two classes with helical parameters similar to the initial estimates and well-resolved 3D features, and one junk class with aberrant helical parameters and distorted features (***Figure 3—figure supplement 1***). Segments contributing to the two good classes were then pooled (215,369 particles for the metavinculin ABD-actin dataset and 414,486 particles for the α-catenin ABD-actin dataset) for 3D auto-refinement.

The first round of auto-refinement was then performed using one of the two good 3D averages as an initial reference. All masks for subsequent post-processing steps were calculated with 0 pixel extension and a six pixel soft edge from the converged reconstruction produced by that round of refinement, low-pass filtered to 15 Å and thresholded to fully encompass the density map. The first-round post-processing was performed with a 50% z length mask, followed by CTF refinement without beam-tilt estimation and Bayesian polishing (***Zivanov et al., 2019***). A second round of auto-refinement was then performed using the converged reconstruction from the first round as the initial reference. The second-round post-processing was performed with a 30% z length mask, followed by a second round of CTF refinement with beam-tilt estimation and Bayesian polishing. A final round of auto-refinement was then performed using the converged reconstruction from the second round as the initial reference. We found that this iterative procedure of tightening the mask for polishing resulted in substantial resolution improvements, potentially by mitigating the effects of medium-range disorder in F-actin previously speculated to limit the resolution of reconstructions of this filament (***Galkin et al., 2012***; ***Merino et al., 2018***).

The final reconstructions converged with helical rise of 27.1 Å and twist of −167.1˚ for the metavinculin ABD–F-actin complex, and a helical rise of 27.0 Å and twist of −166.9˚ for the α-catenin ABD-F-actin complex, consistent with our finding that actin rearrangements evoked by these ABPs are minimal (***Figure 5H***). Final post-processing was performed with a 30% z length mask, leading to global resolution estimates of 2.9 Å for the metavinculin ABD–F-actin complex and 3.2 Å for the α-catenin ABD–F-actin complex by the gold-standard Fourier shell correlation (FSC) 0.143 criterion (***Figure 3—figure supplement 1***). B-factors of both datasets estimated during post-processing were then used to generate sharpened, local-resolution filtered maps with RELION. The key statistics summarizing cryo-EM image processing are reported in ***Table 1***.

Asymmetric focused classification (without alignment) utilizing masks isolating the ABD region showed no evidence of segments with unoccupied binding sites (data not shown), suggesting that decoration of actin filaments by both 10 μM metavinculin ABD and 20 μM α-catenin ABD was essentially complete, with 100% occupancy at the limit of detection of current methods.

Model building and refinement

Sharpened, local-resolution filtered maps as described above were used for model building. The 2.9 Å and 3.2 Å density maps were of sufficient quality for de novo atomic model building. As structures of components were available, initial models of actin (PDB 3j8a), metavinculin ABD (PDB 3jbk) truncated to residues 981–1131 and α-catenin ABD (PDB 4igg chain B) truncated to residues 699–871 were fit into the density map using Rosetta (***Wang et al., 2016***). Models were subsequently inspected and adjusted with Coot (***Brown et al., 2015***; ***Emsley et al., 2010***), and regions that underwent significant conformational rearrangements were manually rebuilt. The models were then subjected to several rounds of simulated annealing followed by real-space refinement in Phenix (***Adams et al., 2010***; ***Afonine et al., 2018***) alternating with manual adjustment in Coot. A final round of real-space refinement was performed without simulated annealing. The key statistics summarizing model building, refinement, and validation are reported in ***Table 1***.

Molecular graphics and structure analysis

Structural figures and movies were prepared with ChimeraX (***Goddard et al., 2018***). Per-residue RMSD analysis was performed with UCSF Chimera (***Pettersen et al., 2004***) as previously described (***Zhang et al., 2015***). The surface area of actin-binding interfaces was calculated with PDBePISA (***Krissinel and Henrick, 2007***; (EMBL-EBI). Model quality was assessed with EMRinger (***Barad et al., 2015***) and MolProbity (***Chen et al., 2010***) as implemented in Phenix.

Sequence alignments

Protein sequences of human vinculin (UniProt Accession Code P18206-2), human metavinculin (P18206-1), human αE-catenin (P35221), human αN-catenin (P26232), and human αT-catenin (Q9UI47) were aligned with ClustalOmega (***Sievers and Higgins, 2014***; EMBL-EBI).

Quantification and statistical analysis

Plotting and statistical analysis of data from TIRF force reconstitution assays and force-spectroscopy/confocal microscopy assays was performed with GraphPad Prism 8. All the details can be found in the figure legends of these figures and in the Method details. The data collection and refinement statistics of the cryo-EM structures can be found in ***Table 1***. Resolution estimations of cryo-EM density maps and statistical validation performed on the deposited models are described in the Method details.

Data and code availability

The atomic coordinates for the metavinculin ABD–F-actin complex and α-catenin ABD–F-actin complex have been deposited in the Protein Data Bank (PDB) with accession codes 6UPW and 6UPV, and the corresponding cryo-EM density maps in the Electron Microscopy Data Bank (EMDB) with accession codes EMD-20844 and EMD-20843.

The code for analyzing TIRF movies is freely available as an ImageJ plugin with a graphical user interface at https://github.com/alushinlab/ActinEnrichment. (copy archived at https://github.com/elifesciences-publications/ActinEnrichment; ***Alushinlab, 2020***).

All other data are available in the manuscript or supplementary materials.

Acknowledgements

We gratefully acknowledge Pinar Gurel (RU) for initial efforts in establishing the force reconstitution TIRF assay, Luke Lavis (HHMI Janelia) for the gift of JF-646 for pilot studies, and Yasuharu Takagi and James Sellers (NHLBI DIR) for the gift of myosin proteins and training in their purification. We also thank Sara Tafoya and Jordi Cabanas-Danés (LUMICKS) for assistance with C-trap experiments and data analysis, Muzaddid Sarker and Sharon Campbell (UNC) for the gift of metavinculin ABD used in cryo-EM studies, Rui Gong (RU) for assistance with cryo-EM data collection and analysis, and Mark Ebrahim and Johanna Sotiris (RU Cryo-EM Resource Center) for assistance with cryo-EM data collection. Template cDNA for α-catenin constructs was obtained from David Rimm via AddGene (#24194). This work was funded by grants from the Irma T Hirschl/Monique Weill-Caulier Trust and Pew Charitable Trusts to GMA, and NIH High-Risk High-Reward grants to GMA (5DP5OD017885, Early Independence Award) and SL (1DP2HG010510, New Innovator Award).

Additional information

Funding

Funder	Grant reference number	Author
Irma T. Hirschl Trust	Research Award	Gregory M Alushin
Pew Charitable Trusts	Pew Scholar Award	Gregory M Alushin
National Institutes of Health	5DP5OD017885	Gregory M Alushin
National Institutes of Health	1DP2HG010510	Shixin Liu

The funders had no role in study design, data collection and interpretation, or the decision to submit the work for publication.

Author contributions

Lin Mei, Conceptualization, Resources, Data curation, Formal analysis, Validation, Investigation, Visualization, Methodology, Writing - original draft, Writing - review and editing; Santiago Espinosa de los Reyes, Matthew J Reynolds, Software, Formal analysis, Methodology, Writing - review and editing; Rachel Leicher, Investigation, Methodology, Writing - review and editing; Shixin Liu, Formal analysis, Supervision, Funding acquisition, Methodology, Project administration, Writing - review and editing; Gregory M Alushin, Conceptualization, Data curation, Formal analysis, Supervision, Funding acquisition, Visualization, Methodology, Writing - original draft, Project administration, Writing - review and editing

Author ORCIDs

Lin Mei http://orcid.org/0000-0002-5056-4547
Santiago Espinosa de los Reyes http://orcid.org/0000-0003-4510-8296
Matthew J Reynolds http://orcid.org/0000-0002-2501-9280
Shixin Liu http://orcid.org/0000-0003-4238-7066
Gregory M Alushin https://orcid.org/0000-0001-7250-4484

Decision letter and Author response

Decision letter https://doi.org/10.7554/eLife.62514.sa1
Author response https://doi.org/10.7554/eLife.62514.sa2

Additional files

Supplementary files

- Transparent reporting form

Data availability

The atomic coordinates for the metavinculin ABD-F-actin complex and α-catenin ABD-F-actin complex have been deposited in the Protein Data Bank (PDB) with accession codes 6UPW and 6UPV, and the corresponding cryo-EM density maps in the Electron Microscopy Data Bank (EMDB) with accession codes EMD-20844 and EMD-20843. The code for analyzing TIRF movies is freely available as an ImageJ plugin with a graphical user interface at https://github.com/alushinlab/ActinEnrichment (copy archived at https://github.com/elifesciences-publications/ActinEnrichment). All other data are available in the manuscript or supplementary materials.

The following datasets were generated:

Author(s)	Year	Dataset title	Dataset URL	Database and Identifier
Mei L, Alushin GM	2020	Metavinculin ABD-F-actin complex	https://www.rcsb.org/structure/6UPW	RCSB Protein Data Bank, 6UPW
Mei L, Alushin GM	2020	Alpha-E-catenin ABD-F-actin complex	https://www.rcsb.org/structure/6UPV	RCSB Protein Data Bank, 6UPV

References

Adams PD, Afonine PV, Bunkóczi G, Chen VB, Davis IW, Echols N, Headd JJ, Hung LW, Kapral GJ, Grosse-Kunstleve RW, McCoy AJ, Moriarty NW, Oeffner R, Read RJ, Richardson DC, Richardson JS, Terwilliger TC, Zwart PH. 2010. *PHENIX*: a comprehensive Python-based system for macromolecular structure solution. *Acta Crystallographica Section D Biological Crystallography* **66**:213–221. DOI: https://doi.org/10.1107/S0907444909052925, PMID: 20124702

Afonine PV, Poon BK, Read RJ, Sobolev OV, Terwilliger TC, Urzhumtsev A, Adams PD. 2018. Real-space refinement in *PHENIX* for cryo-EM and crystallography. *Acta Crystallographica Section D Structural Biology* **74**: 531–544. DOI: https://doi.org/10.1107/S2059798318006551

Alushinlab. 2020. ActinEnrichment. *GitHub*. 679f3d0. https://github.com/alushinlab/ActinEnrichment

Avery AW, Fealey ME, Wang F, Orlova A, Thompson AR, Thomas DD, Hays TS, Egelman EH. 2017. Structural basis for high-affinity actin binding revealed by a β-III-spectrin SCA5 missense mutation. *Nature Communications* **8**:1350. DOI: https://doi.org/10.1038/s41467-017-01367-w, PMID: 29116080

Bakolitsa C, de Pereda JM, Bagshaw CR, Critchley DR, Liddington RC. 1999. Crystal structure of the vinculin tail suggests a pathway for activation. *Cell* **99**:603–613. DOI: https://doi.org/10.1016/S0092-8674(00)81549-4, PMID: 10612396

Bakolitsa C, Cohen DM, Bankston LA, Bobkov AA, Cadwell GW, Jennings L, Critchley DR, Craig SW, Liddington RC. 2004. Structural basis for vinculin activation at sites of cell adhesion. *Nature* **430**:583–586. DOI: https://doi.org/10.1038/nature02610, PMID: 15195105

Barad BA, Echols N, Wang RY, Cheng Y, DiMaio F, Adams PD, Fraser JS. 2015. EMRinger: side chain-directed model and map validation for 3D cryo-electron microscopy. *Nature Methods* **12**:943–946. DOI: https://doi.org/10.1038/nmeth.3541, PMID: 26280328

Beausang JF, Schroeder HW, Nelson PC, Goldman YE. 2008. Twirling of actin by myosins II and V observed via polarized TIRF in a modified gliding assay. *Biophysical Journal* **95**:5820–5831. DOI: https://doi.org/10.1529/biophysj.108.140319, PMID: 18931255

Bieling P, Li TD, Weichsel J, McGorty R, Jreij P, Huang B, Fletcher DA, Mullins RD. 2016. Force feedback controls motor activity and mechanical properties of Self-Assembling branched actin networks. *Cell* **164**:115–127. DOI: https://doi.org/10.1016/j.cell.2015.11.057, PMID: 26771487

Brown A, Long F, Nicholls RA, Toots J, Emsley P, Murshudov G. 2015. Tools for macromolecular model building and refinement into electron cryo-microscopy reconstructions. *Acta Crystallographica Section D Biological Crystallography* **71**:136–153. DOI: https://doi.org/10.1107/S1399004714021683, PMID: 25615868

Buckley CD, Tan J, Anderson KL, Hanein D, Volkmann N, Weis WI, Nelson WJ, Dunn AR. 2014. Cell adhesion the minimal cadherin-catenin complex binds to actin filaments under force. *Science* **346**:1254211. DOI: https://doi.org/10.1126/science.1254211, PMID: 25359979

Charras G, Yap AS. 2018. Tensile forces and mechanotransduction at Cell-Cell junctions. *Current Biology* **28**: R445–R457. DOI: https://doi.org/10.1016/j.cub.2018.02.003, PMID: 29689229

Chen VB, Arendall WB, Headd JJ, Keedy DA, Immormino RM, Kapral GJ, Murray LW, Richardson JS, Richardson DC. 2010. *MolProbity*: all-atom structure validation for macromolecular crystallography. *Acta Crystallographica Section D Biological Crystallography* **66**:12–21. DOI: https://doi.org/10.1107/S0907444909042073, PMID: 20057044

Chou SZ, Pollard TD. 2019. Mechanism of actin polymerization revealed by cryo-EM structures of actin filaments with three different bound nucleotides. *PNAS* **116**:4265–4274. DOI: https://doi.org/10.1073/pnas.1807028115, PMID: 30760599

Courtemanche N, Lee JY, Pollard TD, Greene EC. 2013. Tension modulates actin filament polymerization mediated by formin and profilin. *PNAS* **110**:9752–9757. DOI: https://doi.org/10.1073/pnas.1308257110, PMID: 23716666

Dominguez R, Holmes KC. 2011. Actin structure and function. *Annual Review of Biophysics* **40**:169–186. DOI: https://doi.org/10.1146/annurev-biophys-042910-155359
Drees F, Pokutta S, Yamada S, Nelson WJ, Weis WI. 2005. Alpha-catenin is a molecular switch that binds E-cadherin-beta-catenin and regulates actin-filament assembly. *Cell* **123**:903–915. DOI: https://doi.org/10.1016/j.cell.2005.09.021, PMID: 16325583
Dumbauld DW, Lee TT, Singh A, Scrimgeour J, Gersbach CA, Zamir EA, Fu J, Chen CS, Curtis JE, Craig SW, García AJ. 2013. How vinculin regulates force transmission. *PNAS* **110**:9788–9793. DOI: https://doi.org/10.1073/pnas.1216209110, PMID: 23716647
Egelman EH. 2007. The iterative helical real space reconstruction method: surmounting the problems posed by real polymers. *Journal of Structural Biology* **157**:83–94. DOI: https://doi.org/10.1016/j.jsb.2006.05.015, PMID: 16919474
Emsley P, Lohkamp B, Scott WG, Cowtan K. 2010. Features and development of *coot*. *Acta Crystallographica. Section D, Biological Crystallography* **66**:486–501. DOI: https://doi.org/10.1107/S0907444910007493, PMID: 20383002
Finer JT, Simmons RM, Spudich JA. 1994. Single myosin molecule mechanics: piconewton forces and nanometre steps. *Nature* **368**:113–119. DOI: https://doi.org/10.1038/368113a0, PMID: 8139653
Galkin VE, Orlova A, Salmazo A, Djinovic-Carugo K, Egelman EH. 2010a. Opening of tandem calponin homology domains regulates their affinity for F-actin. *Nature Structural & Molecular Biology* **17**:614–616. DOI: https://doi.org/10.1038/nsmb.1789, PMID: 20383143
Galkin VE, Orlova A, Schröder GF, Egelman EH. 2010b. Structural polymorphism in F-actin. *Nature Structural & Molecular Biology* **17**:1318–1323. DOI: https://doi.org/10.1038/nsmb.1930, PMID: 20935633
Galkin VE, Orlova A, Egelman EH. 2012. Actin filaments as tension sensors. *Current Biology* **22**:R96–R101. DOI: https://doi.org/10.1016/j.cub.2011.12.010, PMID: 22321312
Gibson DG, Young L, Chuang RY, Venter JC, Hutchison CA, Smith HO. 2009. Enzymatic assembly of DNA molecules up to several hundred kilobases. *Nature Methods* **6**:343–345. DOI: https://doi.org/10.1038/nmeth.1318, PMID: 19363495
Goddard TD, Huang CC, Meng EC, Pettersen EF, Couch GS, Morris JH, Ferrin TE. 2018. UCSF ChimeraX: meeting modern challenges in visualization and analysis. *Protein Science* **27**:14–25. DOI: https://doi.org/10.1002/pro.3235, PMID: 28710774
Grant T, Grigorieff N. 2015. Measuring the optimal exposure for single particle cryo-EM using a 2.6 å reconstruction of Rotavirus VP6. *eLife* **4**:e06980. DOI: https://doi.org/10.7554/eLife.06980, PMID: 26023829
Grimm JB, English BP, Chen J, Slaughter JP, Zhang Z, Revyakin A, Patel R, Macklin JJ, Normanno D, Singer RH, Lionnet T, Lavis LD. 2015. A general method to improve fluorophores for live-cell and single-molecule microscopy. *Nature Methods* **12**:244–250. DOI: https://doi.org/10.1038/nmeth.3256, PMID: 25599551
Grimm JB, Brown TA, English BP, Lionnet T, Lavis LD. 2017. Synthesis of janelia fluor HaloTag and SNAP-Tag ligands and their use in cellular imaging experiments. *Methods in Molecular Biology* **1663**:179–188. DOI: https://doi.org/10.1007/978-1-4939-7265-4_15, PMID: 28924668
Gurel PS, Kim LY, Ruijgrok PV, Omabegho T, Bryant Z, Alushin GM. 2017. Cryo-EM structures reveal specialization at the myosin VI-actin interface and a mechanism of force sensitivity. *eLife* **6**:e31125. DOI: https://doi.org/10.7554/eLife.31125, PMID: 29199952
Hansen SD, Kwiatkowski AV, Ouyang CY, Liu H, Pokutta S, Watkins SC, Volkmann N, Hanein D, Weis WI, Mullins RD, Nelson WJ. 2013. αE-catenin actin-binding domain alters actin filament conformation and regulates binding of nucleation and disassembly factors. *Molecular Biology of the Cell* **24**:3710–3720. DOI: https://doi.org/10.1091/mbc.e13-07-0388, PMID: 24068324
Harris AR, Jreij P, Fletcher DA. 2018. Mechanotransduction by the actin cytoskeleton: converting mechanical stimuli into biochemical signals. *Annual Review of Biophysics* **47**:617–631. DOI: https://doi.org/10.1146/annurev-biophys-070816-033547
Harris AR, Belardi B, Jreij P, Wei K, Shams H, Bausch A, Fletcher DA. 2019. Steric regulation of tandem calponin homology domain actin-binding affinity. *Molecular Biology of the Cell* **30**:3112–3122. DOI: https://doi.org/10.1091/mbc.E19-06-0317, PMID: 31693446
Hashemi Shabestari M, Meijering AEC, Roos WH, Wuite GJL, Peterman EJG. 2017. Recent advances in biological Single-Molecule applications of optical tweezers and fluorescence microscopy. *Methods in Enzymology* **582**:85–119. DOI: https://doi.org/10.1016/bs.mie.2016.09.047, PMID: 28062046
Hayakawa K, Tatsumi H, Sokabe M. 2011. Actin filaments function as a tension sensor by tension-dependent binding of cofilin to the filament. *The Journal of Cell Biology* **195**:721–727. DOI: https://doi.org/10.1083/jcb.201102039, PMID: 22123860
He S, Scheres SHW. 2017. Helical reconstruction in RELION. *Journal of Structural Biology* **198**:163–176. DOI: https://doi.org/10.1016/j.jsb.2017.02.003, PMID: 28193500
Huang DL, Bax NA, Buckley CD, Weis WI, Dunn AR. 2017. Vinculin forms a directionally asymmetric catch bond with F-actin. *Science* **357**:703–706. DOI: https://doi.org/10.1126/science.aan2556, PMID: 28818948
Humphrey JD, Dufresne ER, Schwartz MA. 2014. Mechanotransduction and extracellular matrix homeostasis. *Nature Reviews Molecular Cell Biology* **15**:802–812. DOI: https://doi.org/10.1038/nrm3896, PMID: 25355505
Ishiyama N, Tanaka N, Abe K, Yang YJ, Abbas YM, Umitsu M, Nagar B, Bueler SA, Rubinstein JL, Takeichi M, Ikura M. 2013. An autoinhibited structure of α-Catenin and its implications for vinculin recruitment to adherens junctions. *Journal of Biological Chemistry* **288**:15913–15925. DOI: https://doi.org/10.1074/jbc.M113.453928
Ishiyama N, Sarpal R, Wood MN, Barrick SK, Nishikawa T, Hayashi H, Kobb AB, Flozak AS, Yemelyanov A, Fernandez-Gonzalez R, Yonemura S, Leckband DE, Gottardi CJ, Tepass U, Ikura M. 2018. Force-dependent

allostery of the α-catenin actin-binding domain controls adherens junction dynamics and functions. *Nature Communications* **9**:5121. DOI: https://doi.org/10.1038/s41467-018-07481-7, PMID: 30504777

Iwamoto DV, Huehn A, Simon B, Huet-Calderwood C, Baldassarre M, Sindelar CV, Calderwood DA. 2018. Structural basis of the filamin A actin-binding domain interaction with F-actin. *Nature Structural & Molecular Biology* **25**:918–927. DOI: https://doi.org/10.1038/s41594-018-0128-3, PMID: 30224736

Jaalouk DE, Lammerding J. 2009. Mechanotransduction gone awry. *Nature Reviews Molecular Cell Biology* **10**: 63–73. DOI: https://doi.org/10.1038/nrm2597, PMID: 19197333

Janssen ME, Kim E, Liu H, Fujimoto LM, Bobkov A, Volkmann N, Hanein D. 2006. Three-dimensional structure of vinculin bound to actin filaments. *Molecular Cell* **21**:271–281. DOI: https://doi.org/10.1016/j.molcel.2005.11.020, PMID: 16427016

Janssen ME, Liu H, Volkmann N, Hanein D. 2012. The C-terminal tail domain of metavinculin, Vinculin's splice variant, severs actin filaments. *The Journal of Cell Biology* **197**:585–593. DOI: https://doi.org/10.1083/jcb.201111046, PMID: 22613835

Jégou A, Carlier MF, Romet-Lemonne G. 2013. Formin mDia1 senses and generates mechanical forces on actin filaments. *Nature Communications* **4**:1883. DOI: https://doi.org/10.1038/ncomms2888, PMID: 23695677

Johnson RP, Craig SW. 1995. F-actin binding site masked by the intramolecular association of vinculin head and tail domains. *Nature* **373**:261–264. DOI: https://doi.org/10.1038/373261a0, PMID: 7816144

Kaufman L, Rousseeuw PJ. 2009. *Finding Groups in Data: An Introduction to Cluster Analysis*. **344** John Wiley & Sons.

Kim LY, Thompson PM, Lee HT, Pershad M, Campbell SL, Alushin GM. 2016. The structural basis of actin organization by vinculin and metavinculin. *Journal of Molecular Biology* **428**:10–25. DOI: https://doi.org/10.1016/j.jmb.2015.09.031

Kobielak A, Fuchs E. 2004. Alpha-catenin: at the junction of intercellular adhesion and actin dynamics. *Nature Reviews Molecular Cell Biology* **5**:614–625. DOI: https://doi.org/10.1038/nrm1433, PMID: 15366705

Krissinel E, Henrick K. 2007. Inference of macromolecular assemblies from crystalline state. *Journal of Molecular Biology* **372**:774–797. DOI: https://doi.org/10.1016/j.jmb.2007.05.022, PMID: 17681537

Krokhotin A, Sarker M, Sevilla EA, Costantini LM, Griffith JD, Campbell SL, Dokholyan NV. 2019. Distinct binding modes of vinculin isoforms underlie their functional differences. *Structure* **27**:1527–1536. DOI: https://doi.org/10.1016/j.str.2019.07.013, PMID: 31422909

Kron SJ, Spudich JA. 1986. Fluorescent actin filaments move on myosin fixed to a glass surface. *PNAS* **83**:6272–6276. DOI: https://doi.org/10.1073/pnas.83.17.6272, PMID: 3462694

Lecuit T, Yap AS. 2015. E-cadherin junctions as active mechanical integrators in tissue dynamics. *Nature Cell Biology* **17**:533–539. DOI: https://doi.org/10.1038/ncb3136, PMID: 25925582

Liem RK. 2016. Cytoskeletal integrators: the spectrin superfamily. *Cold Spring Harbor Perspectives in Biology* **8**: a018259. DOI: https://doi.org/10.1101/cshperspect.a018259, PMID: 27698030

Mastronarde DN. 2005. Automated electron microscope tomography using robust prediction of specimen movements. *Journal of Structural Biology* **152**:36–51. DOI: https://doi.org/10.1016/j.jsb.2005.07.007, PMID: 16182563

Merino F, Pospich S, Funk J, Wagner T, Küllmer F, Arndt HD, Bieling P, Raunser S. 2018. Structural transitions of F-actin upon ATP hydrolysis at near-atomic resolution revealed by cryo-EM. *Nature Structural & Molecular Biology* **25**:528–537. DOI: https://doi.org/10.1038/s41594-018-0074-0, PMID: 29867215

Mueller J, Szep G, Nemethova M, de Vries I, Lieber AD, Winkler C, Kruse K, Small JV, Schmeiser C, Keren K, Hauschild R, Sixt M. 2017. Load adaptation of lamellipodial actin networks. *Cell* **171**:188–200. DOI: https://doi.org/10.1016/j.cell.2017.07.051

Oda T, Takeda S, Narita A, Maéda Y. 2019. Structural polymorphism of actin. *Journal of Molecular Biology* **431**: 3217–3228. DOI: https://doi.org/10.1016/j.jmb.2019.05.048, PMID: 31181287

Oztug Durer ZA, McGillivary RM, Kang H, Elam WA, Vizcarra CL, Hanein D, De La Cruz EM, Reisler E, Quinlan ME. 2015. Metavinculin tunes the flexibility and the architecture of Vinculin-Induced bundles of actin filaments. *Journal of Molecular Biology* **427**:2782–2798. DOI: https://doi.org/10.1016/j.jmb.2015.07.005, PMID: 26168869

Pappas DJ, Rimm DL. 2006. Direct interaction of the C-terminal domain of alpha-catenin and F-actin is necessary for stabilized cell-cell adhesion. *Cell Communication & Adhesion* **13**:151–170. DOI: https://doi.org/10.1080/15419060600726142, PMID: 16798615

Pardee JD, Spudich JA. 1982. Purification of muscle actin. *Methods in Enzymology* **85**:164–181. DOI: https://doi.org/10.1016/0076-6879(82)85020-9, PMID: 7121269

Pedregosa F, Varoquaux G, Gramfort A, Michel V, Thirion B, Grisel O, Blondel M, Prettenhofer P, Weiss R, Dubourg V, Vanderplas J, Passos A, Cournapeau D, Brucher M, Perrot M, Duchesnay E. 2011. Scikit-learn: machine learning in Python. *The Journal of Machine Learning Research* **12**:2825–2830.

Pettersen EF, Goddard TD, Huang CC, Couch GS, Greenblatt DM, Meng EC, Ferrin TE. 2004. UCSF chimera–a visualization system for exploratory research and analysis. *Journal of Computational Chemistry* **25**:1605–1612. DOI: https://doi.org/10.1002/jcc.20084, PMID: 15264254

Pokutta S, Drees F, Takai Y, Nelson WJ, Weis WI. 2002. Biochemical and structural definition of the l-afadin- and actin-binding sites of alpha-catenin. *Journal of Biological Chemistry* **277**:18868–18874. DOI: https://doi.org/10.1074/jbc.M201463200, PMID: 11907041

Putkey JA, Slaughter GR, Means AR. 1985. Bacterial expression and characterization of proteins derived from the chicken calmodulin cDNA and a calmodulin processed gene. *The Journal of Biological Chemistry* **260**: 4704–4712. PMID: 2985564

Rangarajan ES, Izard T. 2013. Dimer asymmetry defines α-catenin interactions. *Nature Structural & Molecular Biology* **20**:188–193. DOI: https://doi.org/10.1038/nsmb.2479, PMID: 23292143
Razinia Z, Mäkelä T, Ylänne J, Calderwood DA. 2012. Filamins in mechanosensing and signaling. *Annual Review of Biophysics* **41**:227–246. DOI: https://doi.org/10.1146/annurev-biophys-050511-102252, PMID: 22404683
Risca VI, Wang EB, Chaudhuri O, Chia JJ, Geissler PL, Fletcher DA. 2012. Actin filament curvature biases branching direction. *PNAS* **109**:2913–2918. DOI: https://doi.org/10.1073/pnas.1114292109, PMID: 22308368
Rohou A, Grigorieff N. 2015. CTFFIND4: fast and accurate defocus estimation from electron micrographs. *Journal of Structural Biology* **192**:216–221. DOI: https://doi.org/10.1016/j.jsb.2015.08.008, PMID: 26278980
Romet-Lemonne G, Jégou A. 2013. Mechanotransduction down to individual actin filaments. *European Journal of Cell Biology* **92**:333–338. DOI: https://doi.org/10.1016/j.ejcb.2013.10.011, PMID: 24252518
Schiffhauer ES, Luo T, Mohan K, Srivastava V, Qian X, Griffis ER, Iglesias PA, Robinson DN. 2016. Mechanoaccumulative elements of the mammalian actin cytoskeleton. *Current Biology* **26**:1473–1479. DOI: https://doi.org/10.1016/j.cub.2016.04.007, PMID: 27185555
Schneider CA, Rasband WS, Eliceiri KW. 2012. NIH image to ImageJ: 25 years of image analysis. *Nature Methods* **9**:671–675. DOI: https://doi.org/10.1038/nmeth.2089, PMID: 22930834
Sievers F, Higgins DG. 2014. Clustal Omega, accurate alignment of very large numbers of sequences. *Methods in Molecular Biology* **1079**:105–116. DOI: https://doi.org/10.1007/978-1-62703-646-7_6, PMID: 24170397
Sun Y, Schroeder HW, Beausang JF, Homma K, Ikebe M, Goldman YE. 2007. Myosin VI walks "wiggly" on actin with large and variable tilting. *Molecular Cell* **28**:954–964. DOI: https://doi.org/10.1016/j.molcel.2007.10.029, PMID: 18158894
Swaminathan V, Alushin GM, Waterman CM. 2017. Mechanosensation: a catch bond that only hooks one way. *Current Biology* **27**:R1158–R1160. DOI: https://doi.org/10.1016/j.cub.2017.09.023, PMID: 29112867
Thompson PM, Tolbert CE, Shen K, Kota P, Palmer SM, Plevock KM, Orlova A, Galkin VE, Burridge K, Egelman EH, Dokholyan NV, Superfine R, Campbell SL. 2014. Identification of an actin binding surface on vinculin that mediates mechanical cell and focal adhesion properties. *Structure* **22**:697–706. DOI: https://doi.org/10.1016/j.str.2014.03.002, PMID: 24685146
Tropea JE, Cherry S, Waugh DS. 2009. Expression and purification of soluble his(6)-tagged TEV protease. *Methods in Molecular Biology* **498**:297–307. DOI: https://doi.org/10.1007/978-1-59745-196-3_19, PMID: 18988033
Vaezi A, Bauer C, Vasioukhin V, Fuchs E. 2002. Actin cable dynamics and rho/Rock orchestrate a polarized cytoskeletal architecture in the early steps of assembling a stratified epithelium. *Developmental Cell* **3**:367–381. DOI: https://doi.org/10.1016/S1534-5807(02)00259-9, PMID: 12361600
Wang F, Chen L, Arcucci O, Harvey EV, Bowers B, Xu Y, Hammer JA, Sellers JR. 2000. Effect of ADP and ionic strength on the kinetic and motile properties of recombinant mouse myosin V. *Journal of Biological Chemistry* **275**:4329–4335. DOI: https://doi.org/10.1074/jbc.275.6.4329
Wang RY-R, Song Y, Barad BA, Cheng Y, Fraser JS, DiMaio F. 2016. Automated structure refinement of macromolecular assemblies from cryo-EM maps using rosetta. *eLife* **5**:e17219. DOI: https://doi.org/10.7554/eLife.17219
Wasserman MR, Schauer GD, O'Donnell ME, Liu S. 2019. Replication fork activation is enabled by a Single-Stranded DNA gate in CMG helicase. *Cell* **178**:600–611. DOI: https://doi.org/10.1016/j.cell.2019.06.032, PMID: 31348887
Wioland H, Jegou A, Romet-Lemonne G. 2019. Torsional stress generated by ADF/cofilin on cross-linked actin filaments boosts their severing. *PNAS* **116**:2595–2602. DOI: https://doi.org/10.1073/pnas.1812053116, PMID: 30692249
Xu XP, Pokutta S, Torres M, Swift MF, Hanein D, Volkmann N, Weis WI. 2020. Structural basis of αE-catenin-F-actin catch bond behavior. *eLife* **9**:e60878. DOI: https://doi.org/10.7554/eLife.60878, PMID: 32915141
Yamada S, Pokutta S, Drees F, Weis WI, Nelson WJ. 2005. Deconstructing the Cadherin-Catenin-Actin complex. *Cell* **123**:889–901. DOI: https://doi.org/10.1016/j.cell.2005.09.020
Yonemura S, Wada Y, Watanabe T, Nagafuchi A, Shibata M. 2010. alpha-Catenin as a tension transducer that induces adherens junction development. *Nature Cell Biology* **12**:533–542. DOI: https://doi.org/10.1038/ncb2055, PMID: 20453849
Zhang R, Alushin GM, Brown A, Nogales E. 2015. Mechanistic origin of microtubule dynamic instability and its modulation by EB proteins. *Cell* **162**:849–859. DOI: https://doi.org/10.1016/j.cell.2015.07.012, PMID: 26234155
Zheng SQ, Palovcak E, Armache JP, Verba KA, Cheng Y, Agard DA. 2017. MotionCor2: anisotropic correction of beam-induced motion for improved cryo-electron microscopy. *Nature Methods* **14**:331–332. DOI: https://doi.org/10.1038/nmeth.4193, PMID: 28250466
Ziegler WH, Liddington RC, Critchley DR. 2006. The structure and regulation of vinculin. *Trends in Cell Biology* **16**:453–460. DOI: https://doi.org/10.1016/j.tcb.2006.07.004, PMID: 16893648
Zimmermann D, Homa KE, Hocky GM, Pollard LW, De La Cruz EM, Voth GA, Trybus KM, Kovar DR. 2017. Mechanoregulated inhibition of formin facilitates contractile actomyosin ring assembly. *Nature Communications* **8**:703. DOI: https://doi.org/10.1038/s41467-017-00445-3, PMID: 28951543
Zivanov J, Nakane T, Forsberg BO, Kimanius D, Hagen WJ, Lindahl E, Scheres SH. 2018. New tools for automated high-resolution cryo-EM structure determination in RELION-3. *eLife* **7**:e42166. DOI: https://doi.org/10.7554/eLife.42166, PMID: 30412051
Zivanov J, Nakane T, Scheres SHW. 2019. A bayesian approach to beam-induced motion correction in cryo-EM single-particle analysis. *IUCrJ* **6**:5–17. DOI: https://doi.org/10.1107/S205225251801463X, PMID: 30713699

APPENDIX 2

Sarker, M., Lee, H.T., **Mei, L.**, Krokhotin, A., de los Reyes, S.E., Yen, L., Costantini, L.M., Griffith, J., Dokholyan, N.V., Alushin, G.M., et al. (2019). Cardiomyopathy Mutations in Metavinculin Disrupt Regulation of Vinculin-Induced F-Actin Assemblies. Journal of Molecular Biology 431, 1604–1618.

Article

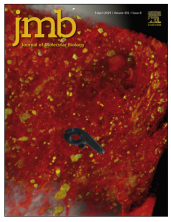

Cardiomyopathy Mutations in Metavinculin Disrupt Regulation of Vinculin-Induced F-Actin Assemblies

Muzaddid Sarker[1], Hyunna T. Lee[1], Lin Mei[2], Andrey Krokhotin[1], Santiago Espinosa de los Reyes[2], Laura Yen[3], Lindsey M. Costantini[4], Jack Griffith[4], Nikolay V. Dokholyan[1], Gregory M. Alushin[2] and Sharon L. Campbell[1]

1 - Department of Biochemistry and Biophysics and Lineberger Comprehensive Cancer Center, *University of North Carolina at Chapel Hill, Chapel Hill, NC 27599, USA*
2 - Laboratory of Structural Biophysics and Mechanobiology, *The Rockefeller University, New York, NY 10065, USA*
3 - Simons Electron Microscopy Center, *New York Structural Biology Center, New York, NY 10025, USA*
4 - Department of Microbiology and Immunology, *University of North Carolina at Chapel Hill, Chapel Hill, NC 27599, USA*

Correspondence to Sharon L. Campbell: *campbesl@med.unc.edu.*
https://doi.org/10.1016/j.jmb.2019.02.024
Edited by: Prof. M.F. Summers

Abstract

Debilitating heart conditions, notably dilated and hypertrophic cardiomyopathies (CMs), are associated with point mutations in metavinculin, a larger isoform of the essential cytoskeletal protein vinculin. Metavinculin is co-expressed with vinculin at sub-stoichiometric ratios in cardiac tissues. CM mutations in the metavinculin tail domain (MVt) occur within the extra 68-residue insert that differentiates it from the vinculin tail domain (Vt). Vt binds actin filaments (F-actin) and promotes vinculin dimerization to bundle F-actin into thick fibers. While MVt binds to F-actin in a similar manner to Vt, MVt is incapable of F-actin bundling and inhibits Vt-mediated F-actin bundling. We performed F-actin co-sedimentation and negative-stain EM experiments to dissect the coordinated roles of metavinculin and vinculin in actin fiber assembly and the effects of three known metavinculin CM mutations. These CM mutants were found to weakly induce the formation of disordered F-actin assemblies. Notably, they fail to inhibit Vt-mediated F-actin bundling and instead promote formation of large assemblies embedded with linear bundles. Computational models of MVt bound to F-actin suggest that MVt undergoes a conformational change licensing the formation of a protruding sub-domain incorporating the insert, which sterically prevents dimerization and bundling of F-actin by Vt. Sub-domain formation is destabilized by CM mutations, disrupting this inhibitory mechanism. These findings provide new mechanistic insights into the ability of metavinculin to tune actin organization by vinculin and suggest that dysregulation of this process by CM mutants could underlie their malfunction in disease.

Introduction

Vinculin is an essential cytoskeletal protein that localizes to focal adhesions and adherens junctions [1,2]. At these sites of adhesion, vinculin acts as a scaffold to link transmembrane receptors to actin filaments, thereby playing a crucial role in cell adhesion, motility, and force transmission between cells and the cell–matrix interface. Without vinculin, defects in heart and nerve formation are observed, and mouse embryos do not survive past E10 [3]. In addition, lack of vinculin in cells leads to rounded morphology, increased motility [3,4] and resistance to apoptosis and anoikis [5].

Vinculin is a 117-kDa protein that functions as a molecular scaffold. It comprises a large 90-kDa head domain (Vh), a flexible proline-rich linker, and a 22-kDa tail domain (Vt) [6]. Vh interacts with talin at focal adhesions, α-catenin at cell–cell junctions, and α-actinin [7,8,9]. The proline-rich linker that connects Vh to Vt can bind to VASP, vinexin, CAP/ponsin, and the Arp2/3 complex [10,11,12,13]. Vt directly binds to filamentous actin (F-actin) [14], phosphatidylinositol 4,5-bisphosphate [15] and Raver1

[16]. Autoinhibitory interactions between Vh and Vt retain vinculin in its closed inactive state, which obscures ligand binding [6]. Although mechanisms of activation are not fully understood, it is currently believed that engagement of talin or catenin to Vh in conjunction with binding of additional ligands such as actin [2,7,17], post-translational modifications [18], and/or force [19,20,21,22] promotes activation and exposure of multiple ligand binding sites.

While vinculin is ubiquitously expressed, metavinculin, a larger splice isoform, is selectively expressed in smooth and cardiac muscle cells [23,24,25]. Metavinculin expression is tightly controlled at sub-stoichiometric levels relative to vinculin (9%–42%) and correlates with contractile needs of muscle cells [26,27]. Reduced metavinculin expression level is associated with cardiomyopathy (CM) and disorganized intercalated disc structures [28], suggesting that metavinculin is necessary for the maintenance of smooth muscle actin-membrane adhesion sites and in force generation and transmission through its interaction with the actin cytoskeleton.

While the tail domain of vinculin possesses an N-terminal strap (NtS) followed by a 5-helix bundle fold and a C-terminal hairpin (CtHP) [6], metavinculin contains an additional exon that encodes a 68-amino-acid insert between helix 1 (H1) and helix 2 (H2) within the tail domain (MVt) [23]. MVt also adopts a 5-helix bundle fold similar to Vt; however, the sequence that makes up H1 and NtS of Vt is displaced by homologous H1′ and NtS′ sequences contained within the 68-amino-acid insert [29]. Similar to vinculin, metavinculin can directly associate with F-actin [29,30,31]; however, unlike Vt, MVt does not bundle filamentous actin *in vitro* [30,31,32]. Point mutations identified within the 68-residue insert cause altered actin organization and heart disease, notably dilated cardiomyopathy (DCM) and hypertrophic cardiomyopathy (HCM) [28,32,33]. The A934V and ΔL954 metavinculin mutations are associated with DCM [32], whereas the R975W mutation has been identified in patients with both DCM and HCM [33]. Both DCM and HCM are diseases of myocardium that prevent normal blood flow within the heart resulting from disruption in force transmission, consistent with the prevailing notion that metavinculin–actin interactions play a key role in force transmission.

We and others have previously shown that binding of F-actin to Vt causes a conformational change in Vt that promotes dimerization and actin filament bundling [34,35]. However, the structure of the actin-induced Vt dimer is currently unknown. As H1 is sensitive to proteolysis upon addition of F-actin [36] and is not observed in our cryo-EM reconstruction of the Vt–actin complex [31], H1 likely partitions away from the helix bundle upon engagement with filamentous actin to promote vinculin dimerization. Similarly, electron density for metavinculin H1′ is lacking in the cryo-EM reconstruction of the metavinculin–actin complex [31]. Notably, the presence of displaced H1 appears to interfere with the ability of metavinculin to bundle F-actin, as its deletion promotes actin filament bundling [29].

While vinculin and metavinculin show similar modes of binding to F-actin, metavinculin is unable to bundle actin filaments. However, metavinculin mutants associated with DCM and HCM are able to form higher-order actin assemblies *in vitro* [32]. As metavinculin is co-expressed with vinculin in smooth muscle and cardiac tissues [23,25,26,27], it is likely that vinculin and metavinculin coordinately regulate the architecture of F-actin networks. In fact, we and others have previously observed that the presence of metavinculin at sub-stoichiometric ratios impairs vinculin-mediated F-actin bundling [31,36], suggesting that MVt may negatively regulate Vt-mediated actin bundling.

To better understand the coordinated role of metavinculin and vinculin in F-actin fiber assembly and the consequences of CM-related mutations, we conducted a series of actin co-sedimentation and negative-stain EM experiments utilizing MVt and Vt constructs. Consistent with our previous findings [31], MVt is unable to induce actin bundling, whereas the presence of sub-stoichiometric amounts MVt relative to Vt inhibits the assembly of actin filaments into parallel bundles. In contrast to wild-type (WT) MVt, and consistent with previous fluorescence microscopy data [32], MVt CM mutants alone weakly induce the formation of disordered higher-order F-actin assemblies. Strikingly, in the more physiological scenario of Vt–MVt mixtures, CM mutants lose the ability to inhibit Vt-mediated bundles, instead promote the formation of very large assemblies, which are morphologically consistent with aggregations of Vt-mediated bundles. To investigate the molecular basis for MVt's negative regulation of Vt-mediated actin bundling, we performed discrete molecular dynamics (DMD) simulations. Actin binding to vinculin promotes release of H1 from the tail domain helix bundle, exposing an interface in vinculin that promotes dimerization [31]. However, in the case of metavinculin, our simulations suggest that the insert and displaced H1 form a new structural element, a protruding sub-domain, with H1′ released from the helix bundle upon actin binding. This additional MVt sub-domain, generated upon actin engagement, could sterically block actin assembly into parallel F-actin bundles. Our DMD simulations also indicate that CM mutations within the C-terminus of metavinculin destabilize formation of this protruding actin-induced sub-domain, likely exposing residues which can mediate the formation of disordered assemblies. In summary, our results provide new mechanistic insights into the coordinated activities of vinculin and metavinculin in controlling F-actin network architecture and suggest that

regulation of vinculin-mediated actin bundling activity by metavinculin constitutes one key function that is compromised by the CM mutants.

Results

WT MVt domain does not induce F-actin bundling

The F-actin binding sites of vinculin and metavinculin are located in their tail domains, Vt and MVt, respectively, but these binding sites are occluded in the context of the full-length proteins due to autoinhibitory interactions between the head and tail domains. As the tail domains are functional in isolation, we have used recombinantly expressed Vt and MVt protein constructs in this study (shown by schematics in Fig. 1A) to probe the effects of MVt WT and MVt CM mutations on the formation of actin assemblies in the absence and presence of Vt. The Vt domain encompasses 188 C-terminal residues of vinculin and consists of five α-helices (H1–H5) flanked on both sides by flexible regions, an NtS and a CtHP. MVt contains an extra 68-residue insert between helices H1 and H2 of the corresponding sequence of Vt. Part of the insert displaces the 37 N-terminal residues comprising H1 (PDB ID 3MYI) and the NtS, with H1′ and NtS′ [29]. Here we investigate single-point mutations specific to the metavinculin insert region, namely, A934V, ΔL954 and R975W, associated with CMs and atherosclerosis [32,37]. We have also utilized a construct we designate as MVtp, which includes the additional 21-residue proline-rich linker preceding the NtS of MVt.

The core regions of both Vt and MVt comprise a compactly folded H2–H5 bundle. In the absence of actin, the H1–H5 helices are observable in X-ray crystal structures of full-length vinculin and Vt, and correspondingly, H1′–H5 are resolved in crystal structures of full-length metavinculin and MVt [29]. However, the regions preceding the H2–H5 bundle in both Vt and MVt were not detectable in our previously published cryo-EM reconstructions of these domains bound to F-actin [31]. We reported a twisting structural rearrangement of H2–H5 concomitant with actin binding that displaces H1/H1′ from the helical bundle by remodeling its hydrophobic core, which we inferred renders these regions disordered and/or dynamic. Vt and MVt both engage F-actin in an indistinguishable manner at subnanometer resolution through their compactly folded H2–H5 regions [31], which are identical in sequence (Fig. 1B).

Before investigating the effects of CM mutants, we first validated our WT Vt and MVt constructs to recapitulate previously reported binding and bundling activities [30,31,32,36], and also verified F-actin bundling inhibition by both MVt and MVtp proteins. We acquired negative-stain EM images of actin filaments in the absence and presence of WT

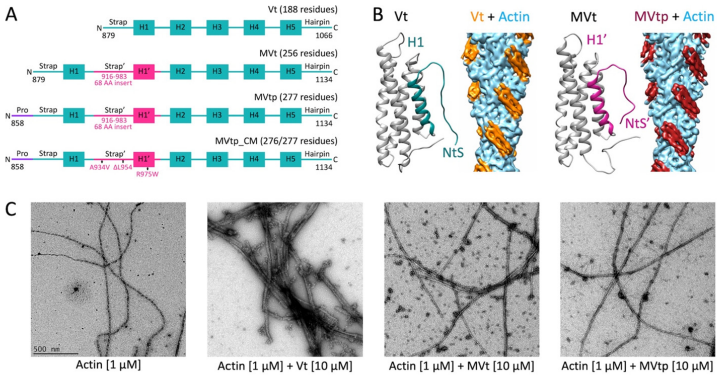

Fig. 1. MVt domain exhibits similar F-actin binding affinity but dramatically reduced bundling (crosslinking) of the filaments relative to the Vt domain. (A) Schematic representation of Vt and MVt constructs used in this study. Vt consists of five α-helices (H1–H5) flanked by an NtS and a CtHP. MVt contains a 68-residue insert between helices H1 and H2 that replaces the original H1 and NtS by H1′ and NtS′. MVtp includes the 21-residue proline-rich linker preceding the NtS of MVt. Mutations within the metavinculin insert region, namely, A934V, ΔL954 and R975W, have been identified in CMs. (B) X-ray crystal structures of Vt (PDB ID 1TR2) and MVt (PDB ID 3MYI) as well as the cryo-EM reconstruction of Vt–actin (EMD-6446) and MVt–actin (EMD-6447) interfaces. Vt and MVt comprise a highly similar 5-helix bundle fold in the absence of actin, where H1′ of MVt swaps with H1 of Vt. Upon actin engagement, regions N-terminal of H2 are not detectable in the cryo-EM reconstructions. (C) Negative-stain EM images of actin filaments. Micrographs are acquired at the same magnification (scale bar represents 500 nm, shown in the left panel). Crosslinking or bundling of actin filaments by Vt generates thick fibers. In contrast, MVt and MVtp do not promote actin filament bundling.

Vt, MVt and MVtp (Fig. 1C). The actin-alone sample showed single, linear actin filaments, whereas Vt induced crosslinking of filaments into parallel bundles as expected, resulting in the formation of thick fibers. When either MVt or MVtp was added to F-actin instead of Vt, F-actin bundling was dramatically reduced, with few observable thick fibers. This is consistent with previous reports by our group and others that MVt does not induce large linear actin bundles like Vt [30,31,32,36], indicating that the MVt insert region prohibits actin-induced MVt dimerization and negatively regulates F-actin bundling. In addition, inclusion of the proline-rich linker, as in MVtp, has a minor, albeit significant effect on its regulatory activity.

MVt CM mutants induce higher-order F-actin assemblies

Having validated our constructs and confirmed similar behavior of MVt and MVtp by negative-stain EM (Fig. 1C), we next used F-actin co-sedimentation assays to examine the F-actin binding and aggregation activities of MVtp constructs featuring the CM mutations A934V, ΔL954 and R975W. First, we compared the F-actin binding of MVtp WT and CM mutants relative to Vt. Samples containing actin (10 or 20 μM) plus individual tail domains (10 μM) were subjected to high-speed centrifugation (see Materials and Methods for experimental details). Under these conditions, the supernatant (S) contains unbound tail domain, while the pellet (P) contains F-actin and bound protein. The amount of tail domain present in each fraction was analyzed by SDS-PAGE (Fig. 2A) and quantified using ImageJ [38]. WT Vt, MVt, and MVtp, as well as all three MVtp CM mutants, exhibited similar binding affinity to F-actin (Fig. 2B). From these data, we conclude that MVt mutations do not impair F-actin binding. This is consistent with the known actin binding interface, comprising the compactly folded H2–H5 region,

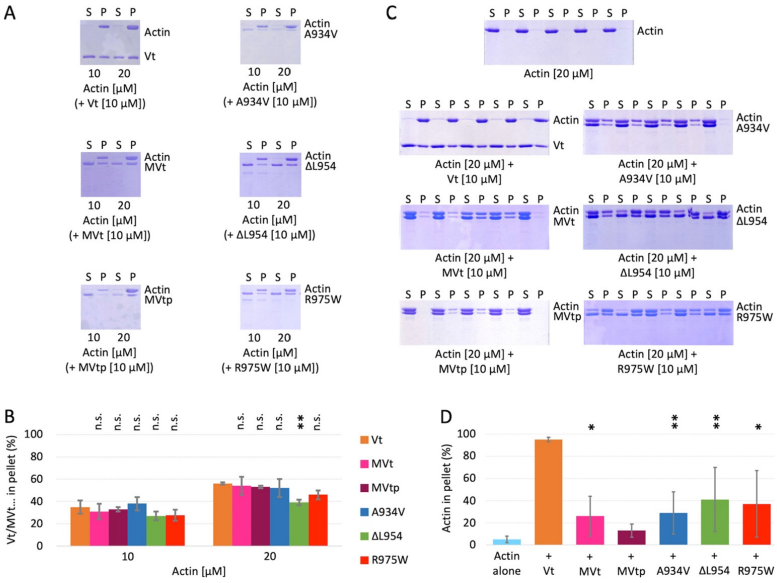

Fig. 2. MVt domain WT and CM mutants exhibit similar F-actin binding but differ in the ability to form higher-order actin assemblies. (A) Representative SDS-PAGE results obtained from high speed F-actin co-sedimentation (100,000 g, 30 min) assays in the presence of Vt, MVt, or MVtp WT and CM proteins (S, supernatant; P, pellet). (B) Quantification of protein fractions present in pellets representing individual sub-populations of Vt, MVt, or MVtp constructs bound to F-actin. Error bars represent standard deviation (SD) (n = 2, 2 replicates for each n). (C) Representative SDS-PAGE results obtained from low-speed F-actin co-sedimentation (12,000 g, 15 min) assays in the presence of Vt, MVt, or MVtp WT and CM proteins. (D) Quantification of actin fractions in pellets representing sub-populations of F-actin present in bundles or in higher-order assemblies induced by Vt, MVt, or MVtp constructs. Error bars represent SD (n = 2, 5 replicates for each n). Vt and MVt or MVtp WT (labeled as MVt and MVtp), as well as all MVtp CM mutants (labeled as A934V, ΔL954 and R975W), bind actin filaments similarly. However, while Vt drives almost the entire population of actin filaments into bundles or higher-order assemblies (~95%), MVt or MVtp WT display little assembly formation (~15%–20%). In contrast, increased F-actin assembly formation is observed for MVtp CM mutants (~30%–40%) compared to MVtp WT. Statistical significances in panels B (with respect to Vt) and D (with respect to MVtp) are indicated by the following: non-significant (n.s.), $*p < 0.05$, $**p < 0.01$.

which is not predicted to be impacted by any of the CM mutations [31].

We next employed low-speed centrifugation assays to assess the F-actin crosslinking activities of this same panel of constructs (see Materials and Methods for experimental details). Under these conditions, only large cross-linked assemblies of F-actin and bound protein are pelleted, while individual actin filaments are retained in the supernatant. The fraction of actin present in the pellet was quantified as described above to determine the subpopulations of F-actin involved in higher-order assemblies (Fig. 2D). It should be noted that while this is often referred to as a "bundling" assay, the pellets from low-speed centrifugation may contain both thick fibers representing canonically bundled actin filaments, as in the case with Vt (Fig. 1C), but also other sufficiently large structures (ordered or disordered) that pellet under these conditions. These assays were conducted in parallel with negative-stain EM, to visualize the actin assemblies formed in the presence of Vt and MVt proteins. For isolated F-actin, little actin was found in the pellet (~5%), but upon the addition of Vt, almost all of the F-actin was found in the pellet (~95%), consistent with the negative-stain EM data (Fig. 1C). Also consistent with the negative-stain EM results (Fig. 1C), the amount of actin found in the pellet was dramatically reduced when MVt was added (~26%) and to an even lower amount when MVtp was added (~13%). Interestingly, an increase in the amounts of pelleted actin was found for the MVtp CM mutants: A934V (~29%), ΔL954 (~41%), and R975W (37%).

Quantitative negative-stain EM assay probes F-actin assemblies

To visualize and quantify differences in actin filament organization in the presence of Vt and MVt WT, as well as MVt CM mutants, we developed a quantitative negative-stain transmission electron microscopy (TEM) assay (Fig. 3, Supplementary Fig. 1). The quantitative power of traditional negative-stain EM imaging of F-actin assemblies is limited by selection bias, as choosing which part of the grid to image is dependent on input of an experienced user. In addition, the frequently irregular structure of these assemblies, compounded by their inherently variable contrast after negative staining, is refractory to image analysis methodology which depends on classification or averaging.

To overcome selection bias, we targeted grid squares at low magnification where their contents were invisible. We then imaged the entirety of each targeted square at a magnification sufficient to resolve individual actin filaments, tiling it with overlapping fields of view which were subsequently stitched together (Fig. 3A). We next implemented an image analysis procedure to detect and quantify the size of higher-order assemblies which is insensitive to their variable internal structure. Images were thresholded (the only step requiring user input due to stain variability) and binarized, then automatically segmented into continuous regions using the "Analyze Particles" procedure in ImageJ [38]. To analyze these data, we plot the cumulative fraction of F-actin + bound proteins detected in all regions *versus* region size (Fig. 3C, Supplementary Fig. 1), which we find to be a sensitive metric of higher-order assembly state that is robust against variations in background noise between different datasets (see Materials and Methods for details).

MVt CM mutants form mesh-like actin assemblies

To validate this assay, we first examined the known differential F-actin assembly properties of Vt, which strongly bundles actin, in comparison to MVt WT, which does not induce assemblies as previously established [30,31,32,36], and here re-validated through qualitative negative-stain EM and quantitative low-speed co-sedimentation assays (Figs. 1C and Fig. 2C–D). As expected, although other assembly states are present as a minor fraction, we find that the presence of Vt primarily induces the formation of linear actin bundles (Fig. 3A) and correspondingly shifts the distribution towards larger assemblies *versus* actin alone (Fig. 3C). While the presence of MVt WT did produce a slight but significant shift relative to actin alone, the effects were modest, with substantially fewer large assemblies than for Vt (Fig. 3C). Consistently, no obvious bundles and few other assemblies were visible in the images, which were qualitatively similar in appearance to F-actin alone (Fig. 3A).

We next examined the effects of MVt CM mutants. These experiments, which require small amounts of material, were initiated mostly with the tail domain constructs (i.e., MVt) and later we confirmed that inclusion of the proline-rich linker (i.e., MVtp) does not adversely affect metavinculin's regulatory role (Figs. 1C and 2C–D). Thus, we investigated R975W and ΔL954 in the MVt background and MVtp A934V in our negative-stain EM experiments. As our studies establish MVt and MVtp show similar activity profiles (Figs. 1 and 2), we believe that experiments between mutants in these backgrounds can safely be compared.

Consistent with low-speed co-sedimentation assays (Fig. 2C–D), we observed a significant increase in assemblies in the presence of CM mutants MVtp A934V, MVt ΔL954, and MVt R975W, with R975W having the most dramatic effect (Fig. 3C), in accordance with the severity of disease caused by this mutation in patients [32,33]. Examination of the images shows primarily an irregular, mesh-like organization of actin filaments (Fig. 3B), unlike the majority species present as linear bundles formed in the presence of Vt (Figs. 1C and 3A).

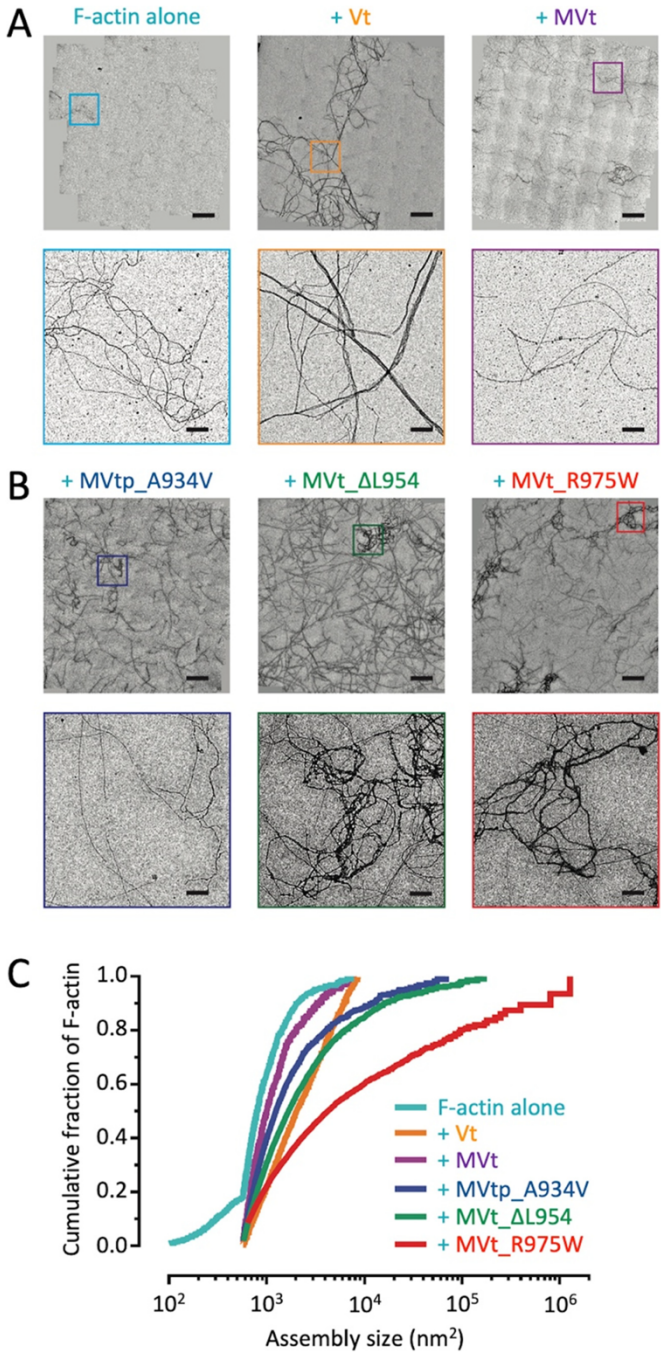

Fig. 3. Metavinculin CM mutants promote formation of disordered, mesh-like F-actin assemblies. (A) Stitched negative-stain EM images of F-actin alone and in the presence of WT Vt and MVt proteins (bars represent 10 μm). Zoomed views of the boxed regions are shown in the bottom panel (bars represent 1 μm). (B) Stitched negative-stain EM images of F-actin in the presence of MVt or MVtp proteins featuring CM mutations (bars represent 10 μm). Zoomed views of the boxed regions are shown in the bottom panel (bars represent 1 μm). (C) Cumulative plots of F-actin assemblies from the indicated conditions. Pairwise comparisons show all distributions to be significantly different (KS test, $p < 0.01$). $N \geq 10$ fields and $n \geq 764$ regions were quantified for each condition. F-actin, 0.5 μM; Vt/MVt/MVtp constructs, 2.0 μM.

MVt CM mutants fail to inhibit Vt-induced higher-order actin assemblies

Metavinculin is co-expressed with vinculin at sub-stoichiometric levels in smooth muscle and cardiac tissues [25,26,27]. We and others have previously reported that the presence of sub-stoichiometric MVt impairs Vt-mediated F-actin bundling [31,36]. Hence, metavinculin likely acts as a negative regulator of vinculin-mediated F-actin bundling. Here, we employed low-speed pelleting assays to probe the effects of MVtp CM mutants in comparison to MVtp WT, on Vt-induced F-actin assemblies. Three sets of actin co-sedimentation data were acquired, with 20 μM actin and Vt:MVtp at 5:5, 10:10, and 10:5 μM (Fig. 4). Supernatant and pellet fractions were analyzed by SDS-PAGE (Fig. 4A–C) and quantified (Fig. 4D) as described above. In the presence of MVtp WT, a proportionate reduction of Vt-induced F-actin assemblies was observed: as ~47–52% F-actin was found in the pellet for Vt:MVtp at 1:1 and ~74% F-actin was found in the pellet for Vt:MVtp at 2:1, as opposed to 95% F-actin in the pellet for Vt alone. Interestingly, for all 3 MVtp CM mutants, at both 1:1 and 1:2 ratios with Vt, almost all of F-actin was found in the pellet fractions: ~87–95% for A934V, ~81–90% for ΔL954, and ~84–89% for R975W. Thus, in a dramatic contrast to the MVtp

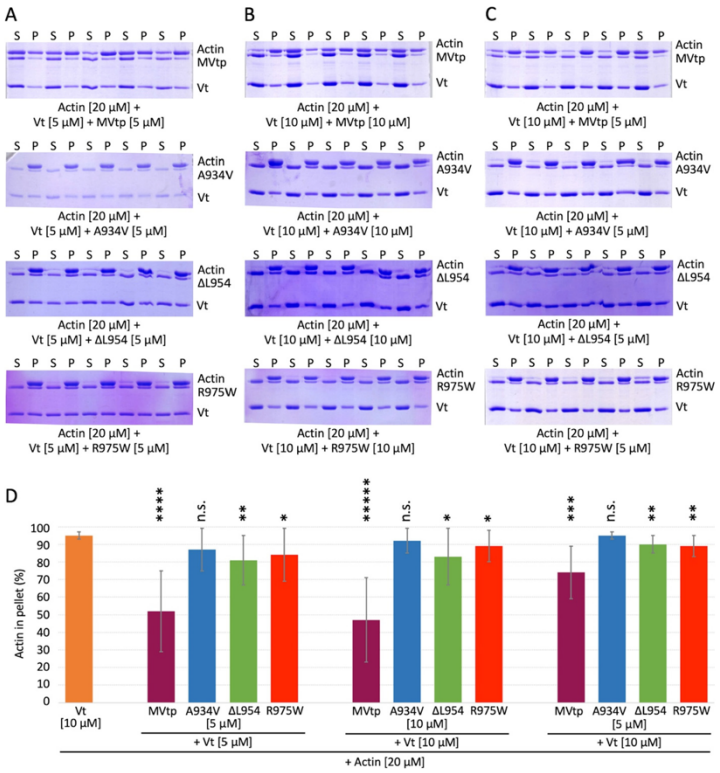

Fig. 4. MVt CM mutants fail to inhibit Vt-induced F-actin bundling. (A–C) Representative SDS-PAGE analysis of low-speed F-actin co-sedimentation (12,000 g, 15 min) assays incubated with Vt in the presence of MVtp WT protein (labeled as MVtp) or MVtp CM mutants (labeled as A934V, ΔL954, and R975W) at indicated concentrations (S, supernatant; P, pellet). (D) Quantification of the actin fraction present in pellets representing higher-order F-actin assemblies that include F-actin bundles in case of Vt. Error bars represent standard deviation (SD) (n = 2, 5 replicates for each n). At both 1:1 and 2:1 ratios with Vt, MVtp WT proportionately reduces the amounts of higher-order F-actin assemblies, but in all cases, MVtp CM mutants fail to inhibit such Vt-induced higher-order F-actin assemblies. Statistical significances in panel D are indicated by the following: non-significant (n.s.), *$p < 0.05$, **$p < 0.01$, ***$p < 0.001$, ****$p < 0.0001$, *****$p < 0.00001$ with respect to Vt.

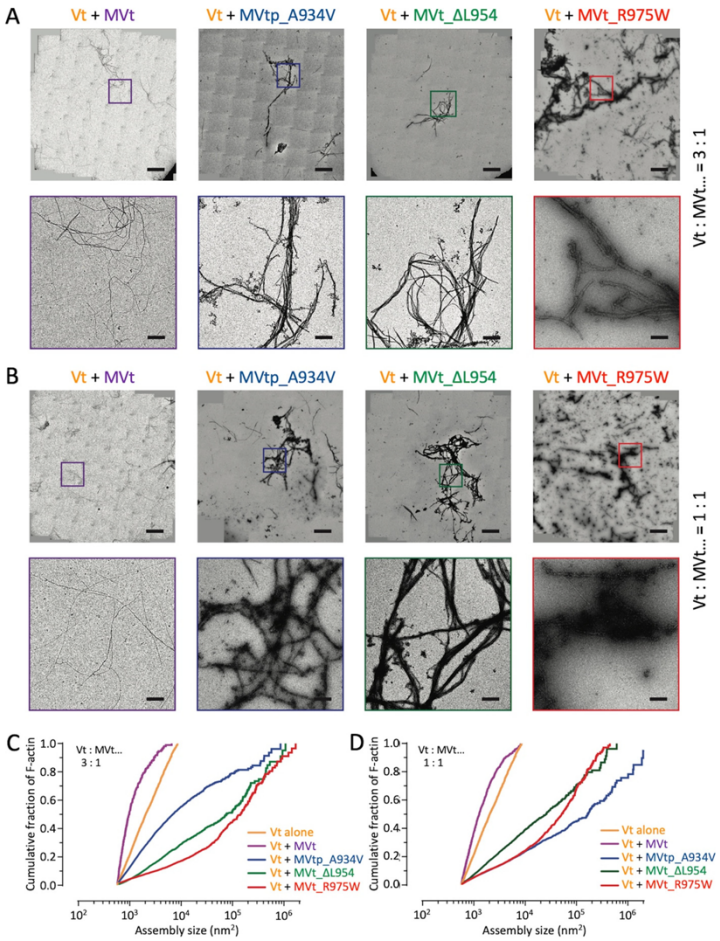

Fig. 5. MVt CM mutants aggregate Vt-induced actin bundles. (A) Stitched negative-stain EM images of F-actin in the presence of Vt + WT or CM mutant MVt(p) at Vt to MVt(p) ratio of 3:1 (bars represent 10 μm). Zoomed views of the boxed regions are shown in the bottom panel (bars represent 1 μm). F-actin 0.5 μM, Vt 3.75 μM, and MVt(p) 1.25 μM. (B) Stitched negative-stain EM images of F-actin in the presence of Vt + WT or CM mutant MVt(p) at Vt to MVt(p) ratio of 1:1 (bars represent 10 μm). Zoomed views of the boxed regions are shown in the bottom panel (bars represent 1 μm). F-actin 0.5 μM, Vt 2.5 μM, and MVt(p) 2.5 μM. (C) Cumulative plots of F-actin assemblies in the presence of Vt to MVt(p) at ratio of 3:1. (D) Cumulative plots of F-actin assemblies in the presence of Vt to MVt(p) at ratio of 1:1. Pairwise comparisons show all distributions to be significantly different (KS test, $p < 0.0001$) in panels C and D. N > 10 fields and n > 655 regions were quantified for each condition in panel C, and N > 10 fields and n > 2241 regions were quantified for each condition in panel D. Vt alone data are replotted from Fig. 3.

WT, the amount of F-actin existing in the pellets representing higher-order actin assemblies was reduced only marginally by the MVtp CM mutants. These results indicate that unlike WT MVt or MVtp, MVtp CM mutants are unable to negatively regulate higher-order actin assemblies in the presence of Vt.

MVt CM mutants coalesce Vt-mediated bundles into large higher-order actin assemblies

We next employed negative-stain EM to visualize the morphology and quantify the size distributions of higher-order assemblies formed in the presence of

both Vt and MVt or MVtp WT and CM mutants. Consistent with previous reports [30,32,36] and co-sedimentation assays (Fig. 4), we find that the presence of MVt WT inhibits the bundling activity of Vt at both a sub-stoichiometric 1:3 ratio (Fig. 5A, C) and a stoichiometric 1:1 ratio (Fig. 5B, D). An examination of the images suggests a reduction in large parallel bundles (Fig. 5A, B). However, we find that all MVt or MVtp CM mutants dramatically increase the size of F-actin assemblies formed in the presence of Vt, at both ratios (Fig. 5A–D). These results are consistent with our co-sedimentation assays demonstrating almost the entire population of actin pelleting in the presence of Vt + MVtp CM mutants as with Vt alone (Fig. 4), but additionally suggest that even larger assemblies are formed than in the presence of Vt alone.

The morphology of these assemblies is consistent with a combined effect between what we observe for the MVt or MVtp CM mutants alone, which primarily form disordered meshes (Fig. 3B) and Vt-mediated bundling. Linear bundles are clearly visible (Fig. 5A–B); however, these are frequently coated with large, amorphous aggregates (Fig. 5A–B), which are rarely observed in the presence of Vt alone, MVt alone, or Vt + MVt WT (Fig. 3A–B). This observation is consistent with MVt or MVtp CM mutants driving the coalescence and aggregation of Vt-induced actin bundles rather than inhibiting their formation, as is the case for MVt WT.

The MVt-specific insert region forms an additional sub-domain upon actin binding

In the cryo-EM reconstruction of the MVt–F-actin complex [31], density for the N-terminus, including H1′, the displaced H1, and straps, was not observable. This is likely due to dynamics or disorder associated with these regions. To gain structural insight into rearrangements associated with MVt NT, CT, and the insert upon actin binding, we employed DMD simulations [39]. Our model system comprises a single MVt including residues 896–1134 bound to an actin homodimer (F-actin) using the deposited model based on the cryo-EM reconstruction as the starting point (PDB ID 3JBK) for MVt residues 985–1115 and actin. The simulations were performed using replica exchange for 2 million steps (see Materials and Methods for details). One hundred minimal energy structures were selected and clustered.

We identified two clusters (Fig. 6), which differ in N- and C-termini conformations. While structures from the first cluster have tightly intertwined N- and C-termini (Fig. 6A), structures from the second cluster show the C-terminus interacting with the surface of F-actin (Fig. 6B). The common feature of both clusters is formation of a new additional structural sub-domain protruding outwards from F-actin. We further explored stability of the protruding sub-domains in both clusters. We subjected structures representing centroids of these clusters to DMD simulations. For each structure, we ran 10 independent simulations at two different temperatures [T_1 = 0.5 kcal/(mol k_B) and T_2 = 0.55 kcal/(mol k_B)]. In further support of the protruding MVt sub-domain that is formed upon F-actin engagement, the insert-dependent protruding structural element did not unfold and appeared stable throughout the simulations (Supplemental Videos 1 and 2). We argue that this sub-domain mediates unique biological functions of MVt relative to Vt, such as the inability to produce F-actin bundles [30,31,32] and the ability to suppress Vt-mediated F-actin bundling [31,36]. We also propose that formation of this higher-order structure may sterically occlude formation of tightly packed parallel bundles. As the CM mutants perturb the ability of MVt to inhibit bundling, we hypothesize that CM mutations within the insert impair formation of the protruding globular structure formed at the N-terminus.

To test this hypothesis, we assessed the effect of these mutants on the stability of the globule for each of the two clusters [40]. We find that A934V and R975W are indeed destabilizing to formation of the

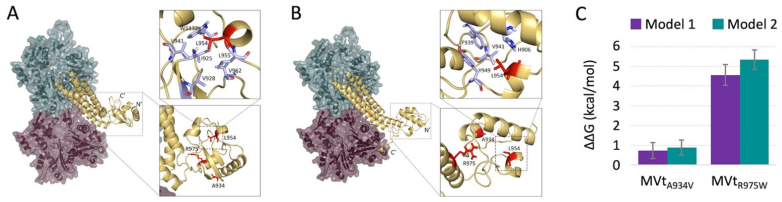

Fig. 6. Actin binding to MVt may induce a higher-order structural element that prevents F-actin bundling. DMD simulations identify two distinct MVt–actin clusters. In contrast to Vt, actin binding to MVt induces a protruding sub-domain. Representative MVt and F-actin models show that additional structure is formed between N-terminus, insert, and C-terminus in the first cluster (A) and between N-terminus and insert in the second cluster (B). MVt residues mutated in CMs (A934, L954, R975) are colored red. Point mutations A934V and R975W cause an increase in ΔΔG (D) and thus destabilize the folded sub-domain. These findings suggest that MVt CM mutants fail to antagonize Vt-induced actin bundling due to destabilization of the additional folded structure.

actin-induced MVt higher-order structure observed in both clusters. For the first model, ΔΔG-A934V = 0.73 ± 0.41 and ΔΔG-R975W = 4.56 ± 0.52, and for the second model, ΔΔG-A934V = 0.88 ± 0.39 and ΔΔG-R975W = 5.34 ± 0.49. We are unable to calculate ΔΔG for the ΔL954 since backbone is altered by the deletion [40]. However, we note that in each of the models, L954 forms an extensive network of hydrophobic contacts (zoomed in regions, Fig. 6A–B) and its deletion would be expected to cause disruptions of these networks. Interestingly, correlating with the severity of CM mutations [32,33], the R975W exhibits a much higher ΔΔG.

Discussion

Debilitating heart conditions resulting from CMs are a major health issue. According to the Centers for Disease Control and Prevention, as many as 1 in 500 adults may have this condition [41,42]. Both DCM and HCM have been shown to be associated with inherited and sporadic mutations in genes encoding the cardiac tissue-specific vinculin isoform, metavinculin. Here we have investigated the effects of disease-associated point mutations that occur within the 68-residue metavinculin insert that differentiates the actin-binding tail domains of vinculin (Vt) and metavinculin (MVt). We and others have previously shown that MVt lacks the actin bundling activity of Vt, and furthermore that MVt can negatively regulate the formation of Vt-induced bundles at physiologically relevant sub-stoichiometric ratios [26,27]. It is interesting to note that, while vinculin is ubiquitously expressed in all tissue types, metavinculin is co-expressed only in cardiac and smooth muscle cells. Both of these cell types exhibit a high degree of contractility for proper functioning, with increased metavinculin expression corresponding to the contractile load on the tissue [26]. Cardiomyocytes, in particular, undergo rapid contraction and expansion during beating for regular heart function. It is plausible that if only vinculin is present, the heart muscle would become stiff due to a large network of thick F-actin fibers and would not retain the necessary contractile properties. Co-expression of metavinculin may thus reduce vinculin-mediated actin bundling so that cardiac cells remain flexible and functional, acting as a molecular rheostat. The main finding of our study, that metavinculin CM mutants are dysfunctional in this regard, makes the strong prediction that cardiomyocytes expressing them should stiffen, and experiments are ongoing to test this hypothesis.

In this paper, we dissect the biophysical mechanisms underlying the metavinculin–vinculin interplay in F-actin fiber formation, and the dysregulation of this process by disease-associated point mutations in metavinculin. We previously reported that the N-terminal helices in both Vt (H1) and MVt (H1′) are released from the H2–H4 helical bundle upon actin engagement, and that Vt H1 residue M898, which is buried in the bundle's hydrophobic core in the pre-bound conformation, is important for actin bundling by Vt [31]. This led us to speculate that the H1 could mediate bundling contacts between Vt molecules after actin binding (Fig. 7A), and furthermore, that released H1′ and NtS′ plus upstream disordered sequence in MVt could be important for its inhibitory

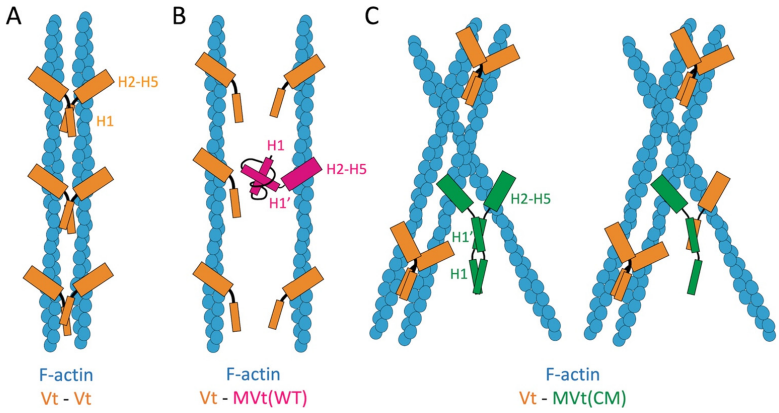

Fig. 7. Model for inhibition of Vt-induced F-actin bundle by WT MVt [labeled as MVt(WT)] but failure of that by MVt CM mutants [labeled as MVt(CM)]. (A) Release of H1 upon F-actin engagement enables Vt dimerization, thus resulting in parallel F-actin bundle formation. (B) An additional protruding structural sub-domain formed by the insert and displaced H1 at the N-terminus of MVt(WT) blocks homo- or hetero-dimer formation with Vt, thus preventing F-actin bundling. (C) The protruding sub-domain is destabilized by the CM related mutations in MVt(CM), resulting in disordered F-actin assemblies due to alternative interactions with another subunit of MVt(CM) (left) or a subunit of Vt (right).

activity by unknown mechanisms. As metavinculin CM-associated point mutants are located within the insert composing H1′ and NtS′, but distal from the direct actin-binding H2–H4 regions, we hypothesized that these lesions would compromise MVt's regulation of Vt-mediated actin bundling without impacting actin binding. The results we present here are broadly consistent with this model. Using co-sedimentation assays, we find that all of the CM mutants we examined have unimpaired actin binding affinity. However, both co-sedimentation assays and negative-stain EM experiments clearly demonstrate that all of the mutants have a strikingly similar defect in regulating Vt's actin bundling activity. These results strongly indicate that the H1′–NtS′ region is required for metavinculin's regulation of vinculin and furthermore motivate us to speculate that defects in this process may underlie the pathophysiology of metavinculin CM mutants *in vivo*, a hypothesis that will guide future cell biological and animal studies.

Mechanistically, our studies lead us to propose a steric occlusion model for metavinculin's ability to negatively regulate vinculin-mediated actin bundling in sub-stoichiometric amounts, orchestrated by differential folding of the MVt domain upon actin binding. Our simulation studies suggest that the MVt specific-insert coordinates the folding of a protruding globular sub-domain upon actin-binding-induced release from the H2–H4 helical bundle. While the detailed structure of the Vt-dimer that promotes 3D actin bundles is unknown and remains an important subject for future studies, electron tomographic studies of Vt-induced 2D F-actin arrays on lipid monolayers suggested that filaments are very tightly apposed when cross-linked by Vt, with intimate contacts between Vt molecules mediating the interface [43]. We thus propose that the MVt sub-domain acts a steric block and prevents actin filaments from coming close enough together for Vt molecules to bind (Fig. 7B). We note that this simple model readily explains the ability of sub-stoichiometric amounts of MVt to inhibit Vt bundling, as it does not require any specific molecular interactions between MVt and Vt to, for example, occupy a binding interface required for dimerization on Vt.

Consistent with this model, our computational studies suggest that MVt CM mutants destabilize sub-domain formation, thereby removing the steric block to Vt dimerization and bundle formation (a loss of function). Furthermore, the R975W substitution had the greatest impact on $\Delta\Delta G$ of sub-domain formation (Fig. 6C) consistent with the enhanced severity of this lesion *in vivo* [32,33] relative to the other the CM mutations we tested [32]. However, the sub-domain blockage model can only partially explain the behavior we observed for the CM mutants. All of the mutants we tested also have a gain-of-function effect on their own, inducing increased formation of higher-order F-actin assemblies (Fig. 3) with a disordered, mesh-like morphology. Furthermore, our studies suggest that the CM mutants drive the coalescence of Vt-induced bundles into aberrantly large assemblies (Fig. 5), which could also play a role in their pathophysiology *in vivo*. We speculate that CM mutations stimulate aggregation through the MVt insert region, which becomes exposed due to defects in sub-domain or globule folding, an effect that would be enhanced by high local concentrations within F-actin assemblies (Fig. 7C). Overall, our results suggest that small molecules that enhance the folding and stability of the predicted MVt globule may have therapeutic potential for patients with CM mutations in the metavinculin insert, abrogating both loss- and gain-of-function effects, and the findings we have presented will motivate future efforts in this direction.

While our studies have focused on Vt and MVt interactions with F-actin, vinculin is a scaffold protein that interacts with a number of proteins and inositol phospholipids (e.g., phosphatidylinositol 4,5-bisphosphate). Hence, the metavinculin insert may alter association with other ligands that bind to the tail domain. Experiments are in progress to investigate whether metavinculin coordinately regulates membrane association of vinculin through direct binding to phosphatidylinositol 4,5-bisphosphate or additional ligand interactions with the tail and proline-rich domain. Modulation of these additional interactions could affect localization, formation of structural assemblies, and mechanotransduction properties.

Materials and Methods

Protein expression and purification

Vt containing residues 879–1066 of the chicken sequence was cloned into pQlinkH vector (Addgene, Cambridge, MA). MVt containing residues 879–1134 and MVt plus proline-rich linker (MVtp) containing residues 858–1134 of the human sequence were cloned in 2HR-T vector (Addgene, Cambridge, MA). Plasmids for the MVt and MVtp CM mutants, namely, A934V, ΔL954, and R975W, were prepared using appropriate primers (IDT, Skokie, IL) and QuikChange site-directed mutagenesis kit (Stratagene, La Jolla, CA) and verified by DNA sequencing (Genewiz, South Plainfield, NJ). All of the Vt and MVt/MVtp vectors contained an N-terminal TEV cleavable hexa-histidine tag. Vectors were transformed into *Escherichia coli* strain BL21(DE3), and cells were first grown at 37 °C to an optical density of 0.6–0.8 (600 nm). Protein expression was then initiated by addition of IPTG (0.5 mM for Vt, 1 mM for MVt/MVtp). Cells were then grown at 18 °C overnight and harvested by centrifugation (4,500 rpm, 30 min). Cell pellets were resuspended in lysis

buffer [20 mM Tris, 150 mM NaCl, 5 mM imidazole, 2 mM β-mercaptoethanol (pH 7.5) for Vt and 50 mM Tris, 200 mM NaCl, 10 mM imidazole, 2 mM β-mercaptoethanol (pH 8.0) for MVt/MVtp]. Cells were lysed by sonication. Vt and MVt/MVtp proteins remained in the soluble fractions that were separated from the particulate fractions by centrifugation (15,000 rpm, 45 min). Proteins were purified by affinity separation using Ni-NTA-agarose beads (Qiagen). Proteins were bound to the beads through His-tag. Wash buffer [20 mM Tris, 150 mM NaCl, 60 mM imidazole, 2 mM β-mercaptoethanol (pH 7.5) for Vt and 50 mM Tris, 200 mM NaCl, 25 mM imidazole, 2 mM β-mercaptoethanol (pH 8.0) for MVt/MVtp) was run through the column before eluting target proteins using elution buffer [20 mM Tris, 150 mM NaCl, 500 mM imidazole, 2 mM β-mercaptoethanol (pH 7.5) for Vt and 50 mM Tris, 200 mM NaCl, 250 mM imidazole, 2 mM β-mercaptoethanol (pH 8.0) for MVt/MVtp). For His-tag removal, eluted volume was dialyzed into TEV cleavage buffer [20 mM Tris, 150 mM NaCl, 50 mM imidazole, 2 mM β-mercaptoethanol (pH 7.5) for Vt and 50 mM Tris, 200 mM NaCl, 20 mM imidazole, 2 mM β-mercaptoethanol (pH 8.0) for MVt/MVtp] overnight at 4 °C in presence of TEV protease. Vt and MVt/MVtp proteins were collected by re-running the dialyzed/cleaved volumes over Ni-NTA-agarose beads. Size exclusion chromatography by S100 column (GE, Pittsburg, PA) was used to obtain the highest level of purity in gel filtration buffer [10 mM Tris, 200 mM KCl, 10 mM imidazole, 2.5 mM $MgCl_2$, 1 mM EGTA, 2 mM DTT (pH 7.5)]. Purified proteins were concentrated between 200 and 500 μM by centrifugation, aliquoted, and snap frozen using liquid nitrogen. Protein stocks were stored at – 80 °C.

Actin co-sedimentation

The actin binding and bundling (cross-linking) properties of individual Vt and MVt/MVtp WT and CM proteins as well as their mixtures were investigated using an adapted actin co-sedimentation assay previously reported [44]. Monomeric actin (G-actin), purified from rabbit muscle acetone powder (Pel-Freez Biologicals, Rogers, AR), was stored at – 80 °C in storage buffer [50 mM imidazole, 100 mM NaCl, 10 mM $MgCl_2$, 10 mM EGTA, 0.5 mM DTT, 0.2 mM ATP (pH 7.0)]. Polymerization to filamentous actin (F-actin) was done by diluting and incubating G-actin at 100 μM concentration in actin polymerization buffer [10 mM Tris, 200 mM KCl, 10 mM imidazole, 2.5 mM $MgCl_2$, 1 mM EGTA, 2 mM DTT (pH 7.5)] at room temperature for 30 min. The actin concentrations reported in this work were based on G-actin concentration, since the heterogeneity of F-actin polymers made it difficult to quantify F-actin concentrations. Vt and MVt/MVtp variants were also diluted by actin polymerization buffer to prepare 100 μM stocks. To assess actin binding, 100 μl samples were prepared containing 10 μM Vt/MVt/MVtp variants and 10 or 20 μM actin. The samples were incubated at room temperature for 1 h and then centrifuged at 100,000 RCF for 30 min. To assess actin bundling, 100 μl samples were prepared containing 10–20 μM Vt/MVt/MVtp variants and 10 μM actin. The samples were incubated at room temperature for 1 h and then centrifuged at 12,000 RCF for 15 min. For both binding and bundling co-sedimentation, the supernatant and pellet were separated, resuspended to equal volumes, and analyzed by 15% SDS-PAGE. Actin binding properties were calculated by determining the fractions of Vt/MVt/MVtp variants present in pellets using the densities of the pellet and supernatant bands. Actin bundling properties were calculated by determining the fractions of actin present in pellets using the densities of the pellet and supernatant bands. Densitometry was performed using ImageJ [38]. Statistical significances (p values) of the measurements were determined using the Microsoft Excel t-Test function.

Negative staining and TEM

For the experiments displayed in Fig. 1, an aliquot of actin (1 μM) without or with Vt, MVt, or MVtp (10 μM) was incubated in actin polymerization buffer [10 mM Tris, 200 mM KCl, 10 mM imidazole, 2.5 mM $MgCl_2$, 1 mM EGTA, 2 mM DTT (pH 7.5)] for 15 min and absorbed directly onto glow-discharged carbon-coated 400 mesh copper grids for 3 min, and then stained with 2% (w/v) uranyl acetate in water. TEM images were obtained using a FEI Tecnai 12 electron microscope at 80 kV and captured on a Gatan First Light CCD camera using Gatan Digital Micrograph software (Gatan, Pleasanton, CA).

For the experiments displayed in Figs. 3 and 5, F-actin and the indicated Vt ± MVt constructs were mixed in KMEI [50 mM KCl, 1 mM $MgCl_2$, 1 mM ethylene glycol bis(*b*-aminoethyl ether) *N,N*-tetraacetic acid (EGTA), 10 mM imidazole, 1 mM dithiothreitol (DTT), pH 7.0)] and incubated at room temperature for 15 min. Sample (4 μl) was then applied to a glow-discharged continuous carbon grid (Ted Pella) and incubated for 60 s. After incubation, the grid was washed with three 100 μl drops of 1% uranyl acetate, then blotted to dryness. Images were acquired with the SerialEM package [45] on a Tecnai F20 operating at 120 kV with a Gatan Ultrascan 4000 CCD camera. Tiled images with 20% overlap were acquired at 7800× magnification, 3 μm underfocus, and 4-fold camera binning, corresponding to a calibrated pixel size of 5.7 nm at the specimen level. Stitched images were assembled with the "blendmont" program from the IMOD software package [46].

F-actin assembly quantification

Images were thresholded and binarized using ImageJ [38], then segmented into continuous regions of pixels using the built-in "Analyze Particles" plugin, including regions 100–500,000 pixels in size and with a circularity of 0–0.3. This procedure does not always capture every region that an expert user would designate to contain F-actin in every image (e.g., areas of Supplementary Fig. 1A, right, which are not outlined in yellow). However, we find its performance superior to both manual segmentation of the images, which requires user decisions on region boundaries and the minimum size of regions, as well as a sliding-box quantification (a measure of local density), which is extremely sensitive to noise introduced by slight differences in thresholding (data not shown).

Size measurements of regions were pooled from all images for a given condition, then divided into 10,000 equal sized bins per data set and plotted via a normalized cumulative histogram (Supplementary Fig. 1B). Data were binned and cumulative sums calculated with a python script (available at www.github.com/alushinlab/FactinAssemblyQuant) using the function "binned_statistic" implemented in SciPy (www.scipy.org). Plots were generated and statistical tests were conducted with GraphPad Prism.

MD simulation

Modeling was performed using a DMD package [39,40,47]. The initial structure was obtained by extending missing N- and C-termini of MVt (PDB ID: 3JBK) [31] with PYMOL built-in tool to include residues 896–1134. The initial structure was relaxed at temperature $T = 0.5$ with high heat exchange coefficient $C_{ex} = 10$ for 10,000 steps. The temperature unit is kcal/(mol k_B).The relaxation was followed by replica exchange simulations with 10 replicas ($T = 0.330$, 0.360, 0.390, 0.420, 0.450, 0.480, 0.510, 0.540, 0.570, 0.600; $C_{ex} = 0.1$ for 2 million steps). Replicas were exchanged every 1000 steps. To preserve contacts between MVt and actin, we applied harmonic constraints to the N, CA, and C backbone atoms of selected residues (R1044, I1045, N1048, R1055, T1058, I1059, Q1062, I1065, Q1086, E1089, M1090, H1093, N1094, E1104, R1107, E1108, A1111, I1114). These constraints restrict atoms to move within 2A around initial positions. All atoms within actin were considered static and were not allowed to move. The 100 lowest-energy structures were selected and clustered based on pairwise root mean square distance between structures. Two clusters were identified.

Structures representing the centroids of the two clusters were subject to DMD simulations at two constant temperatures $T_1 = 0.5$ kcal/(mol k_B) and $T_2 = 0.55$ kcal/(mol k_B). For each temperature and for each structure, 5 independent simulations were run for 1 million steps with $C_{ex} = 0.1$. To preserve contacts between MVt and actin, we applied harmonic constraints to N, CA, and C backbone atoms of selected MVt residues (as described above). All atoms within actin were considered static.

Acknowledgments

We gratefully acknowledge Jenny Hinshaw (NIDDK) for shared use of her F20 TEM and Lucas Axiotakis Jr. for preliminary efforts in quantification of EM data. This work was supported by the National Institutes of Health (RO1GM115597, PI: S.C.; 7DP5OD017885, PI: G.M.A.; (F31HL131429, PI: H. L.; GM31819 and ES013773, PI: J.G.; GM114015 and GM123247, PI: N. V. D.) and start-up funds from the Rockefeller University (PI: G.M.A).

Appendix A. Supplementary data

Supplementary data to this article can be found online at https://doi.org/10.1016/j.jmb.2019.02.024.

Received 27 November 2018;
Received in revised form 22 February 2019;
Accepted 22 February 2019
Available online 5 March 2019

Keywords:
vinculin;
metavinculin;
actin;
cardiomyopathy;
heart

Present address: Departments of Pharmacology, Biochemistry & Molecular Biology, Pennsylvania State College of Medicine, Hershey, PA 17033, USA.

Abbreviations used:
Vh, vinculin head domain; Vt, vinculin tail domain; MVt, metavinculin tail domain; CM, cardiomyopathy; NtS, N-terminal strap; CtHP, C-terminal hairpin; DCM, dilated cardiomyopathy; HCM, hypertrophic cardiomyopathy; WT, wild-type; DMD, discrete molecular dynamics; TEM, transmission electron microscopy.

References

[1] J.T. Parsons, A.R. Horwitz, M.A. Schwartz, Cell adhesion: integrating cytoskeletal dynamics and cellular tension, Nat. Rev. Mol. Cell Biol. 11 (2010) 633–643.
[2] W.H. Ziegler, R.C. Liddington, D.R. Critchley, The structure and regulation of vinculin, Trends Cell Biol. 16 (2006) 453–460.

[3] W. Xu, H. Baribault, E.D. Adamson, Vinculin knockout results in heart and brain defects during embryonic development, Development 125 (1998) 327–337.
[4] J.L. Coll, A. Ben-Ze'ev, R.M. Ezzell, J.L. Rodriguez Fernandez, H. Baribault, R.G. Oshima, E.D. Adamson, Targeted disruption of vinculin genes in F9 and embryonic stem cells changes cell morphology, adhesion, and locomotion, Proc. Natl. Acad. Sci. U. S. A. 92 (1995) 9161–9165.
[5] M.C. Subauste, O. Pertz, E.D. Adamson, C.E. Turner, S. Junger, K.M. Hahn, Vinculin modulation of paxillin–FAK interactions regulates ERK to control survival and motility, J. Cell Biol. 165 (2004) 371–381.
[6] C. Bakolitsa, D.M. Cohen, L.A. Bankston, A.A. Bobkov, G.W. Cadwell, L. Jennings, D.R. Critchley, S.W. Craig, R.C. Liddington, Structural basis for vinculin activation at sites of cell adhesion, Nature 430 (2004) 583–586.
[7] R.P. Johnson, S.W. Craig, An intramolecular association between the head and tail domains of vinculin modulates talin binding, J. Biol. Chem. 269 (1994) 12611–12619.
[8] E.E. Weiss, M. Kroemker, A.H. Rudiger, B.M. Jockusch, M. Rudiger, Vinculin is part of the cadherin–catenin junctional complex: complex formation between alpha-catenin and vinculin, J. Cell Biol. 141 (1998) 755–764.
[9] M. Kroemker, A.H. Rudiger, B.M. Jockusch, M. Rudiger, Intramolecular interactions in vinculin control alpha-actinin binding to the vinculin head, FEBS Lett. 355 (1994) 259–262.
[10] N.P. Brindle, M.R. Holt, J.E. Davies, C.J. Price, D.R. Critchley, The focal-adhesion vasodilator-stimulated phosphoprotein (VASP) binds to the proline-rich domain in vinculin, Biochem J 318 (1996) 753–757 Pt 3.
[11] K.A. DeMali, C.A. Barlow, K. Burridge, Recruitment of the Arp2/3 complex to vinculin: coupling membrane protrusion to matrix adhesion, J. Cell Biol. 159 (2002) 881–891.
[12] N. Kioka, S. Sakata, T. Kawauchi, T. Amachi, S.K. Akiyama, K. Okazaki, C. Yaen, K.M. Yamada, S. Aota, Vinexin: a novel vinculin-binding protein with multiple SH3 domains enhances actin cytoskeletal organization, J. Cell Biol. 144 (1999) 59–69.
[13] K. Mandai, H. Nakanishi, A. Satoh, K. Takahashi, K. Satoh, H. Nishioka, A. Mizoguchi, Y. Takai, Ponsin/SH3P12: an l-afadin- and vinculin-binding protein localized at cell–cell and cell–matrix adherens junctions, J. Cell Biol. 144 (1999) 1001–1017.
[14] S. Huttelmaier, P. Bubeck, M. Rudiger, B.M. Jockusch, Characterization of two F-actin-binding and oligomerization sites in the cell-contact protein vinculin, Eur. J. Biochem. 247 (1997) 1136–1142.
[15] R.P. Johnson, V. Niggli, P. Durrer, S.W. Craig, A conserved motif in the tail domain of vinculin mediates association with and insertion into acidic phospholipid bilayers, Biochemistry 37 (1998) 10211–10222.
[16] J.H. Lee, E.S. Rangarajan, S.D. Yogesha, T. Izard, Raver1 interactions with vinculin and RNA suggest a feed-forward pathway in directing mRNA to focal adhesions, Structure 17 (2009) 833–842.
[17] J. Winkler, H. Lunsdorf, B.M. Jockusch, The ultrastructure of chicken gizzard vinculin as visualized by high-resolution electron microscopy, J. Struct. Biol. 116 (1996) 270–277.
[18] J. Golji, T. Wendorff, M.R. Mofrad, Phosphorylation primes vinculin for activation, Biophys. J. 102 (2012) 2022–2030.
[19] C.G. Galbraith, K.M. Yamada, M.P. Sheetz, The relationship between force and focal complex development, J. Cell Biol. 159 (2002) 695–705.
[20] G. Giannone, G. Jiang, D.H. Sutton, D.R. Critchley, M.P. Sheetz, Talin1 is critical for force-dependent reinforcement of initial integrin-cytoskeleton bonds but not tyrosine kinase activation, J. Cell Biol. 163 (2003) 409–419.
[21] D. Riveline, E. Zamir, N.Q. Balaban, U.S. Schwarz, T. Ishizaki, S. Narumiya, Z. Kam, B. Geiger, A.D. Bershadsky, Focal contacts as mechanosensors: externally applied local mechanical force induces growth of focal contacts by an mDia1-dependent and ROCK-independent mechanism, J. Cell Biol. 153 (2001) 1175–1186.
[22] C. Grashoff, B.D. Hoffman, M.D. Brenner, R. Zhou, M. Parsons, M.T. Yang, M.A. McLean, S.G. Sligar, C.S. Chen, T. Ha, M.A. Schwartz, Measuring mechanical tension across vinculin reveals regulation of focal adhesion dynamics, Nature 466 (2010) 263–266.
[23] B.J. Byrne, Y.J. Kaczorowski, M.D. Coutu, S.W. Craig, Chicken vinculin and meta-vinculin are derived from a single gene by alternative splicing of a 207-base pair exon unique to meta-vinculin, J. Biol. Chem. 267 (1992) 12845–12850.
[24] K. Burridge, J.R. Feramisco, Microinjection and localization of a 130K protein in living fibroblasts: a relationship to actin and fibronectin, Cell 19 (1980) 587–595.
[25] J.R. Feramisco, J.E. Smart, K. Burridge, D.M. Helfman, G.P. Thomas, Co-existence of vinculin and a vinculin-like protein of higher molecular weight in smooth muscle, J. Biol. Chem. 257 (1982) 11024–11031.
[26] A.M. Belkin, O.I. Ornatsky, A.E. Kabakov, M.A. Glukhova, V. E. Koteliansky, Diversity of vinculin/meta-vinculin in human tissues and cultivated cells. Expression of muscle specific variants of vinculin in human aorta smooth muscle cells, J. Biol. Chem. 263 (1988) 6631–6635.
[27] S. Witt, A. Zieseniss, U. Fock, B.M. Jockusch, S. Illenberger, Comparative biochemical analysis suggests that vinculin and metavinculin cooperate in muscular adhesion sites, J. Biol. Chem. 279 (2004) 31533–31543.
[28] M. Maeda, E. Holder, B. Lowes, S. Valent, R.D. Bies, Dilated cardiomyopathy associated with deficiency of the cytoskeletal protein metavinculin, Circulation 95 (1997) 17–20.
[29] E.S. Rangarajan, J.H. Lee, S.D. Yogesha, T. Izard, A helix replacement mechanism directs metavinculin functions, PLoS One 5 (2010), e10679.
[30] M.E. Janssen, H. Liu, N. Volkmann, D. Hanein, The C-terminal tail domain of metavinculin, vinculin's splice variant, severs actin filaments, J. Cell Biol. 197 (2012) 585–593.
[31] L.Y. Kim, P.M. Thompson, H.T. Lee, M. Pershad, S.L. Campbell, G.M. Alushin, The structural basis of actin organization by vinculin and metavinculin, J. Mol. Biol. 428 (2016) 10–25.
[32] T.M. Olson, S. Illenberger, N.Y. Kishimoto, S. Huttelmaier, M. T. Keating, B.M. Jockusch, Metavinculin mutations alter actin interaction in dilated cardiomyopathy, Circulation 105 (2002) 431–437.
[33] V.C. Vasile, M.L. Will, S.R. Ommen, W.D. Edwards, T.M. Olson, M.J. Ackerman, Identification of a metavinculin missense mutation, R975W, associated with both hypertrophic and dilated cardiomyopathy, Mol. Genet. Metab. 87 (2006) 169–174.
[34] K. Shen, C.E. Tolbert, C. Guilluy, V.S. Swaminathan, M.E. Berginski, K. Burridge, R. Superfine, S.L. Campbell, The vinculin C-terminal hairpin mediates F-actin bundle formation, focal adhesion, and cell mechanical properties, J. Biol. Chem. 286 (2011) 45103–45115.
[35] R.P. Johnson, S.W. Craig, Actin activates a cryptic dimerization potential of the vinculin tail domain, J. Biol. Chem. 275 (2000) 95–105.

[36] Z.A. Oztug Durer, R.M. McGillivary, H. Kang, W.A. Elam, C.L. Vizcarra, D. Hanein, E.M. De La Cruz, E. Reisler, M.E. Quinlan, Metavinculin tunes the flexibility and the architecture of vinculin-induced bundles of actin filaments, J. Mol. Biol. 427 (2015) 2782–2798.
[37] T. Meyer, U. Brink, C. Unterberg, S. Stohr, H. Kreuzer, A.B. Buchwald, Expression of meta-vinculin in human coronary arteriosclerosis is related to the histological grade of plaque formation, Atherosclerosis 111 (1994) 111–119.
[38] C.A. Schneider, W.S. Rasband, K.W. Eliceiri, NIH image to ImageJ: 25 years of image analysis, Nat. Methods 9 (2012) 671–675.
[39] F. Ding, D. Tsao, H. Nie, N.V. Dokholyan, Ab initio folding of proteins with all-atom discrete molecular dynamics, Structure 16 (2008) 1010–1018.
[40] S. Yin, F. Ding, N.V. Dokholyan, Eris: an automated estimator of protein stability, Nat. Methods 4 (2007) 466–467.
[41] B.J. Maron, J.J. Doerer, T.S. Haas, D.M. Tierney, F.O. Mueller, Sudden deaths in young competitive athletes: analysis of 1866 deaths in the United States, 1980–2006, Circulation 119 (2009) 1085–1092.
[42] B.J. Maron, W.J. McKenna, G.K. Danielson, L.J. Kappenberger, H.J. Kuhn, C.E. Seidman, P.M. Shah, W.H. Spencer 3rd, P. Spirito, F.J. Ten Cate, E.D. Wigle, American College of Cardiology/European Society of Cardiology clinical expert consensus document on hypertrophic cardiomyopathy. A report of the American College of Cardiology Foundation Task Force on Clinical Expert Consensus Documents and the European Society of Cardiology Committee for Practice Guidelines, J. Am. Coll. Cardiol. 42 (2003) 1687–1713.
[43] M.E. Janssen, E. Kim, H. Liu, L.M. Fujimoto, A. Bobkov, N. Volkmann, D. Hanein, Three-dimensional structure of vinculin bound to actin filaments, Mol. Cell 21 (2006) 271–281.
[44] R.D. Dixon, D.K. Arneman, A.S. Rachlin, N.R. Sundaresan, M.J. Costello, S.L. Campbell, C.A. Otey, Palladin is an actin cross-linking protein that uses immunoglobulin-like domains to bind filamentous actin, J. Biol. Chem. 283 (2008) 6222–6231.
[45] D.N. Mastronarde, Automated electron microscope tomography using robust prediction of specimen movements, J. Struct. Biol. 152 (2005) 36–51.
[46] J.R. Kremer, D.N. Mastronarde, J.R. McIntosh, Computer visualization of three-dimensional image data using IMOD, J. Struct. Biol. 116 (1996) 71–76.
[47] E.A. Proctor, F. Ding, N.V. Dokholyan, Discrete molecular dynamics, Wiley I.R.C. Mol. Sci. 1 (2011) 80–92.

BIBLIOGRAPHY

Adams, A.E.M., Botstein, D., and Drubin, D.G. (1991). Requirement of yeast fimbrin for actin organization and morphogenesis in vivo. Nature 354, 404–408.

Adams, P.D., Afonine, P.V., Bunkoczi, G., Chen, V.B., Davis, I.W., Echols, N., Headd, J.J., Hung, L.W., Kapral, G.J., Grosse-Kunstleve, R.W., et al. (2010). PHENIX: a comprehensive Python-based system for macromolecular structure solution. Acta Crystallogr D Biol Crystallogr 66, 213-221.

Afonine, P.V., Poon, B.K., Read, R.J., Sobolev, O.V., Terwilliger, T.C., Urzhumtsev, A., and Adams, P.D. (2018). Real-space refinement in PHENIX for cryo-EM and crystallography. Acta Crystallogr D Struct Biol 74, 531-544.

Avery, A.W., Fealey, M.E., Wang, F., Orlova, A., Thompson, A.R., Thomas, D.D., Hays, T.S., and Egelman, E.H. (2017). Structural basis for high-affinity actin binding revealed by a beta-III-spectrin SCA5 missense mutation. Nature communications 8, 1350.

Axelrod, D. (2008). Chapter 7 Total Internal Reflection Fluorescence Microscopy. In Methods in Cell Biology, (Elsevier), pp. 169–221.

Bakolitsa, C., Cohen, D.M., Bankston, L.A., Bobkov, A.A., Cadwell, G.W., Jennings, L., Critchley, D.R., Craig, S.W., and Liddington, R.C. (2004). Structural basis for vinculin activation at sites of cell adhesion. Nature 430, 583-586.

Bakolitsa, C., de Pereda, J.M., Bagshaw, C.R., Critchley, D.R., and Liddington, R.C. (1999). Crystal structure of the vinculin tail suggests a pathway for activation. Cell 99, 603-613.

Barad, B.A., Echols, N., Wang, R.Y., Cheng, Y., DiMaio, F., Adams, P.D., and Fraser, J.S. (2015). EMRinger: side chain-directed model and map validation for 3D cryo-electron microscopy. Nat Methods 12, 943-946.

Beausang, J.F., Schroeder, H.W., 3rd, Nelson, P.C., and Goldman, Y.E. (2008). Twirling of actin by myosins II and V observed via polarized TIRF in a modified gliding assay. Biophys J 95, 5820-5831.

Bieling, P., Li, T.D., Weichsel, J., McGorty, R., Jreij, P., Huang, B., Fletcher, D.A., and Mullins, R.D. (2016). Force Feedback Controls Motor Activity and Mechanical Properties of Self-Assembling Branched Actin Networks. Cell 164, 115-127.

Blanchoin, L., Boujemaa-Paterski, R., Sykes, C., and Plastino, J. (2014). Actin Dynamics, Architecture, and Mechanics in Cell Motility. Physiological Reviews 94, 235–263.

Bretscher, A., and Weber, K. (1980). Fimbrin, a new microfilament-associated protein present in microvilli and other cell surface structures. Journal of Cell Biology 86, 335–340.

Brown, A., Long, F., Nicholls, R.A., Toots, J., Emsley, P., and Murshudov, G. (2015). Tools for macromolecular model building and refinement into electron cryo-microscopy reconstructions. Acta Crystallogr D Biol Crystallogr 71, 136-153.

Buckley, C.D., Tan, J., Anderson, K.L., Hanein, D., Volkmann, N., Weis, W.I., Nelson, W.J., and Dunn, A.R. (2014). Cell adhesion. The minimal cadherin-catenin complex binds to actin filaments under force. Science 346, 1254211.

Burridge, K., and Chrzanowska-Wodnicka, M. (1996). FOCAL ADHESIONS, CONTRACTILITY, AND SIGNALING. Annu. Rev. Cell Dev. Biol. 12, 463–519.

Burridge, K., and Feramisco, J. (1980). Microinjection and localization of a 130K protein in living fibroblasts: a relationship to actin and fibronectin. Cell 19, 587–595.

Bustamante, C.J., Chemla, Y.R., Liu, S., and Wang, M.D. (2021). Optical tweezers in single-molecule biophysics. Nat Rev Methods Primers 1, 25.

Byrne, B.J., Kaczorowski, Y.J., Coutu, M.D., and Craig, S.W. (1992). Chicken vinculin and meta-vinculin are derived from a single gene by alternative splicing of a 207-base pair exon unique to meta-vinculin. Journal of Biological Chemistry 267, 12845–12850.

Charras, G., and Yap, A.S. (2018). Tensile Forces and Mechanotransduction at Cell–Cell Junctions. Current Biology 28, R445–R457.

Chen, V.B., Arendall, W.B., 3rd, Headd, J.J., Keedy, D.A., Immormino, R.M., Kapral, G.J., Murray, L.W., Richardson, J.S., and Richardson, D.C. (2010). MolProbity: all-atom structure validation for macromolecular crystallography. Acta Crystallogr D Biol Crystallogr 66, 12-21.

Cheng, Y., Grigorieff, N., Penczek, P.A., and Walz, T. (2015). A Primer to Single-Particle Cryo-Electron Microscopy. Cell 161, 438–449.

Chou, S.Z., and Pollard, T.D. (2019). Mechanism of actin polymerization revealed by cryo-EM structures of actin filaments with three different bound nucleotides. Proceedings of the National Academy of Sciences of the United States of America.

Claessens, M.M.A.E., Bathe, M., Frey, E., and Bausch, A.R. (2006). Actin-binding proteins sensitively mediate F-actin bundle stiffness. Nature Mater 5, 748–753.

Courtemanche, N., Lee, J.Y., Pollard, T.D., and Greene, E.C. (2013). Tension modulates actin filament polymerization mediated by formin and profilin. Proceedings of the National Academy of Sciences of the United States of America 110, 9752-9757.

Croll, T.I. (2018). ISOLDE : a physically realistic environment for model building into low-resolution electron-density maps. Acta Crystallogr D Struct Biol 74, 519–530.

de Almeida Ribeiro, E., Pinotsis, N., Ghisleni, A., Salmazo, A., Konarev, P.V., Kostan, J., Sjöblom, B., Schreiner, C., Polyansky, A.A., Gkougkoulia, E.A., et al. (2014). The Structure and Regulation of Human Muscle α-Actinin. Cell 159, 1447–1460.

del Rio, A., Perez-Jimenez, R., Liu, R., Roca-Cusachs, P., Fernandez, J.M., and Sheetz, M.P. (2009). Stretching Single Talin Rod Molecules Activates Vinculin Binding. Science 323, 638–641.

DeRosier, D., Tilney, L., and Flicker, P. (1980). A change in the twist of the actin-containing filaments occurs during the extension of the acrosomal process in Limulus sperm. Journal of Molecular Biology 137, 375–389.

Dominguez, R., and Holmes, K.C. (2011). Actin structure and function. Annu Rev Biophys 40, 169-186.

Drees, F., Pokutta, S., Yamada, S., Nelson, W.J., and Weis, W.I. (2005). Alpha-catenin is a molecular switch that binds E-cadherin-beta-catenin and regulates actin-filament assembly. Cell 123, 903-915.

Dumbauld, D.W., Lee, T.T., Singh, A., Scrimgeour, J., Gersbach, C.A., Zamir, E.A., Fu, J., Chen, C.S., Curtis, J.E., Craig, S.W., et al. (2013). How vinculin regulates force transmission. Proceedings of the National Academy of Sciences of the United States of America 110, 9788-9793.

Egelman, E.H. (2007). The iterative helical real space reconstruction method: surmounting the problems posed by real polymers. J Struct Biol 157, 83-94.

Egelman, E.H., Francis, N., and DeRosier, D.J. (1982). F-actin is a helix with a random variable twist. Nature 298, 131–135.

Emsley, P., Lohkamp, B., Scott, W.G., and Cowtan, K. (2010). Features and development of Coot. Acta Crystallogr D Biol Crystallogr 66, 486-501.

Fäßler, F., Dimchev, G., Hodirnau, V.-V., Wan, W., and Schur, F.K.M. (2020). Cryo-electron tomography structure of Arp2/3 complex in cells reveals new insights into the branch junction. Nat Commun 11, 6437.

Falzone, T.T., Lenz, M., Kovar, D.R., and Gardel, M.L. (2012). Assembly kinetics determine the architecture of α-actinin crosslinked F-actin networks. Nat Commun 3, 861.

Feramisco, J.R., Smart, J.E., Burridge, K., Helfman, D.M., and Thomas, G.P. (1982). Co-existence of vinculin and a vinculin-like protein of higher molecular weight in smooth muscle. Journal of Biological Chemistry 257, 11024–11031.

Finer, J.T., Simmons, R.M., and Spudich, J.A. (1994). Single myosin molecule mechanics: piconewton forces and nanometre steps. Nature 368, 113-119.

Fujii, T., Iwane, A.H., Yanagida, T., and Namba, K. (2010). Direct visualization of secondary structures of F-actin by electron cryomicroscopy. Nature 467, 724-728.

Galkin, V.E., Orlova, A., and Egelman, E.H. (2012). Actin filaments as tension sensors. Current biology : CB 22, R96-101.

Galkin, V.E., Orlova, A., Salmazo, A., Djinovic-Carugo, K., and Egelman, E.H. (2010a). Opening of tandem calponin homology domains regulates their affinity for F-actin. Nature structural & molecular biology 17, 614-616.

Galkin, V.E., Orlova, A., Schroder, G.F., and Egelman, E.H. (2010b). Structural polymorphism in F-actin. Nature structural & molecular biology 17, 1318-1323.

Garbett, D., Bisaria, A., Yang, C., McCarthy, D.G., Hayer, A., Moerner, W.E., Svitkina, T.M., and Meyer, T. (2020). T-Plastin reinforces membrane protrusions to bridge matrix gaps during cell migration. Nat Commun 11, 4818.

Gibson, D.G., Young, L., Chuang, R.Y., Venter, J.C., Hutchison, C.A., 3rd, and Smith, H.O. (2009). Enzymatic assembly of DNA molecules up to several hundred kilobases. Nat Methods 6, 343-345.

Gimona, M., and Mital, R. (1998) The single CH domain of calponin is neither sufficient nor necessary for F- actin binding. J Cell Sci. 111, 1813-1821

Gimona, M., Djinovic-Carugo, K., Kranewitter, W.J., and Winder, S.J. (2002). Functional plasticity of CH domains. FEBS Letters 513, 98–106.

Gingras, A.R., Bate, N., Goult, B.T., Hazelwood, L., Canestrelli, I., Grossmann, J.G., Liu, H., Putz, N.S.M., Roberts, G.C.K., Volkmann, N., et al. (2008). The structure of the C-terminal actin-binding domain of talin. EMBO J 27, 458–469.

Goddard, T.D., Huang, C.C., Meng, E.C., Pettersen, E.F., Couch, G.S., Morris, J.H., and Ferrin, T.E. (2018). UCSF ChimeraX: Meeting modern challenges in visualization and analysis. Protein Sci 27, 14-25.

Goldstein, D., Djeu, J., Latter, G., Burbeck, S., and Leavitt, J. (1985). Abundant Synthesis of the Transformation-induced Protein of Neoplastia Human Fibroblasts, Plastin, in Normal Lymphocytes. Cancer Res. 45, 6.

Goult, B.T., Yan, J., and Schwartz, M.A. (2018). Talin as a mechanosensitive signaling hub. Journal of Cell Biology 217, 3776–3784.

Grant, T., and Grigorieff, N. (2015). Measuring the optimal exposure for single particle cryo-EM using a 2.6 A reconstruction of rotavirus VP6. Elife 4, e06980.

Grimm, J.B., Brown, T.A., English, B.P., Lionnet, T., and Lavis, L.D. (2017). Synthesis of Janelia Fluor HaloTag and SNAP-Tag Ligands and Their Use in Cellular Imaging Experiments. Methods Mol Biol 1663, 179-188.

Grimm, J.B., English, B.P., Chen, J., Slaughter, J.P., Zhang, Z., Revyakin, A., Patel, R., Macklin, J.J., Normanno, D., Singer, R.H., et al. (2015). A general method to improve fluorophores for live-cell and single-molecule microscopy. Nat Methods 12, 244-250.

Gumbiner, B.M. (1996). Cell Adhesion: The Molecular Basis of Tissue Architecture and Morphogenesis. Cell 84, 345–357.

Gurel, P.S., Kim, L.Y., Ruijgrok, P.V., Omabegho, T., Bryant, Z., and Alushin, G.M. (2017). Cryo-EM structures reveal specialization at the myosin VI-actin interface and a mechanism of force sensitivity. Elife 6, e31125

Hansen, S.D., Kwiatkowski, A.V., Ouyang, C.Y., Liu, H., Pokutta, S., Watkins, S.C., Volkmann, N., Hanein, D., Weis, W.I., Mullins, R.D., et al. (2013). alphaE-catenin actin-binding domain alters actin filament conformation and regulates binding of nucleation and disassembly factors. Mol Biol Cell 24, 3710-3720.

Harris, A.R., Jreij, P., and Fletcher, D.A. (2018). Mechanotransduction by the Actin Cytoskeleton: Converting Mechanical Stimuli into Biochemical Signals. Annu. Rev. Biophys. 47, 617–631.

Harris, A.R., Belardi, B., Jreij, P., Wei, K., Shams, H., Bausch, A., and Fletcher, D.A. (2019). Steric regulation of tandem calponin homology domain actin-binding affinity. Mol. Biol. Cell. 30, 3112-3122.

Hashemi Shabestari, M., Meijering, A.E.C., Roos, W.H., Wuite, G.J.L., and Peterman, E.J.G. (2017). Recent Advances in Biological Single-Molecule Applications of Optical Tweezers and Fluorescence Microscopy. Methods Enzymol 582, 85-119.

Hayakawa, K., Tatsumi, H., and Sokabe, M. (2011). Actin filaments function as a tension sensor by tension-dependent binding of cofilin to the filament. J. Cell. Biol. 195, 721-727.

He, S., and Scheres, S.H.W. (2017). Helical reconstruction in RELION. J Struct Biol 198, 163-176.

Higgs, H.N., and Pollard, T.D. (2001). Regulation of Actin Filament Network Formation Through ARP2/3 Complex: Activation by a Diverse Array of Proteins. Annu. Rev. Biochem. 70, 649–676.

Holmes, K.C., Popp, D., Gebhard, W., and Kabsch, W. (1990). Atomic model of the actin filament. Nature 347, 44–49.

Huang, D.L., Bax, N.A., Buckley, C.D., Weis, W.I., and Dunn, A.R. (2017). Vinculin forms a directionally asymmetric catch bond with F-actin. Science 357, 703-706.

Humphrey, J.D., Dufresne, E.R., and Schwartz, M.A. (2014). Mechanotransduction and extracellular matrix homeostasis. Nat Rev Mol Cell Biol 15, 802–812.

Ishida, H., Jensen, K.V., Woodman, A.G., Hyndman, M.E., and Vogel, H.J. (2017). The Calcium-Dependent Switch Helix of L-Plastin Regulates Actin Bundling. Sci Rep 7, 40662.

Ishiyama, N., Sarpal, R., Wood, M.N., Barrick, S.K., Nishikawa, T., Hayashi, H., Kobb, A.B., Flozak, A.S., Yemelyanov, A., Fernandez-Gonzalez, R., et al. (2018). Force-dependent allostery of the alpha-catenin actin-binding domain controls adherens junction dynamics and functions. Nature communications 9, 5121.

Ishiyama, N., Tanaka, N., Abe, K., Yang, Y.J., Abbas, Y.M., Umitsu, M., Nagar, B., Bueler, S.A., Rubinstein, J.L., Takeichi, M., et al. (2013). An autoinhibited structure of alpha-catenin and its implications for vinculin recruitment to adherens junctions. J Biol Chem 288, 15913-15925.

Iskratsch, T., Wolfenson, H., and Sheetz, M.P. (2014). Appreciating force and shape — the rise of mechanotransduction in cell biology. Nat Rev Mol Cell Biol 15, 825–833.

Iwamoto, D.V., Huehn, A., Simon, B., Huet-Calderwood, C., Baldassarre, M., Sindelar, C.V., and Calderwood, D.A. (2018). Structural basis of the filamin A actin-binding domain interaction with F-actin. Nature structural & molecular biology 25, 918-927.

Jaalouk, D.E., and Lammerding, J. (2009). Mechanotransduction gone awry. Nat Rev Mol Cell Biol 10, 63-73.

Janssen, M.E., Kim, E., Liu, H., Fujimoto, L.M., Bobkov, A., Volkmann, N., and Hanein, D. (2006). Three-dimensional structure of vinculin bound to actin filaments. Molecular cell 21, 271-281.

Janssen, M.E., Liu, H., Volkmann, N., and Hanein, D. (2012). The C-terminal tail domain of metavinculin, vinculin's splice variant, severs actin filaments. The Journal of cell biology 197, 585-593.

Jegou, A., Carlier, M.F., and Romet-Lemonne, G. (2013). Formin mDia1 senses and generates mechanical forces on actin filaments. Nature communications 4, 1883.

Jegou, A., and Romet-Lemonne, G. (2021). Mechanically tuning actin filaments to modulate the action of actin-binding proteins. Current Opinion in Cell Biology 68, 72–80.

Johnson, R.P., and Craig, S.W. (1995). F-actin binding site masked by the intramolecular association of vinculin head and tail domains. Nature 373, 261-264.

Kanchanawong, P., Shtengel, G., Pasapera, A.M., Ramko, E.B., Davidson, M.W., Hess, H.F., and Waterman, C.M. (2010). Nanoscale architecture of integrin-based cell adhesions. Nature 468, 580–584.

Kim, D.E., Chivian, D., and Baker, D. (2004). Protein structure prediction and analysis using the Robetta server. Nucleic Acids Research 32, W526–W531.

Kim, L.Y., Thompson, P.M., Lee, H.T., Pershad, M., Campbell, S.L., and Alushin, G.M. (2016). The Structural Basis of Actin Organization by Vinculin and Metavinculin. J Mol Biol 428, 10-25.

Klein, M.G., Shi, W., Ramagopal, U., Tseng, Y., Wirtz, D., Kovar, D.R., Staiger, C.J., and Almo, S.C. (2004). Structure of the Actin Crosslinking Core of Fimbrin. Structure 12, 999–1013.

Kobielak, A., and Fuchs, E. (2004). Alpha-catenin: at the junction of intercellular adhesion and actin dynamics. Nat Rev Mol Cell Biol 5, 614-625.

Krissinel, E., and Henrick, K. (2007). Inference of macromolecular assemblies from crystalline state. J Mol Biol 372, 774-797.

Krokhotin, A., Sarker, M., Sevilla, E.A., Costantini, L.M., Griffith, J.D., Campbell, S.L., and Dokholyan, N.V. (2019). Distinct Binding Modes of Vinculin Isoforms Underlie Their Functional Differences. Structure. 27, 1527-1536

Kron, S.J., and Spudich, J.A. (1986). Fluorescent actin filaments move on myosin fixed to a glass surface. Proceedings of the National Academy of Sciences of the United States of America 83, 6272-6276.

Kuhlbrandt, W. (2014). The Resolution Revolution. Science 343, 1443–1444.

Ladoux, B., and Mège, R.-M. (2017). Mechanobiology of collective cell behaviours. Nat Rev Mol Cell Biol 18, 743–757.

Langford, G.M. (2002). Myosin-V, a Versatile Motor for Short-Range Vesicle Transport: Myosin-V Vesicle Transport. Traffic 3, 859–865.

Lecuit, T., and Yap, A.S. (2015). E-cadherin junctions as active mechanical integrators in tissue dynamics. Nat Cell Biol 17, 533-539.

Liem, R.K. (2016). Cytoskeletal Integrators: The Spectrin Superfamily. Cold Spring Harb Perspect Biol 8.

Lin, C.S., Park, T., Chen, Z.P., and Leavitt, J. (1993). Human plastin genes. Comparative gene structure, chromosome location, and differential expression in normal and neoplastic cells. Journal of Biological Chemistry 268, 2781–2792.

Maeda, M., Holder, E., Lowes, B., Valent, S., and Bies, R.D. (1997). Dilated Cardiomyopathy Associated With Deficiency of the Cytoskeletal Protein Metavinculin. Circulation. 1997, 95, 17-20

Mastronarde, D.N. (2005). Automated electron microscope tomography using robust prediction of specimen movements. J Struct Biol 152, 36-51.

Mei, L., Espinosa de los Reyes, S., Reynolds, M.J., Leicher, R., Liu, S., and Alushin, G.M. (2020). Molecular mechanism for direct actin force-sensing by α-catenin. ELife 9, e62514.

Merino, F., Pospich, S., Funk, J., Wagner, T., Kullmer, F., Arndt, H.D., Bieling, P., and Raunser, S. (2018). Structural transitions of F-actin upon ATP hydrolysis at near-atomic resolution revealed by cryo-EM. Nature structural & molecular biology 25, 528-537.

Moores, C.A., and Kendrick-Jones, J. (2000). Biochemical characterisation of the actin-binding properties of utrophin. Cell Motility and the Cytoskeleton. 46, 116-128

Mueller, J., Szep, G., Nemethova, M., de Vries, I., Lieber, A.D., Winkler, C., Kruse, K., Small, J.V., Schmeiser, C., Keren, K., et al. (2017). Load Adaptation of Lamellipodial Actin Networks. Cell 171, 188-200 e116.

Namba, Y., Ito, M., Zu, Y., Shigesada, K., and Maruyama, K. (1992). Human T Cell L-Plastin Bundles Actin Filaments in a Calcium Dependent Manner1. The Journal of Biochemistry 112, 503–507.

Oda, T., Iwasa, M., Aihara, T., Maéda, Y., and Narita, A. (2009). The nature of the globular- to fibrous-actin transition. Nature 457, 441–445.

Oda, T., Takeda, S., Narita, A., and Maeda, Y. (2019). Structural Polymorphism of Actin. J Mol Biol 431, 3217-3228.

Olson, T.M., Illenberger, S., Kishimoto, N.Y., Huttelmaier, S., Keating, M.T., and Jockusch, B.M. (2002). Metavinculin Mutations Alter Actin Interaction in Dilated Cardiomyopathy. Circulation 105, 431–437.

Otani, T., and Furuse, M. (2020). Tight Junction Structure and Function Revisited. Trends in Cell Biology 30, 805–817.

Owen, L.M., Bax, N.A., Weis, W.I., and Dunn, A.R. (2020). The C-terminal actin binding domain of talin forms an asymmetric catch bond with F-actin. bioRxiv. doi: 10.1101/2020.09.01.276568

Oztug Durer, Z.A., McGillivary, R.M., Kang, H., Elam, W.A., Vizcarra, C.L., Hanein, D., De La Cruz, E.M., Reisler, E., and Quinlan, M.E. (2015). Metavinculin Tunes the Flexibility and the Architecture of Vinculin-Induced Bundles of Actin Filaments. J Mol Biol 427, 2782-2798.

Pappas, D.J., and Rimm, D.L. (2006). Direct interaction of the C-terminal domain of alpha-catenin and F-actin is necessary for stabilized cell-cell adhesion. Cell Commun Adhes 13, 151-170.

Pardee, J.D., and Spudich, J.A. (1982). Purification of muscle actin. Methods Enzymol 85 Pt B, 164-181.

Pertea, M., Shumate, A., Pertea, G., Varabyou, A., Chang, Y.-C., Madugundu, A.K., Pandey, A., and Salzberg, S.L. (2018). Thousands of large-scale RNA sequencing experiments yield a comprehensive new human gene list and reveal extensive transcriptional noise. bioRxiv. doi: 10.1101/332825

Pettersen, E.F., Goddard, T.D., Huang, C.C., Couch, G.S., Greenblatt, D.M., Meng, E.C., and Ferrin, T.E. (2004). UCSF Chimera--a visualization system for exploratory research and analysis. J Comput Chem 25, 1605-1612.

Pokutta, S., Drees, F., Takai, Y., Nelson, W.J., and Weis, W.I. (2002). Biochemical and structural definition of the l-afadin- and actin-binding sites of alpha-catenin. J Biol Chem 277, 18868-18874.

Pokutta, S., and Weis, W.I. (2000). Structure of the Dimerization and β-Catenin- Binding Region of α-Catenin. Mol Cell. 5, 533-543

Pollard, T.D. (2016). Actin and Actin-Binding Proteins. Cold Spring Harb Perspect Biol 8, a018226.

Pollard, T.D., Cooper J.A. (2009). Actin, a Central Player in Cell Shape and Movement. Science 326, 1208-1212

Putkey, J.A., Slaughter, G.R., and Means, A.R. (1985). Bacterial expression and characterization of proteins derived from the chicken calmodulin cDNA and a calmodulin processed gene. J Biol Chem 260, 4704-4712.

Rangarajan, E.S., and Izard, T. (2013). Dimer asymmetry defines alpha-catenin interactions. Nature structural & molecular biology 20, 188-193.

Rangarajan, E.S., Lee, J.H., Yogesha, S.D., and Izard, T. (2010). A helix replacement mechanism directs metavinculin functions. PLoS One 5, e10679.

Razinia, Z., Makela, T., Ylanne, J., and Calderwood, D.A. (2012). Filamins in mechanosensing and signaling. Annu Rev Biophys 41, 227-246.

Reymann, A.-C., Boujemaa-Paterski, R., Martiel, J.-L., Guerin, C., Cao, W., Chin, H.F., De La Cruz, E.M., Thery, M., and Blanchoin, L. (2012). Actin Network Architecture Can Determine Myosin Motor Activity. Science 336, 1310–1314.

Risca, V.I., Wang, E.B., Chaudhuri, O., Chia, J.J., Geissler, P.L., and Fletcher, D.A. (2012). Actin filament curvature biases branching direction. Proceedings of the National Academy of Sciences of the United States of America 109, 2913-2918.

Robinson, R.C., Turbedsky, K., Kaiser, D.A., Marchand, J.-B., Higgs, H.N., Choe, S., and Pollard, T.D. (2001). Crystal Structure of Arp2/3 Complex. 294, 7.

Rohou, A., and Grigorieff, N. (2015). CTFFIND4: Fast and accurate defocus estimation from electron micrographs. J Struct Biol 192, 216-221.

Romet-Lemonne, G., and Jegou, A. (2013). Mechanotransduction down to individual actin filaments. Eur J Cell Biol 92, 333-338.

Sarker, M., Lee, H.T., Mei, L., Krokhotin, A., de los Reyes, S.E., Yen, L., Costantini, L.M., Griffith, J., Dokholyan, N.V., Alushin, G.M., et al. (2019). Cardiomyopathy Mutations in Metavinculin Disrupt Regulation of Vinculin-Induced F-Actin Assemblies. Journal of Molecular Biology 431, 1604–1618.

Sauvanet, C., Wayt, J., Pelaseyed, T., and Bretscher, A. (2015). Structure, Regulation, and Functional Diversity of Microvilli on the Apical Domain of Epithelial Cells. Annu. Rev. Cell Dev. Biol. 31, 593–621.

Schiffhauer, E.S., Luo, T., Mohan, K., Srivastava, V., Qian, X., Griffis, E.R., Iglesias, P.A., and Robinson, D.N. (2016). Mechanoaccumulative Elements of the Mammalian Actin Cytoskeleton. Current biology : CB 26, 1473-1479.

Schmid, M.F., Jakana, J., Matsudaira, P., and Chiu, W. (1993). Imaging Frozen, Hydrated Acrosomal Bundle from Limulus Sperm at 7 Å Resolution with a 400 kV Electron Cryomicroscope. J Mol Biol 230, 384-386

Schmid, M.F., Sherman, M.B., Matsudaira, P., and Chiu, W. (2004). Structure of the acrosomal bundle. Nature 431, 104–107.

Schneider, C.A., Rasband, W.S., and Eliceiri, K.W. (2012). NIH Image to ImageJ: 25 years of image analysis. Nat Methods 9, 671-675.

Schuh, M. (2011). An actin-dependent mechanism for long-range vesicle transport. Nat Cell Biol 13, 1431–1436.

Schwebach, C.L., Agrawal, R., Lindert, S., Kudryashova, E., and Kudryashov, D.S. (2017). The Roles of Actin-Binding Domains 1 and 2 in the Calcium-Dependent Regulation of Actin Filament Bundling by Human Plastins. Journal of Molecular Biology 429, 2490–2508.

Schwebach, C.L., Kudryashova, E., Zheng, W., Orchard, M., Smith, H., Runyan, L.A., Egelman, E.H., and Kudryashov, D.S. (2020). Osteogenesis imperfecta mutations in plastin 3 lead to impaired calcium regulation of actin bundling. Bone Res 8, 21.

Shaaban, M., Chowdhury, S., and Nolen, B.J. (2020). Cryo-EM reveals the transition of Arp2/3 complex from inactive to nucleation-competent state. Nat Struct Mol Biol 27, 1009–1016.

Shapiro, L., and Weis, W.I. (2009). Structure and Biochemistry of Cadherins and Catenins. Cold Spring Harbor Perspectives in Biology 1, a003053.

Shimizu, K., and Stopfer, M. (2013). Gap junctions. Current Biology 23, R1026–R1031.
Shin, H., Drew, K.R.P., Bartles, J.R., Wong, G.C.L., and Grason, G.M. (2009). Cooperativity and Frustration in Protein-Mediated Parallel Actin Bundles. Phys. Rev. Lett. 103, 238102.

Shin, H., Drew, K.R.P., Bartles, J.R., Wong, G.C.L., and Grason, G.M. (2009). Cooperativity and Frustration in Protein-Mediated Parallel Actin Bundles. Phys. Rev. Lett. 103, 238102.

Shin, J.H., Mahadevan, L., Waller, G.S., Langsetmo, K., and Matsudaira, P. (2003). Stored elastic energy powers the 60-µm extension of the Limulus polyphemus sperm actin bundle. Journal of Cell Biology 162, 1183–1188.

Shin, J.H., Mahadevan, L., So, P.T., and Matsudaira, P. (2004). Bending Stiffness of a Crystalline Actin Bundle. Journal of Molecular Biology 337, 255–261.

Shinomiya, H. (2012). Plastin Family of Actin-Bundling Proteins: Its Functions in Leukocytes, Neurons, Intestines, and Cancer. International Journal of Cell Biology 2012, 1–8.

Sievers, F., and Higgins, D.G. (2014). Clustal Omega, accurate alignment of very large numbers of sequences. Methods Mol Biol 1079, 105-116.

Simon, S.M. (2009). Partial internal reflections on total internal reflection fluorescent microscopy. Trends in Cell Biology 19, 661–668.

Sindelar, C., and Huehn, A. (2016). Vinculin: An Unfolding Tale. Journal of Molecular Biology 428, 1–4.

Stevenson, R.P., Veltman, D., and Machesky, L.M. (2012). Actin-bundling proteins in cancer progression at a glance. Journal of Cell Science 125, 1073–1079.

Stokes, D.L. (2007). Desmosomes from a structural perspective. Current Opinion in Cell Biology 19, 565–571.

Sun, X., Phua, D.Y.Z., Axiotakis, L., Smith, M.A., Blankman, E., Gong, R., Cail, R.C., Espinosa de los Reyes, S., Beckerle, M.C., Waterman, C.M., et al. (2020). Mechanosensing through Direct Binding of Tensed F-Actin by LIM Domains. Developmental Cell 55, 468-482.e7.

Sun, Y., Schroeder, H.W., 3rd, Beausang, J.F., Homma, K., Ikebe, M., and Goldman, Y.E. (2007). Myosin VI walks "wiggly" on actin with large and variable tilting. Molecular cell 28, 954-964.

Svitkina, T.M. (2020). Actin Cell Cortex: Structure and Molecular Organization. Trends in Cell Biology 30, 556–565.

Sweeney, H.L., and Holzbaur, E.L.F. (2018). Motor Proteins. Cold Spring Harb Perspect Biol 10, a021931.

Tee, Y.H., Shemesh, T., Thiagarajan, V., Hariadi, R.F., Anderson, K.L., Page, C., Volkmann, N., Hanein, D., Sivaramakrishnan, S., Kozlov, M.M., et al. (2015). Cellular chirality arising from the self-organization of the actin cytoskeleton. Nat Cell Biol 17, 445–457.

Thompson, P.M., Tolbert, C.E., Shen, K., Kota, P., Palmer, S.M., Plevock, K.M., Orlova, A., Galkin, V.E., Burridge, K., Egelman, E.H., et al. (2014). Identification of an actin binding surface on vinculin that mediates mechanical cell and focal adhesion properties. Structure 22, 697-706.

Tropea, J.E., Cherry, S., and Waugh, D.S. (2009). Expression and purification of soluble His(6)-tagged TEV protease. Methods Mol Biol 498, 297-307.

Tojkander, S., Gateva, G., and Lappalainen, P. (2012). Actin stress fibers – assembly, dynamics and biological roles. Journal of Cell Science 125, 1855–1864.

Vaezi, A., Bauer, C., Vasioukhin, V., and Fuchs, E. (2002). Actin cable dynamics and Rho/Rock orchestrate a polarized cytoskeletal architecture in the early steps of assembling a stratified epithelium. Dev Cell 3, 367-381.

Vasile, V.C., Ommen, S.R., Edwards, W.D., and Ackerman, M.J. (2006). A missense mutation in a ubiquitously expressed protein, vinculin, confers susceptibility to hypertrophic cardiomyopathy. Biochemical and Biophysical Research Communications 345, 998–1003.

Volkmann, N., et al. (2001). Structure of Arp2/3 Complex in Its Activated State and in Actin Filament Branch Junctions. Science 293, 2456–2459.

von der Ecken, J., Müller, M., Lehman, W., Manstein, D.J., Penczek, P.A., and Raunser, S. (2015). Structure of the F-actin–tropomyosin complex. Nature 519, 114–117.

von der Ecken, J., Heissler, S.M., Pathan-Chhatbar, S., Manstein, D.J., and Raunser, S. (2016). Cryo-EM structure of a human cytoplasmic actomyosin complex at near-atomic resolution. Nature 534, 724–728.

Walko, G., Castañón, M.J., and Wiche, G. (2015). Molecular architecture and function of the hemidesmosome. Cell Tissue Res 360, 363–378.

Wang, F., Chen, L., Arcucci, O., Harvey, E.V., Bowers, B., Xu, Y., Hammer, J.A., 3rd, and Sellers, J.R. (2000). Effect of ADP and ionic strength on the kinetic and motile properties of recombinant mouse myosin V. J Biol Chem 275, 4329-4335.

Wang, R.Y., Song, Y., Barad, B.A., Cheng, Y., Fraser, J.S., and DiMaio, F. (2016). Automated structure refinement of macromolecular assemblies from cryo-EM maps using Rosetta. Elife 5, e17219

Weirich, K.L., Banerjee, S., Dasbiswas, K., Witten, T.A., Vaikuntanathan, S., and Gardel, M.L. (2017). Liquid behavior of cross-linked actin bundles. Proc Natl Acad Sci USA 114, 2131–2136.

Winkelman, J.D., Anderson, C.A., Suarez, C., Kovar, D.R., and Gardel, M.L. (2020). Evolutionarily diverse LIM domain-containing proteins bind stressed actin filaments through a conserved mechanism. Proc Natl Acad Sci USA 117, 25532–25542.

Wioland, H., Jegou, A., and Romet-Lemonne, G. (2019). Torsional stress generated by ADF/cofilin on cross-linked actin filaments boosts their severing. Proc Natl Acad Sci USA 116, 2595–2602.

Xu, X.-P., Pokutta, S., Torres, M., Swift, M.F., Hanein, D., Volkmann, N., and Weis, W.I. (2020). Structural basis of αE-catenin–F-actin catch bond behavior. ELife 9, e60878.

Yamada, S., Pokutta, S., Drees, F., Weis, W.I., and Nelson, W.J. (2005). Deconstructing the cadherin-catenin-actin complex. Cell 123, 889-901.

Yang, H., Lin, L., Sun, K., Zhang, T., Chen, W., Li, L., Xie, Y., Wu, C., Wei, Z., and Yu, C. (2021). Complex structures of Rsu1 and PINCH1 reveal a regulatory mechanism of the ILK/PINCH/Parvin complex for F-actin dynamics. ELife 10, e64395.

Yonemura, S., Wada, Y., Watanabe, T., Nagafuchi, A., and Shibata, M. (2010). alpha-Catenin as a tension transducer that induces adherens junction development. Nat Cell Biol 12, 533-542.

Zhang, R., Alushin, G.M., Brown, A., and Nogales, E. (2015). Mechanistic Origin of Microtubule Dynamic Instability and Its Modulation by EB Proteins. Cell 162, 849-859.

Zheng, S.Q., Palovcak, E., Armache, J.P., Verba, K.A., Cheng, Y., and Agard, D.A. (2017). MotionCor2: anisotropic correction of beam-induced motion for improved cryo-electron microscopy. Nat Methods 14, 331-332.

Ziegler, W.H., Liddington, R.C., and Critchley, D.R. (2006). The structure and regulation of vinculin. Trends Cell Biol 16, 453-460.

Zimmermann, D., Homa, K.E., Hocky, G.M., Pollard, L.W., De La Cruz, E.M., Voth, G.A., Trybus, K.M., and Kovar, D.R. (2017). Mechanoregulated inhibition of formin facilitates contractile actomyosin ring assembly. Nature communications 8, 703.

Zivanov, J., Nakane, T., Forsberg, B.O., Kimanius, D., Hagen, W.J., Lindahl, E., and Scheres, S.H. (2018). New tools for automated high-resolution cryo-EM structure determination in RELION-3. Elife 7.

Zivanov, J., Nakane, T., and Scheres, S.H.W. (2019). A Bayesian approach to beam-induced motion correction in cryo-EM single-particle analysis. IUCrJ 6, 5-17.